

## ABSTRACT

JOSHIPURA, ISHAN DHIREN. Wet and Dry Approaches to Preventing the Adhesion of Soft, Oxide-coated Liquid Metals for Reconfigurable Electronics (Under the direction of Dr. Michael D. Dickey).

Room-temperature liquid metals are a class of materials that uniquely combine low viscosities of liquids with high conductivities of metals (both electrical and thermal), as well as being optically reflective. These materials are useful as conductors for new platforms of electronics that may be: softer than skin, flexible or stretchable, as well as reconfigurable. This work studies the behavior of alloys of gallium (Ga), which possess low melting points ( $<30^{\circ}\text{C}$ ), low toxicities (relative to mercury), high surface tension ( $\sim 400$  to  $600\text{ mN/m}$ ), and are also commercially available. In addition, alloys of Ga form a thin ( $\sim 3\text{ nm}$ ) surface oxide that alters its interfacial behavior. Specifically, this oxide ‘skin’ exhibits a yield stress and adheres to many surfaces. The adhesion of the oxide is useful for patterning the metal, yet a challenge for reconfiguring the metal within confined spaces (i.e., capillaries, microfluidic channels, and cavities). In this work, we study this adhesion process and utilize it to pattern the metal when useful over conventional techniques (i.e., lithography) First, we review methods to pattern liquid metals, which we differentiate into four broad categories: injection-based, lithography-enabled, additive, and subtractive. Thereafter, the main objective of this work is to address the challenge of reconfiguring liquid metals in confined spaces by preventing oxide adhesion.

One approach to preventing oxide adhesion is to inject water into channels prior to injecting the liquid metal. As a result, water forms an interfacial slip-layer between the metal and channel wall. Thereafter, applying voltage to the ends of the channels actuates the metal by creating a gradient of surface tension along the length of the metal; this effect is known as continuous electrowetting (CEW). We study the electro-hydrodynamics of CEW effect and determine that

CEW is possible in aqueous electrolytes with the oxide present. In addition, we show that non-aqueous electrolytes can also enable CEW. Compared to water, non-aqueous electrolytes absorb less electromagnetic radiation. As such, we utilize CEW in methanol to demonstrate electrically reconfigurable filters in the terahertz (THz) region.

Alternatively, rough surfaces can prevent the adhesion of oxide-coated liquid metals. Through contact angle measurements, we show that surface roughness is more important than surface chemistry for preventing the adhesion. Herein, we show a simple approach to form rough surfaces via superhydrophobic spray-coating; we utilize these coatings to actuate liquid metals in closed channels and demonstrate reconfigurable monopole antennas. Furthermore, we utilize these rough surfaces to selectively pattern sub-mm traces of liquid metals, which are open-to-air and electrically addressable.

In addition, we examine the wetting behavior of oxide-coated liquid metals to flat surfaces, in comparison to water, using conventional tools that measure contact angles. During these measurements, the oxide pins to the substrate, which prevents the drop from truly receding and subsequently leads to irreversible adhesion. In addition, results from these measurements depend on whether the oxide ruptures upon contact with the substrate. In comparison to simple fluids such as water, the oxide skin complicates the quantitative interpretation of contact angle measurements.

Finally, we provide a brief overview on future directions of research with liquid metals and a topical highlight on current and future directions for stretchable bioelectronics.

© Copyright 2018 by Ishan Dhiren Joshipura

All Rights Reserved

Wet and Dry Approaches to Preventing the Adhesion of Soft, Oxide-coated Liquid Metals for Reconfigurable Electronics

by  
Ishan Dhiren Joshipura

A dissertation submitted to the Graduate Faculty of  
North Carolina State University  
in partial fulfillment of the  
requirements for the degree of  
Doctor of Philosophy

Chemical Engineering

Raleigh, North Carolina

2018

APPROVED BY:

---

Dr. Michael Dickey  
Committee Chair

---

Dr. Jacob Adams

---

Dr. Orlin Velev

---

Dr. Peter Fedkiw

## **DEDICATION**

*To my parents, Dhiren and Smita Joshipura, whose hard work, sacrifice, endless support and love made this opportunity possible.*

*This thesis is in loving memory of Dadi, Dada, and Pappaji. Your sacrifices, support, forward-thinking attitude allowed us to live in the US and pursue higher education. You are not with us today but we remember you daily.*

## BIOGRAPHY

Ishan Dhiren Joshipura was born in Ahmedabad, Gujarat, India, a hot semi-arid climate, to parents Dhiren and Smita Joshipura. In 1998, his family immigrated to the United States. After a brief stay in a humid, subtropical climate in Richmond, VA, Ishan grew up in Phoenix, AZ, a hot dessert climate part of the Sonoran Desert. Ishan attended the University of Arizona in Tucson, AZ for baccalaureate studies, following the footsteps of his elder sister, Keta Pandit. At the University of Arizona, Ishan participated in research with Prof. Anthony Muscat on thin-film deposition for inorganic solar cells and Prof. Paul Blowers on environmental modeling of dry cleaning systems through NASA Space Grant. Upon graduating from the University of Arizona with a BS in Chemical Engineering (December 2012, *cum laude*), he pursued graduate studies for chemical engineering at North Carolina State University in Raleigh, NC, which is a humid, subtropical climate. Under the guidance of Prof. Michael Dickey, Ishan studied liquid metals for flexible, stretchable, and reconfigurable electronics. In 2015, Ishan received an MS in Chemical Engineering from NC State University and completed an internship at MIT Lincoln Laboratories working on microfluidic technologies with Dr. Jacob Kedzierski. At NC State, Ishan also participated in the Preparing the Professoriate Fellowship with the mentorship of Prof. Matthew Cooper and Prof. Lisa Bullard. Upon graduating from NC State University, manifest destiny will guide Ishan to the Bay Area in California, a Mediterranean climate. There, Ishan will begin his professional career as a post-doctoral researcher at Lawrence Livermore National Laboratory.

## ACKNOWLEDGMENTS

The support of many people, from both personal and professional aspects, has allowed me to both pursue and attain a PhD. I cannot possibly thank everyone that has helped me in achieving a PhD. Nevertheless, I would like to acknowledge several whom have played a crucial role.

*Mummy, Pappa, Keta, Parth:* Thank you for the sacrifices you have made that allowed me to pursue higher education. Your constant encouragement, endless support, and laughter carried me through my trials and tribulations. Thank you for your patience with me as I learned lessons the hard way. Each of you are wonderful role-models and I am grateful beyond words for everything you have provided me. I still can't afford (at least) two mortgages. ;)

*Eira:* You instilled joy and hope into my life since the day you started kicking your feet. Your boundless spirit and positivity allowed our family to get through difficult times. Dhingloo, keep dancing, singing and learning. Wanna go to Yellowstone!?

*Aruna Foi and Digant Fua:* I am so grateful for your endless support, kindness, and love that has allowed me and so many others to live and pursue opportunities in the US.

*Dr. Michael Dickey:* I am privileged to be your student. I am blessed to have your constant support, kindness, encouragement, enthusiasm, stream of ideas, and optimism. Thank you also for your patience with me as I learned to be both a better researcher and person. I am so appreciative of you for providing me with countless opportunities both within and outside our lab. Despite your best efforts with teaching me to write, I am unable to fully and properly articulate my gratitude towards you. It has been an opportunity of a lifetime to be in your group. I am forever grateful for your guidance and friendship.

I would like to thank Dr. Michael Dickey, Dr. Orlin Velev, Dr. Glenn Walker, Dr. Peter Fedkiw, and Dr. Jacob Adams for serving on my thesis committee. Thank you for your encouragement, helpful feedback, and guidance over the last 5 years.

*Dr. Matthew Cooper:* Thank you so much for stopping me in the hallway during Summer 2016 and offering to be my teaching mentor. The next year and half became an opportunity of a lifetime. I learned so much from you regarding the teaching profession, life, and baseball. I am so grateful for your mentorship and friendship.

*Dr. Bullard:* Thank you for the opportunities to TA for 205 (twice), your encouragement, and warmth. I admire your positivity, professional spirit, and drive to educate and mentor students.

*Dr. Abolhasani, Dr. Hsiao, and Dr. San Miguel:* Thank you for being supportive, sharing ideas, and for your patience as we navigated CHE 205.

*Dr. Genzer:* Your positive nature, sense of humor, and encouragement guided me through difficult periods of graduate school (via LASER, of course). Through our interactions, you cultivated a curiosity about science (interfacial behavior, soft materials, and carotenoids), and perhaps most importantly provided me with inner confidence.

*Dr. Velev* Thank you for kind attitude, enthusiasm, support with academic and professional pursuits, teaching me about colloids and interfacial science, and as well as your inspirational work.

*Dr. Adams:* Thank you for providing me opportunities to work on interdisciplinary topics. I am grateful for your guidance, support, and patience over last few years.

*Dr. Kiani:* Thanks for patiently teaching all of us electrochemistry and for being so kind.

*To CBE Staff:* Sandra Bailey, Joan O'Sullivan, Mike Mantini, Sandra Doby, Angela Efimenko, Michelle Bunce, Kathleen Berding, and Amy Alexander. I often came to your offices in with

confusion, doubt, and stress and left feeling better and with more certainty. Thank you so much for the countless times you helped me and doing so with patience, kindness, and positivity.

*AIF Staff:* Thanks to Chuck Mooney and Elaine Zhou of AIF for all their help with SEM and TOF-SIMS measurements, respectively. This work would have been possible without your support and advice.

I also would like to thank the following people for their help with various professional development programs I participated at NC State. Casey Boutwell, Elena Veety, and Ember Melcher of ASSIST Center, Jason Cramer of the Graduate School, as well as the PTP Program. Thanks all for your advice and encouragement that provided me with a well-rounded learning experience at NC State.

*Dean Peter Harries:* Thank you for the opportunity to participate in the PTP program. I appreciate your wisdom and guidance regarding academia, and your positive attitude.

*Dickey Group:* I want to thank Dickey Group Members, past and present, for their collegiality, support, and friendship. I learned so much from all the group members and I wouldn't have made it without your support and friendship. Collin Eaker, I am so grateful for your mentorship, patience, and friendship. I am grateful for the support and comradery provided by Dishit Parekh, Yiliang Lin, Amber Hubbard, Taylor Neumann, Minyung Song, Tim Shay, Collin Ladd, Gilbert Castillo, Duncan Davis, Dan Armstrong, Ying Liu, Kunal Mondal, Sungjune Park, Kural Arutselvan, Collin Ladd, Yang Jin, Daniel Morales, Russ Mailen, Farzard Rezai, Mohammed Mohammed, and Rashed Khan. Dishit, Yiliang, Amber, Taylor, Minyung, Tim, and Gilbert, I am so grateful for your friendship, kindness, and support that extends beyond the lab. I also want to thank the undergraduate students who worked with me in the lab: Hudson Ayers, Alex Hsain, Alex Johnson, Michael Larkins, Chujun Ni, Mohanad Alsafatwi, Alex Persson, Daehong Kim, Yubo Ouyang,

Ethan Strubinger, Casey Hillenburg, Yash Patil, and Chris Cooper, for your enthusiasm, hard work, dedication, and patience. All of you taught and inspired me as much as I (hopefully) taught you.

I also would like to thank my collaborators for making the research so meaningful. Thanks for Dr. Chris Tabor for providing me and others the opportunity to pursue reconfigurable liquid metals! Thanks to the rest of the AFRL/Cincinnati team: Prof. Jason Heikenfeld, Sarah Holcomb, Alex Watson, and Nahid Ilyas. Thanks to Vivek Bharambe for patiently explaining me electromagnetics, hard work, and sense of humor. Thank you Kim Reichel for your curiosity, positivity, and enthusiasm; an unexpected collaboration led to a great friendship! Thank you to Shiyang Tang for being an inspirational role model, collaborator, and friend. Working with you all on interdisciplinary topics was invigorating and enriched my graduate experience. Finally, thanks to Prof. Carmel Majidi and Prof. Darren Lipomi for providing feedback and patiently editing my writing for the mini-reviews. It was a pleasure to work with you all, travel to conferences, and become friends!

*Centennial Toastmaster's*: Thank you for being a supportive and enthusiastic group, particularly Robin Boudwin, Roger Margaery, Chuck Gaisel, Andrea Sato, Dave Warner, and Robert Blaser. I learned so much and gained self-confidence from Toastmaster's. I will miss this club very much.

*2009 Firth of Tay Way*. Anurodh Tripathi, Devangana Triptahi, Rohan Patil (4.0), Prajesh Adhikari (20 and counting), Ankit Chandra, and Kruti Suchde. I hold dear the memories we made: Brownian motion, bottom-up and top-down processes, yard/house cleaning, BBQs on the deck, settlements in living room, food we made in the kitchen, failed gardening, inventions in garage, scary stories in the laundry room, and many more. Thank you for your friendship, patience, and support. I hope for many “debuts” for years to come.

I am so grateful to friends that made my time in Raleigh special meaningful provided support through difficult times. Ryan R. Barton, Ph.D., Ph.D., Jennifer A. Clark (crane it), Marius and Suzette Rutkevicius, Admiral Matthew Melillo, Shreya Erramilli, Joe and Deepti Tilly, David Chang, Chris Zhou, Amit Mishra, Jess Yano, Sangchul Roh, Adam and Shennie Quintanilla, Jason Coffman (*Clear eyes, Full Hearts, Can't Lose*), Vasudev Haribal, STP Bharadwaja, Ryan Leenay, Jenny Ovental, Eric Stevens, Mariah and Dex King, Kevin and Brittany Mertens, Trang Nguyen, Jonathan Tortensen, Dikran Kesal, Dan and Jenna Armstrong, Marty and Margaret Dufficy, Paul Lemaire, Mack Geiger, Zach Mundy, Ryan Dudek, Dilara Sen, Rachel Nye, Victoria Karakis, Dan Jackson, and Emily Krzystowczyk. Your friendship made me look forward to coming to EB1 every day and to Trophy Brewing on some days instead!

Finally, thanks to friends from “back home” who are now dispersed across many climates that helped me get through graduate school: Nimish and Sarika Sheth, Adam Olshansky, David Olshansky, Dan Quach, Hillary Vance, Mohan Narayanan, Alex Tiplea, Ben Anderson, Nabila Huq, Alex Harris, Jon Yang, Teresa Cove, Heather Rogan, and Sarah Dischinger!

# TABLE OF CONTENTS

<b>LIST OF TABLES</b> .....	xi
<b>LIST OF FIGURES</b> .....	xii
<b>Chapter 1 Methods to Pattern Liquid Metals</b> .....	1
<b>Abstract</b> .....	2
<b>Why pattern liquid metals?</b> .....	2
<b>How to pick a liquid metal?</b> .....	4
<b>Overview</b> .....	6
<b>Patterning techniques for liquid metal</b> .....	7
Lithography-enabled patterning.....	7
Injection .....	9
Subtractive .....	11
Additive.....	12
<b>Current challenges and opportunities with Ga-based liquid metals</b> .....	14
<b>Outlook</b> .....	17
<b>Acknowledgements</b> .....	17
<b>List of Supplemental Figures</b> .....	18
<b>References</b> .....	21
<b>Chapter 2 Wet Approach: Electro-hydrodynamics of Continuous Electrowetting</b> .....	24
<b>Abstract</b> .....	25
<b>Introduction</b> .....	25
Electrochemical Impedance Spectroscopy (EIS).....	28
<b>Results</b> .....	29
Characterizing the displacement of drops.....	29
Reconfigurable Terahertz Waveguides.....	36
Electrochemical impedance spectroscopy (EIS).....	37
Equivalent circuit modeling.....	44
Conclusions and Future Work .....	50
<b>Acknowledgements</b> .....	51
<b>References</b> .....	52
<b>Chapter 3 Dry Approach: Patterning and Reversible Actuation of Liquid Gallium Alloys by Preventing Adhesion on Rough Surface</b> .....	54
<b>Abstract</b> .....	55
<b>Introduction</b> .....	55
<b>Experimental Design</b> .....	58
<b>Results</b> .....	60
Composition and Morphology of NeverWet .....	67
<b>Applications</b> .....	72
Patterning .....	72
Reversible actuation inside closed channels .....	74
Reconfigurable monopole antenna .....	76
<b>Conclusions</b> .....	77
<b>Acknowledgements</b> .....	78

<b>References</b> .....	80
<b>Chapter 4 Are Contact Angle Measurements Useful for Oxide-Coated Liquid Metals?</b> ....	84
<b>Abstract</b> .....	85
<b>Introduction</b> .....	85
Oxide ‘Skin’ of Liquid Metals .....	86
Conventional Contact Angle Measurements .....	89
Sliding angle measurements .....	91
<b>Results</b> .....	92
Dynamic contact angle measurements.....	92
Dynamic contact angle measurements: Advancing measurements .....	93
Dynamic contact angle measurements: Receding measurements.....	96
Oxide spider-web patterns .....	101
Sliding angle measurements .....	104
<b>Discussion</b> .....	107
<b>Conclusions</b> .....	110
<b>Acknowledgements</b> .....	111
<b>References</b> .....	112
<b>Chapter 5 Stretchable bioelectronics— current and future</b> .....	116
<b>Abstract</b> .....	117
<b>Introduction</b> .....	117
<b>Materials and mechanics</b> .....	123
<b>Soft Robotics</b> .....	126
<b>Outlook and future challenges</b> .....	128
Biological integration.....	128
Materials and mechanics.....	129
Power .....	129
Creating real-world solution .....	130
<b>Conclusions</b> .....	130
<b>Acknowledgements</b> .....	131
<b>References</b> .....	133
<b>Chapter 6 Conclusions and Future Work</b> .....	138
<b>APPENDICES</b> .....	140
<b>Appendix A Supporting Information for Chapter 2</b> .....	141
<b>Appendix B Supporting Information for Chapter 3</b> .....	151
<b>Appendix C Supporting Information for Chapter 4</b> .....	160

## LIST OF TABLES

<b>Table 2-1:</b> Ratios of displacement and velocity of NaOH to NaF for 1.0 V <sub>pp</sub> and 2.0 V <sub>pp</sub> at 0.5 Hz, 1.0 Hz, and 3.0 Hz. ....	33
<b>Table A-1:</b> Solution resistance values for Cu, W, and Pt electrodes. Solution resistance values for Cu, W, and Pt electrodes were measured using EIS of a glass capillary filled with an electrolyte (1 M NaOH and 1 M NaF). Tabulated values are impedance values at 100 kHz.....	142
<b>Table A-2:</b> Displacement and velocity comparison for 1 M NaOH for change in voltage (Voltage Ratio) at 0.5 Hz, 1.0 Hz, and 1 Hz. ....	143
<b>Table A-3:</b> Displacement and velocity ratios for 1 M NaF for changes in voltage (Voltage Ratio) at 0.5 Hz, 1.0 Hz, and 1 Hz. ....	143
<b>Table A-4:</b> Displacement and velocity ratios for changes in frequency (Frequency Ratio) for 1 M NaOH at 1.0 V and 2.0 V. ....	143
<b>Table A-5:</b> Displacement and velocity ratios for changes in frequency (Frequency Ratio) for 1 M NaF at 1.0 V and 2.0 V. ....	144
<b>Table A-6:</b> Model parameters for 1.6 cm EGaIn plug in 1 M NaOH. Standard deviations are from model fits of 100 iterations.....	149
<b>Table A-7:</b> Model parameters for 3.6 cm EGaIn plug in 1 M NaOH. Standard deviations are from model fits of 100 iterations. Model parameters for 3.6 cm EGaIn plug in 1 M NaOH. Standard deviations are from model fits of 100 iterations. ....	150
<b>Table C-1:</b> Effect of flow rate on advancing and receding contact angles for DI water on silane-treated glass. Average and standard deviation values are provided of three experimental trials. Total average and standard deviation values are of the average values for all flow rates.....	162
<b>Table C-2:</b> Effect of flow rate on advancing and receding contact angles for EGaIn on glass and silane-treated glass. Average and standard deviation values are provided of three experimental trials. Total average and standard deviation values are of the average values for all flow rates.....	163

## LIST OF FIGURES

- Figure 1-1:** Overview of liquid metals. Gallium and its alloys form a surface oxide, which allows them to be micro-moldable<sup>14</sup>. The oxide enables several patterning techniques, including direct-write (as shown above) and potential applications<sup>16-19</sup>. Figure from Liquid Metals adapted from Ref. 14. Copyright Wiley 2011. Figure from Applications (i) adapted from Ref. 16. Copyright Wiley 2011. Figure from Applications (iv) reprinted with permission from Ref. 19. Copyright Applied Physics Letters, AIP Publishing LLC ..... 4
- Figure 1-2:** Lithography-enabled techniques allow for high resolution patterning of liquid metals, such as imprint lithography<sup>22</sup>. Figures adapted from Ref. 22. Copyright Wiley 2014..... 7
- Figure 1-3:** Injection is a versatile technique for embedding two and three-dimension metal structures in elastomers. (i) Photolithography or rapid prototyping creates an elastomeric topographical mold. An additional layer of elastomer seals the replica mold. Inlet and outlet holes are punched. (ii) A syringe (not pictured) injects liquid metal into the void space of the elastomer. (iii) A flexible and stretchable dipole antenna made by injecting EGaIn into PDMS..... 9
- Figure 1-4:** Direct laser patterning (i, and ii)<sup>55</sup> creates traces of liquid metals and other soft conductors in a rapid, subtractive, and inexpensive fashion. Meanwhile, ‘recapillarity’ (iii, and iv)<sup>56</sup> selectively withdraws liquid metals from microfluidic channels by localized electrochemical reduction of the oxide layer. Figures adapted from Refs. 55 and 56. Copyright Wiley 2015. ....11
- Figure 1-5:** Additive patterning techniques produce free standing 3D structures (i)<sup>50</sup>, and conformal 2D (ii, and iii)<sup>57</sup>. Scale bar on (ii) is 5 mm. Figure (i) adapted from Ref. 50. Copyright Wiley 2013. Figures (i) and (ii), adapted from Ref. 57. Copyright Wiley 2014..... 12
- Figure 1-6:** Unlike most liquids, planar thin films of EGaIn are difficult to produce using spin coating due to its high surface tension and surface oxide, which causes the metal to flow along paths where the oxide yields..... 18
- Figure 1-7:** Method for patterning Galinstan with selective surface wetting. Figure adapted from Ref. 23. Copyright Wiley 2013..... 18
- Figure 1-8:** Method for molding EGaIn using vacuum filling and freeze casting. Figure adapted from Ref. 54 with permission from The Royal Society of Chemistry. .... 19
- Figure 1-9:** Droplet-by-droplet  $\mu$ CP with EGaIn. (i) Process steps: <sup>1</sup>dip PDMS tip into pool of EGaIn, <sup>2</sup>retract tip, <sup>3</sup>move wetted tip to substrate, <sup>4</sup>press tip into substrate to deposit EGaIn droplet; (ii) 340  $\mu$ m diameter droplets; (iii) solid lines produced by spacing droplets 200  $\mu$ m apart. Adapted with permission from Ref. 63. Copyright 2013 American Chemical Society. .... 19

- Figure 1-10:** Traditional spreading techniques do not allow for smooth thin films of EGaIn (a). Inspection under an optical microscope (b) shows a thin but non-uniform coating of EGaIn. The sample is back-lit with light. If the film was uniform, it would not be possible to see through the film, but it is apparent that light travels through the films suggesting the thickness is not uniform. Scale bar on (b) is 1 mm ..... 20
- Figure 2-1:** Schematic of CEW using EGaIn. A gray border around the metal plug (black) indicates the presence of an oxide skin. Applying a voltage (V) at the end of the capillaries creates a surface tension ( $\gamma$ ) gradient in the plug. In the schematic, the right side of the plug is shown to have a higher surface tension ( $\gamma_R$ ) than the left side ( $\gamma_L$ ). Accordingly, the metal moves to the left (from high to low surface tension)..... 27
- Figure 2-2:** (a) Plot of a sinusoidal waveform of voltage (red) and current (blue) over time. The current and voltage are out of phase by a phase lag ( $\phi$ ). (b) Example Nyquist diagrams for EIS measurements, adapted from literature.<sup>21</sup> ..... 28
- Figure 2-3:** (a) Position of the center of a liquid metal plug (1.0 cm to 1.5 in length) over time in response to an AC voltage (1 Hz, square wave). The figure shows the position in 1 M NaOH (blue) and 1 M NaF (red) for 1  $V_{pp}$  (squares) and 2  $V_{pp}$  (circles). Error bars indicate standard deviations of 3 trials. (b) Column groups of mean displacement of the metal plug for 1 M NaOH (blue, solid) and 1 M NaF (red with diagonal checks) for three frequencies (0.5 Hz, 1 Hz, and 3 Hz) at 1  $V_{pp}$  and 2  $V_{pp}$ . (c) Average velocity for 1 M NaOH (blue, solid) and 1 M NaF (red with diagonal checks) for three frequencies (0.5 Hz, 1 Hz, and 3 Hz) at 1  $V_{pp}$  and 2  $V_{pp}$ . ..... 31
- Figure 2-4:** Droplet splitting of an EGaIn plug in 1 M NaF when 0.2 mV<sub>RMS</sub> (sine wave) with 1 V<sub>DC</sub> bias is applied. Scale bar is 1 mm. .... 34
- Figure 2-5:** Reconfigurable THz Waveguide. (a and b) Incident view of setup. THz waveguide sandwiches an quartz capillary filled with a plug of liquid metal (Galinstan, 8 mm, in length) in 1.75 M NaOH in MeOH. Applying an AC voltage (4  $V_{pp}$ , 2 Hz, square wave) actuates the liquid metal in (a) and out (b) of the waveguide. (c) Data transmission measurements out of Port 3 of bottom wave guide. When liquid metal is in path of waveguide (configuration in (a)), THz signal is blocked (red line on (c)). When metal is outside the path of the waveguide (configuration in (b)), THz signal couples through Port 3 (black curve). Inset shows finite element modeling of THz transport through waveguide at 165 GHz. Figure adapted from literature.<sup>26</sup> ..... 36
- Figure 2-6:** EIS Measurements with and without metal plug. (a and b) Bode plot showing spectra of impedance (a) and phase angle (b) from 1 GHz to 1 Hz. Black curve is of electrolyte only (no metal plug-in capillary). Red curve is impedance of CEW system with a plug length of 1.2 cm, which shows a resonance near 15 Hz. (c) Corresponding Nyquist diagram plotting negative of the imaginary component

of impedance ( $-Z_{imag}$ , y-axis) vs. real component of impedance ( $Z_{real}$ ). Black curve is of electrolyte only (no metal plug in capillary). Red curve is spectra of CEW system with a plug length of 1.2 cm, which shows an inductive loop at the corresponding frequency of the resonance in (a and b). ..... 38

**Figure 2-7:** EIS spectra with and without oxide. Data points with squares are of electrolyte only (no metal plug-in capillary, blue for 100 mM NaCl and red for 1 M NaOH). Data points with circles are of CEW system (blue for 1.4 cm plug in 100 mM NaCl and red for 1.2 cm in 1 M NaOH). (a and b) Bode plot showing spectra of impedance (a) and phase angle (b) from 1 GHz to 1 Hz. A resonance appears only for 1 M NaOH in both impedance (a) and phase angle (b). (c) Corresponding Nyquist diagram plotting negative of the imaginary component of impedance ( $-Z_{imag}$ , y-axis) vs. real component of impedance ( $Z_{real}$ ). An inductive loop appears only for 1 M NaOH (red, circle) corresponding frequency of the resonance in (a and b). ..... 43

**Figure 2-8:** a) Schematic of CEW system with EGaIn in capillary filled with electrolyte (top). The proposed equivalent circuit model for CEW with EGaIn (bottom). (b) Bode (top) and Nyquist (bottom) diagrams of experimental data points for a plug of 1.6 cm with model fitting. .... 44

**Figure 2-9:** Bode (left) and Nyquist (right) diagrams of experimental data points for a plug of 1.6 cm with model fits of Control Model (CPE element with no Inductor element, a and b) and Warburg model (Warburg unit replacing CPE element, Inductor element included, c and d). ..... 46

**Figure 2-10:** Estimating slip-layer thickness (a) Schematic of cylindrical annulus used to model slip-layer ( $\delta$ ), (b) Comparison of  $\delta$  (nm) and plug length (cm). Dotted line serves as a guide. .... 49

**Figure 3-1:** Dynamic contact angle measurements on surfaces of interest. For dynamic contact angle experiments (left column), a drop of liquid metal contacts on surfaces of interest ((a) Glass, (c) FluoroPel, and (e) NeverWet). The advancing contact angle of the drop is measured as the drop first increases in volume. Upon receding the drop, oxide residue remains on the surface of glass and FluoroPel. Meanwhile, no oxide residue is present on the surface of NeverWet. The right column (b, d, and f) show representative graphs of the evolution of contact angle of EGaIn and DI water over time, which is normalized to scale all experiments. On (b, d, and f), a red star (\*) indicates the beginning of the withdrawal of the volume (i.e., volume of the drop decreases). (b) On Glass, EGaIn initially increases in contact angle as volume is increased. Upon decreasing the volume (indicated by a red star), the contact angle initially decreases but never reaches an equilibrium value. (d) Similar behavior is observed for EGaIn on FluoroPel (black cross marks). ..... 61

**Figure 3-2:** EGaIn on rough, hydrophilic surfaces. (a) Water wetting on NeverWet treated with O<sub>2</sub> plasma for one minute at 100% power, (b) A drop of EGaIn advancing

on NeverWet treated with O<sub>2</sub> plasma. (c) After contact angle measurements, EGaIn drop does not leave behind residue on on NeverWet treated with O<sub>2</sub> plasma. (d) Diagram and optical micrograph of square posts of SU-8 fabricated using direct-write photolithography. Each square post is 200 μm in length with a spacing of 200 μm between posts in all directions. (e) Time-lapse photographs of water wicking into square posts. (f) (top) EGain advancing on square posts of SU-8. (bottom) After contact angle measurements, drop of EGaIn does not leave behind oxide residue on the posts ..... 65

**Figure 3-3:** Surface morphology and roughness of NeverWet. (a) Scanning electron micrograph (SEM) of NeverWet coating at 150× magnification. Scale bar is 300 μm. (b) SEM of NeverWet at a higher magnification (25,000×). The micrograph in (b) is a select region of SEM in (a), marked by a white box. Scale bar is 2 μm. Both SEM micrographs (a, b) measure secondary electron emissions using an Everhart-Thornley dector on a FEI Verios 460L SEM, which operated at 2.0 kV, 6.3 pA, and no stage bias. Samples are tilted at 55° to observe the roughness at a glancing angle and were imaged without a coating of metallic thin-film. (c) A representative line scan of contact-mode profilometer of NeverWet. Inset shows statistical values of average roughness and RMS roughness from five scans. (d) TEM of silica particles that comprise the NeverWet, Step 2 spray (JEOLF 2010F TEM) operating at 200 kV)..... 67

**Figure 3-4:** Chemical composition of surface and sub-surface NeverWet. (a) Fourier-transform infrared spectroscopy in attenuated reflection mode (FTIR-ATR) of a sample of NeverWet. The scan in black line is of NeverWet Step 1 spray (binder). The red scan indicates NeverWet coating consisting of both Step 1 and Step 2. (Step 1 + Step 2) The blue line is a subtraction of Step 1 and Step 1+2. Two green drop lines indicate the FTIR peaks for Si-CH<sub>3</sub> and Si-O moieties. (b) X-ray photoelectron spectroscopy of NeverWet with graphs corresponding to peaks of O 1s, C 1s, and Si 2p. .... 70

**Figure 3-5:** Schematic of a method to patterning liquid metal against a surface of NeverWet. (i) Schematic of a molded elastomer (using either a laser writer or photolithography). Holes punched in the elastomer serve as inlet and outlet for the liquid metal. (ii) Next, the molded elastomer is placed against the NeverWet surface. (iii) Liquid metal is injected into the inlet of the elastomer. (iv) Optical photograph of liquid metal patterned into a spiral feature after removing the mold from the NeverWet surface. (v) Optical photograph of the metal trace in series with a red LED light shows that the metal trace is electrically conductive. The LED light bulb is connected in series with a 12V battery and resistor, which are not shown. Scale bar on (iv) is 1.0 cm. .... 73

**Figure 3-6:** Reversible actuation of liquid metal inside a closed channel. (a) A channel coated with NeverWet is sealed against another slide coated with NeverWet to form a closed channel. A reservoir of liquid metal is place below the inlet of the channel and sealed with a membrane of PDMS. (b) Applying pressure from hand actuates liquid metal into the NeverWet-coated channel. (c) Upon releasing

- pressure, the metal leaves the channel without forming any residue within the channel. Scale bar (a) is 1.0 cm. .... 74
- Figure 3-7:** Reconfigurable monopole antenna. (a) An illustration of the prototype monopole antenna used for antenna measurement. A block of PMMA with etched microchannel rests on a Cu ground plane. The channel is coated with NeverWet to prevent oxide adhesion. The amount of liquid metal in the channel is controlled via injection through a septum (red circle). An SMA (not shown) connects the liquid metal to the copper ground plane. (b) Antenna characterization of reconfigurable monopole antenna at four states (i.e, length of metal in channel). An inset shows the measured frequency (y-axis) vs. the predicted frequency..... 76
- Figure 4-1:** Two drops of eutectic gallium indium (‘EGaIn’) sitting atop each other in an asymmetric orientation. The bottom drop exhibits an asymmetric apparent contact angle ( $119^\circ$  on left and  $115^\circ$  on right). Scale bar is 1.0 mm ..... 88
- Figure 4-2:** Advancing and receding contact angle measurements of EGaIn and water on hydrophobic (fluoropolymer) and hydrophilic substrates (glass). (a) Apparent contact angle versus time for EGaIn on a hydrophobic substrate (fluoropolymer, red star) and on hydrophilic substrate (glass, black squares), and water on fluoropolymer (blue, circle, control experiment). A purple star denotes the time at which volume recedes from the drop. Images of EGaIn on hydrophobic substrate are shown as insets for advancing portion (left) and receding portion (right) for the measurement. (b) Advancing and receding contact angle on the hydrophobic substrate as a function of the volume of the drop. The abscissa on this group is a scaled function of the volume to show the evolution and hysteresis curve of the contact angle. .... 93
- Figure 4-3:** A plot of advancing angle of EGaIn vs. advancing angle of water for various substrates.  $\theta_{A, \text{water}}$  for glass<sup>[52]</sup> and SU-8 (flat)<sup>[53]</sup> are from literature. Water wets into the SU-8 posts (hence  $\theta_{A, \text{water}}$  of  $0^\circ$ ), which are  $200 \mu\text{m}$  squares with  $200 \mu\text{m}$  spacing. .... 95
- Figure 4-4:** Receding measurement divided into three regimes (A, B, and C) for EGaIn on a hydrophobic substrate. .... 97
- Figure 4-5:** a) Advancing and receding contact angle measurement of EGaIn on a plasma-treated silicon wafer. (b) An exploded of view of the (a) during Regime A (beginning of receding angle). (c) Side-view micrographs of EGaIn drops undergoing baseline expansion on various substrates (i: Silicon wafer, ii: Fluoropolymer, iii: NeverWet, iv: SU-8 posts). The top images for all columns show the drop prior to baseline expansion. White dotted vertical lines extend from contact line of the top images to the final row of images; these lines serve as guides to show the expansion of the baseline on each substrate. .... 98

**Figure 4-6:** Oxide ‘spider-web’ residue. (a) Optical micrograph of EGaIn residue on flat SU-8 (hydrophilic) after dynamic contact angle measurement. Green background is due to polarization of light. Scale bar is 1.0 mm, (b) Optical micrograph of EGaIn residue on hydrophobic substrate (fluoropolymer). Red and green dotted lines indicate radial fibers and concentric rings, respectively for (b-e). Scale bar is 1.0 mm for (b), (c) Optical micrograph at 50× magnification at the edge of the drop from image in (b). Scale bar is 100 μm, (d) Optical micrograph at 100× magnification within the drop. Diagonal lines show pinning of the drop during advancing measurement. Scale bar is 50 μm. (e) Optical micrograph at 100× magnification of (b) between two radial fibers. Scale bar is 50 μm. .... 101

**Figure 4-7:** EGaIn dynamic contact angle experiment on square posts made from SU-8 (100 μm squares, with 100 μm spacing). (a) EGaIn advancing. (b) EGaIn residue at end of receding measurement (Regime C). For (a) and (b), needle diameter of 0.39 mm serves as a scale bar. (c and d) Optical micrographs of oxide residue on square posts. The radial fibers suggest a thin film or membrane of oxide suspended between posts. Scale bar is 100 μm (e) SEM image of oxide membrane (blue circle) between posts (white dotted line marks the edge of a post). Scale bar is 50 μm. (f) SEM image of oxide membrane (blue circle) that is ruptured in certain locations (red circles). Scale bar is 200 μm. SEM Operating Conditions (e-g): FEI Verios 460L, 2.00 kV, 13 pA, 6.1 mm WD with TLD detector in secondary electron mode..... 103

**Figure 4-8:** For sliding angle experiments (a-c), a drop of liquid metal is placed atop a surface of interest, which is oriented horizontally and subsequently tilted (via a screw under the substrate). d) (a) On FluoroPel, the drop of liquid metal remains affixed to its original placement due to pinning of the oxide (a, bottom) when tilted to 30°. (b) On NeverWet, the drop of liquid metal readily slides upon reaching a tilt angle of 14.6°. (c) Sliding angle experiment on larger droplet. (top) Large drop of EGaIn (~300 μL) resting on a flat and horizontal substrate (Si wafer, coated with FluoroPel™). (bottom) Drop slides down substrate when tilted to 20°..... 105

**Figure 5-1:** A Venn diagram shows the organization of stretchable bioelectronics into three categories: (a) materials and mechanics, (b) soft robotics, and (c) biological integration. (a) Illustration of stretchable rechargeable battery using hydrogel and conductive paste. Reproduced with permission from Reference 13. © 2013 Royal Society of Chemistry. (b) Soft robotic gripper that uses an optical signal feedback to sense and handle soft and fragile objects. Reprinted with permission from Reference 69. © 2016 AAAS. (c) Soft device, called “e-dura,” which is implanted into damaged spinal tissue to restore its function. The device consists of a patterned microfluidic device that enables drug delivery and soft and flexible electrodes to transmit an electrical signal and excite surrounding nervous tissue. Reprinted with permission from Reference 15. © 2015 AAAS. Rigid to Stretchable: Challenges..... 118

**Figure 5-2:** (a) Graphene is printed onto a thin, flexible polymer to form (i) a transparent electronic tattoo. The serpentine pattern of the graphene traces allows it to function while undergoing deformations. The top image shows the tattoo in its relaxed state. Due to the elasticity of the tattoo and skin, the tattoo can function while being compressed (middle) or stretched (bottom). The tattoo sensor can monitor physiological activities, (ii) electroencephalogram (EEG), (iii) electromyogram (EMG). The EEG sensor is placed on the forehead (ii, left) to measure neurophysiological activities such as (right) blinking of eyelids. (iii, left) The EMG sensor is placed on the forearm to show sensing of muscle movements, such as hand clenching. A common commercial sensor is placed nearby the tattoo sensor to benchmark the performance. (Right) The accuracy of the tattoo sensors and commercial sensors are similar. Adapted with permission from Reference 23. © 2017 American Chemical Society. (b[i]) Three individual electrodes are screen printed onto a nitrile glove to (ii) serve as a traditional three-electrode electrochemical cell (ii). Scale bar = 10 mm. (Left, ii) The three electrodes are printed onto the index finger. (Right, ii) The thumb contains a collector pad that accumulates or gathers the chemical or biomarker of interest. The collector pad contains immobilized enzyme (OPH) that reacts with the biomarkers. (iii) The electrodes are printed on a glove, and the sensors are flexible and stretchable up to 50% of its original length. Scale bar = 10 mm. The electrodes sense electrochemical reactions with (iv) biomarkers and (v) chemicals based on a change in current. (vi) A portable potentiostat is placed onto the back of the hand and wirelessly transmits a voltamogram to (vii) a mobile device. The inset of (vii) shows (I and II) the three electrode pins that are placed on (III) an adjustable Velcro ring. Adapted with permission from Reference 34. © 2017 American Chemical Society. Note: OP, organophosphate; OPH, organophosphate hydrolyase; R, any chemical group containing a hydrocarbon that is attached to the chemical functional group. .... 120

**Figure 5-3:** Materials and mechanics. (a) (Top) A wearable tattoo sensor is composed of screen-printed metal contacts (islands) with serpentine-shaped bridges. (Bottom, left) Several types of conductor materials (carbon, Ag/AgCl, and CNT) can be screen printed. (Bottom, right) The serpentine bridges serve as stretchable interconnects. Adapted with permission from Reference 39. © 2017 Wiley. (b) A hydrogel piece mounted on (top, left) of 3M very high bond (VHB) film is utilized as a (top, right) wearable transparent, conductive touch screen. The touch sensing mechanism works based on change in (bottom, left) current. The authors demonstrate a (bottom, right) touch-screen for writing, playing music (not shown), or games (not shown). Reprinted with permission from Reference 50. © 2016 AAAS. Note: CNT, carbon nanotube; A1–A4, separate current collectors that provide the location and sensitivity of the touch point;  $\alpha$ ,  $\beta$ , normalized Cartesian coordinates on the hydrogel touch panel. .... 122

**Figure 5-4:** Soft robotics. (a) Elastomeric grippers are produced by molding an uncured elastomer. (Top) A gallium alloy liquid metal is injected into hollow cavities of the elastomer to form a monolithic conductive element. (Bottom) A pneumatic feed inflates cavities with air to actuate the gripper. Scale bar = 1.0 cm for both

top and bottom images. Reprinted with permission from Reference 47. © 2015 IEEE. (b) Soft pneumatic actuators are fabricated with direct ink writing of two different inks. (Top) A side view image shows the architecture of the soft actuator, which consists of embedded pneumatic chambers with adjacent electrical conductors. Metallic wiring and pneumatic tubing (shown at bottom of image) are embedded within the composite. (Bottom) The two inks (one of conductive hydrogel and the other of an insulating elastomer) are printed in an alternating fashion and cured under UV light. Electrical contacts from metallic wires and tubing for pneumatic control are embedded within the hydrogel material. Reprinted with permission from Reference 75. © 2015 Elsevier. .... 126

**Figure A-1:** a) Comparing the effect of a surface oxide on the movement of EGaIn plug (~1.0 cm, in length) using low AC voltages (200<sub>RMS</sub> to 800 mV<sub>RMS</sub>, sine wave). The closed data points are in 1 M NaOH, where there is no oxide present. The open data points are performed in 1 M NaF, where an oxide ‘skin’ is present. (b) Velocity measurements of EGaIn plug (2 and 3 cm, in length) in hydrophillic glass capillary (oxygen plasma cleaned, blue) and hydrophobic glass capillary (fluorosilane-treated, red). .... 144

**Figure A-2:** EIS spectra of 10 consecutive measurements for 1.6 cm and 3.6 cm plugs in 1 M NaOH. (a and b) Bode diagrams for 1.6 cm (a) and 3.6 cm (b) showing impedance (left y-axis, black) and phase angle (right y-axis, blue). Error bars are standard deviations(n=10) of impedance (black) and phase angle (blue) for a given frequency. (c) Nyquist diagram for both 1.6 cm (black) and 3.6 cm (blue). Each data point is for a specific frequency. X and y error bars are standard deviations (n=10) for  $-Z_{real}$  and  $Z_{imag}$ . .... 146

**Figure A-3:** EIS spectra of 2.6 cm EGaIn plug in 1 M NaOH comparing the direction of measured frequency. Forward sweep (blue, square) refers to measurements starting from 1 GHz to 1 Hz. Reverse sweep (red, circle) refers to EIS spectra measured starting from 1 Hz to 1 GHz. .... 146

**Figure A-4:** Bode diagrams ((a) impedance and (b) phase angle) from EIS experiments of EGaIn in 1 M NaOH plugs of varying length from no plug (electrolyte only) to 6.5 cm. .... 147

**Figure A-5:** Photographs of Ga film after 24 hour soak in air (a, left, control), 1 M NaCl (middle), 1 M NaOH (c, right). Prior to experiment Ga film is spread over a Si wafer (three inches, in diameter) and soaked into a petri dish containing the electrolyte. Scale bar is 1.5 inches or 3.8 cm. .... 148

**Figure A-6:** Exploded view of Bode diagram of EGaIn (1.6 cm in length) from Fig. 2-9d at high frequency range. Blue square data points are of experimental data. Black line is the model fit of the Warburg model (with inductor element). Blue dotted line is a linear fit of experimental data in the region marked by yellow. Slope of fitted line is 3.8. Fitting is performed using Origin 2016 plotting software. .... 148

- Figure B-1:** TOF-SIMS spectra of NeverWet sample after being grazed with EGaIn; afterwards, the liquid metal or its oxide does not adhere to the surface or leave a microscopic residue. TOF-SIMS spectra shows that there is no nano-scale residue or imprint of Ga, In, and their oxides. Data shows spectra of positive ions (a) and negative ions (b) associated with NeverWet (black). Spectra associated with Ga, In, and their oxides are denoted by red star and dotted drop lines. The placement of the red stars, relative to the vertical axis, is arbitrary. .... 151
- Figure B-2:** Surface characterization of NeverWet. (a) Optical micrograph of NeverWet coating at 5x resolution. Large clusters of particles (~100 to 300  $\mu\text{m}$ ) are scattered across the surface, in a non-repetitive fashion. (b) AFM measurement of NeverWet coating shows spherical particles composing the NeverWet. (c) SEM micrograph of NeverWet at higher shows clusters of nanoparticles that compose the surface of NeverWet. (d) EDS spectra of “Spectrum 4” (boxed area in (c)) shows that the surface comprises only of Si, C, and O. .... 152
- Figure B-3:** Fast Fourier Transform (FFT) of profilometry scan (as shown in Fig. 2c). The graph depicts the frequency (y axis) of spacing between particle clusters that compose the surface (x axis, log-scale). Based on this analysis, the roughness of the surface varies from ~50s  $\mu\text{m}$  to ~1000  $\mu\text{m}$ . The roughness at larger length scales (~500  $\mu\text{m}$ s and greater) is likely due to variations in the thickness and uniformity of the surface coating (because it is spray coated by hand). Meanwhile, the roughness of lower length scales is due to the coating itself. .... 153
- Figure B-4:** FTIR spectra of Step 2 of NeverWet (subtraction, black bottom line) in comparison to PDMS (red line, middle) and PVMS (blue line, top). .... 154
- Figure B-5:** Accuracy of patterning traces. (a) Laser cut channel before injection, (b) after injection, (c) PDMS microchannel (made using soft lithography) before injection (d) PDMS microchannel after injection, (e) Examining accuracy of laser cut channels as a function of line width. Y-axis shows the width of the metal within the channel. X-axis denotes the designed line-width (i.e., width of microchannel prior to injection). For larger widths (>500  $\mu\text{m}$ ), the width of the metal in the microchannel does not follow a linear trend. This phenomenon occurs because the metal does not adhere to the side walls of the microchannel. Concurrently, the high surface tension of the metal causes the metal to minimize its surface area; thus, it retracts away from the side walls of the channel. .... 154
- Figure B-6:** Photograph of the prototype reconfigurable antenna shown in Figure 6. Scale bar is 1.0 cm. .... 155
- Figure C-1:** (a) Side-view photographs of EGaIn residue on silane-treated glass after advancing and receding measurements varying in height between needle and substrate (red arrow on top photograph, height enumerated in red below each photograph). (b) Advancing (black) and receding (red) contact angle measurements as a function of scaled volume for varying needle heights ..... 160

**Figure C-2:** (a) Average advancing angles of EGaIn on glass, EGaIn on fluoro-silane treated glass, and water on fluoro-silane treated glass as a function of the flow-rate. (b) Average advancing angles for the same surfaces as (a), as a function of Z, which is a ratio of the distance between the needle and substrate to axial length of the drop. .... 162

**Figure C-3** Pendant drop experiments. (a) Pendant drop of EGaIn increases in volume (first two images from left). As the volume is reduced from the drop (third and fourth image), the metal drop elongates due to gravity and forms wrinkles on its surface. At the end of the experiment, the remaining oxide skin hangs from the needle. (b) Buckling during compression of an elastic film of bacteria at the interface of oil and water. Reproduced from literature.<sup>[55]</sup> (c) Buckling of a thermos-responsive, free-standing membrane as the drop is compressed internally. Reproduced from literature.<sup>[56]</sup> ..... 163

# CHAPTER 1

## METHODS TO PATTERN LIQUID METALS<sup>1</sup>

---

<sup>1</sup>This work is published in *Journal of Materials Chemistry C* in 2015 with Hudson Ayers, Carmel Majidi, and Michael Dickey as co-contributors. Full citation below:  
I. D. Joshipura, H. R. Ayers, C. Majidi and M. D. Dickey, *J. Mater. Chem. C*, 2015, **3**, 3834–3841.

## **Abstract**

This highlight describes emerging methods to pattern metals that are liquid at room temperature. The ability to pattern liquid metals is important for fabricating metallic components that are soft, stretchable, conformal, and in some cases, shape-reconfigurable. Applications include electrodes, antennas, micro-mirrors, plasmonic structures, sensors, switches, and interconnects. Gallium (Ga) and its liquid metal alloys are attractive alternatives to toxic mercury. This family of alloys spontaneously forms a surface oxide that dominates the rheological and wetting properties of the metal. These properties pose challenges using conventional fabrication methods, but present new opportunities for patterning innovations. For example, Ga-based liquid metals may be injected, imprinted, or 3D printed on either soft or hard substrates. The use of a liquid metal also enables rapid and facile room temperature processing. The patterning techniques organize into four categories: (i) patterning enabled by lithography, (ii) injection, (iii) subtractive techniques, and (iv) additive techniques. Although many of these approaches take advantage of the surface oxide that forms on Ga and its alloys, some of the approaches may also be suitable for patterning other soft-conductors (e.g., conductive inks, pastes, elastomeric composites).

## **Why pattern liquid metals?**

There are at least four reasons for patterning metals or other fluidic conductors that are liquid near room temperature. First, they enable electrical and optical components that are stretchable, soft, and deformable as shown in Fig. 1-1.<sup>1</sup> Liquid metal components encapsulated in soft materials, such as elastomers, can bend and stretch in ways that are unattainable with conventional electronic materials. Liquid metals facilitate extreme “stretchability” (e.g. stretchable wires that maintain electrical conductivity up to  $\sim 1000\%$  strain<sup>2</sup>) and unique coupling of mechanical deformation to electronic function. In principle, soft-matter electronics can integrate

into clothing, medical implants, or wearable technologies without interfering with the natural mechanics of the human body.<sup>3</sup>

Second, liquid metals enable simple, unconventional patterning techniques. In some cases, a liquid may not be necessary for the end-application but may be used anyhow because it is easier to pattern than solid metals. For example, it is possible to inject liquids into microfluidic channels or direct-write liquids (Fig. 1-1) onto a wide range of substrates. Patterning with liquid metals also allows for inexpensive and fast fabrication of devices outside of a cleanroom and without the need for vacuum processing (e.g., physical vapor deposition or sputtering).

Third, it is possible to pattern liquid metals using room temperature processes at ambient pressures that are compatible with a variety of substrates including polymers, gels, elastomers, self-assembled monolayers, and biological materials. The deposition of solid metals often requires melting (e.g., sintering, soldering) or evaporating (e.g., physical vapor deposition) metals above room temperature or in vacuum in a way that is destructive or incompatible with thermally sensitive or volatile substrates. It is possible to deposit metals at room temperature using electro-deposition, but this requires electrolytes, electrical potential, and a conductive substrate.

Fourth, the ability of liquid metals to flow on demand allows for conductive elements with dynamic behavior or response; as such, these devices can be designed to be “reconfigurable.”

## Liquid Metals (MP)

Mercury	(-39 °C)
Francium	(27 °C)
Cesium	(29 °C)
Gallium	(30 °C)
Gallium alloys	(< 30 °C)
Rubidium	(40 °C)



## Fabrication Methods

1. Lithography-enabled
2. Injection
3. Subtractive
4. Additive (*below*)



## Applications

- i. Microfluidic Electrodes
- ii. Sensors & Robotics
- iii. Stretchable Electronics
- iv. Reconfigurable Circuits

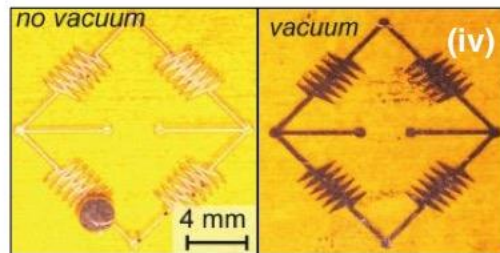
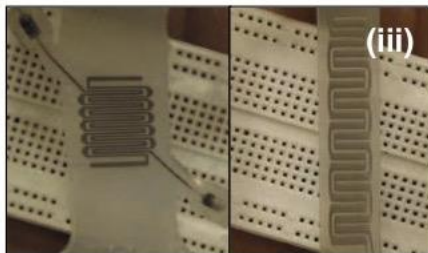


**Figure 1-1:** Overview of liquid metals. Gallium and its alloys form a surface oxide, which allows them to be micro-moldable<sup>14</sup>. The oxide enables several patterning techniques, including direct-write (as shown above) and potential applications<sup>16-19</sup>. Figure from Liquid Metals adapted from Ref. 14. Copyright Wiley 2011. Figure from Applications (i) adapted from Ref. 16. Copyright Wiley 2011. Figure from Applications (iv) reprinted with permission from Ref. 19. Copyright Applied Physics Letters, AIP Publishing LLC.

### How to pick a liquid metal?

Mercury (Hg) is the most commonly known liquid metal (M.P.  $-38.8\text{ }^{\circ}\text{C}$ ) and has been proposed for stretchable electrical wiring since the 1940s.<sup>4</sup> Hg is electrically conductive ( $\sigma = 1.04 \times 10^6\text{ m}^{-1}\text{ Ohm}^{-1}$ ,  $\sim 1/50^{\text{th}}$  that of Cu) and has been utilized for electrochemical measurements

(e.g. hanging drop electrodes for polarography), thermostat switches, fluorescent bulbs, thermometers, and MEMS devices.<sup>5,6</sup> However, Hg is toxic, which limits its application.

Gallium-based alloys, such as eutectic gallium indium (“EGaIn”, 75% Ga, 25% In, by weight) and gallium indium tin (“Galinstan”, 68% Ga, 22% In, 10% Sn, by weight), are promising alternatives to Hg. Both EGaIn (M.P. 15.5 °C<sup>7</sup>) and Galinstan (M.P. –19 °C<sup>6</sup>) are in the liquid state at room temperature, possess virtually no vapor pressure,<sup>6</sup> and are considered to have low toxicity.<sup>8</sup> Although both Hg and Ga-based alloys exhibit high surface tension (480 mN m<sup>-1</sup>, 624 mN m<sup>-1</sup>, and 534 mN m<sup>-1</sup> for Hg,<sup>7</sup> EGaIn,<sup>7</sup> and Galinstan,<sup>6</sup> respectively), Ga-based alloys form a passivating oxide (~1–3 nm) spontaneously in air.<sup>7,9–13</sup> This oxide “skin” allow these metals to be molded into non-spherical shapes,<sup>14</sup> as shown in Fig. 1-1 (left). The oxide also may lower the surface tension of the metal.<sup>15</sup>

The oxide skin behaves as an elastic material until the surface stress exceeds a critical point of 500–600 mN m<sup>-1</sup>. Beyond this surface stress, the oxide skin breaks and the liquid flows readily (e.g., within microfluidic channels).<sup>7</sup> Below the yield stress, the oxide holds the metal into non-spherical shapes. The mechanical properties of the oxide and its ability to adhere to many surfaces enable many of the patterning techniques described in this Highlight. Due to their low toxicity, liquid-state at room temperature, and relatively high conductivity (~1/16th that of Cu), Ga-based alloys are well-suited for a variety of applications that would not be possible using solid metals.<sup>1</sup> It is not the intent of this Highlight to review applications,<sup>1,3</sup> but rather describe the state-of-the-art patterning techniques that make them possible.

Finally, it should be noted that several other metals and their alloys exist with MPs near room temperature, such as shown in Fig. 1-1. However, these metals have disadvantages due to their radioactivity (Cs and Fr), short half-life (Fr), or violent reactive nature (Cs and Rb).

Accordingly, these metals are not well suited for electronic applications. Therefore, this Highlight focuses on state-of-the-art patterning methods using gallium-based alloys. Hereafter, the use of “liquid metal” refers to Ga-based alloys, unless otherwise stated. However, Hg, and other fluidic conductors may be compatible with some of the fabrication techniques presented here. Similarly, molten metals (including low-melting point solders) may also be compatible for techniques and materials that can tolerate elevated temperatures.

## **Overview**

Gallium-based alloys possess several properties that enable micron- scale patterning: (1) they are injectable into cavities and channels and onto surfaces, (2) they form a surface oxide that dramatically impacts the rheological and wetting properties of the metal, and (3) they freeze or melt at experimentally accessible temperatures.

These same properties also render these metals incompatible with many existing patterning techniques. For example, the semi- conductor manufacturing industry has developed sophisticated ‘conventional’ micro- and nano-fabrication techniques for patterning thin films of solid-state materials (e.g. metals, polymers, and inorganics) on planar substrates.<sup>20</sup> In general, these techniques are poorly suited for patterning liquids due to their tendency to flow (both during and after processing) and inability to cast smooth, thin (<1 mm) films, as shown in Fig. 1-6. Due to their tendency to flow, liquid metals cannot easily be etched in a controlled manner. In contrast, injection-based and direct-write techniques offer a number of low cost patterning methods that are better suited for liquid metals than conventional approaches. In addition, Ga-based liquid metals may be patterned by some ‘unconventional’ fabrication techniques that exploit both its fluidic and moldable properties.

We organize the patterning techniques of liquid metal into four categories\*:

- i. Lithography-enabled processes:** use of lithographic processes (e.g., photolithography), either directly or indirectly (e.g., to fabricate stencils or molds), to achieve desired patterns.
- ii. Injection:** use of pneumatics or other forces to fill the metal into pre-defined features (e.g., microchannels). Although the features are often produced with lithographic-techniques, injection represents a unique capability of liquid metals that it warrants its own category.
- iii. Subtractive:** selective removal of the metal from a substrate.
- iv. Additive:** formation of objects or structures by depositing the metal only in desired regions; this includes microcontact printing ( $\mu$ CP), direct-write 3D printing, and jetting.

\* Several of the techniques use principles from more than one category and thus, the categories are intended to only facilitate organization.

## Patterning techniques for liquid metal

### *Lithography-enabled patterning*

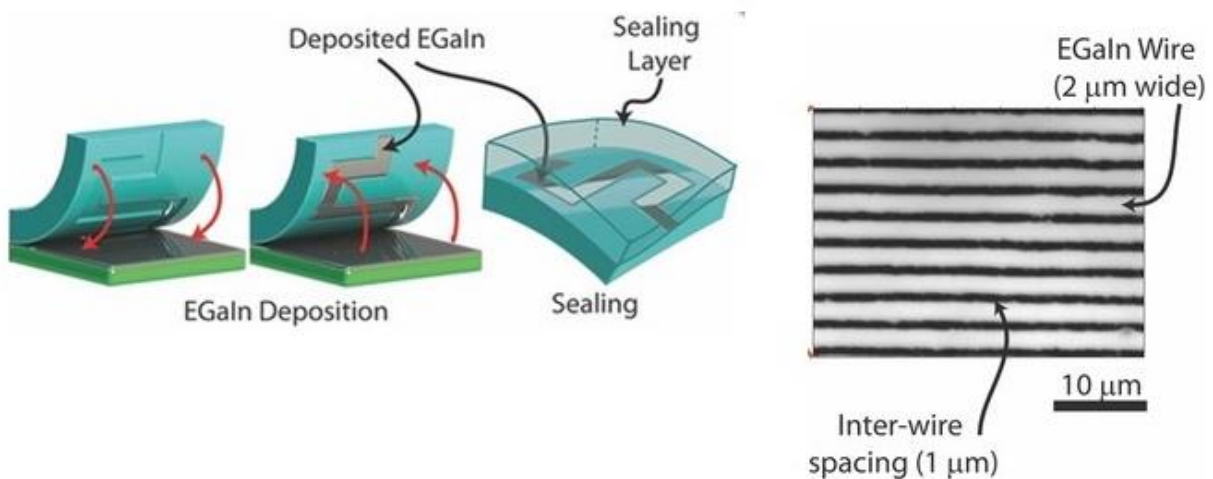


**Figure 1-2:** Lithography-enabled techniques allow for high resolution patterning of liquid metals, such as imprint lithography<sup>22</sup>. Figures adapted from Ref. 22. Copyright Wiley 2014.

**Conventional methods.** Photolithography, the most common of lithographic methods,<sup>20</sup> utilizes light to change the local solubility of polymer films (photoresist) coated on a substrate. Immersing the substrate into a developing solution dissolves away the soluble portions of the resist to expose the underlying substrate. Thereafter, etching processes can remove exposed metal from a metal film pre-coated on the substrate to create metallic patterns in a subtractive fashion. Schematics and illustrations of processes involving photolithography can be found in the literature.<sup>20</sup> Alternatively, physical vapor deposition or electrochemical plating can deposit metal into the openings in the photoresist. Photolithography has yet to be used to directly pattern liquid metals, but is often used to make topographical molds or stencils. Notably, liquid metal injected into microchannels can serve as a photomask to create reconfigurable patterns from a single mask with feature sizes as low as 10  $\mu\text{m}$ .<sup>21</sup>

**Imprinting.** Imprinting liquid metal with elastomeric molds (e.g., polydimethylsiloxane (PDMS)) is a simple patterning technique.<sup>22</sup> After spreading a thin film of liquid metal on a flat surface, an elastomeric mold with topographical features presses against the flat liquid metal film, which forces the liquid metal into the recesses of the mold. EGaIn, which is otherwise non-wetting on PDMS, is believed to adhere to the walls of the cavity with the aid of a Ga-oxide layer that forms at the interface between the metal and the PDMS.<sup>7</sup> As a result, the metal remains within the features even after removing the mold from the substrate.<sup>22</sup> Using this approach, it is possible to form liquid metal traces with two-micron line width and submicron depth, as shown in Fig. 1-2.

**Stencil lithography.** Stencil lithography is a high throughput technique to pattern liquid metals.<sup>23,24</sup> In the simplest embodiment, a draw rod spreads liquid metal across a stiff stencil (e.g., water-soluble poly(acrylic acid)<sup>23</sup> or Cu<sup>24</sup>) placed atop a desired substrate. The metal adheres to the substrate in exposed regions of the stencil. Depending on the stencil preparation, this method

achieves features as small as 200  $\mu\text{m}$  separated by 100  $\mu\text{m}$ ; however, the edges are often rough.<sup>23,24</sup>

Illustrations and schematics of patterning using stencils may be found in the literature.<sup>23,24</sup>

**Selective surface wetting.** The surface composition and morphology of a substrate can influence the wetting behavior of alloys of gallium.<sup>25–27</sup> Spreading the metal across pre-patterned wetting and non-wetting regions on a substrate offers another route to pattern the metal. The use of wetting substrates (e.g., coatings of  $\text{Sn}^{23}$  or  $\text{Au}^{28}$ ) and sacrificial release coatings on the stencil promotes the patterning process. A schematic illustration of selective surface wetting is shown in Fig. 1-7.

### *Injection*

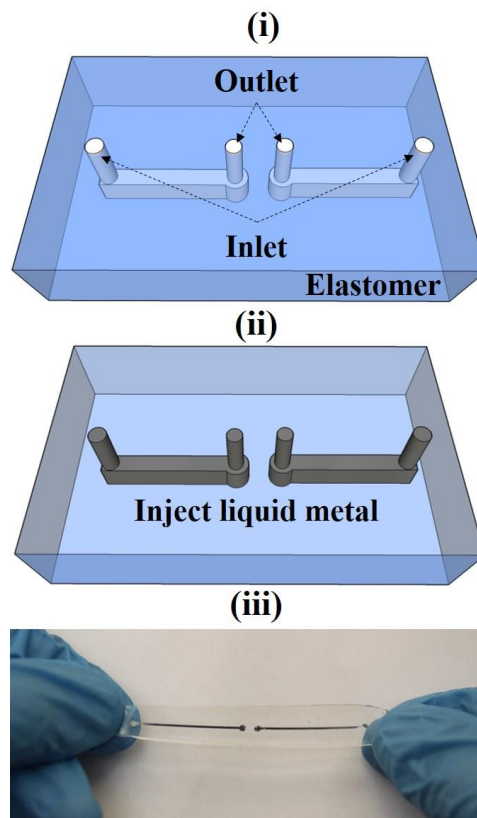


**Figure 1-3:** Injection is a versatile technique for embedding two and three-dimension metal structures in elastomers. (i) Photolithography or rapid prototyping creates an elastomeric topographical mold. An additional layer of elastomer seals the replica mold. Inlet and outlet holes are punched. (ii) A syringe (not pictured) injects liquid metal into the void space of the elastomer. (iii) A flexible and stretchable dipole antenna made by injecting EGaIn into PDMS.

Microfluidic injection of conductors is a common approach to create soft matter electronics, due to its simplicity and ability to faithfully replicate features pre-defined by lithography or 3D

printing.<sup>3,7,18,19,28-40</sup> These pre-defined features often have better resolution and smoother sidewalls than the other methods reported here, and result in structures in which the metal is automatically encapsulated.

A syringe injects the liquid metal into inlet holes of the microchannel. Once injected into channels, the Ga-oxide that forms adheres to the channel walls, resulting in stable microstructures.<sup>7</sup> Hydrochloric acid can remove the surface oxide from Ga and its alloys and thereby prevent it from adhering.<sup>7,40-43</sup> Alternatively, it is possible to create a slip layer between the oxide and the walls by pre-filling the channels with a carrier fluid;<sup>44,45</sup> such approaches allow for reversibly actuation of metal within microchannels.

As shown in Fig. 1-3, it is also possible to fill pores<sup>46</sup> or hollow fibers<sup>2,47</sup> with liquid metal, which can flow into the void space as long as the applied pressure exceeds the Laplace pressure.<sup>7</sup> To date, EGaIn has been injected into capillaries with diameters as small as 150 nm.<sup>48</sup> Evenly spaced posts or bars (so-called “Laplace barriers”<sup>19</sup>) in microchannels can be designed to block the metal and guide it to only desired areas.<sup>29,49</sup>

The encasing materials determine the mechanical properties of these structures, allowing for flexible and stretchable metallic components. Conversely, dissolving the encasing material (e.g., PDMS) of a microfluidic channel filled with liquid metal in an appropriate solvent produces free-standing structures.<sup>50</sup> Injection-based patterning is well suited for other liquid conductors (e.g., ionic liquids,<sup>51</sup> metal-salt mixtures,<sup>52</sup> and solders<sup>53</sup>). Although it is possible to inject Hg into microchannels, the metal will adopt a shape that minimizes surface energy.

**Vacuum filling.** Vacuum filling is a process similar to the injection method, by which pre-fabricated microchannels define the shape of the metal pattern.<sup>54</sup> The liquid metal flows into pre-defined trenches by applying vacuum to create a pressure differential. The process does not require

inlet and outlet holes, and works well for creating deep features or filling channels with step-changes in height. A schematic illustration for this technique is provided in Fig. 1-8.

Freezing the gallium alloy allows for removal and transfer of these patterns from the mold using simple tools such as tweezers, a process known as freeze casting. When performed in a temperature- controlled chamber filled with cold, dry air, the frozen gallium alloy can be assembled with rigid circuit elements and then sealed in elastomer.<sup>54</sup>

### Subtractive

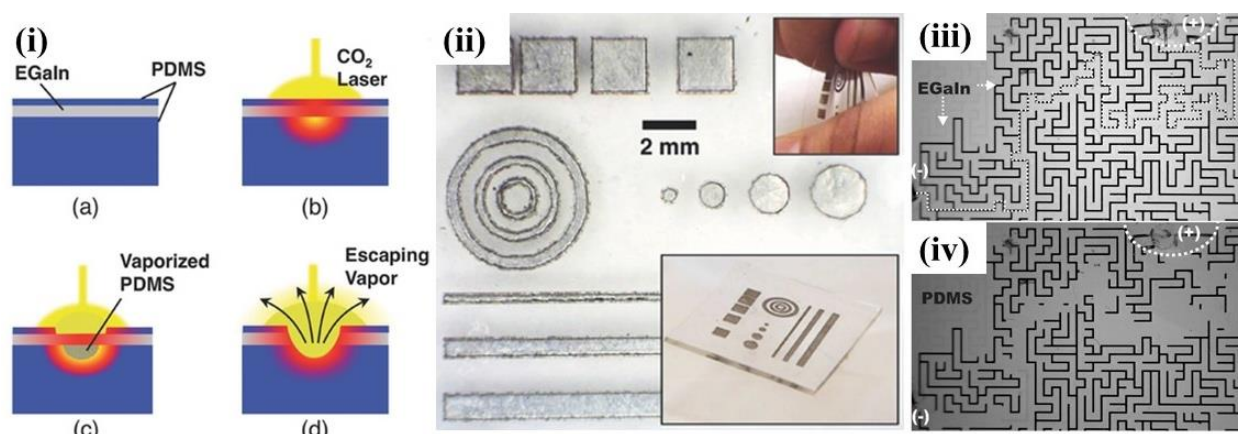


**Figure 1-4:** Direct laser patterning (i, and ii)<sup>55</sup> creates traces of liquid metals and other soft conductors in a rapid, subtractive, and inexpensive fashion. Meanwhile, ‘recapillarity’ (iii, and iv)<sup>56</sup> selectively withdraws liquid metals from microfluidic channels by localized electrochemical reduction of the oxide layer. Figures adapted from Refs. 55 and 56. Copyright Wiley 2015.

**Direct laser patterning.** Direct laser patterning is an inexpensive and facile approach to pattern liquid metals and other conductive materials with features as small as 100  $\mu\text{m}$ .<sup>55</sup> The process, depicted in Fig. 1-4, begins with sealing or encasing a layer of liquid metal between PDMS sheets. Thereafter, a carbon dioxide ( $\text{CO}_2$ ) laser ( $\lambda = 10.6 \mu\text{m}$ ) traces over the surface to selectively remove the metal. The energy from the  $\text{CO}_2$  laser evaporates the bottom layer of PDMS and displaces the metal away from undesired regions.

**Recapillarity.** Electrochemistry can locally reduce the oxide skin that forms on Ga and its alloys, and therefore induce these liquid metals to flow via capillary action.<sup>56</sup> This technique is termed

‘recapillarity’ due to the use of reductive potentials to induce capillary behavior. As shown in Fig. 1-4(iii) and (iv), it is possible to selectively remove liquid metal from complex microchannels by induced capillary action. Although there is no net metal lost in this process, the metal does flow out of channels to a reservoir to alter patterns in a subtractive manner.<sup>15</sup>

*Additive*

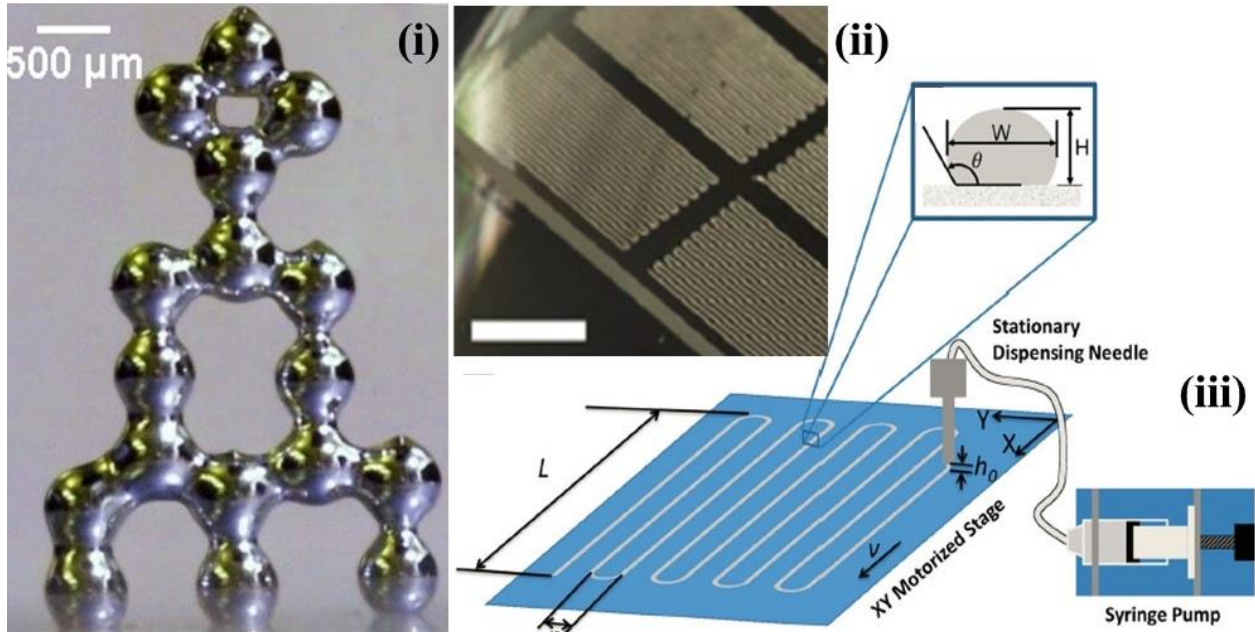


**Figure 1-5:** Additive patterning techniques produce free standing 3D structures (i)<sup>50</sup>, and conformal 2D (ii, and iii)<sup>57</sup>. Scale bar on (ii) is 5 mm. Figure (i) adapted from Ref. 50. Copyright Wiley 2013. Figures (i) and (ii), adapted from Ref. 57. Copyright Wiley 2014.

Rapid prototyping (RP), direct write (DW), and other additive manufacturing (AM) techniques are a class of techniques in which material is deposited in only desired locations. Examples include inkjet printing,<sup>58</sup> gravure or roll-to-roll (R2R) printing,<sup>59,60</sup> and direct write.<sup>61</sup> “3D printing” is the colloquial term for AM processes done in a layer by layer fashion to create three-dimensional objects.<sup>62</sup> Additive methods such as 3D printing enable high throughput patterning using automated processing and user customization by utilizing computer-aided design (CAD) models. Furthermore, these methods inherently reduce material waste and may form structures, which are often complex and may possess out-of-plane geometries.<sup>50</sup>

**Microcontact printing ( $\mu$ CP).**  $\mu$ CP is attractive for depositing inks and soft conductors in a potentially automated manner that requires limited manual labor.<sup>63,64</sup>  $\mu$ CP with gallium-based liquid metals relies on the adhesive nature of the gallium-oxide to elastomeric molds.<sup>63</sup> There are two primary methods to patterning liquid metals via elastomeric  $\mu$ CP: (i) manually transferring EGaIn using a topographical stamp, or (ii) depositing individual dots of EGaIn with a hemispherical PDMS tip (print head).

In the first method, a PDMS mold with protruding features of the desired geometry gently presses against a film of EGaIn. As a result, the metal oxide adheres only to the protruding features and does not invade into any cavities of the transfer mold. Thereafter, pressing the mold against the target substrate transfers the metal with mm resolution. This technique could also be considered lithography- enabled due to the use of a topographic mold.

In the latter method, a PDMS ‘needle’ with a hemispherical tip dips into a pool of liquid metal, which forms a bead of liquid metal on the print head.<sup>63</sup> The print head then contacts the substrate to transfer droplets of metal in a desired location; sequential printing of droplets coalesce to form a functional pattern. Mounting the print head and stage to a motorized 3-axis Cartesian system helps automate this process (see Fig. 1-9).

**Direct-write.** The formation of the surface oxide enables a variety of modes of direct write printing for liquid metals. In general, direct write patterning relies on extruding liquid metal onto a substrate through the nozzle of a syringe. Extruding droplets, wires, and other structures directly from a nozzle onto a substrate using pressure produces patterns in an additive fashion. This technique produces 2D patterns<sup>57</sup> and 3D structures<sup>50</sup> that are stabilized by the oxide skin (Fig. 1-5).

The nozzle inner diameter, distance between direct-write tip and substrate, and extrusion flow rate are important parameters effecting the geometry and diameter of wires and traces, both

in 2D and 3D.<sup>57</sup> Stacking droplets of the metal while shifting a translational stage is one approach to form free-standing 3D structures of liquid metal. Lowering the stage or platform of the substrate while extruding liquid metal can form free-standing wires, with heights up to ~1 cm.<sup>50</sup> The 3D printing approach has the appeal of not requiring a mold and the ability to make out of plane structures.

Although electro-hydrodynamic jetting (e-jetting) is a common approach to directly print colloids, biological materials, and inks, this technique is not yet possible with liquid metals.<sup>65,66</sup> The surface oxide clogs the nozzle, even in oxygen near-free environments, and thus impedes the process.<sup>63</sup> However, using a nozzle comprised of a porous material (e.g., paper or PDMS), which is impregnated with acid, allows for printing of liquid metal without clogging from the oxide.<sup>67</sup>

### **Current challenges and opportunities with Ga-based liquid metals**

This Highlight describes state-of-the-art methods to pattern liquid metals into a wide variety of structures or patterns and focuses almost exclusively on the use of Ga and its alloys. However, there are challenges with patterning this class of liquid metals, which provide opportunities for further work.

**Resolution.** The methods described here have relatively poor resolution compared to conventional fabrication techniques. For example, the best resolution of the methods reported including imprint (~2  $\mu\text{m}$ ), injection (~10  $\mu\text{m}$ ), and direct-write (~100  $\mu\text{m}$ ) need to be improved. Challenges include the formation of the oxide layer, and overcoming the large surface tension of the metal,<sup>15</sup> which provides an energetic barrier for coercing the metal into smaller features. Gallium has been found inside the hollow core of carbon nanotubes,<sup>68,69</sup> which suggests that it may be possible to get liquid metal into finer features.

**Sharp features.** All of the metal patterning techniques reported to date have some finite level of curvature, presumably due to the surface tension of the metal. That is, it is difficult to pattern the metal into sharp features, including corners or sharp tips.

**Precision.** Precision of patterning features is important for large-scale manufacturing processes. The patterning resolution is characterized by two important metrics: (i) critical dimension (CD),<sup>20</sup> which is the size of the smallest feature, and (ii) line edge roughness (LER), which measures the spatial variation of the width of the CD.<sup>70</sup> Standard manufacturing practices require that the LER should be within two or three standard deviations from the CD.<sup>20</sup> Several of the methods (e.g., imprinting, stencil lithography, and  $\mu$ CP) described exhibit poor LER. The roughness is likely due to the rheology of the oxide-coated liquid; that is, it flows along the path of least resistance and not necessarily uniformly. This issue of LER can be overcome by injecting into microchannels because the metal fills the void space. It would be useful to find ways to pattern the metal outside these confinements, yet with high resolution and low LER.

**Smooth films.** New methods for creating flat, thin, and uniform films of high quality are an area of opportunity. Many conventional patterning methods start with a smooth film. However, it is difficult to spread thin, uniform films of liquid-phase metal (Fig. 1-10).<sup>63</sup> Thick films possess a smooth surface finish, but often exhibit a curvature due to the surface tension of the metal. Since spin coated films of liquid metal are not uniform, thin films must be spread manually, which are often rough or have holes. In general, handling gallium and its alloys can be messy because these metals adhere to most surfaces due to their oxide.

**Adhesion.** The techniques described here benefit from or are influenced by the adhesion of the oxide-coated metal to substrates it contacts.<sup>71</sup> The adhesion of these oxide-coated metals to a substrate depends on the roughness,<sup>25,26</sup> dryness,<sup>44</sup> and composition<sup>72</sup> of the substrate. Furthermore,

the ability of the oxide to break and reform as it is injected, spread, or manipulated further complicates its adhesive behavior. The influence on this dynamic process on adhesion is only beginning to be understood.<sup>26</sup>

**Contacts.** Most devices require connecting the metal to other components. Gallium is known to alloy with many other metals (e.g., Cu, Al, Fe, and Au).<sup>6</sup> This feature could be used strategically to make ohmic contacts, but can also lead to inadvertent destruction of the contact and handling challenges. In addition, the oxide is resistive, which could create an issue for sensitive external electrical contacts. Finding the best way to contact these liquid metals electrically is an open question, although initial work suggests graphene or other forms of conductive carbon may offer a solution to this challenge.<sup>73</sup>

**Scalability.** Most of the techniques developed to date rely on laboratory techniques. Although additive manufacturing approaches (e.g., contact printing or direct-write) seem promising for large-scale production, liquid metal patterning may also be possible by adapting existing manufacturing techniques, such as roll-to-roll printing and slot-die coating. It remains to be proven how well these methods scale to high throughput processes. Likewise, recent work on deposition of liquid metal particles by atomization shows promise for large throughput printing but lacks the resolution offered by other methods.<sup>74</sup>

**Improved materials.** Gallium and its alloys are expensive. Given the small volumes needed in microsystems, the cost should not be prohibitive for systems that benefit from the properties of a fluid conductor. Nevertheless, new materials should be explored that lower cost, improve conductivity, or provide some additional benefit such as new rheological properties. Although this Highlight focuses on patterning with gallium-based alloys, many of these techniques can be used

with other soft conductors (i.e., liquid-phase metal–salt mixtures<sup>52</sup> and semi- conductors,<sup>52</sup> inks<sup>60</sup> and elastomeric composites<sup>31,75</sup>) given their physical properties allow for printing or patterning.

**Reconfigurability.** Improving shape reconfigurability remains an active area of research. The use of liquid metals could enable shape reconfigurable metallic components. The oxide skin adheres to channel walls and forms a residue on the walls upon evacuation of the metal from the channel. This adhesion limits the ability to reconfigure the shape of the metal. Potential solutions include the use of acid,<sup>21,42,43</sup> non- wetting surfaces,<sup>27,72,76</sup> slip layers,<sup>44,45</sup> or electrochemistry<sup>15,56</sup> (to remove the oxide).

## **Outlook**

This Highlight suggests there are a wide variety of methods to pattern Ga-based liquid metals from the micron to mm length scales. Many of these methods are simple and provide new approach for patterning that are not possible with conventional approaches. These patterning techniques are opening up new approaches for making stretchable electronics, metallic micro-fluidic components, and conductors for soft robotics and sensors. We hope this Highlight raises awareness of these techniques and inspires better patterning techniques that transcend current challenges and obstacles.

## **Acknowledgements**

M.D.D. acknowledges support from the Air Force Research Lab and the NSF (CAREER CMMI-0954321, ERC EEC-1160483, CMMI- 1362284, Research Triangle MRSEC on Programmable Soft Matter DMR-1121107) and the efforts of many colleagues who made this Highlight possible. The authors also thank Collin Ladd, Lazar Panich, and Dishit Parekh for assistance with the cover art.

## List of Supplemental Figures

*Nota bene:* The following figures appeared in the Supporting Information of the manuscript (as Fig. S1 to S5). For continuity, they are renumbered in the thesis document as Fig. 1-6 to Fig. 1-10).

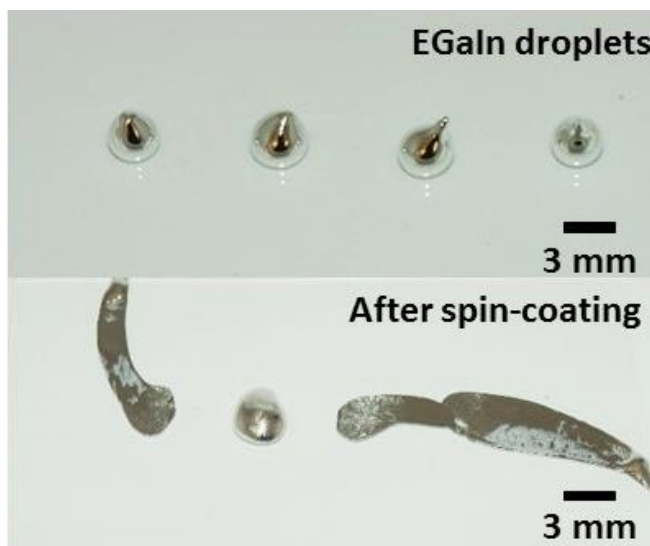


**Figure 1-6:** Unlike most liquids, planar thin films of EGaIn are difficult to produce using spin coating due to its high surface tension and surface oxide, which causes the metal to flow along paths where the oxide yields.

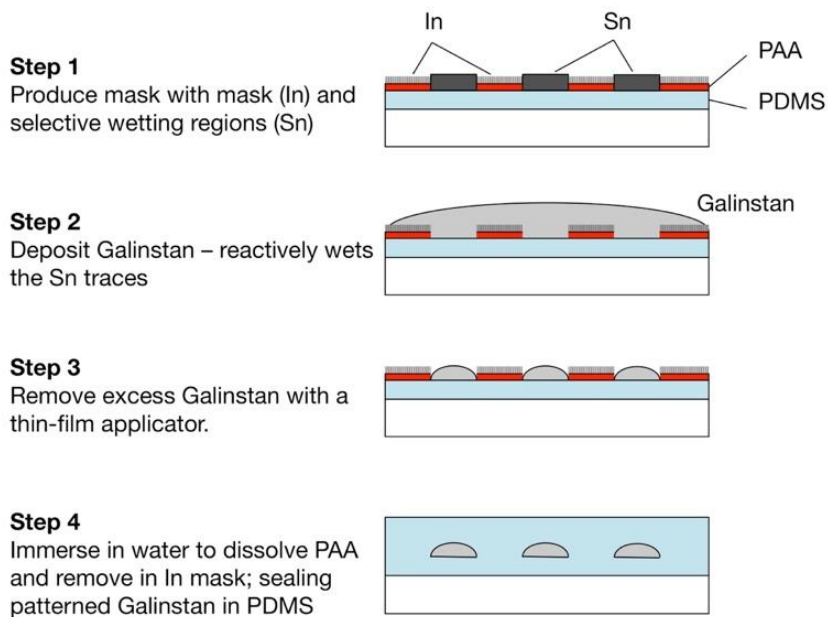


**Figure 1-7:** Method for patterning Galinstan with selective surface wetting. Figure adapted from Ref. 23. Copyright Wiley 2013.

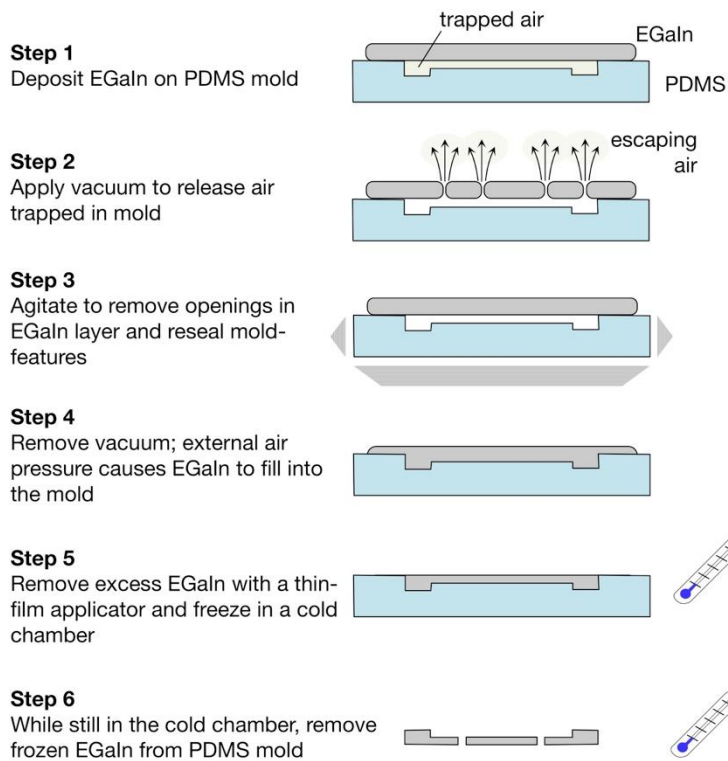


**Figure 1-8:** Method for molding EGaIn using vacuum filling and freeze casting. Figure adapted from Ref. 54 with permission from The Royal Society of Chemistry.

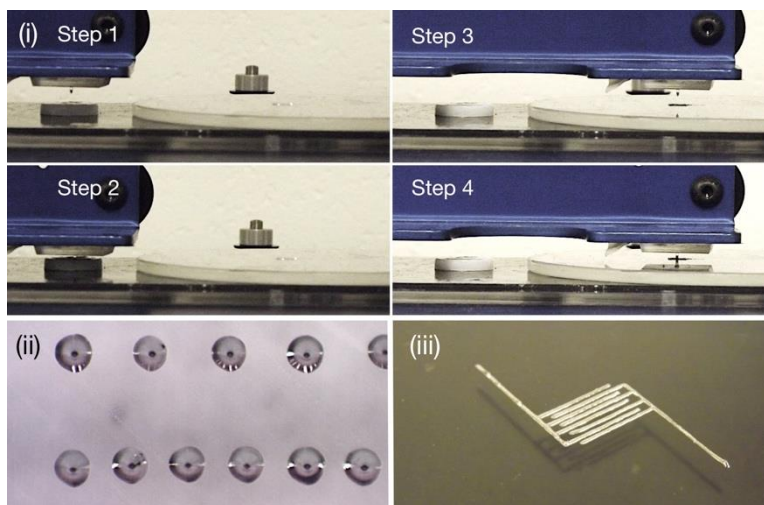


**Figure 1-9:** Droplet-by-droplet  $\mu$ CP with EGaIn. (i) Process steps: <sup>1</sup>dip PDMS tip into pool of EGaIn, <sup>2</sup>retract tip, <sup>3</sup>move wetted tip to substrate, <sup>4</sup>press tip into substrate to deposit EGaIn droplet; (ii) 340  $\mu$ m diameter droplets; (iii) solid lines produced by spacing droplets 200  $\mu$ m apart. Adapted with permission from Ref. 63. Copyright 2013 American Chemical Society.

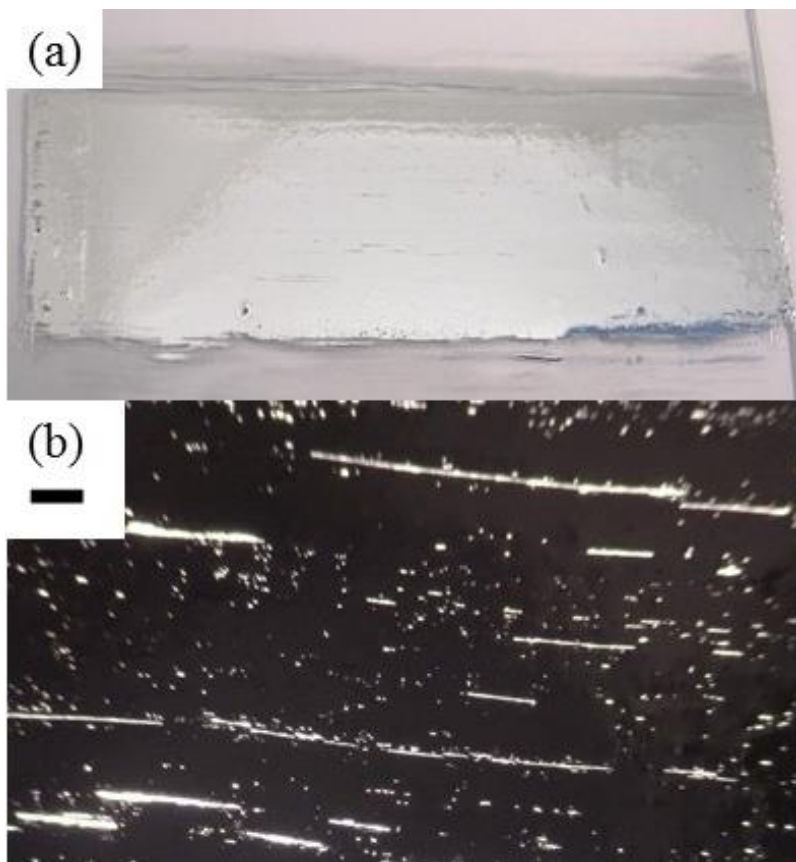


**Figure 1-10:** Traditional spreading techniques do not allow for smooth thin films of EGaIn (a). Inspection under an optical microscope (b) shows a thin but non-uniform coating of EGaIn. The sample is back-lit with light. If the film was uniform, it would not be possible to see through the film, but it is apparent that light travels through the films suggesting the thickness is not uniform. Scale bar on (b) is 1 mm.

## References

- (1) M. D. Dickey, *ACS Appl. Mater. Interfaces*, 2014, **6**, 18369–18379.
- (2) S. Zhu, J.-H. So, R. Mays, S. Desai, W. R. Barnes, B. Pourdeyhimi and M. D. Dickey, *Adv. Funct. Mater.*, 2013, **23**, 2308–2314.
- (3) S. Cheng and Z. Wu, *Lab Chip*, 2012, **12**, 2782.
- (4) R. J. Whitney, *J. Physiol.*, 1953, **121**, 1–27.
- (5) G. Beni, S. Hackwood and J. L. Jackel, *Appl. Phys. Lett.*, 1982, **40**, 912–914.
- (6) T. Liu, P. Sen and C.-J. Kim, *J. Microelectromech. Syst.*, 2012, **21**, 443–450.
- (7) M. D. Dickey, R. C. Chiechi, R. J. Larsen, E. A. Weiss, D. A. Weitz and G. M. Whitesides, *Adv. Funct. Mater.*, 2008, **18**, 1097–1104.
- (8) J. E. Chandler, H. H. Messer and G. Ellender, *J. Dent. Res.*, 1994, **73**, 1554–1559.
- (9) L. Cademartiri, M. M. Thuo, C. A. Nijhuis, W. F. Reus, S. Tricard, J. R. Barber, R. N. S. Sodhi, P. Brodersen, C. Kim, R. C. Chiechi and G. M. Whitesides, *J. Phys. Chem. C*, 2012, **116**, 10848–10860.
- (10) M. J. Regan, H. Tostmann, P. S. Pershan, O. M. Magnussen, E. DiMasi, B. M. Ocko and M. Deutsch, *Phys. Rev. B: Condens. Matter Mater. Phys.*, 1997, **55**, 10786–10790.
- (11) F. Scharmann, G. Cherkashinin, V. Breternitz, C. Knedlik, G. Hartung, T. Weber and J. A. Schaefer, *Surf. Interface Anal.*, 2004, **36**, 981–985.
- (12) A. Plech, U. Klemradt, H. Metzger and J. Peisl, *J. Phys.: Condens. Matter*, 1998, **10**, 971.
- (13) J. M. Chabala, *Phys. Rev. B: Condens. Matter Mater. Phys.*, 1992, **46**, 11346–11357.
- (14) R. C. Chiechi, E. A. Weiss, M. D. Dickey and G. M. Whitesides, *Angew. Chem., Int. Ed.*, 2008, **47**, 142–144.
- (15) M. R. Khan, C. B. Eaker, E. F. Bowden and M. D. Dickey, *Proc. Natl. Acad. Sci. U. S. A.*, 2014, **111**, 14047–14051.
- (16) H. Koo, J. So, M. D. Dickey and O. D. Velev, *Adv. Mater.*, 2011, **23**, 3559–3564.
- (17) P. Roberts, D. D. Damian, W. Shan, T. Luand, C. Majidi, in *2013 IEEE International Conference on Robotics and Automation (ICRA)*, IEEE, New York, 2013, pp. 3529–3534.
- (18) A. Fassler and C. Majidi, *Smart Mater. Struct.*, 2013, **22**, 055023.
- (19) B. L. Cumby, G. J. Hayes, M. D. Dickey, R. S. Justice, C. E. Tabor and J. C. Heikenfeld, *Appl. Phys. Lett.*, 2012, **101**, 174102.
- (20) M. J. Madou, *Fundamentals of microfabrication and nano- technology*, CRC, Boca Raton, Fla., 3rd edn, 2012.
- (21) D. Kim, J. H. Yoo, W. Choi, K. Yoo and J.-B. Lee, in *2014 IEEE 27th International Conference on Micro Electro Mechanical Systems (MEMS)*, 2014, pp. 540–543.
- (22) B. A. Gozen, A. Tabatabai, O. B. Ozdoganlar and C. Majidi, *Adv. Mater.*, 2014, **26**, 5211–5216.
- (23) R. K. Kramer, C. Majidi and R. J. Wood, *Adv. Funct. Mater.*, 2013, **23**, 5292–5296.
- (24) S. H. Jeong, A. Hagman, K. Hjort, M. Jobs, J. Sundqvist and Z. Wu, *Lab Chip*, 2012, **12**, 4657.
- (25) R. K. Kramer, J. W. Boley, H. A. Stone, J. C. Weaver and R. J. Wood, *Langmuir*, 2014, **30**, 533–539.
- (26) K. Doudrick, S. Liu, E. M. Mutunga, K. L. Klein, V. Damle, K. K. Varanasi and K. Rykaczewski, *Langmuir*, 2014, **30**, 6867–6877.
- (27) D. Kim, D. Jung, J. H. Yoo, Y. Lee, W. Choi, G. S. Lee, K. Yoo and J.-B. Lee, *J.*

- Micromech. Microeng.*, 2014, **24**, 055018.
- (28) H.-J. Kim, C. Son and B. Ziaie, *Appl. Phys. Lett.*, 2008, **92**, 011904.
- (29) J.-H. So and M. D. Dickey, *Lab Chip*, 2011, **11**, 905–911.
- (30) N. Pekas, Q. Zhang and D. Juncker, *J. Micromech. Microeng.*, 2012, **22**, 097001.
- (31) T. Sekitani, Y. Noguchi, K. Hata, T. Fukushima, T. Aida and T. Someya, *Science*, 2008, **321**, 1468–1472.
- (32) S. Rosset, M. Niklaus, P. Dubois and H. R. Shea, *Adv. Funct. Mater.*, 2009, **19**, 470–478.
- (33) J. Park, S. Wang, M. Li, C. Ahn, J. K. Hyun, D. S. Kim, D. K. Kim, J. A. Rogers, Y. Huang and S. Jeon, *Nat. Commun.*, 2012, **3**, 916.
- (34) C. Majidi, R. Kramer and R. J. Wood, *Smart Mater. Struct.*, 2011, **20**, 105017.
- (35) Y.-L. Park, C. Majidi, R. Kramer, P. Bérard and R. J. Wood, *J. Micromech. Microeng.*, 2010, **20**, 125029.
- (36) J. Vetrovec, A. S. Litt, D. A. Copeland, J. Junghans and R. Durkee, *Liquid metal heat sink for high-power laser diodes*, ed. M. S. Zediker, 2013, p. 86050E.
- (37) K.-Q. Ma and J. Liu, *Phys. Lett. A*, 2007, **361**, 252–256.
- (38) M. Gao and L. Gui, *Lab Chip*, 2014, **14**, 1866–1872.
- (39) D. Kim, Y. Lee, D. Lee, W. Choi and J. B. Lee, in *2013 Transducers Eurosensors XXVII: The 17th International Conference on Solid-State Sensors, Actuators and Microsystems (TRANSDUCERS EUROSensors XXVII)*, 2013, pp. 2620–2623.
- (40) J. Wang, S. Liu and A. Nahata, *Opt. Express*, 2012, **20**, 12119–12126.
- (41) J. Wang, S. Liu, S. Guruswamy and A. Nahata, *Appl. Phys. Lett.*, 2013, **103**, 221116.
- (42) D. Kim, P. Thissen, G. Viner, D.-W. Lee, W. Choi, Y. J. Chabal and J.-B. Lee, *ACS Appl. Mater. Interfaces*, 2013, **5**, 179–185.
- (43) D. Kim, R. G. Pierce, R. Henderson, S. J. Doo, K. Yoo and J.-B. Lee, *Appl. Phys. Lett.*, 2014, **105**, 234104.
- (44) M. R. Khan, C. Trlica, J.-H. So, M. Valeri and M. D. Dickey, *ACS Appl. Mater. Interfaces*, 2014, **6**, 22467–22473.
- (45) C. Koo, B. E. LeBlanc, M. Kelley, H. E. Fitzgerald, G. H. Huff and A. Han, *J. Microelectromechanical Syst.*, 2015, DOI: 10.1109/JMEMS.2014.2381555.
- (46) H.-J. Kim, T. Maleki, P. Wei and B. Ziaie, *J. Microelectromechanical Syst.*, 2009, **18**, 138–146.
- (47) K. P. Mineart, Y. Lin, S. C. Desai, A. S. Krishnan, R. J. Spontak and M. D. Dickey, *Soft Matter*, 2013, **9**, 7695.
- (48) W. Zhao, J. L. Bischof, J. Hutasoit, X. Liu, T. C. Fitzgibbons, J. R. Hayes, P. J. A. Sazio, C. Liu, J. Jain, J. Badding and M. H. W. Chan, *Nano Lett.*, 2015, **15**, 153–158.
- (49) M. R. Khan, G. J. Hayes, J.-H. So, G. Lazzi and M. D. Dickey, *Appl. Phys. Lett.*, 2011, **99**, 013501.
- (50) C. Ladd, J.-H. So, J. Muth and M. D. Dickey, *Adv. Mater.*, 2013, **25**, 5081–5085.
- (51) H. Ota, K. Chen, Y. Lin, D. Kiriya, H. Shiraki, Z. Yu, T.-J. Ha and A. Javey, *Nat. Commun.*, 2014, **5**, 5032.
- (52) F. Hensel, *Angew. Chem., Int. Ed. Engl.*, 1980, **19**, 593–606.
- (53) A. C. Siegel, D. A. Bruzewicz, D. B. Weibel and G. M. Whitesides, *Adv. Mater.*, 2007, **19**, 727–733.
- (54) A. Fassler and C. Majidi, *Lab Chip*, 2013, **13**, 4442–4450.
- (55) T. Lu, L. Finkenauer, J. Wissman and C. Majidi, *Adv. Funct. Mater.*, 2014, **24**, 3351–3356.
- (56) M. R. Khan, C. Trlica and M. D. Dickey, *Adv. Funct. Mater.*, 2015, **25**, 671–678.

- (57) J. W. Boley, E. L. White, G. T.-C. Chiu and R. K. Kramer, *Adv. Funct. Mater.*, 2014, **24**, 3501–3507.
- (58) P. Calvert, *Chem. Mater.*, 2001, **13**, 3299–3305.
- (59) G. A. of America, G. E. Foundation, *Gravure: Process and Technology*, Gravure Association of America, Gravure Education Foundation, Rochester, NY, 1991.
- (60) E. Hrehorova, M. Rebros, A. Pekarovicova, B. Bazuin, A. Ranganathan, S. Garner, G. Merz, J. Tosch and R. Boudreau, *J. Disp. Technol.*, 2011, **7**, 318–324.
- (61) K. K. B. Hon, L. Li and I. M. Hutchings, *CIRP Ann. Manuf. Technol.*, 2008, **57**, 601–620.
- (62) F42 Committee, Terminology for Additive Manufacturing Technologies, ASTM International, 2012.
- (63) A. Tabatabai, A. Fassler, C. Usiak and C. Majidi, *Langmuir*, 2013, **29**, 6194–6200.
- (64) C. A. Gunawan, M. Ge and C. Zhao, *Nat. Commun.*, 2014, **5**, 3744.
- (65) S. Lee, J. Song, H. Kim and J. Chung, *J. Aerosol Sci.*, 2012, **52**, 89–97.
- (66) S. N. Jayasinghe, A. N. Qureshi and P. A. M. Eagles, *Small*, 2006, **2**, 216–219.
- (67) D. Kim, J. H. Yoo, Y. Lee, W. Choi, K. Yoo and J.-B. Lee, in *2014 IEEE 27th International Conference on Micro Electro Mechanical Systems (MEMS)*, 2014, pp. 967–970.
- (68) Y. Gao and Y. Bando, *Nature*, 2002, **415**, 599.
- (69) Z. Liu, Y. Bando, M. Mitome and J. Zhan, *Phys. Rev. Lett.*, 2004, **93**, 095504.
- (70) G. M. Gallatin, *Proc. SPIE*, 2005, **5754**, 38–52.
- (71) S. H. Jeong, K. Hjort and Z. Wu, *Sensors*, 2014, **14**, 16311–16321.
- (72) D. Kim, D.-W. Lee, W. Choi and J.-B. Lee, in *2012 IEEE 25th International Conference on Micro Electro Mechanical Systems (MEMS)*, 2012, pp. 1005–1008.
- (73) P. Ahlberg, S. H. Jeong, M. Jiao, Z. Wu, U. Jansson, S.-L. Zhang and Z.-B. Zhang, *IEEE Trans. Electron Devices*, 2014, **61**, 2996–3000.
- (74) S. H. Jeong, K. Hjort and Z. Wu, *Sci. Rep.*, 2015, **5**, 8419.
- (75) M. Z. Seyedin, J. M. Razal, P. C. Innis and G. G. Wallace, *Adv. Funct. Mater.*, 2014, **24**, 3104.
- (76) G. Li, M. Parmar, D. Kim, J.-B. (JB) Lee and D.-W. Lee, *Lab. Chip*, 2014, **14**, 200.

## **CHAPTER 2**

# **WET APPROACH: ELECTRO-HYDRODYNAMICS OF CONTINUOUS ELECTROWETTING**

## **Abstract**

This work examines the electro-hydrodynamic behavior of the continuous electrowetting (CEW) effect for plugs of oxide-coated liquid metal. Utilizing optical microscopy, we measure the displacement and velocity of the metal plugs in glass capillaries over a range of conditions (e.g., applied voltage, electrolyte composition, plug length). In addition, we perform electrochemical impedance spectroscopy (EIS) on the CEW system and propose an equivalent circuit model to gain clarity on its interfacial electrochemical behavior. These experiments show that the plug of metal moves only if the electrolyte (1) forms an interfacial slip-layer, which we estimate to be ~200 to 500 nm in thickness from EIS measurements, and (2) allows metal to exhibit electrocapillarity behavior. Given these conditions are met, the metal plug can actuate with or without the presence of an oxide skin. EIS experiments show that the basic electrolytes etch the metal, which can be modeled by artificial inductor element. Over long time periods, the dissolution of Ga can impede the CEW motion. This work provides guidelines for experimental conditions that enable reversible actuation of liquid metals in capillaries and microfluidics with high velocities (~cm/s) using low voltages (< 2 V). Finally, we use CEW to demonstrate reconfigurable filter switches for THz waveguides, which may be extended for other reconfigurable electromagnetic components such as RF antennas and metamaterials.

## **Introduction**

Reconfiguring the shape of metals is promising because metals are optically reflective, have high thermal and electrical conductivities, and possess a surface Plasmon resonance.<sup>1,2</sup> However, conventional devices that utilize metals have a static design or function (i.e., antennas). Therefore, shape-changeable liquid metals may be useful in forming devices with reconfigurable properties. In addition, moving liquid metals within capillaries or confined systems is of interest

for microfluidic applications (pumps and actuators),<sup>3</sup> opto-electronics,<sup>4</sup> and thermal energy management.

Due to the high surface tension of the metal (400 to 600 mN/m), large pressures are required to actuate the metal within microchannels.<sup>5</sup> Although it is possible to achieve such pressures with pumps or compressed gasses, pneumatics requires large external equipment. In contrast to mechanical forces (i.e., pneumatics), using voltage to actuate liquid metals is beneficial for several reasons. Electrical signals do not require any moving parts, provides mobility, and reduces the size and complexity of the entire system. In addition, electrical signals can be easily programmed to create complex or customized motions.

There are two primary approaches to actuating liquid metals using voltages: electrocapillarity and electrochemical oxidation (or oxidative spreading).<sup>6</sup> Electrocapillarity is a change in the interfacial tension across a liquid metal-electrolyte interface in response to an electric potential across the interface.<sup>7</sup> Applying a voltage across the interface changes the density of the electric double layer at the surface of the metal, which results in the change in interfacial tension. Beyond a certain voltage, electrochemical reactions can take place on the surface of the metal, which marks the end of the ‘classic’ electrocapillarity. Furthermore, the formation of a surface oxide on liquid metal can further lower its surface tension (to near zero).<sup>8</sup> This approach been utilized to reconfigure its shape in open and closed environments. Meanwhile, electrochemically reducing the oxide can also be utilized for reconfigurability.<sup>9,10</sup> Similarly, redox reactions have been utilized to actuate liquid metals.<sup>11</sup> However, these approaches are limited by the actuation speed and material consumption (i.e., continuous oxidation or reduction of a finite amount of metal or electrolyte).<sup>3,12</sup>

The electrocapillarity effect may be utilized to actuate drops or plugs of metal within capillary, which is illustrated in Figure 2–1. Applying a voltage to a drop of liquid metal in a capillary filled with an electrolyte creates a surface tension gradient (due to an imbalance of charges) along the length of the metal plug. This phenomenon is known as continuous electrowetting (CEW) and is analogous to Marangoni flow of liquids.<sup>13</sup> CEW is useful because it can move liquid metals at high speeds ( $\sim$ cm/s) with low voltages ( $<2$  V). In general, electrowetting is a type of electrocapillarity behavior whereby the wetting property of a material (either liquid or solid) is changed by applying voltage to this material.<sup>14</sup> Conventionally, CEW refers to the electrowetting phenomenon occurs across a liquid-liquid interface. This type of movement is a different mechanism than other electro-kinetic flows, such as electro-osmosis, electrophoresis, that move charges or ions along the electric field.

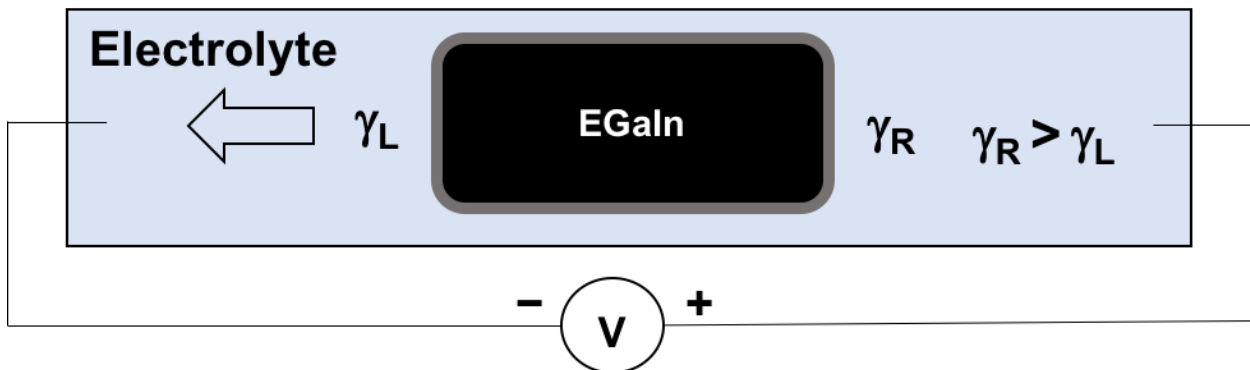


**Figure 2-1:** Schematic of CEW using EGaln. A gray border around the metal plug (black) indicates the presence of an oxide skin. Applying a voltage ( $V$ ) at the end of the capillaries creates a surface tension ( $\gamma$ ) gradient in the plug. In the schematic, the right side of the plug is shown to have a higher surface tension ( $\gamma_R$ ) than the left side ( $\gamma_L$ ). Accordingly, the metal moves to the left (from high to low surface tension).

CEW was first reported using Hg in sulfuric acid and demonstrated as light switches and later for micro-actuators.<sup>13,15–17</sup> However, Hg is toxic and thus not ideal for practical usage. CEW with other liquid metals (Ga alloys, Au amalgams, etc.) is also possible but more complicated. For the case Ga alloys, Ga readily forms an oxide skin in presence of oxygen. This oxide adheres to the channel walls, which prevents the metal from moving. To overcome the adhesion of the oxide,

electrolyte must be pre-injected to wet the walls of the capillary.<sup>18</sup> Upon injecting the liquid metal thereafter, the electrolyte forms an interfacial slip-layer between the metal surface and channel wall. In addition, a popular approach to remove the oxide is to use acids or bases. Even in such cases, pre-injecting electrolyte into the capillary is necessary to form the slip-layer. Thus, the slip-layer of water or electrolyte is crucial to achieve CEW motion. CEW with Ga alloys have been utilized previously to actuate liquid metals within microchannels for reconfigurable antennas<sup>12,19</sup> as well as in open systems to create microfluidic pumps.<sup>3,20</sup> This work further examines the electrohydrodynamics of CEW with Ga alloys, specifically the influence of aqueous electrolytes on the actuation behavior.

### *Electrochemical Impedance Spectroscopy (EIS)*

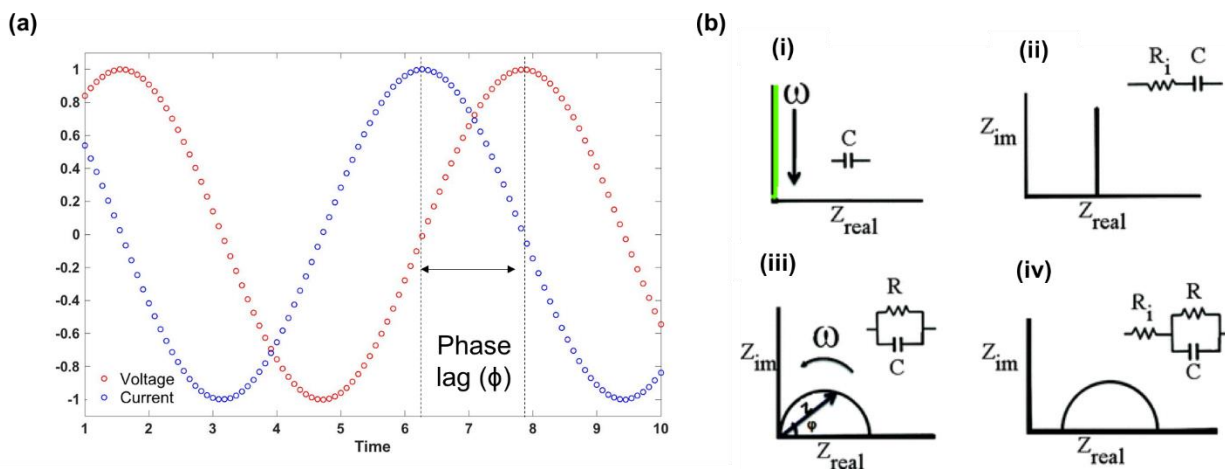


**Figure 2-2:** (a) Plot of a sinusoidal waveform of voltage (red) and current (blue) over time. The current and voltage are out of phase by a phase lag ( $\phi$ ). (b) Example Nyquist diagrams for EIS measurements, adapted from literature.<sup>21</sup>

This work utilizes electrochemical impedance spectroscopy (EIS) to better understand the interface of the liquid metal and electrolyte. EIS involves applying a small AC voltage (sinusoidal waveform,  $\sim 10\text{-}15\text{ mV}_{\text{RMS}}$ ) to a system of interest and measuring the current and phase shift (also known as phase lag or phase angle) of this system; an example of the voltage, current, and phase lag of an sinusoidal waveform is illustrated in **Figure 2-2a**. This measurement is taken across a range of frequencies (of the applied AC voltage) to generate a spectrum of the impedance, which

is the AC analog of electrical resistance, and phase angle. These diagrams of impedance and phase angle vs. frequency are referred as Bode plots. Using the same information, the impedance can be expressed in real and imaginary components, which are known as Nyquist plots. The shape of this curve provides an insight on the physico-chemical interactions that make up the system.<sup>21,22</sup> Examples for these curves are shown in Fig. 2–2b with corresponding circuit models. For example, the Nyquist plot for a capacitor is a straight line. Meanwhile, diffusion-limited charge transfer processes cause angular shift in the Nyquist plot. In general, any interface involving a metal and an electrolyte can be modeled as a capacitor in parallel with a resistor (herein, “RC element”). On Nyquist diagrams, metal-electrolyte interfaces exhibit a semi-circular shape and can be modeled using an RC component. In addition, electrolytes can be considered an electrical conductor with some value of resistance based on its physical parameters (length, size) and properties (i.e., conductivity). Based on the shape of Bode and Nyquist plots, electrical circuit diagrams are often used to model the electrochemical behavior of EIS.

## **Results**

### *Characterizing the displacement of drops*

The goal of the characterization studies is to determine experimental conditions that allow the metal plug to translate through a glass capillary. For these experiments, we measure the distance an EGaIn plug (~1 cm, in length) moves within a cylindrical capillary made from glass (0.8 mm, inner diameter) under various conditions (i.e., electrolyte composition, applied voltage, and AC frequency). These experiments involve applying an AC voltage using a Pt electrode to the system and measuring the movement of the plug of metal. An optical microscope aids in examining and quantifying plug movement behavior. A ruler placed parallel to the glass capillary serves as a scale guide. For these experiments, we measure change in position over time for varying conditions

of pH of electrolyte, AC voltage ( $V_{\text{peak-to-peak}}$  ( $V_{\text{pp}}$ ) using square wave), and frequency of the AC voltage. Based on this information, we calculate the mean displacement and average velocity of the metal plug.

From these experiments, we observe three major trends. (1) Increasing the applied voltage increases the displacement of the metal. (2) The displacement of the plug varies inversely with AC frequency. (3) The presence of the oxide (based on the pH of electrolyte) suppresses the displacement. In addition, we notice that CEW does not occur for all aqueous electrolytes. Below, we discuss these trends in more detail.

Increasing the voltage subsequently increases the displacement of the metal by creating a larger surface gradient. **Figure 2–3** shows a representative graph of the position ( $x$ ) of the metal with respect to time during an oscillation cycle; the graph compares the movement for 1.0  $V_{\text{pp}}$  and 2.0  $V_{\text{pp}}$  at 1 Hz in 1 M NaOH and 1 M NaF. For both electrolytes, increasing the voltage from 1.0 V to 2.0 V results in a larger mean displacement ( $\Delta x$ ) (increase in displacement from  $3.6 \pm 0.1$  mm to  $8.1 \pm 0.1$  mm in NaOH and  $3.2 \pm 0.1$  mm to  $5.4 \pm 0.1$  mm in NaF). To quantify the relative change in the displacement, we calculate the ratio of the change in the mean displacement between the two voltages. This comparison informs us that, for an increase in one volt, the metal plug displaces 2.28 $\times$  farther in NaOH and 1.68 $\times$  farther in NaF. Across 0.5 Hz to 3.0 Hz, the metal plug exhibits a similar behavior (an average of 2.55 $\times \pm 0.47$  for NaOH and 1.75 $\times \pm 0.8$  for NaF). The values of these displacements are tabulated in **Appendix A**.

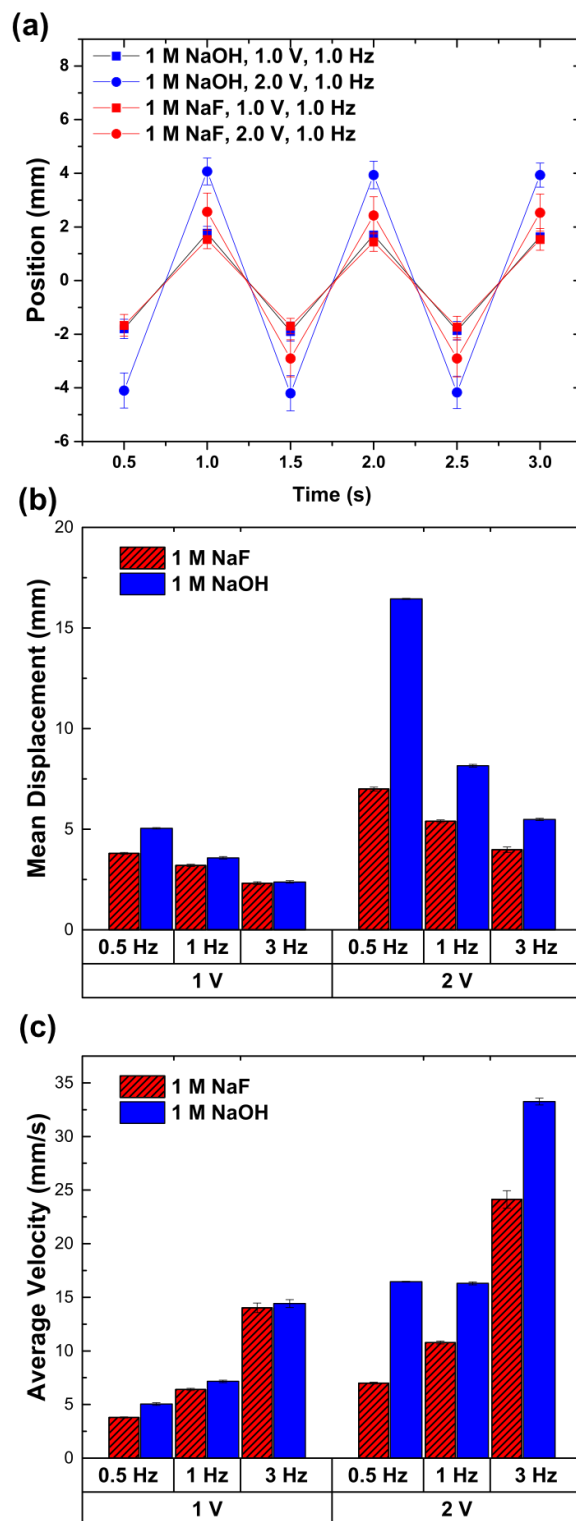


**Figure 2-3:** (a) Position of the center of a liquid metal plug (1.0 cm to 1.5 in length) over time in response to an AC voltage (1 Hz, square wave). The figure shows the position in 1 M NaOH (blue) and 1 M NaF (red) for 1  $V_{pp}$  (squares) and 2  $V_{pp}$  (circles). Error bars indicate standard deviations of 3 trials. (b) Column groups of mean displacement of the metal plug for 1 M NaOH (blue, solid) and 1 M NaF (red with diagonal checks) for three frequencies (0.5 Hz, 1 Hz, and 3 Hz) at 1  $V_{pp}$  and 2  $V_{pp}$ . (c) Average velocity for 1 M NaOH (blue, solid) and 1 M NaF (red with diagonal checks) for three frequencies (0.5 Hz, 1 Hz, and 3 Hz) at 1  $V_{pp}$  and 2  $V_{pp}$ .

Next, we see that the displacement of the metal is inversely proportional to the AC frequency. This relationship is intuitive because higher frequency results in less time for the plug to travel in one direction. Fig. 2–3b shows the effect of frequency and mean displacement for 1 M NaOH and 1 M NaF at 1.0 V and 2.0 V. For NaOH at 2.0 V, the displacement decreases from  $17.0 \text{ mm} \pm 0.02 \text{ mm}$  to  $5.5 \text{ mm} \pm 0.05 \text{ mm}$  as the frequency increases from 0.5 Hz to 3 Hz. Similarly, for NaF, the displacement decreases from  $7.0 \text{ mm} \pm 0.1 \text{ mm}$  to  $4.0 \text{ mm} \pm 0.1 \text{ mm}$ . In addition to displacement, for both electrolytes, the average velocity of the plug increases with an increase in frequency, as shown in Fig. 2–3c. This difference is more apparent at 2 V than 1 V, likely because a greater surface tension gradient is generated at larger voltages. However, the relationship between displacement and velocity to frequency is not linear; Tables 2 to 4 in the Appendix A compare the ratios of the change in displacements and velocity for given change in frequency. This comparison shows that the changes in displacement and velocity are not proportional to the change in frequency.

Combined, these results provide design parameters for actuating the liquid metal plugs using CEW. For example, it is difficult to discern the motion of a plug larger than one mm for AC frequencies exceeding 15 Hz (Fig. A–1 in Appendix A). Thus, lower frequencies are ideal achieving large translations (i.e., one Hz or less creates displacements greater than four to five mm). However, when higher frequencies are required, such as for optical switches, applying a DC bias may help achieve larger displacements. Although not studied further, we demonstrate the utility of DC biases with higher frequencies in the section Reconfigurable Terahertz Waveguides.

Finally, we examine whether the presence of a surface oxide influences plug movement behavior. In aqueous solutions, pH of the electrolyte will determine whether an oxide is present or not. The oxide is amphoteric and dissolves in solutions with pH less than three and greater than

ten.23 Moving EGaIn using CEW is possible with the oxide because of a thin slip layer of water that separates the metal from the channel wall. In general, EGaIn plugs displace farther along the capillary channel in 1 M NaOH (no oxide) than 1 M NaF (oxide present). Table 2–1 compares relative ratios of displacement and velocity of the metal between 1 M NaOH to 1 M NaF. At 1.0 V, the metal plug displaces on average 1.16× farther ( $\pm 0.15\times$ ) in NaOH vs. NaF for a given voltage. This discrepancy is larger at 2.0 V, where the metal actuates 1.75× farther ( $\pm 0.53\times$ ) in NaOH than NaF. This difference is also inversely proportional to frequency. That is, the difference in displacement subsides at higher frequencies. This result shows that it is possible to achieve similar displacements for CEW with the oxide present (i.e., without using corrosive electrolytes such as NaOH).

**Table 2-1:** Ratios of displacement and velocity of NaOH to NaF for 1.0 V<sub>pp</sub> and 2.0 V<sub>pp</sub> at 0.5 Hz, 1.0 Hz, and 3.0 Hz.

1.0 V <sub>pp</sub>			2.0 V <sub>pp</sub>		
Frequency [Hz]	Displacement Ratio	Velocity Ratio	Frequency [Hz]	Displacement Ratio	Velocity Ratio
0.5	1.33	1.33	0.5	2.35	2.35
1	1.12	1.12	1	1.51	1.51
3	1.03	1.03	3	1.38	1.38
<b>Average</b>	1.16		<b>Average</b>	1.75	
<b>Std. Dev.</b>	0.15		<b>Std. Dev.</b>	0.53	

Overall, the shorter displacements in presence of an oxide may be for several reasons. First, the oxide exhibits a yield stress. Therefore, this yield stress may suppress Marangoni flow around the metal plug due to the surface tension gradient. In addition, the presence of an oxide lowers the capacitance of the metal drop. Due to a lower capacitance (i.e., less charge density), the magnitude of surface tension gradient is smaller. Finally, the presence of the oxide may affect the slip-layer between the metal and channel wall due to differences in wetting behavior of water on metal vs. metal oxide. Nevertheless, these experiments inform us that CEW can occur in the presence of an oxide (i.e., without the use of corrosive electrolytes).

Finally, the metal does not exhibit CEW motion for all aqueous electrolytes. Results from Fig. 2–3 show that CEW occurs in aqueous solutions of NaOH and NaF. In both solutions, the electrolyte provides both a slip-layer and supports electrocapillarity. However, simply pre-injecting an aqueous electrolyte does not create a slip-layer. For example, we do not observe CEW effect in aqueous solutions of NaCl. In such cases, a plug of EGaIn does not translate even when tilting the capillary that is pre-filled with aqueous NaCl. Similarly, a plug of EGaIn does not move in tilted capillaries that are filled with 1 M LiCl. In contrast, a plug of EGaIn readily moves upon tilting capillaries that are filled with 1 M LiCl. In contrast, a plug of EGaIn readily moves upon tilting capillaries that are filled with either aqueous NaOH or DI water alone. This suggests that the composition of salts in the electrolyte plays a role on whether a slip-layer forms.

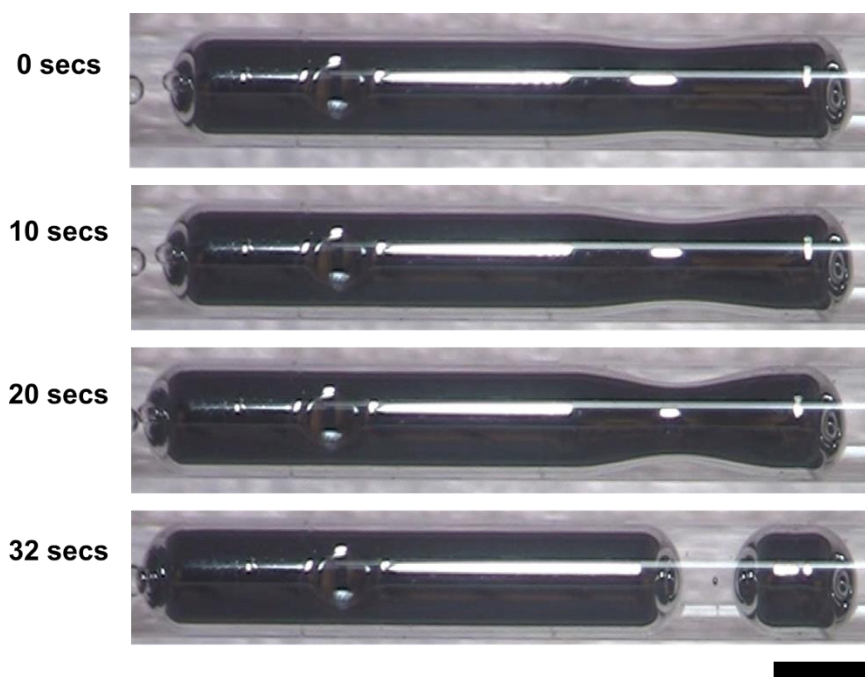


**Figure 2-4:** Droplet splitting of an EGaIn plug in 1 M NaF when  $0.2 \text{ mV}_{\text{RMS}}$  (sine wave) with  $1 \text{ V}_{\text{DC}}$  bias is applied. Scale bar is 1 mm.

Likewise, electrocapillarity behavior does not outright occur in all aqueous electrolytes. Results from Fig. 2–3 demonstrate that electrocapillarity occurs in both aqueous NaOH and NaF. However, upon applying voltage to the CEW capillary setup filled with EGaIn and aqueous NaCl

does not cause the drop to translate along the length of the capillary. Instead, after 30 secs, the plug begins to deform and split into two droplets. Curiously, the plug translates immediately after the plug splitting, which suggests that a threshold voltage is required to form a slip-layer. We observe a similar droplet-splitting phenomenon in 1 M NaF under conditions where the drop does not translate horizontally. **Figure 2–4** shows the time evolution of an EGaIn plug splitting apart in 1 M NaF at low AC amplitude voltages with a DC bias (200 mV<sub>RMS</sub>, and 1 to 3 V<sub>DC</sub>). We observe similar behavior in 100 mM NaF; in such case, the splitting requires higher voltage, likely due to the solution having a lower conductivity. The splitting is likely due to Plateau-Rayleigh instability, whereby a stream of liquid preferentially breaks into smaller droplets.<sup>24</sup> For such an instability to occur, applying a voltage may cause a local change in surface tension where the splitting occurs. The droplet splitting behavior in both NaCl and NaF suggest that applying a voltage to the CEW setup does change the surface tension of the drop. However, it may be that a threshold voltage is required to either form a slip-layer or generate a sufficient surface tension gradient to cause translational motion. A similar behavior for CEW of Hg whereby the electrolyte wets the metal plug prior to actuating.<sup>13</sup> Nevertheless, aqueous electrolytes for CEW have challenges that may limit its use. Water may evaporate over time and thus CEW in aqueous electrolytes have limited life-spans. In addition, water absorbs EM radiation, which makes it unfavorable for use in reconfigurable EM components.

Therefore, we wondered whether other liquids that wet the liquid metal could form a slip-layer and subsequently enable CEW. We attempted CEW with methanol (MeOH) because it wets EGaIn and can dissolve NaOH (to remove its oxide). Furthermore, the polarity of MeOH provides it lower absorption of EM radiation, in comparison to water, in the THz regime (300 GHz to 3 THz, or 1 mm to 100  $\mu$ m in wavelength).<sup>25</sup> Curiously, we were only able to actuate the metal in

NaOH/MeOH mixtures (1.5 to 2.0 M) with large AC amplitudes ( $4 V_{\text{peak-to-peak}}$ ) with a DC-offset voltage (2 V). Below the threshold DC bias, we observed droplet splitting to occur in a similar fashion to aqueous electrolytes. This result suggests the slip-layer does not form immediately within MeOH and applying voltage to the system forms the slip-layer by causing MeOH wet the liquid metal plug. Further work in identifying other liquids that enable CEW that do not evaporate over time and transmit RF energy.

### Reconfigurable Terahertz Waveguides

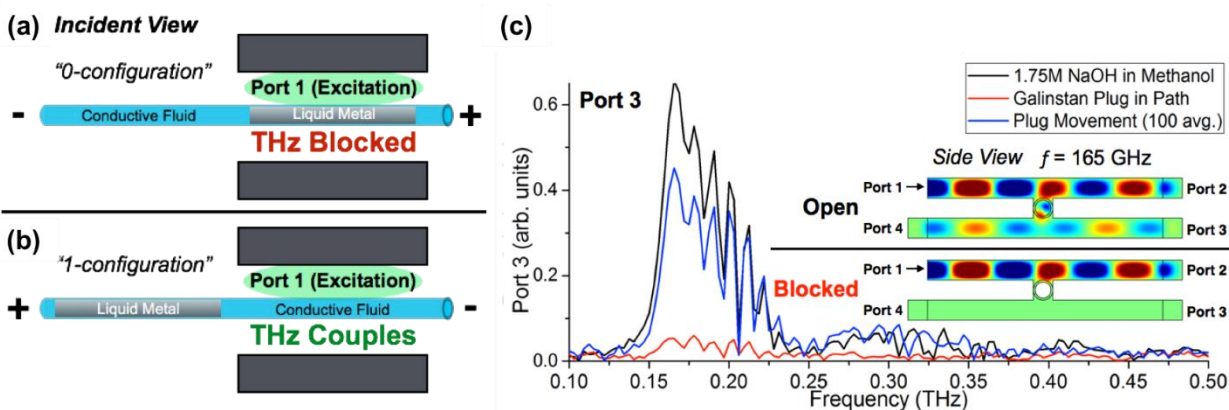


**Figure 2-5:** Reconfigurable THz Waveguide. (a and b) Incident view of setup. THz waveguide sandwiches an quartz capillary filled with a plug of liquid metal (Galinstan, 8 mm, in length) in 1.75 M NaOH in MeOH. Applying an AC voltage ( $4 V_{\text{pp}}$ , 2 Hz, square wave) actuates the liquid metal in (a) and out (b) of the waveguide. (c) Data transmission measurements out of Port 3 of bottom wave guide. When liquid metal is in path of waveguide (configuration in (a)), THz signal is blocked (red line on (c)). When metal is outside the path of the waveguide (configuration in (b)), THz signal couples through Port 3 (black curve). Inset shows finite element modeling of THz transport through waveguide at 165 GHz. Figure adapted from literature.<sup>26</sup>

We utilize the characterization studies of CEW to demonstrate reconfigurable terahertz (THz) waveguides.<sup>26,27</sup> As shown in **Figure 2–5**, this demonstration involves actuating liquid metal through glass capillaries (pre-filled with 1.75 M NaOH in MeOH); the capillaries are partially inserted between two waveguide plates. Applying an AC voltage to the capillary actuates the metal in and out of the waveguide. When metal is actuated within waveguides, the metal blocks the THz signal by reflection. When metal is outside the waveguide, the electrolyte allows the THz signals to couple and pass through the bottom waveguide (Port 3 in Fig. 2–5b). This oscillatory motion effectively creates a switch or filter for THz waveguides.<sup>25</sup>

### *Electrochemical impedance spectroscopy (EIS)*

We utilize EIS to elucidate the electro-hydrodynamics of CEW in aqueous electrolytes. Specifically, we seek to better understand how different components of this system influence the overall behavior (i.e., movement of the metal plug). To best characterize the CEW effect, these experiments are performed in the same experimental configuration as the displacement studies. We note that the metal plug does not move while acquiring the impedance spectra due to the low the applied voltage (10 to 15 mV<sub>RMS</sub>, sine wave).

**Figure 2–6** shows the impedance spectra for EIS measurements for CEW with ~1 cm plug in 1 M NaOH. As a control experiment, we perform EIS on a glass capillary filled only with the electrolyte (i.e., no liquid metal plug). As expected, the data points in black in Fig. 2–6a show that impedance increases in the system at lower frequencies. At the high frequency (100 kHz), the impedance represents the resistance of the electrolyte solution (6 kΩ). Meanwhile, the impedance value at the low frequency (1 Hz) represents the overall impedance in the system (i.e., resistive losses across the Pt-electrolyte interface and through the electrolyte solution). Likewise, the phase angle (Fig. 2–6b, in red) is zero degrees at high frequency (3 kHz), which indicates that the system is dominated by resistive effects (i.e., solution resistance). At low frequencies (~100 Hz and lower), the system transitions to capacitive behavior, which is marked by the change in phase angle transitions from 0° to –65°.

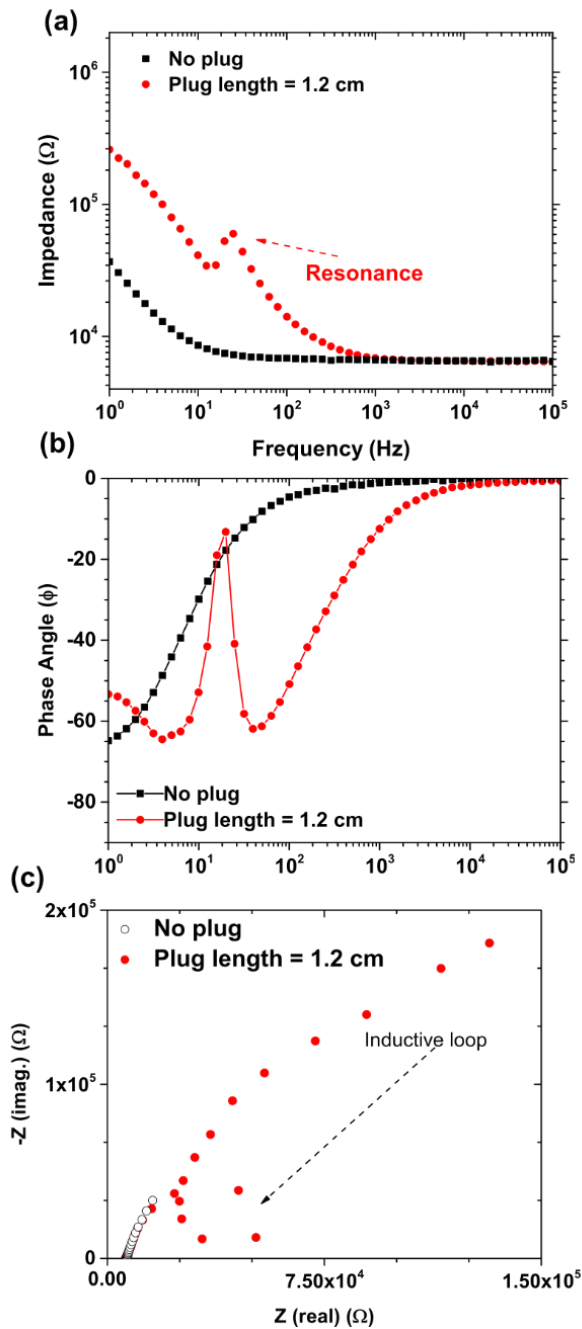


**Figure 2-6:** EIS Measurements with and without metal plug. (a and b) Bode plot showing spectra of impedance (a) and phase angle (b) from 1 GHz to 1 Hz. Black curve is of electrolyte only (no metal plug-in capillary). Red curve is impedance of CEW system with a plug length of 1.2 cm, which shows a resonance near 15 Hz. (c) Corresponding Nyquist diagram plotting negative of the imaginary component of impedance ( $-Z_{imag}$ , y-axis) vs. real component of impedance ( $Z_{real}$ ). Black curve is of electrolyte only (no metal plug in capillary). Red curve is spectra of CEW system with a plug length of 1.2 cm, which shows an inductive loop at the corresponding frequency of the resonance in (a and b).

Fig. 2–6a (in red) shows the impedance spectra for a plug of liquid metal (1.2 cm in length). Introducing a plug of liquid metal into a capillary filled with an electrolyte increases the overall impedance in the system. Fig. 2–6a (in red) shows that the impedance converges with the data from the control experiment at high frequencies (above one kHz). This behavior is expected because the solution resistance dominates at this frequency range. Beginning at 1 kHz through 1 Hz, the impedance begins to increase dramatically, relative to the control experiment at the same frequency range. In addition, we observe resonance behavior in both the impedance as well as the phase angle. This experimental anomaly is discussed in detail later.

Notably, the impedance of the system at 1 Hz is  $\sim 7.5x$  higher with the metal plug than without ( $\sim 300\text{ k}\Omega$  for 1.2 cm metal plug vs.  $40\text{ k}\Omega$  for control experiment). This result is not intuitive but is of importance to the CEW mechanism. Why would adding a plug of metal increase the overall impedance of the system? The metal plug possesses a higher electrical conductivity (or lower electrical resistance) than the electrolyte, and thus should decrease the impedance. One reason for the increase in impedance is that adding metal creates a new interface for charge transfer (i.e., ionic conduction to electronic conduction). This new interface is evident in the Nyquist plot, which is shown in Fig. 2–6b. Each data point of this spectra represents the real and imaginary impedance values for a given frequency. In both EIS spectra (with and without metal plug), the Nyquist plot exhibits a sloped line, which indicates a capacitive term and charge transfer resistance. As the frequency decreases, the magnitude of the imaginary component also increases because the charge transfer interactions dominate at lower frequencies. In comparison, a purely capacitive behavior would show a vertical line (as illustrated in Fig. 2–2b). The Nyquist plot for the metal plug reaches higher impedance values for both real and imaginary components, which corresponds with the increase in magnitude of the impedance at low frequencies in the Bode plots.

The formation of an interfacial slip-layer also contributes to the increase in impedance. This slip-layer exhibits a large resistance because it is a thinner conductor (relative to the surrounding electrolyte in the capillary); resistance through a conductor is inversely proportional to its width. Because the charge transfer resistance is high (i.e., from ion to electron across the electrolyte-liquid metal interface), current must instead pass through another pathway. As such, the pathway for electrical conduction must be through the thin slip-layer of water between the metal and channel walls. **Figure 2–8** shows an equivalent circuit model of the CEW system that visualizes how current flows through the system; later in this work, we discuss the model and examine the relative contributions of each component to the current pathway.

Interestingly, the Nyquist plot for the metal plug forms a loop in the intermediate frequency range (between 11 and 12 Hz). The corresponding Bode plot in the same frequency range also exhibits resonance peaks for both the impedance and the phase angle. This corresponding behavior suggests adding the plug of liquid metal also creates a different behavior in the system. We first wondered whether this resonance behavior was an experimental artifact (i.e., drift in the system) or a temporal effect. To confirm the validity of the resonance and loop behaviors, we repeat the EIS experiment ten times with one minute intervals in between each experiment. **Figure A-2** in Appendix A shows the Bode and Nyquist plots as an average of the ten trials. The average of the ten runs show nearly the identical behavior with neither a change in the magnitude of the data collected nor a change in frequency for the behavior. The EIS spectra are typically performed starting from high frequency to low frequency (“forward sweep”). To assess whether the resonance occurs at a specific time of the experiment, we repeat this experiment starting from low frequency values to high frequency values (“reverse sweep”). **Figure A-3** in Appendix A shows that both reverse and forward sweep show resonance behavior (Bode plot) and the loop behavior (Nyquist

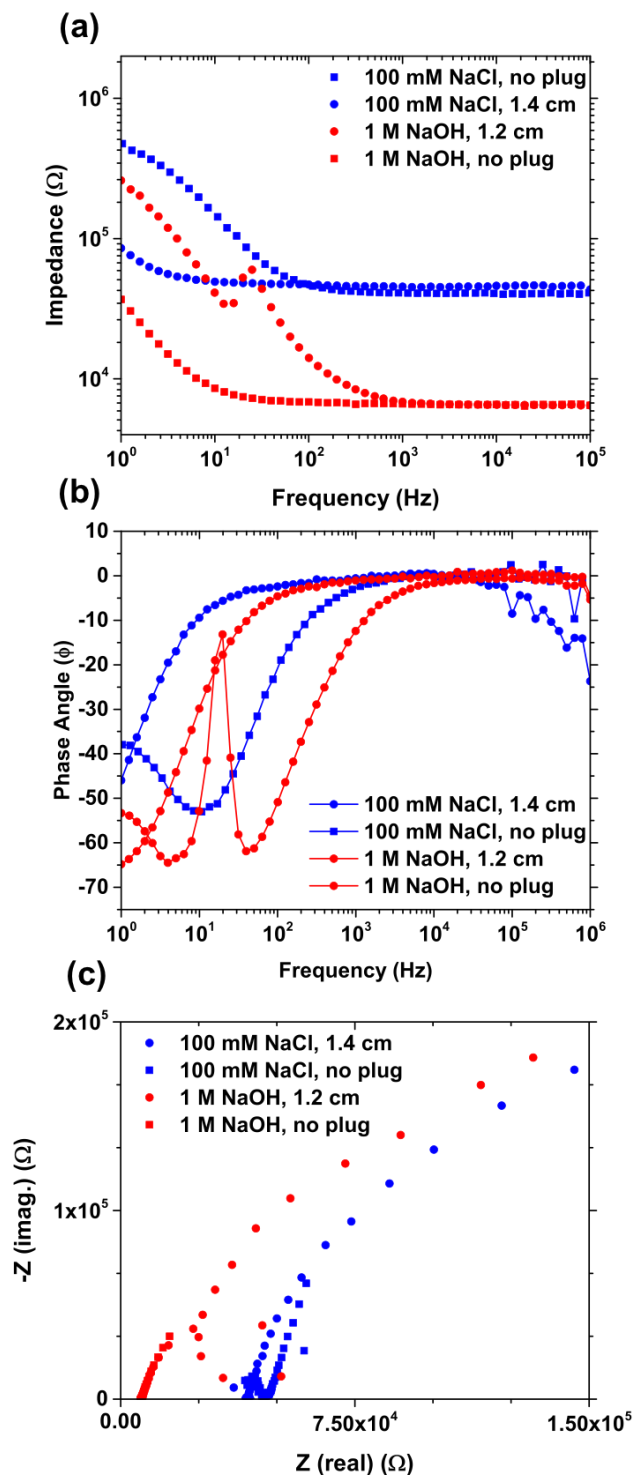
plot) at the same frequency range. We do not see a noticeable difference in the behavior for experiments performed in an isolated frequency range (from 1 Hz to 20 Hz), where the resonance is observed. Finally, we observe the same behavior in potentiostat instruments of different manufacturers (Gamry Ref-600 and Biologic SP-600). Overall, these experiments corroborate the resonance and loop behaviors exhibited in the Bode and Nyquist plots, respectively, which may be a unique signature of the CEW system.

Therefore, what is the cause of this behavior and does it have any physical significance? One possibility is that the CEW system is non-linear with respect to impedance at this frequency range. If so, this non-linear response (i.e., resonant frequency) should change with the size of the drop. To test this hypothesis, we repeat these experiments with varied the length of plug from 1.2 cm to 6.5 cm, shown in **Figure A-4** in Appendix A. In the Bode plots, the resonant frequency shifts from 13 Hz to 10 Hz as the plug length increases. Likewise, the loop in Nyquist plot is larger for smaller plug lengths. These experiments show that there is some variation based on the length of the plug but not dramatic in change.

We wondered whether the presence of the oxide effects the resonance and loop behaviors. To do so, we compare EIS spectra between NaOH (pH~14, no oxide present) and sodium chloride (NaCl, pH~7, oxide present), with the same plug length of liquid metal. **Figure 2-7** shows a comparison of the EIS for a plug of EGaIn (1.4 cm in length) in NaOH, NaCl, and control experiments of the electrolytes alone. In comparison to the NaOH experiments, the EIS spectra for NaCl exhibit neither a resonance for the impedance nor a loop in the Nyquist plots. The loop behavior in Nyquist plots has been reported in the literature associated with corrosion of metals and modeled as a dummy inductor element;<sup>28,29</sup> thus, we refer to this loop as “inductive loop”

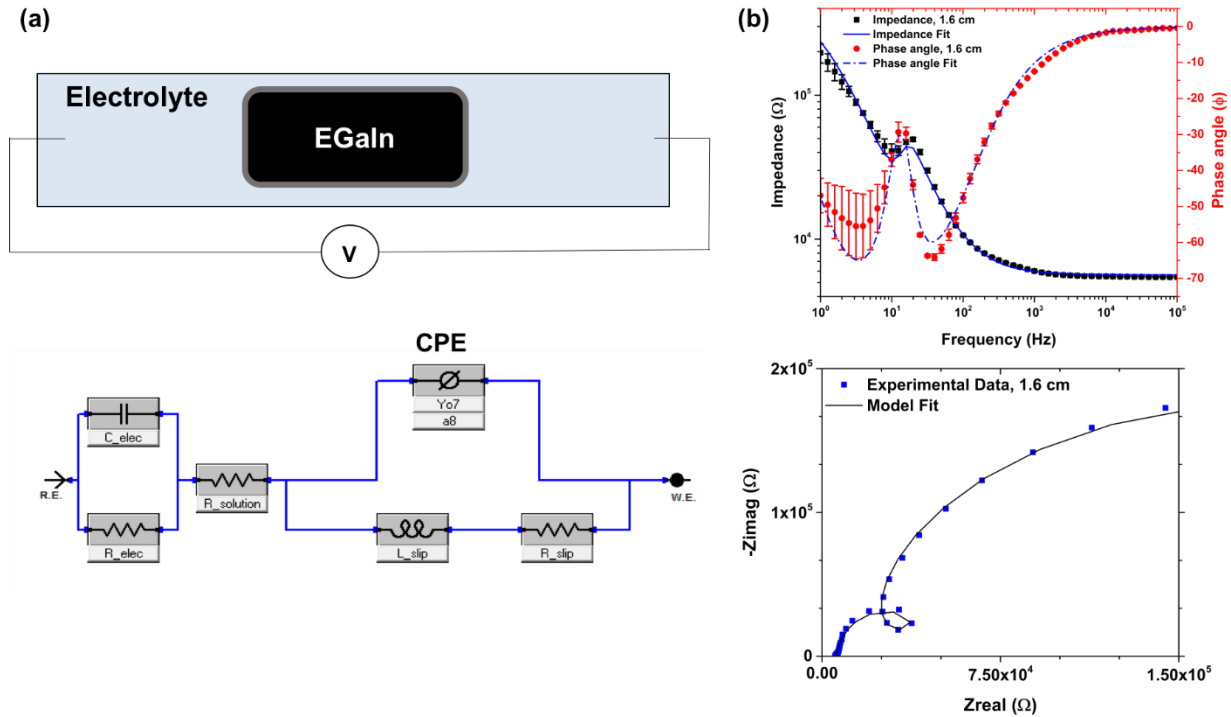
moving forward. Based off the results on the NaCl experiments, we hypothesized that the inductive loop behavior was due to the corrosion of Ga by NaOH.

The corrosion of Ga by NaOH is also visually evident on a macroscopic scale; **Figure A-5** in Appendix A shows photographs of Ga films soaked in 1 M NaOH, 1 M NaCl, and air (control). In comparison to Ga soaked in 1 M NaOH, Ga films in air and 1 M NaCl appear reflective and pristine. Overall, these experiments suggest that resonance and loop behavior may be due to NaOH etching Ga oxide, which can be limited by using an electrolyte of neutral pH. Along with work reported in the literature, the combination of displacement characterization and EIS studies show that NaOH allows for CEW to occur. However, the dissolution of Ga into the electrolyte limits its long-term use, which has been previously reported for the CEW system.<sup>3,12</sup>



**Figure 2-7:** EIS spectra with and without oxide. Data points with squares are of electrolyte only (no metal plug-in capillary, blue for 100 mM NaCl and red for 1 M NaOH). Data points with circles are of CEW system (blue for 1.4 cm plug in 100 mM NaCl and red for 1.2 cm in 1 M NaOH). (a and b) Bode plot showing spectra of impedance (a) and phase angle (b) from 1 GHz to 1 Hz. A resonance appears only for 1 M NaOH in both impedance (a) and phase angle (b). (c) Corresponding Nyquist diagram plotting negative of the imaginary component of impedance ( $-Z_{imag.}$ , y-axis) vs. real component of impedance ( $Z_{real}$ ). An inductive loop appears only for 1 M NaOH (red, circle) corresponding frequency of the resonance in (a and b).

## Equivalent circuit modeling



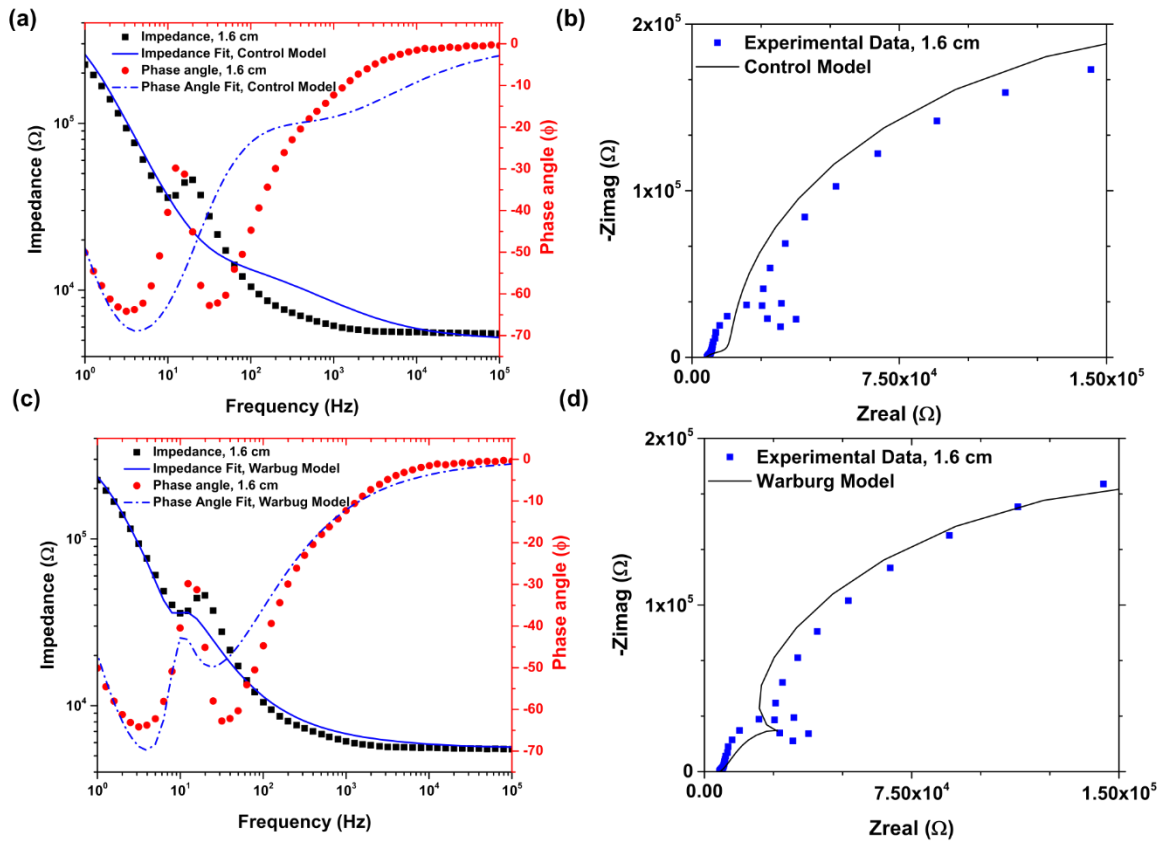
**Figure 2-8:** a) Schematic of CEW system with EGaln in capillary filled with electrolyte (top). The proposed equivalent circuit model for CEW with EGaln (bottom). (b) Bode (top) and Nyquist (bottom) diagrams of experimental data points for a plug of 1.6 cm with model fitting.

Fig. 2–8 shows a cartoon of the CEW system with the proposed equivalent circuit model below. A model for this system has been reported in the literature.<sup>30</sup> however, we believe the reported model does not fully describe the system. Therefore, we propose an alternative model to fully characterize the CEW system. Overall, the CEW system consists of three physical components (liquid metal plug, electrolyte, and electrode). The model consists of a RC element (resistor and capacitor in parallel) to model the Pt electrode and electrolyte interface. Thereafter, a resistor in series ( $R_{\text{solution}}$ ) follows the RC element serves to model the electrolyte in the capillary. To model the liquid metal-electrolyte interface, we utilize a constant phase element (CPE) as a non-ideal capacitor. Physically, a thin slip-layer of electrolyte (between the metal and capillary wall) also exists alongside the metal drop. Therefore, we utilize a resistor ( $R_{\text{slip}}$ ) in parallel to the CPE to model the electrolyte in the slip-layer. In addition, we use a “dummy” inductor element in series

to  $R_{\text{slip}}$  to model the resonance and loop behavior exhibited in EIS spectra. We justify the use of CPE and inductor elements further below.

Fig. 2–8b compares the predicted impedance and phase angles based on the model with an experimental data set. We utilize a commercial software package (EC-Lab by Biologic) included with potentiostat instrumentation to generate model curves for the Bode and Nyquist diagrams as well as parametric fitting. The model curve matches well with the experimental data (goodness of fit of 0.00153). Specifically, the model follows the resonances and loop behaviors shown in the Nyquist and Bode plots. This model does indeed deviate from the experimental data at low-frequencies (less than 5 Hz). This discrepancy may be due to non-linear behavior in the system at this frequency range.

To validate the model rationale, we compare the proposed model in Fig. 2–8 to two other variant models. **Figure 2–9** compares fits from the other two models with experimental data. In addition, **Table A–5** in Appendix A compares the estimated values for the elements for each tested model. First, we show model the EIS spectra with and without the inductor element. For this comparison, we refer to the model without the inductor loop as the “control model” and the model with inductor loop as the “proposed model” (as shown in Fig 2–8). Fig. 2–9a and 2–9b show a comparison of fits for the proposed and control models to the experimental data. Beginning at 10 kHz, the impedance fit for the control model begins to deviate from the experimental values. Moreover, the control model also does not follow the resonance behavior exhibited by the experimental data (goodness of fit of 0.00479 vs. 0.00153 for the proposed model loop in Fig. 2–8). Likewise, the control model also does not accurately model the phase angle of the system. Thus, the inclusion of the inductor element is important for modeling the system.



**Figure 2-9:** Bode (left) and Nyquist (right) diagrams of experimental data points for a plug of 1.6 cm with model fits of Control Model (CPE element with no Inductor element, a and b) and Warburg model (Warburg unit replacing CPE element, Inductor element included, c and d).

Thereafter, we consider the use of a CPE in the proposed model the liquid metal-electrolyte interface. Thus, we replace the CPE element with a Warburg element, which is often used when diffusion of ions dominates the charge transfer process. To isolate the difference between CPE and Warburg elements, both models include a dummy inductor loop. Fig. 2–9c and 2–9d show a comparison of the model with Warburg element with the proposed model (CPE) as well as the experimental data. The model with Warburg element generally follows the trends in the experiment data but does not exhibit the resonance and loop behaviors; the goodness of fit for the Warburg model (0.026) is one order of magnitude higher than the proposed model with CPE element (0.0015). The Warburg model shows a ‘shoulder-like’ feature for the resonance in impedance and phase angle but not a full peak at this frequency range. Likewise, in the Nyquist

plot, the Warburg model displays a ‘pinch’ at the beginning of the loop but does not show a full system. This deviation suggests that the CPE element better fits the experimental data than the Warburg element. Moreover, it suggests that the inductive loop and resonance behavior are not due to diffusion of the ions (which are modeled by the Warburg element). This can be confirmed by examining the slope of the Nyquist plot, which is typically  $\sim 1/2$  for Warburg elements. **Figure A–6** in Appendix A shows a zoomed view of the Nyquist plot at high frequency (beginning of the experiment) for 1.6 cm plug with the Warburg model fitting. We use a linear fit in this region to determine the slope of the Nyquist plot to be 3.6, which is far from the expected value for Warburg elements. This analysis shows that the Warburg element is not appropriate for modeling the CEW system.

CPE elements can often be used to model non-ideal capacitors, where charge leaks across the interface. Indeed, this non-ideality can be confirmed by looking at the  $\alpha$  coefficient for the CPE, which indicates the ideality of the capacitor ( $\alpha_{\max}$  of 1.0 for ideal capacitance). The CEW system of EGaIn in NaOH shows an  $\alpha$  of 0.80, which is similar to alpha coefficients for CPE elements of dielectric materials used for electrowetting.<sup>31</sup> Based on the alpha coefficient, we estimate the capacitance to be  $\sim 1.1 \mu\text{F}/\text{cm}^2$  based on a similar analysis using EIS for low voltage electrowetting systems<sup>32</sup>; details regarding the calculations are discussed in Appendix A. However, the estimated capacitance of  $1.1 \mu\text{F}/\text{cm}^2$  is 10 to 20 times lower than measured capacitance for a sessile drop of EGaIn in NaOH<sup>8</sup>; therefore, the EIS measurement may not provide accurate capacitance for the CEW system. Ultimately, this results suggests that a system utilizing Ga and NaOH may change in performance over time due to dissolution of Ga. Therefore, using Ga-alloys as soft or microfluidic capacitors in NaOH solutions should be done with caution.

The model is useful for comparing the relative resistances of components making up the CEW system. The resistance values are of importance because they inform us on where the voltage drops occur within the system. As expected, the largest drop in the voltage occurs across Pt-electrolyte interface ( $R_{\text{elec}} \sim 350 \text{ k}\Omega \pm 11 \text{ k}\Omega$ ); we use Pt instead of other metals because it limits Faradaic reactions at the interface, which would lead to larger voltage drops. Nevertheless, this voltage drop is unavoidable due to the nature of a metal-electrolyte interface. However, based on the model fit, we determine that the  $R_{\text{solution}}$  and  $R_{\text{slip}}$  are  $5.6 \text{ k}\Omega \pm 0.01 \text{ k}\Omega$  and  $10 \text{ k}\Omega \pm 0.7 \text{ k}\Omega$ , respectively. We note that these resistance values are dependent on the length of ‘element’ in the channel. In these experiments, we are careful to maintain the same length of the electrolyte across various experiments.

Therefore, we scale these values based on their relative lengths to make a proper comparison. Based on a 1.6 cm plug length in 7.5 cm capillary, the resistance values scale to 0.95 k $\Omega$ /cm for  $R_{\text{solution}}$  and 6.3 k $\Omega$ /cm for  $R_{\text{slip}}$ . Therefore, the resistance drop (and subsequently voltage) in the slip-layer is  $\sim 7$  higher than in the remaining electrolyte. This comparison informs us that the distance between the electrode and metal plug should be considered for designing CEW systems. To actuate liquid metal over long distances (i.e., over several cm), multiple electrodes should be utilized to ensure that the solution resistance does not exceed the slip-layer resistance.

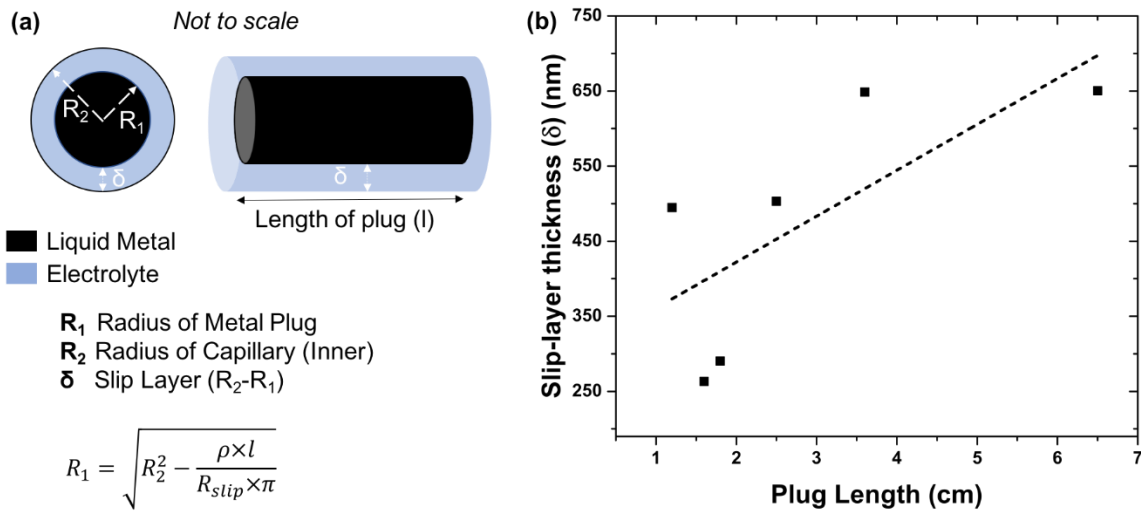


**Figure 2-10:** Estimating slip-layer thickness (a) Schematic of cylindrical annulus used to model slip-layer ( $\delta$ ), (b) Comparison of  $\delta$  (nm) and plug length (cm). Dotted line serves as a guide.

Finally, we estimate the thickness of the slip-layer based on the  $R_{slip}$  value. To do so, we model the slip-layer as an electrical conductor in the shape of a cylindrical annulus, as shown in **Figure 2–10a**. Based on the length of plug, resistivity of the electrolyte, and  $R_{slip}$ , we estimate the slip-layer thickness to be  $\sim 270$  nm for a plug length of 1.6 cm. Fig. 2–10b plots the estimated slip-layer thickness for a range of plug lengths. Based on the aggregate of these values, we estimate the average thickness to be  $475 \text{ nm} \pm 168 \text{ nm}$ . This estimation is close to the measured slip-layer using optical interferometry, which ranges from 270 nm to 500 nm between a Hg drop and mica surface in an aqueous electrolyte (KCl).<sup>33</sup> Overall, the EIS results confirm that the slip-layer is the driving force for the actuation of liquid metal because the thin-film provides the largest resistance within the CEW system.

Although this model provides insights on the interfacial behavior of liquid metal in the CEW system, the EIS measurement faces some inherent limitations. Firstly, the EIS measurements are performed at the open-circuit potential (i.e., the 10-15 mV sine wave is transposed with no DC bias), where the metal does not actuate. In addition, the surface tension and the capacitive behavior

of the metal vary with respect to the voltage. In principle, EIS can be performed at higher voltages (i.e., using a DC bias). However, higher voltages will cause the metal plug to move during the experiment, which effects its accuracy. Thus, the EIS spectra shown in this work cannot provide more information about the liquid metal-electrolyte interface (e.g., surface tension and capacitance) that forms within the capillary.

### *Conclusions and Future Work*

These experiments suggest that CEW occurs when the electrolyte forms an interfacial slip-layer and allows for electrocapillarity behavior for the liquid metal. CEW is possible even with the presence of an oxide (i.e., in non-corrosive electrolytes,  $3 < \text{pH} < 10$ ), albeit with lower displacement and velocities. In general, we find that the displacement of the metal plug scales with the voltage and inversely with frequency. Meanwhile, the velocity of the metal increases with respect to both voltage and frequency. Although NaOH provides higher displacement and velocities than NaF, the base dissolves Ga ions from the surface into the electrolyte, which ultimately limits its long-term use. In addition, we demonstrate that CEW is possible in non-aqueous electrolytes (e.g., NaOH solutions of methanol), which is desirable for RF applications. Using CEW in methanol, we demonstrate reconfigurable add-drop filters for THz waveguides.

We utilize EIS to elucidate interfacial electrochemical behavior of the CEW system. These measurements show that the system displays a signature resonance in the impedance and phase angles near 10-12 Hz; these peaks correspond with an inductive loop in the Nyquist diagrams at the same frequency range. The resonance and loop behaviors ‘turn’ off when the oxide is present (i.e., in NaCl), which suggests that NaOH corrodes the surface of the liquid metal. Based on these EIS spectra, we propose an equivalent circuit model for CEW, which uses a CPE to model the liquid metal-electrolyte interface and a dummy inductor element for the resonance and loop

behavior. Through EIS measurements, we show that the resistance through the interfacial slip-layer is 4.5x larger than within the bulk electrolyte in the capillary. Finally, we estimate the slip-layer thickness to be between ~200 to ~500 nm, which is similar to previously reported experimental measurements between Hg and mica glass.

Combined, these results provide better design guidelines for using CEW to electrically reconfigure liquid metals. Future work in this area should focus on identifying other fluids or interfacial solutions that enable CEW without leaching Ga into the solution and exhibit low absorption of EM waves. ICMPS may be useful in determining the dissolution of Ga ions into the electrolyte solution. In addition, interferometry or a surface force apparatus may be helpful tools for quantifying the thickness of the slip-layer in the CEW system.

### **Acknowledgements**

I would like to acknowledge Mr. Ethan Strubinger, Mr. Alex Johnson, and Mr. Daehong Kim for help with displacement measurements. Thanks for your attention to detail, hard work, and dedication with this project. Thanks to Dr. David Chang for assistance with Figure 2-3. The reconfigurable THz waveguide work was carried out by Dr. Kim Reichel, Mr. Nicolas Lozada-Smith, and Prof. Dan Mittleman at Brown University. Thanks to all of them for being wonderful collaborators. Finally, I would like to thank Prof. Abolfazl Kiani and Dr. Shiyang Tang for helpful suggestions and insights regarding the CEW behavior and EIS measurements.

## References

- (1) Khoshmanesh, K.; Tang, S.-Y.; Zhu, J. Y.; Schaefer, S.; Mitchell, A.; Kalantar-zadeh, K.; Dickey, M. Liquid Metal Enabled Microfluidics. *Lab Chip* **2017**.
- (2) Daeneke, T.; Khoshmanesh, K.; Mahmood, N.; Castro, I. A. de; Esrafilzadeh, D.; Barrow, S. J.; Dickey, M. D.; Kalantar-zadeh, K. Liquid Metals: Fundamentals and Applications in Chemistry. *Chem. Soc. Rev.* **2018**.
- (3) Tang, S.-Y.; Khoshmanesh, K.; Sivan, V.; Petersen, P.; O'Mullane, A. P.; Abbott, D.; Mitchell, A.; Kalantar-zadeh, K. Liquid Metal Enabled Pump. *Proc. Natl. Acad. Sci.* **2014**, *111* (9), 3304–3309.
- (4) Wang, J.; Liu, S.; Vardeny, Z. V.; Nahata, A. Liquid Metal-Based Plasmonics. *Opt. Express* **2012**, *20* (3), 2346–2353.
- (5) Dickey, M. D.; Chiechi, R. C.; Larsen, R. J.; Weiss, E. A.; Weitz, D. A.; Whitesides, G. M. Eutectic Gallium-Indium (EGaIn): A Liquid Metal Alloy for the Formation of Stable Structures in Microchannels at Room Temperature. *Adv. Funct. Mater.* **2008**, *18* (7), 1097–1104.
- (6) Eaker, C. B.; Dickey, M. D. Liquid Metal Actuation by Electrical Control of Interfacial Tension. *Appl. Phys. Rev.* **2016**, *3* (3), 31103.
- (7) Frumkin, A.; Polianovskaya, N.; Grigoryev, N.; Bagotskaya, I. Electrocapillary Phenomena on Gallium. *Electrochimica Acta* **1965**, *10* (8), 793–802.
- (8) Khan, M. R.; Eaker, C. B.; Bowden, E. F.; Dickey, M. D. Giant and Switchable Surface Activity of Liquid Metal via Surface Oxidation. *Proc. Natl. Acad. Sci.* **2014**, *111* (39), 14047–14051.
- (9) Wang, M.; Trlica, C.; Khan, M. R.; Dickey, M. D.; Adams, J. J. A Reconfigurable Liquid Metal Antenna Driven by Electrochemically Controlled Capillarity. *J. Appl. Phys.* **2015**, *117* (19), 194901.
- (10) Khan, M. R.; Trlica, C.; Dickey, M. D. Recapillarity: Electrochemically Controlled Capillary Withdrawal of a Liquid Metal Alloy from Microchannels. *Adv. Funct. Mater.* **2015**, *25* (5), 671–678.
- (11) Gough, R. C.; Dang, J. H.; Moorefield, M. R.; Zhang, G. B.; Hihara, L. H.; Shiroma, W. A.; Ohta, A. T. Self-Actuation of Liquid Metal via Redox Reaction. *ACS Appl. Mater. Interfaces* **2016**, *8* (1), 6–10.
- (12) Gough, R. C.; Morishita, A. M.; Dang, J. H.; Hu, W.; Shiroma, W. A.; Ohta, A. T. Continuous Electrowetting of Non-Toxic Liquid Metal for RF Applications. *IEEE Access* **2014**, *2*, 874–882.
- (13) Beni, G.; Hackwood, S.; Jackel, J. L. Continuous Electrowetting Effect. *Appl. Phys. Lett.* **1982**, *40* (10), 912–914.
- (14) Mugele, F.; Baret, J.-C. Electrowetting: From Basics to Applications. *J. Phys. Condens. Matter* **2005**, *17* (28), R705.
- (15) Yun, K.-S.; Cho, I.-J.; Bu, J.-U.; Kim, C.-J.; Yoon, E. A Surface-Tension Driven Micropump for Low-Voltage and Low-Power Operations. *J. Microelectromechanical Syst.* **2002**, *11* (5), 454–461.
- (16) Sen, P.; Kim, C.-J. A Fast Liquid-Metal Droplet Microswitch Using EWOD-Driven Contact-Line Sliding. *J. Microelectromechanical Syst.* **2009**, *18* (1), 174–185.
- (17) Jackel, J. L.; Hackwood, S.; Beni, G. Electrowetting Optical Switch. *Appl. Phys. Lett.* **1982**, *40* (1), 4–5.

- (18) Khan, M. R.; Trlica, C.; So, J.-H.; Valeri, M.; Dickey, M. D. Influence of Water on the Interfacial Behavior of Gallium Liquid Metal Alloys. *ACS Appl. Mater. Interfaces* **2014**, *6* (24), 22467–22473.
- (19) Gough, R. C.; Dang, J. H.; Morishita, A. M.; Ohta, A. T.; Shiroma, W. A. Frequency-Tunable Slot Antenna Using Continuous Electrowetting of Liquid Metal. In *Microwave Symposium (IMS), 2014 IEEE MTT-S International*; 2014; pp 1–4.
- (20) Tang, S.-Y.; Sivan, V.; Petersen, P.; Zhang, W.; Morrison, P. D.; Kalantar-zadeh, K.; Mitchell, A.; Khoshmanesh, K. Liquid Metal Actuator for Inducing Chaotic Advection. *Adv. Funct. Mater.* **2014**, *24* (37), 5851–5858.
- (21) F. Rubinson, J.; P. Kayinamura, Y. Charge Transport in Conducting Polymers : Insights from Impedance Spectroscopy. *Chem. Soc. Rev.* **2009**, *38* (12), 3339–3347.
- (22) Retter, U.; Lohse, H. Electrochemical Impedance Spectroscopy. In *Electroanalytical Methods*; Scholz, F., Ed.; Springer Berlin Heidelberg, 2010; pp 159–177.
- (23) Pourbaix, M. *Atlas of Electrochemical Equilibria in Aqueous Solutions*, Second English Edition.; Natl Assn of Corrosion: TX, USA, 1974; Vol. 16.1.
- (24) Rayleigh, Lord. On the Capillary Phenomena of Jets. *Proc. R. Soc. Lond.* **1879**, *29* (196–199), 71–97.
- (25) Lozada-Smith, N.; Reichel, K. S.; Joshipura, I.; Mendis, R.; Dickey, M. D.; Mittleman, D. M. Optimization of Conductive Fluids for Liquid Metals in THz Devices. In *2017 42nd International Conference on Infrared, Millimeter, and Terahertz Waves (IRMMW-THz)*; 2017; pp 1–2.
- (26) Reichel, K. S.; Lozada-Smith, N.; Mendis, R.; Joshipura, I.; Dickey, M. D.; Mittleman, D. M. Active THz Waveguides Enabled by Liquid Metal Actuation. In *Conference on Lasers and Electro-Optics (2017), paper SM3J.3*; Optical Society of America, 2017; p SM3J.3.
- (27) Reichel, K. S.; Joshipura, I.; Lozada-Smith, N.; Mendis, R.; Dickey, M. D.; Mittleman, D. M. Liquid Metals for Active Terahertz Waveguides. In *2017 42nd International Conference on Infrared, Millimeter, and Terahertz Waves (IRMMW-THz)*; 2017; pp 1–2.
- (28) Ozanam, F.; Chazalvie, J.-N.; Radi, A.; Etman, M. Resonant and Nonresonant Behavior of the Anodic Dissolution of Silicon in Fluoride Media: An Impedance Study. *J. Electrochem. Soc.* **1992**, *139*, 2491–2501.
- (29) Maleeva, M. A.; Rybkina, A. A.; Marshakov, A. I.; Elkin, V. V. The Effect of Atomic Hydrogen on the Anodic Dissolution of Iron in a Sulfate Electrolyte Studied with Impedance Spectroscopy. *Prot. Met.* **2008**, *44* (6), 548–556.
- (30) Lee, J.; Kim, C. J. Surface-Tension-Driven Microactuation Based on Continuous Electrowetting. *J. Microelectromechanical Syst.* **2000**, *9* (2), 171–180.
- (31) Hu, X.; Mibus, M.; Knospe, C. R.; Zangari, G.; Reed, M. L. Impedance Spectroscopy and Electrical Modeling of Electrowetting on Dielectric Devices. *J. Micromechanics Microengineering* **2015**, *25* (4), 45020.
- (32) Lomax, D. J.; Kant, P.; Williams, A. T.; Patten, H. V.; Zou, Y.; Juel, A.; Dryfe, R. A. W. Ultra-Low Voltage Electrowetting Using Graphite Surfaces. *Soft Matter* **2016**, *12* (42), 8798–8804.
- (33) Horn, R. G.; Asadullah, M.; Connor, J. N. Thin Film Drainage: Hydrodynamic and Disjoining Pressures Determined from Experimental Measurements of the Shape of a Fluid Drop Approaching a Solid Wall. *Langmuir* **2006**, *22* (6), 2610–2619.

## **CHAPTER 3**

# **DRY APPROACH: PATTERNING AND REVERSIBLE ACTUATION OF LIQUID GALLIUM ALLOYS BY PREVENTING ADHESION ON ROUGH SURFACE**

## **Abstract**

This work reports a simple approach to form rough coatings that prevent the adhesion of gallium-based liquid metal alloys. These alloys form a surface oxide ‘skin’ that adhere or pin to many surfaces; rough surfaces may prevent the adhesion but are difficult to incorporate into closed channels. This work renders planar surfaces and closed channels to be “oxide-phobic” via spray-coating (NeverWet, which is commercially-available and inexpensive). Surface spectroscopic techniques and metrology tools elucidate that the coatings comprise of silica nanoparticles coated with silicones that exhibit dual-modes of roughness. Through wetting measurements, we find that engineering the surface roughness is more important than surface chemistry to prevent oxide adhesion. We utilize the NeverWet coating to demonstrate reversible actuation through sub-mm closed channels to form a reconfigurable antenna in the GHz range. In addition, we apply this coating to open surfaces to pattern sub-mm conductive traces of liquid metal. This work provides a simple and inexpensive method to actuate liquid metals for reconfigurable electronics, microfluidics, and energy harvesting as well as patterning soft conductors for flexible electronics, microfluidic sensors, and soft robotics.

## **Introduction**

This paper describes the use of a spray coating to render surfaces rough, and thus, non-wetting towards gallium-based (Ga) liquid metal alloys. Liquid metals offer the high electrical conductivities of metals and the fluidic properties of liquids.<sup>1-4</sup> As a result, they are suitable conductors for electronics that may be soft and stretchable,<sup>2,5,6</sup> as well as shape reconfigurable.<sup>7</sup> Because these metals are fluids, they also show promise for adaptable optical components, such as meta-surfaces, gratings, and polarizers.<sup>8,9</sup> However, the adhesion of these alloys to most surfaces poses a challenge for reconfigurable devices. This work aims to create surfaces that do not adhere

to liquid metal so that it can be handled (i.e., contained, pumped, reconfigured) without leaving residue on surfaces it contacts.

Ga and its alloys remain liquid near room temperature and offer an alternative to toxic mercury (Hg). Ga has a melting point (M.P.) of 29.7 °C.<sup>10</sup> Alloying Ga with other metals lowers its melting point. Two popular alloys are eutectic gallium-indium (“EGaIn”, 85% Ga, 15% In, by weight, (M.P.) of 15.5 °C)<sup>11</sup> and gallium-indium-tin (“Galinstan”, 68% Ga, 22% In, 10% Sn, by weight, M.P. of -19 °C).<sup>12</sup> In addition, Ga alloys display conductivities of  $\sim 1/16^{\text{th}}$  that of Cu, which is sufficiently conductive for most electronic applications.<sup>4</sup> A wide range of soft devices have been created using Ga alloys embedded in a soft elastomer,<sup>6</sup> including wires or fibers that stretch up to 1000% of their original length,<sup>13–15</sup> adaptable antennas,<sup>16–19</sup> and sensors.<sup>20–24</sup> Unlike Hg, Ga and its alloys rapidly form a passivating surface oxide in the presence of oxygen.<sup>25,26</sup>

Although this oxide ‘skin’ is only a few nanometers thick,<sup>26</sup> its presence significantly affects the fluidic and wetting properties of the metal. Per rheological measurements, the oxide exhibits a surface yield stress of  $\sim 0.4$  to  $0.6$  N/m; below this critical stress, the oxide behaves as an elastic shell around the metal. Once the applied stress exceeds the yield stress, the oxide skin ruptures and allows the metal to flow.<sup>26</sup> This property allows Ga alloys to be injected into microfluidic networks,<sup>26</sup> hollow structures (i.e., fibers<sup>15</sup> and carbon-based nanostructures<sup>27,28</sup>), and similar systems that have void space. Once injected, the metal remains arrested within the microchannel due to the ability of the oxide to reform rapidly. The adhesive tendency of the oxide allows for many unique patterning methods of liquid metals.<sup>2,3</sup> In addition, residues of the metal oxide can transform into useful traces of semiconductors.<sup>29</sup>

Despite its usefulness for patterning, the oxide poses challenges for several cases. Because Ga alloys leave metal and oxide residue on most surfaces, it often creates handling challenges in

laboratory or manufacturing settings. Similarly, the oxide adheres to the interior of walls of microfluidic channels. Preventing the formation of the oxide or lowering the adhesion of the oxide is important for achieving reconfigurable electronics, as well as energy harvesting applications.

Several methods exist for removing the oxide skin. First, lowering the concentration of oxygen in air to below one parts per million prevents the formation of the oxide on the surface of Ga.<sup>12</sup> However, it is difficult to create and maintain such an environment, let alone implement into a microfluidic device. It is also possible to dissolve or remove the oxide ‘skin’ in the presence of an aqueous acid or base.<sup>30–32</sup> According to the Pourbaix diagrams for Ga, a dilute acid ( $\text{pH} < 3$ ) or base ( $\text{pH} > 10$ ) can directly remove the oxide skin via dissolution.<sup>33</sup> Likewise, acid vapors (i.e., hydrochloric acid or sulfuric acid) can also remove the oxide skin.<sup>31,34–37</sup> Recent studies show that acidified silicone oils are capable of removing the oxide skin.<sup>38</sup> However, acids and bases are corrosive, and thus not ideal for electronics. Similarly, another approach is to electrochemically reduce the oxide in aqueous electrolytes using only nominal voltages ( $< 2 \text{ V}$ ).<sup>7</sup>

Alternatively, introducing another liquid into a microchannel prior to injecting liquid metal may prevent the oxide from adhering to the walls of the microchannel. Water,<sup>39</sup> oil,<sup>40</sup> and certain surfactants<sup>40</sup> are known to create slip-layers of liquid that physically separates the metal oxide from channel walls. In addition, organic solvents such as toluene may also provide a sufficient lubrication layer to prevent oxide adhesion.<sup>41</sup> Similarly, injecting a solution of phosphonic acid in ethanol into channels prevents oxide adhesion; phosphonic acid spontaneously binds to the metal oxide surface, thereby preventing adhesion between the oxide and a surface.<sup>42</sup> However, incorporating a secondary fluid creates additional processing challenges, particularly for electronics. Therefore, it may be more convenient to create surfaces or coatings that ‘inherently’ prevent adhesion of the Ga oxide skin.

Finally, it is possible to prevent adhesion of liquid metal using rough surfaces. This approach is similar to the way rough surfaces can increase the hydrophobicity toward water. Several methods exist to create ‘oxide-phobic’ rough surfaces (e.g., vertically-aligned carbon nanotubes,<sup>43</sup> sandblasting with alumina grits,<sup>44</sup> silica nanoparticles,<sup>45</sup> patterned micropillar arrays,<sup>46</sup> sputtered metal foils such as In and Sn<sup>47,48</sup>). Although these surfaces prevent the adhesion of liquid metals featuring surface oxides, they all require specialized equipment for fabrication. This work addresses the challenge of creating oxide-phobic rough surfaces in a simple manner.

In this paper, we utilize a commercially available superhydrophobic coating (NeverWet by Rustoleum) to create surfaces to which liquid gallium alloys do not stick. We analyze the chemical and physical properties of the coating and perform wetting studies using control surfaces to show that the surface roughness is more important than the chemical composition. These wetting studies also illustrate the challenges associated with using conventional wetting metrics to characterize the behavior of gallium liquid metals on surfaces. Finally, we show the utility of such non-stick surfaces to pattern the liquid metal and to actuate it in confined spaces for reconfigurable antennas.

## **Experimental Design**

We utilize dynamic contact angle to quantify the wetting properties of oxide-coated liquid metals. Although these measurements typically characterize the wetting properties of liquids surfaces,<sup>49,50</sup> the presence of the native oxide on liquid metal complicates the interpretation of these measurements.

In the case of Ga alloys, the surface oxide is a ‘skin’ that envelops the drop; this oxide ‘skin’ has mechanical properties that impede the liquid from assuming shapes that minimize interfacial energy. For example, it is possible to distort the metal into shapes, such as wires or cones that would not be possible with water. Likewise, it is possible to physically manipulate the

apparent contact angle (i.e, by deforming, squishing, dragging). The surface oxide also dominates and complicates the interfacial behavior of liquid metal drops against surfaces.<sup>51</sup> Notably, the oxide-coated metal ‘adheres’ to most surfaces it contacts. However, in absence of the oxide, the metal drop readily beads up on most non-metallic surfaces (contact angle approaching 180°).

To further complicate matters, during advancing contact angle measurements, the oxide must yield to accommodate the growing volume of the drop. Moreover, oxide may reform during this process. Studies show that rupturing and forming new oxide promotes adhesion.<sup>51-53</sup> Due to the oxide, drops of the metal often completely pin to surfaces so that they never truly recede from the contact line during receding contact angle measurements. *Consequently, the interpretation of contact angles for liquid metals is significantly more complex than water and perhaps misleading if interpreted in the same way as fluids such as water.*

We apply these techniques on drops of EGaIn and DI water on surfaces of varying hydrophobicity as well as surface roughness to provide insight on the adhesion of the oxide-coated liquid. For the case of DI water, we report advancing ( $\Theta_A$ ), and receding angles ( $\Theta_R$ ) to provide context and additional surface characterization. In the case of liquid metals, the measured contact angles do not represent the traditional interpretation of contact angles; thus, we report the values from dynamic contact angle measurements as apparent angles. Whereas traditional advancing and receding measurements emphasize the numerical value of contact angle, we instead seek to arrive at a binary conclusion: either the droplet adheres to the given surface or not. The goal of this work is to identify substrates where liquid metal completely withdraws from the surface (i.e., does not leave an oxide residue).

## Results

Liquid metals with surface oxides adhere to clean glass surfaces ( $\Theta_A$  of  $7^\circ \pm 3^\circ$  for water<sup>50</sup> and  $\Theta_R$  for water is difficult to measure due to evaporation, but appears to be less than  $7^\circ$ ). **Figure 3-1** (a) shows a drop of EGaIn expanding on a bare glass slide (Plain Microscope Glass Slide, 75 mm by 25 mm from VWR, treated with oxygen plasma for 1 minute). Figure 1 (b) shows a representative graph of the evolution of the contact angle versus time for a drop of EGaIn on glass. As the volume of the drop increases, the metal drop of EGaIn exhibits an apparent  $\Theta_A$  of  $139.7^\circ \pm 2.1^\circ$ . Upon receding the drop, the metal drop reduces in volume but does not reach an equilibrium value for  $\Theta_R$ . Previous work on preventing wetting of liquid metals report  $\theta_R$  for various surfaces.<sup>54</sup> However, the evolution of apparent contact angle shows that a true  $\theta_R$  does not exist for oxide-coated liquid metals; this behavior occurs because the oxide pins to the solid substrate. Furthermore, continuing to remove volume from the drop does not remove all the liquid from the substrate; instead, the residual metal drop remains adhered to glass surface and never fully recedes from the surface of glass. *This simple experiment shows that oxide-coated liquid metals can adhere to surfaces despite a large advancing contact angle.*

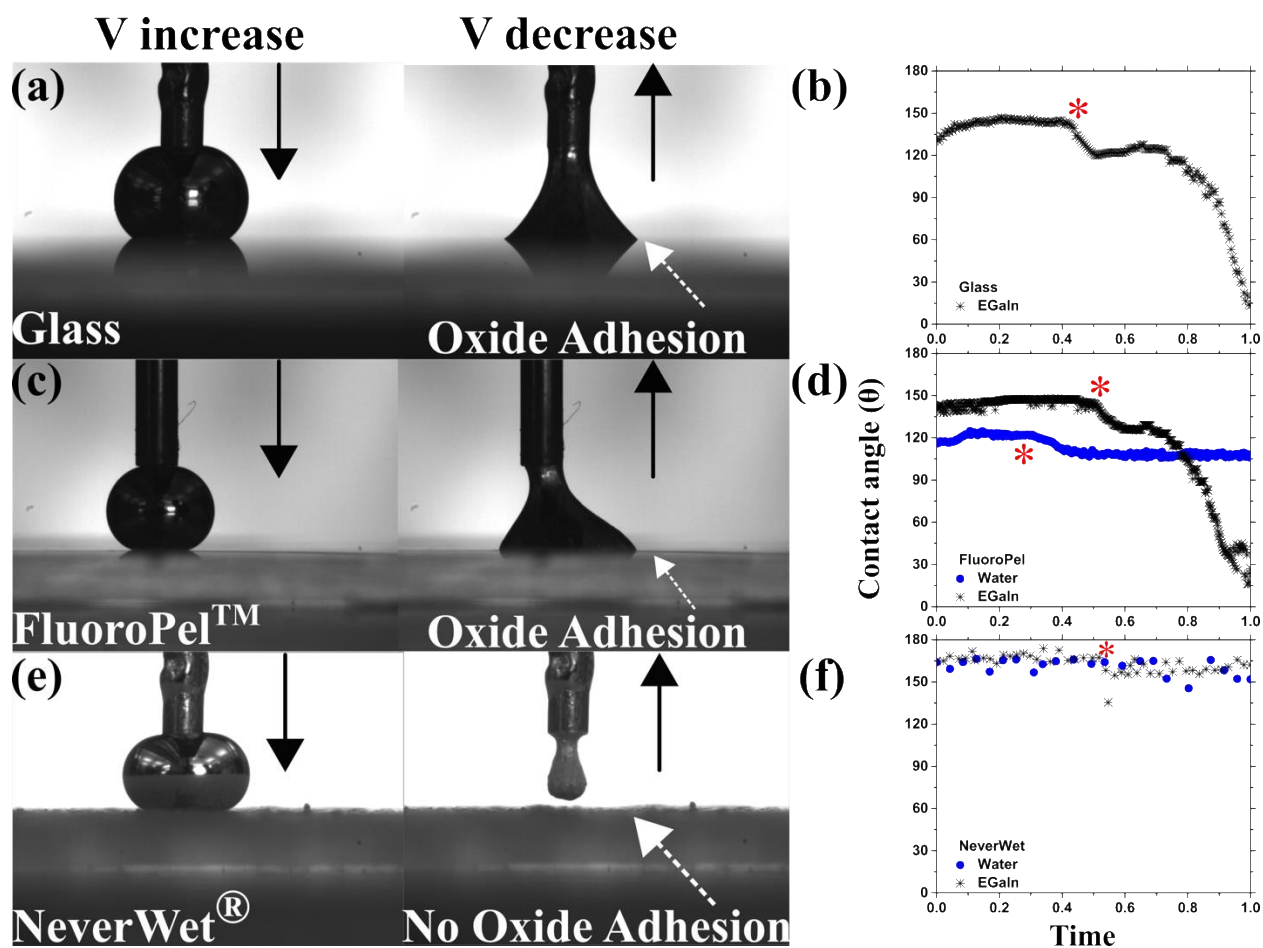


**Figure 3-1:** Dynamic contact angle measurements on surfaces of interest. For dynamic contact angle experiments (left column), a drop of liquid metal contacts on surfaces of interest ((a) Glass, (c) FluoroPel, and (e) NeverWet). The advancing contact angle of the drop is measured as the drop first increases in volume. Upon receding the drop, oxide residue remains on the surface of glass and FluoroPel. Meanwhile, no oxide residue is present on the surface of NeverWet. The right column (b, d, and f) show representative graphs of the evolution of contact angle of EGaIn and DI water over time, which is normalized to scale all experiments. On (b, d, and f), a red star (\*) indicates the beginning of the withdrawal of the volume (i.e., volume of the drop decreases). (b) On Glass, EGaIn initially increases in contact angle as volume is increased. Upon decreasing the volume (indicated by a red star), the contact angle initially decreases but never reaches an equilibrium value. (d) Similar behavior is observed for EGaIn on FluoroPel (black cross marks).

Meanwhile, DI water on FluoroPel (blue circles) reaches equilibrium values for both the advancing and receding phases. (f) In the case of NeverWet, both water (blue circles) and EGaIn (black cross marks) exhibit stable values for advancing and receding angles. The low hysteresis in contact angle is indicative of a Cassie-Baxter wetting state for both liquids. The red star indicates the receding phase for both EGaIn and water.

Because the oxide itself is hydrophilic, we hypothesize that hydrophobic surfaces may mitigate the adhesion of Ga-based liquid metals. To test this hypothesis, we measure the dynamic contact angle of liquid metal on a glass slide with a smooth coating of a commercial hydrophobic fluoropolymer (FluoroPel™,  $\Theta_A$  of  $120.0^\circ \pm 1.8^\circ$  and  $\Theta_R$  of  $107^\circ \pm 0.9^\circ$  for water). Fig. 3-1 (c) shows the behavior of EGaIn on FluoroPel-treated glass. Advancing the liquid metal drop exhibits an apparent  $\Theta_A$  of  $158.1^\circ \pm 1.7$  on FluoroPel. Fig. 3-1 (d) shows that the contact angle evolution for EGaIn on FluoroPel is similar to the behavior for EGaIn on glass. For both substrates, the metal exhibits a large and stable equilibrium values during advancing measurements. However, the metal drop does not achieve an equilibrium  $\Theta_R$  when receding the drop volume. As a comparison, Fig. 1d also shows the contact angle evolution for DI water on FluoroPel. For the case of DI water, the contact angle of the drop reach stable values for both advancing and receding phases ( $\Theta_A$  of  $120.0^\circ \pm 1.8^\circ$  and  $\Theta_R$  of  $107^\circ \pm 0.9^\circ$  for water). Optical images from the contact angle goniometry (side-view profile) and conventional light microscope (top-down profile) on the sample after the measurement shows that oxide pins to the surface; as a result, the metal drop never fully dewets the surface. This result provides further evidence the contact angle of EGaIn is more complex than water.

In our study, although the advancing contact angle of EGaIn on both bare glass and FluoroPel are high ( $>140^\circ$ ), the oxide adheres to both surfaces during the retraction phase. Similar observations of adhesion of oxidized liquid metal polydimethylsiloxane (PDMS)<sup>54</sup> and other fluorinated polymers<sup>51</sup> are reported in the literature. This simple experiment shows that chemically modifying the surface to a hydrophobic state is insufficient in preventing adhesion of liquid metals to surfaces. *Moreover, these results also show that the advancing angle of water does not serve as a useful metric on whether the Ga oxide adheres to the surface.*

In addition to surface chemistry, surface roughness also plays an important role on wetting and adhesion of liquids.<sup>55,56</sup> Therefore, we explore rough surfaces that display Cassie-Baxter-like wetting states to prevent the adhesion of the oxide-coated metal. For these experiments, we utilize a commercially-available spray coating (Rust-Oleum® NeverWet®, herein “NeverWet”) as a model surface with both surface roughness and hydrophobic surface chemistry. Fig. 3-1 (e) shows EGaIn on glass coated with NeverWet ( $\Theta_A$  of  $162.2^\circ \pm 2.2^\circ$  and  $\Theta_R$  of  $161.7^\circ \pm 0.2^\circ$  for water). Advancing the drop of liquid metal exhibits an apparent  $\Theta_A$  of  $163.9^\circ \pm 5.4^\circ$ . Upon receding the drop of EGaIn ( $\Theta_R$  of  $150.1^\circ \pm 5.4^\circ$ ), the surface oxide does not adhere to NeverWet-coated surfaces and the drop completely withdraws from the surface (Fig. 3-1 (e, right)). A video of this experiment is provided in Supplemental Information (**Appendix B**). Due to the surface roughness, both liquids (EGaIn and water) do not exhibit large contact angle hysteresis, that is the difference between advancing and receding angles. The low hysteresis is evident that a Cassie-Baxter wetting state exists for both EGaIn and water on NeverWet. Moreover, it is likely that the contact angle for EGaIn likely approaches  $180^\circ$  —this angle is difficult to observe to rough features that block the line of sight to the exact interface between the drop and underlying surface.

Although several works have utilized rough surfaces to prevent oxide adhesion, this work reports a facile way to render surfaces “oxide-phobic.” Because the spray coating is relatively inexpensive and commercially available, it is an accessible technique and does not require any laboratory equipment. Moreover, NeverWet coated on a variety of other substrates (e.g., thermoplastics, silicone elastomers, paper) exhibit similar ‘oxide-phobic’ behavior. Elastically soft surfaces (polydimethylsiloxane, PDMS, Dow Sylgard-184) coated with NeverWet retain its ‘oxide-phobic’ properties towards the liquid metal even when stretching or deforming the substrate. In addition, we created a superhydrophobic surface from PDMS by subjecting PDMS to

flame.<sup>57</sup> EGaIn does not adhere to the ‘flamed’ PDMS when performing dynamic contact angle measurements. Although the surface composition is no longer characteristic of NeverWet, PDMS or other silicones, this result further confirms the importance of superhydrophobic surfaces (i.e., Cassie-Baxter state) on preventing oxide adhesion.

Although we observe no macroscopic oxide adhesion on NeverWet, we questioned whether a thin, nano-scale oxide residue may exist on NeverWet. We utilized time-of-flight secondary ion mass spectroscopy (TOF-SIMS) to determine whether trace residue remains on the surface. TOF-SIMS is a surface-focused mass spectroscopy technique that has a higher sensitivity than that of x-ray photoelectron spectroscopy (XPS). Prior to surveying the sample using TOF-SIMS, we drag a drop of EGaIn across NeverWet coated on a Si wafer; as an attempt to promote the adhesion of the oxide, we repeat the dragging several times across the sample. In addition, a pristine NeverWet sample serves as a control sample. Remarkably, TOF-SIMS shows that no oxide residue remains on the NeverWet sample exposed to EGaIn; the mass spectra does not show any peaks for Ga, In, GaO, and InO ions (see Appendix B for mass spectra survey of both samples, **Figure B-1**). Because this experiment is more sensitive than traditional surface measurements (i.e., XPS), it represents a unique method of determining the presence of a surface oxide residue. The utilization of this technique could also be useful for verifying and identifying nanoscopic surface oxides (with spatial resolution), which is of interest for patterning and deposition of 2D materials.

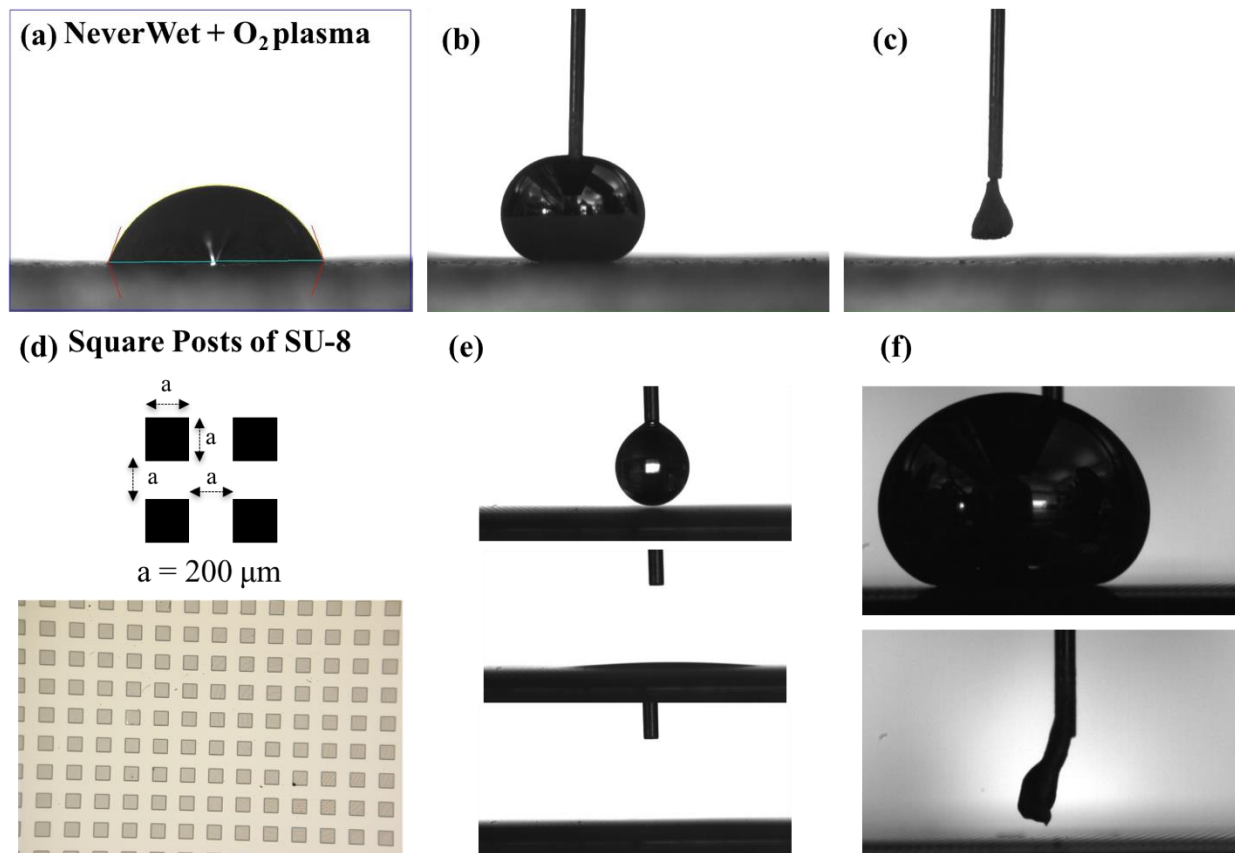


**Figure 3-2:** EGaIn on rough, hydrophilic surfaces. (a) Water wetting on NeverWet treated with O<sub>2</sub> plasma for one minute at 100% power, (b) A drop of EGaIn advancing on NeverWet treated with O<sub>2</sub> plasma. (c) After contact angle measurements, EGaIn drop does not leave behind residue on on NeverWet treated with O<sub>2</sub> plasma. (d) Diagram and optical micrograph of square posts of SU-8 fabricated using direct-write photolithography. Each square post is 200 μm in length with a spacing of 200 μm between posts in all directions. (e) Time-lapse photographs of water wicking into square posts. (f) (top) EGaIn advancing on square posts of SU-8. (bottom) After contact angle measurements, drop of EGaIn does not leave behind oxide residue on the posts.

Finally, we explore whether surface roughness alone prevents the adhesion of the oxide. The results from this work agree with other work in literature in suggesting that surface roughness alone is sufficient to prevent oxide adhesion.<sup>43–47</sup> Previous work with rough surfaces, except for sputtered metals, all utilize surfaces that are already hydrophobic.<sup>43,44,46,54</sup> Therefore, we wondered could the oxide of EGaIn adhere to hydrophilic yet rough surfaces?

Herein, we show two examples of rough surfaces that are hydrophilic, yet ‘oxide-phobic’ for liquid metals. First, we treat NeverWet to oxygen (O<sub>2</sub>) plasma to render it hydrophilic. **Figure 3-2a** shows that water readily wets the surface of NeverWet ( $\theta_s$  of  $69.1^\circ \pm 8.8^\circ$ ) after exposure to O<sub>2</sub> plasma for one minute. The decrease in water contact angle is likely due to the formation of

surface hydroxyl groups on NeverWet surface, which is chemically similar to silicones such as PDMS, which is characterized in detail below; PDMS, which is hydrophobic ( $\theta_s$  of  $107^\circ$ ), becomes hydrophilic upon exposure to UV-ozone or oxygen plasma.<sup>65</sup> Fig. 3-2b and 3-2c show contact angle measurements on EGaIn on  $O_2$  plasma-treated NeverWet. Despite the transforming the NeverWet surface to a hydrophilic state, EGaIn neither pins nor adheres to the surface of plasma-treated NeverWet. In addition, we utilize photolithography to create square micro-posts that mimic a rough surface. Fig. 2d shows a diagram and optical micrograph of the square micro-posts, which are  $200\ \mu\text{m}$  in length and separated by  $200\ \mu\text{m}$  spacing. Fig. 2e shows that water readily wets the micro-posts upon contact, which verifies that the surface is wetting towards water. Meanwhile, a drop of liquid metal on the surface does not penetrate through posts. Furthermore, advancing and receding the drop of liquid metal over the posts does not cause it to adhere to the surface (as shown in Fig. 2f). Indeed, these posts are similar in architecture to previously reported work.<sup>46</sup>

The key distinctions between this work and work from literature on rough surfaces is that we consider both surface roughness and chemistry. Specifically, in comparison to the work on posts from literature,<sup>46</sup> the posts presented in Fig. 2 (1) do not have a hydrophobic top-coating and (2) do not have a second order of roughness atop the posts. Likewise, previous work has utilized rough coatings or surfaces to prevent oxide adhesion. Instead, this work compares the wetting behavior of liquid metals on the same surface (NeverWet) with varied hydrophobicity. *Combined, this result suggests that surface roughness influences the non-wetting behavior of oxidized liquid metals more so than surface chemistry.*

We note that previous work has utilized sputtered metals to render surface “metallophobic.”<sup>47</sup> However, the wetting behavior of liquid metals onto other metals is different phenomena than traditional surfaces. Conventionally, contact angle measurements is an

interpretation to the balance of surfaces forces at the contact point of three interfaces: (1) substrate (solid or liquid), (2) probe fluid (liquid or gas), and (3) ambient environment (gas or liquid)). In contrast, the wetting of liquid metals onto (smooth) metallic surfaces is due to metallic bonding, diffusion, and alloying at the surface.

*Composition and Morphology of NeverWet*

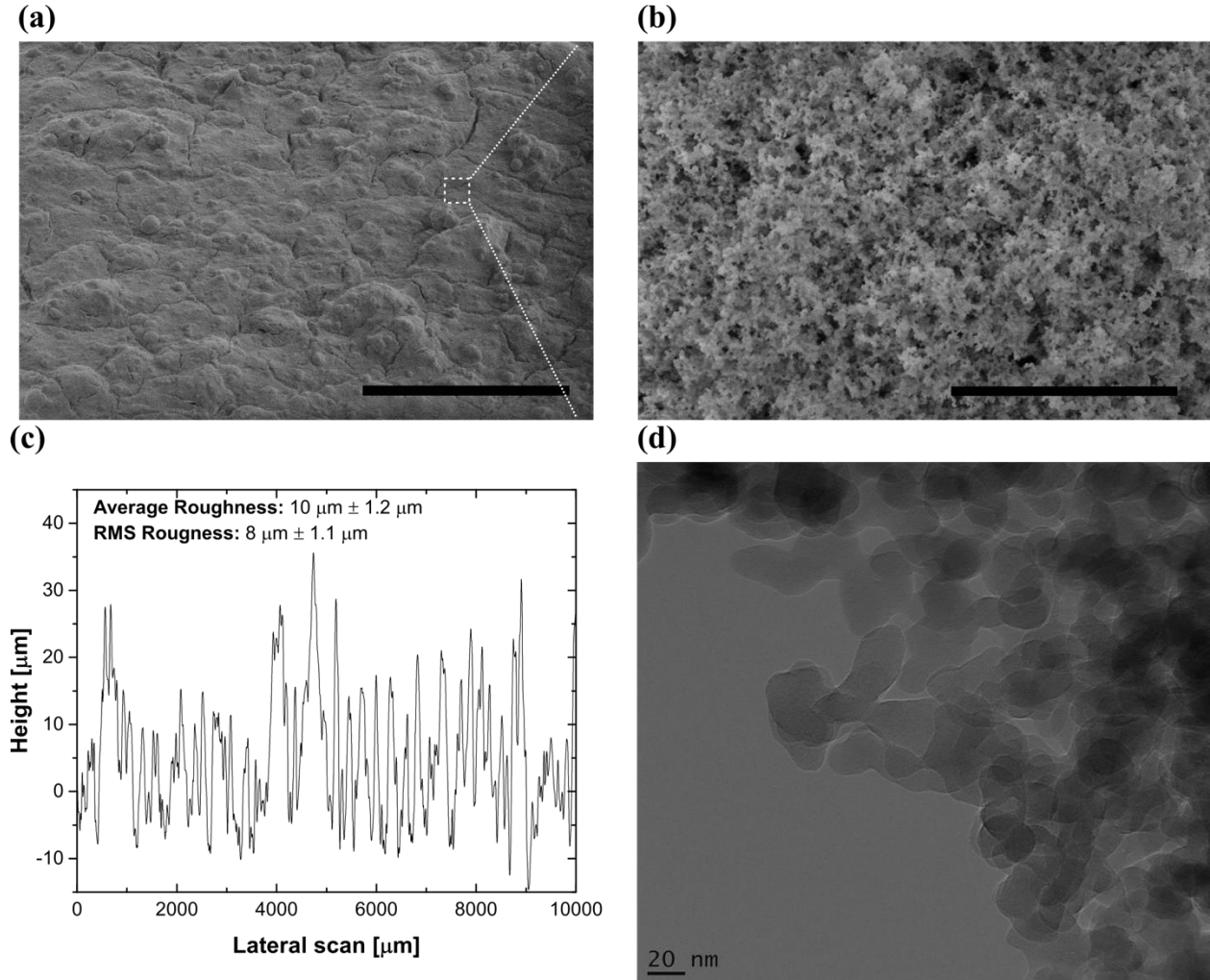


**Figure 3-3:** Surface morphology and roughness of NeverWet. (a) Scanning electron micrograph (SEM) of NeverWet coating at 150× magnification. Scale bar is 300 μm. (b) SEM of NeverWet at a higher magnification (25,000×). The micrograph in (b) is a select region of SEM in (a), marked by a white box. Scale bar is 2 μm. Both SEM micrographs (a, b) measure secondary electron emissions using an Everhart-Thornley dector on a FEI Verios 460L SEM, which operated at 2.0 kV, 6.3 pA, and no stage bias. Samples are tilted at 55° to observe the roughness at a glancing angle and were imaged without a coating of metallic thin-film. (c) A representative line scan of contact-mode profilometer of NeverWet. Inset shows statistical values of average roughness and RMS roughness from five scans. (d) TEM of silica particles that comprise the NeverWet, Step 2 spray (JEOLF 2010F TEM) operating at 200 kV).

We sought to characterize the surface of NeverWet samples using imaging and spectroscopic techniques to understand how it prevents adhesion of the oxide-coated metal. The coating requires a two-step spray procedure; ‘Step 1’ first deposits an adhesive primer layer. Thereafter, ‘Step 2’ creates a topcoat that exhibits hydrophobicity. Much of the surface characterization presented here is on a coating consisting of both steps (i.e., ‘Steps 1+2’). Any experiments involving materials from only one of the steps are noted (e.g., ‘Step 2 only’).

Optical microscopy shows that large clusters of particles compose the surface (Appendix B, **Figure B-2 (a)**). These clusters are spaced by several hundred microns. However, optical micrographs do not reveal complete information on the surface morphology of the NeverWet coatings. Thus, we utilize scanning electron microscopy (SEM) to observe the surface under a higher magnification. The NeverWet samples imaging is performed without a metal coating using a state-of-art field-immersion SEM. In addition, the samples are tilted to  $55^\circ$  to better observe the surface roughness. Although sputtering metal onto insulating surfaces aids in acquiring SEM images, sputtering metal atop NeverWet forms metal nuclei across the sample. The presence of metal nuclei misconstrues the observed surface roughness from SEM micrographs.

**Figures 3-3 a-b** show SEM images of NeverWet coated on a Si wafer. A low magnification image (150x, Fig. 3a) suggests that the NeverWet coating consists of clusters or aggregates that are spaced on order of tens to hundreds of microns. To quantify the roughness of NeverWet, we utilize contact-mode profilometry. Fig. 3-3c shows a representative profilometry scan of a NeverWet sample. Due to the non-periodic nature of the surface, we calculate both an average ( $R_a$ ) and root-mean-square ( $R_{RMS}$ ) value to quantify the surface roughness (in terms of height). We calculate an average roughness ( $R_a$ ) of  $10\ \mu\text{m}$  and root mean square roughness ( $R_{RMS}$ ) of  $8\ \mu\text{m}$ . A Fast Fourier Transform (FFT) of the profilometry scan reveals that the particle clusters are spaced

on the order of several hundred microns. The FFT analysis also shows that spacing on order of tens to hundreds of microns is also frequent; this analysis suggests that there are multiple length scales of roughness (See Appendix B, **Figure B-3**).

At higher magnifications, we observe a secondary mode of roughness atop the micron-scale features. Fig. 3b shows an SEM micrograph one of the features from Fig 3a. This micrograph reveals that the micron-scale ‘hills’ comprise clusters of nanoparticles with diameters close to 100 nm or less. However, we could not image the sample with higher resolutions due to the electrically insulating properties of the coating. Therefore, we observe the particles in the coating at higher resolution using transmission electron microscopy (TEM). To do so, the components of only Step 2 are diluted in hexane and cast on a lacey carbon grid (300 mesh). Figure 3-3 (d) shows a TEM micrograph of the particles that compose the NeverWet Step 2. Individual particles are difficult to discern because they form clusters and linear chains. Image analysis of the micrograph determines that the particles have average diameters of  $20.4 \text{ nm} \pm 4 \text{ nm}$ . Finally, we utilize atomic force microscopy (AFM) to further quantify the roughness. Fig. B-2b in Supporting Information shows an AFM image of a  $4 \text{ }\mu\text{m}$  by  $4 \text{ }\mu\text{m}$  scanned area. Although imaging such rough surfaces is difficult, the AFM confirms that the surface comprises round or spherical particles of 100 nm or less size. These results agree with similar studies on the morphology of NeverWet.<sup>60</sup> Overall, the characterization techniques presented in Fig. 3 and SI reveal that the surface coating comprises dual-modes of roughness length scales, which is characteristic of superhydrophobic surfaces.<sup>58,59</sup>

In addition to roughness, chemical composition of a surface can play a key role in influencing the behavior of liquids on solids. Therefore, we sought to understand the chemical composition of NeverWet using various surface-sensitive spectroscopy methods. We initially hypothesized that fluorinated species compose the NeverWet surface. Energy dispersive x-ray

spectroscopy (EDS) reveals that the NeverWet surface comprises only silicon (Si), oxygen (O), and carbon (C) (See Figure B-3 (c and d) in Appendix B). However, this technique does not reveal any information of the macromolecular composition of the coating.

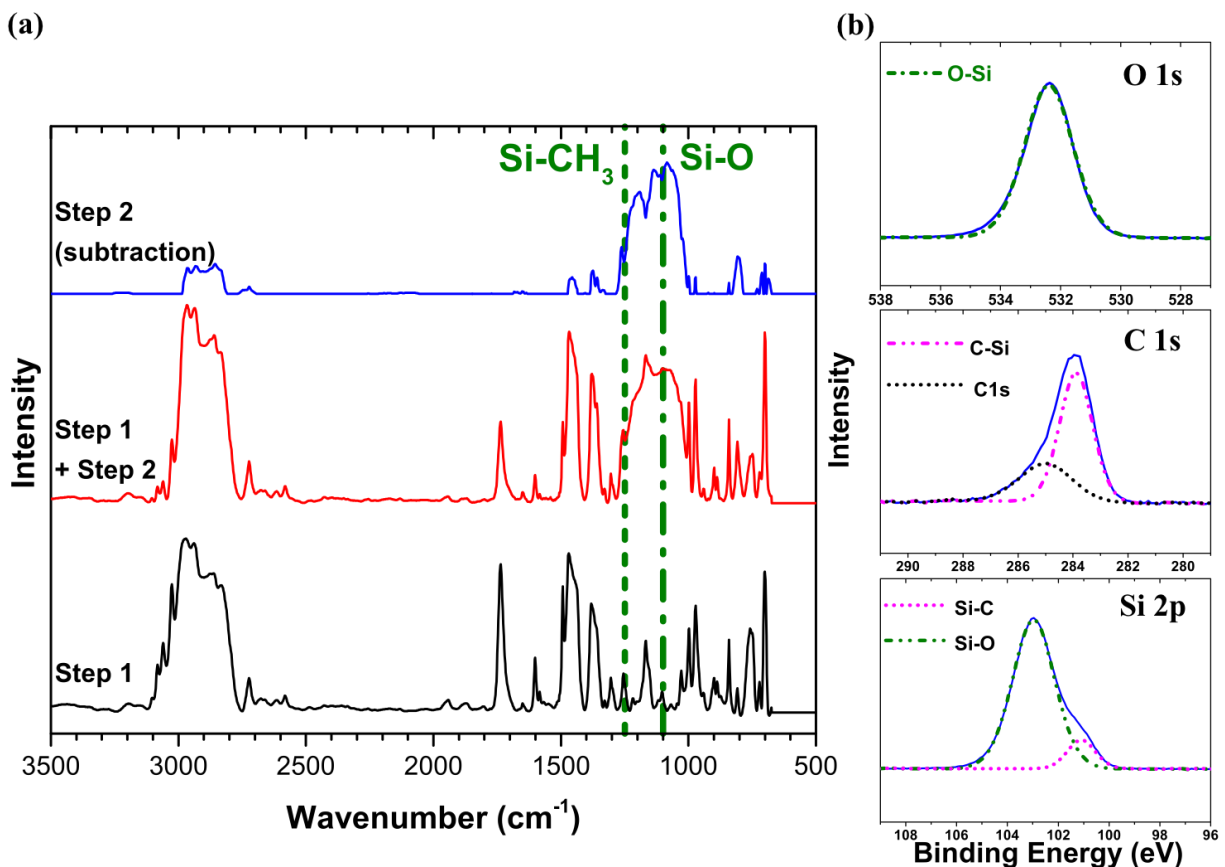


**Figure 3-4:** Chemical composition of surface and sub-surface NeverWet. (a) Fourier-transform infrared spectroscopy in attenuated reflection mode (FTIR-ATR) of a sample of NeverWet. The scan in black line is of NeverWet Step 1 spray (binder). The red scan indicates NeverWet coating consisting of both Step 1 and Step 2. (Step 1 + Step 2) The blue line is a subtraction of Step 1 and Step 1+2. Two green drop lines indicate the FTIR peaks for Si-CH<sub>3</sub> and Si-O moieties. (b) X-ray photoelectron spectroscopy of NeverWet with graphs corresponding to peaks of O 1s, C 1s, and Si 2p.

To elucidate the surface chemical composition of NeverWet, we utilize Fourier transform infrared spectroscopy in attenuated total reflection mode (FTIR-ATR). **Figure 3-4 (a)** shows FTIR measurements two sample types: (i) base coat (“Step 1”) and (ii) base and top coat (“Step 1+2”). A measurement on only Step 1 indicates that hydrocarbons primarily comprise the base coat. We determined the composition of the topcoat by subtracting the spectra of Step 1 from Step 1+2.

From this analysis, the topcoat contains peaks that correspond to Si-O and Si-CH<sub>3</sub> bonds. FTIR-ATR analysis show vibrational stretches at ~1100 cm<sup>-1</sup> and ~1250 cm<sup>-1</sup>, which can be attributed to Si-O and Si-C respectively. These stretches are not present on the base coat. The results from FTIR studies are consistent with EDS in that the surface contains a non-fluorinated polymeric network. In addition, we compare the spectra for Step 2 with FTIR data with conventional silicone elastomers, (poly(dimethylsiloxane (PDMS) and poly(vinyl dimethoxysilane) (PVMS)). **Figure B-4** shows that NeverWet Step 2 exhibits similar stretches as PDMS and PVMS, which suggests the NeverWet coating comprises of a network of poly(siloxane). Indeed, the NeverWet coating is stretchable upon delamination from the substrate, which is indicative of the elastic nature of the coating.

Finally, we perform XPS on the NeverWet surface to further corroborate the chemical composition. As shown in **Figure 3-4 (b)**, the survey spectrum also provides evidence that only silicon, oxygen, and carbon are present in the top coat (Step 2). The XPS results agree with EDS and FTIR measurements regarding the chemical makeup of the surface. Silicon and oxygen represent about 80% atomic composition of the top coat; the remaining 20% is carbon. The C 1s high-resolution spectrum show the peak at ~285 eV corresponding to aliphatic carbon and a second peak at ~283.9 eV, which corresponds to C-Si bonds. The O 1s high-resolution spectra show a peak at ~532 eV, which corresponds to O-Si bonds. The Si 2p high-resolution spectra shows two peaks at ~101 eV and ~103 eV. The first peak can be attributed to Si-C bonds and the second to Si-O bonds.<sup>61,62</sup> Finally, the TOF-SIMS of NeverWet further corroborate that the NeverWet surface is similar in chemical composition to polysiloxanes (i.e., PDMS). Examining the patent literature and technical data sheet verifies the presence of “silicones and siloxanes.”<sup>63</sup> We should note that similar characterization of this coating suggests that the coating does contain fluorinated

species.<sup>64</sup> However, our surface characterization methods, (e.g., XPS, EDS, and TOF-SIMS) do not show any fluorine-containing moieties.

The surface analysis presented in this work provides insights on design guidelines for creating surfaces that are non-wetting to oxide-coated liquid metal. Results from XPS, FTIR, TOF-SIMS, SEM, and AFM, combined, suggest silica particles treated with siloxane-based polymer compose the top coat of NeverWet (Step 2). Therefore, coatings of similar compositions (i.e., micro- or nanoparticles in a polymeric binder) may be utilized to create non-wetting surfaces. These coatings could also be applied to confined spaces such as microfluidic channels to enable reconfigurable circuitry.

## **Applications**

### *Patterning*

Patterning liquid metals is of importance for fabricating electronics that are soft or stretchable. Injecting the metal into microchannels represents a simple way to pattern the metal. When performed conventionally, this approach results in the metal encased entirely in polymer other than at the inlet and outlet ports. The ‘closed’ nature of these methods is a disadvantage for applications requiring the patterned metal to interface with another component. One solution is to seal microchannels directly against electrical components prior to injection.<sup>66</sup> We reasoned that it might also be interesting to create elastomeric, microfluidic surfaces with patterns of liquid metal exposed at the surface, which could be used as soft electrodes.<sup>41,67</sup>

**Figure 3-5** depicts an overview of a process to create surface-exposed metal of arbitrary patterns. First, a molded elastomer is placed against a surface coated with NeverWet. Thereafter, EGaln is injected into the microchannels through the inlet hole. The mold must be pressed against or clamped against the substrate to prevent the metal from leaking during injection. After injection,

oxide adhesion to channel walls arrests the liquid metal within the patterned channel. Meanwhile, the metal does not adhere to the NeverWet. Removing the NeverWet slide completes the patterning process, thereby exposing the metal surface (i.e., the surface of the metal that was previously in contact with NeverWet). The result is a pattern of liquid metal that is both electrically and thermally conductive, as well as nearly flush with the surface of the elastomer. Thereafter, the pattern may be sealed with an elastomer, contacted to another surface, or integrated with another device. This approach may also be a straightforward way to harness the tunable adhesion of Ga.<sup>52</sup>

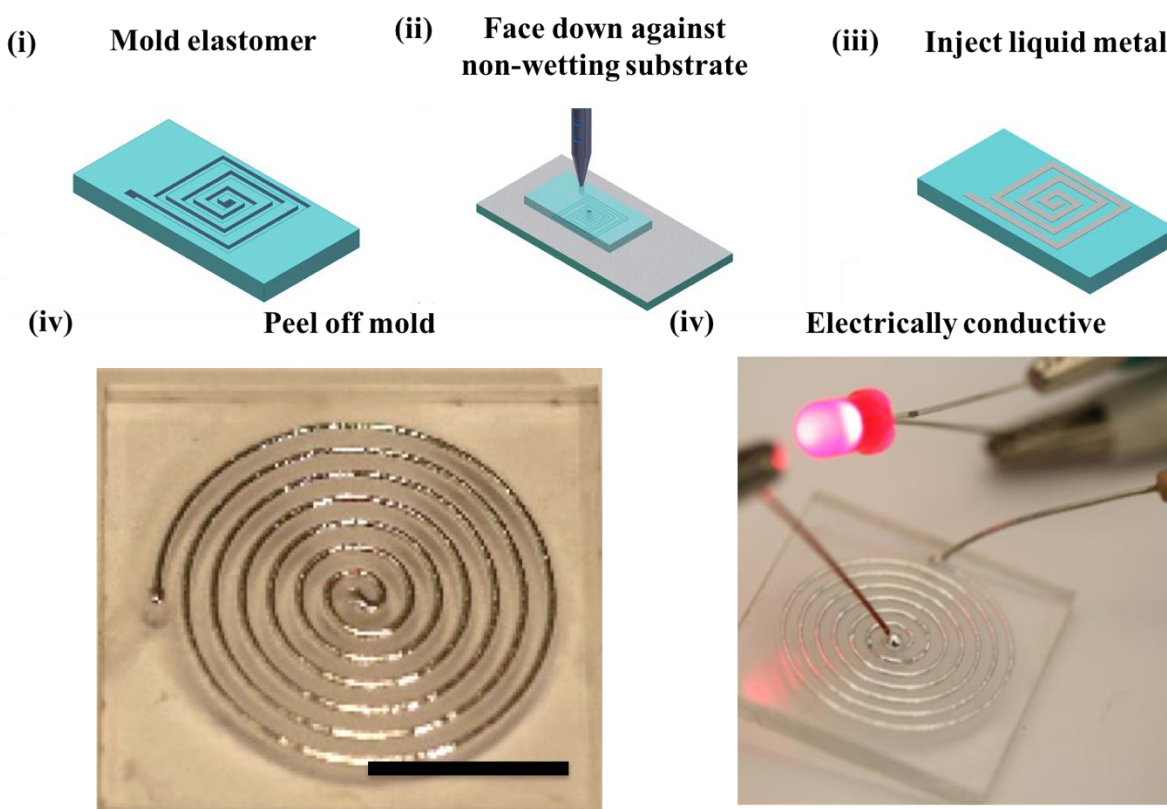


**Figure 3-5:** Schematic of a method to patterning liquid metal against a surface of NeverWet. (i) Schematic of a molded elastomer (using either a laser writer or photolithography). Holes punched in the elastomer serve as inlet and outlet for the liquid metal. (ii) Next, the molded elastomer is placed against the NeverWet surface. (iii) Liquid metal is injected into the inlet of the elastomer. (iv) Optical photograph of liquid metal patterned into a spiral feature after removing the mold from the NeverWet surface. (v) Optical photograph of the metal trace in series with a red LED light shows that the metal trace is electrically conductive. The LED light bulb is connected in series with a 12V battery and resistor, which are not shown. Scale bar on (iv) is 1.0 cm.

Interestingly, we observe the width of liquid metal structures inside microchannels are slightly less than the width of the patterned channel (See **Figure B-5** in Appendix B). We attribute

this phenomenon to two factors: (i) there is no oxide adhesion at the interface of metal and NeverWet, and (ii) curvature of the metal due to the interfacial tension of the metal. Another limitation for this method is that pressure must be applied to the mold during injection, especially for smaller feature sizes. Filling these channels by using a vacuum instead of injection might help mitigate this issue and also allow the metal to fill into smaller features.<sup>68</sup>

#### *Reversible actuation inside closed channels*

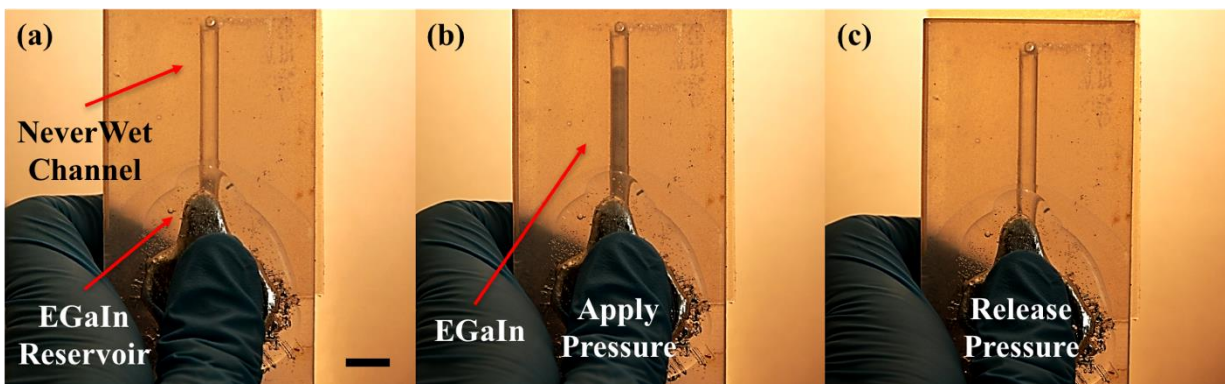


**Figure 3-6:** Reversible actuation of liquid metal inside a closed channel. (a) A channel coated with NeverWet is sealed against another slide coated with NeverWet to form a closed channel. A reservoir of liquid metal is placed below the inlet of the channel and sealed with a membrane of PDMS. (b) Applying pressure from hand actuates liquid metal into the NeverWet-coated channel. (c) Upon releasing pressure, the metal leaves the channel without forming any residue within the channel. Scale bar (a) is 1.0 cm.

In addition to patterning, it is possible to actuate Ga alloys through closed channels by harnessing the non-wetting properties of NeverWet. **Figure 3-6 a-c** demonstrates liquid metal reversibly moving through a closed channel coated with NeverWet; the entire fabrication process is described in the Supporting Information. The actuation does not require any external equipment. Instead, applied pressure from hand to a PDMS membrane covering a liquid metal reservoir drives the metal through the channel. Upon releasing the pressure, liquid metal returns to the reservoir without forming oxide residue on the channel walls. We repeated this process over a hundred cycles without any instances of oxide adhesion. A video of this actuation is shown in Appendix B, **Supplemental Video S2**. Remarkably, this video was recorded nearly 30 months after originally

fabrication the sample. We also note that the mechanical durability of this coating has been previously confirmed.<sup>64</sup>

Although the channel is shown vertically in Fig. 3-6c, the metal can also actuate through the channel horizontally. The metal may be returning to the reservoir due to Laplace pressure in the channel or possibly from the membrane pulling the metal back. Trapped air in the microchannel may also play a role in the recoil of the liquid metal. Unfortunately, coating channels with NeverWet is only effective for channels that are wider than 750  $\mu\text{m}$ . Below this width, the coating clogs the channels upon drying. In addition, applying a uniform coating at the corners of the channels is a challenge. Despite these limitations, this approach is a marked improvement for actuating liquid metal in closed channels. Previous work on actuating liquid metals using PDMS channels with microstructures were limited two to three mm, in width. In addition, these channels were limited to single paths (i.e, straight lines).<sup>46</sup> In contrast, this work can actuate liquid metals through smaller channels (down to 750  $\mu\text{m}$ ). Furthermore, the exact geometry or design for the microchannel can be easily patterned using a laser-writer.

### Reconfigurable monopole antenna

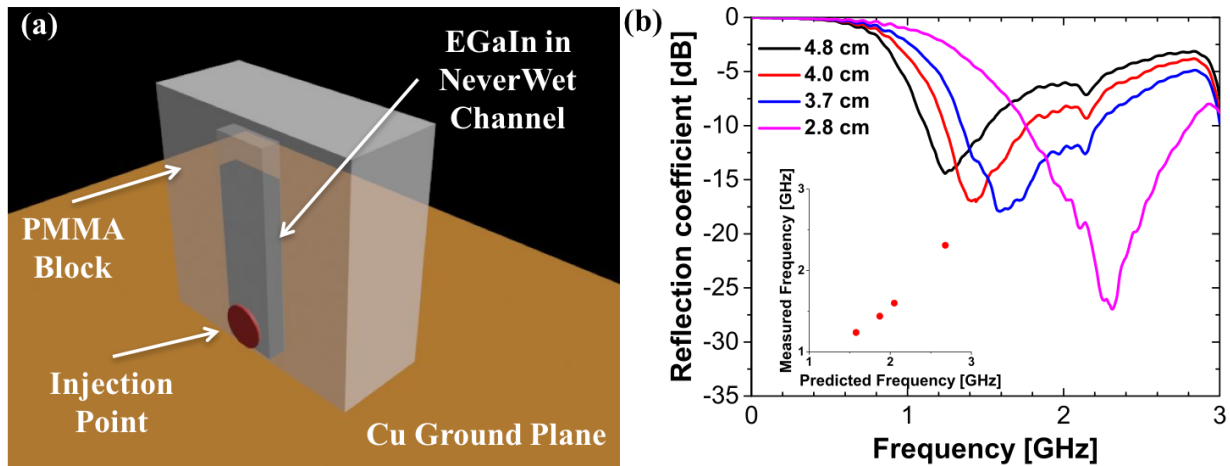


**Figure 3-7:** Reconfigurable monopole antenna. (a) An illustration of the prototype monopole antenna used for antenna measurement. A block of PMMA with etched microchannel rests on a Cu ground plane. The channel is coated with NeverWet to prevent oxide adhesion. The amount of liquid metal in the channel is controlled via injection through a septum (red circle). An SMA (not shown) connects the liquid metal to the copper ground plane. (b) Antenna characterization of reconfigurable monopole antenna at four states (i.e., length of metal in channel). An inset shows the measured frequency (y-axis) vs. the predicted frequency.

We take advantage of the ability to actuate liquid metal within closed channels coated with NeverWet to demonstrate an antenna device with reconfigurable or adjustable behavior. We chose to fabricate a monopole antenna for its simplicity in design. **Figure 3-7 (a)** shows an illustration of the prototype monopole antenna device made from PMMA. A photograph of the prototype device is shown in the Supporting Information (Fig. S7). The length of the metal inside the channel determines the frequency at which the antenna operates. The resonant frequency ( $f_r$ ) of the antenna is inversely proportional to the length ( $l$ ) of liquid metal inside the device.<sup>19</sup> This relation assumes that the channel is very thin and PMMA is transparent to the electromagnetic waves.

Next, we characterized the antenna behavior by filling the channel with liquid to various lengths. The length of metal inside the device is controlled by injection through a port placed at the bottom of the channel. However, other methods such as pneumatics may be more practical for automated control. Figure 3-7 (b) shows the results of the antenna characterization between 0.1 to 3 GHz; specifically, we measured the reflection coefficient of the device, which represents the

ratio between the incident and reflected electromagnetic wave from the antenna. Each trial corresponds to a specified height of liquid metal; the minimum of each trial represents the fundamental resonant frequency of the antenna. The resonant frequency of the antenna varies between to 1.6 GHz to 2.3 GHz based on the extent to which the channel was filled. This frequency range is relevant for telecommunication devices such as mobile phones, wireless internet routers, and radios. A photograph of the prototype antenna and its fabrication procedure are outlined in the Supporting Information.

The experimentally determined resonant frequencies match well to their expected value for a quarter wavelength monopole; a corresponding graph comparing the expected and measured resonant frequencies is provided in the inset of Fig. 3-7b. For each trial length, the observed resonant frequency was 0.5 to 0.7 GHz below their predicted values. We believe there are three causes for this discrepancy. Firstly, the use of a large block of a PMMA body lowers the resonant frequency of the antenna. In addition, the internal length of the SMA pin above the ground plane creates a longer conductive length. Finally, the dimensions of the fabricated channel may also be a cause of error. The predicted values for monopole antennas assume that the traces are infinitely thin. The wide channels may also be the cause of the relatively broadband response of the devices.

## **Conclusions**

This work reports a simple way to create non-stick surfaces for gallium-based liquid metals using a commercial spray (NeverWet). The NeverWet® coating is commercially available, inexpensive, and easy to process rapidly at room temperature. The coating consists of silica nanoparticles embedded in a polysiloxane matrix. Measurements conclude that surfaces that combine micro- and nano-scale roughness prevent oxide adhesion by forming a Cassie-Baxter wetting state. Although liquid metals exhibit high advancing contact angles on smooth

hydrophobic substrates, the metal remains pins to the substrate due to oxide adhesion. Meanwhile, rough surfaces with either hydrophobic or hydrophilic surface chemistry are non-wetting towards the liquid metal. This ‘non-wetting’ property of NeverWet is useful for creating micron-scale, exposed traces of liquid metal by injecting liquid metal in a microchannel placed against these surfaces and then peeling off the microchannel. The resulting structures may be useful as electronic components that are soft or stretchable. Coating channels with NeverWet also allows for reversible actuation of oxide-coated liquid metal allows through confined spaces. Using this approach, we demonstrate a reconfigurable monopole antenna with tunable resonant frequency in the GHz range, which is fabricated using a facile approach.

### **Acknowledgements**

This work is co-authored by Mr. Hudson Ayers, Dr. Gilbert Castillo, Mr. Collin Ladd, Dr. Christopher Tabor (Air Force Research Laboratory), Prof. Jacob Adams (Electrical Engineering, NCSU), and Prof. Michael Dickey. We are grateful to Prof. Jan Genzer, Prof. Hong Zhao, Dr. Collin Eaker, and Mr. Dishit Parekh discussions and suggestions on wetting and patterning. We thank Dr. Matthew Melillo for providing us data on the FTIR spectra of PDMS and PVMS. We thank Ms. Wenyi Xie and Prof. Gregory Parsons for assistance with and access to profilometry, Dr. Kunal Mondal for AFM imaging, Mr. Yiliang Lin for TEM imaging, and Dr. Tim Shay for assistance with FFT. Finally, we thank Mr. Chuck Mooney for assistance with SEM and Dr. Elaine Zhou for TOF-SIMS, respectively. MDD and HRA acknowledge the Triangle MRSEC for funding (DMR-1121107). MDD and IDJ acknowledges support from the Air Force Research Laboratories and NSF ASSIST Center for Advanced Self Powered Systems of Integrated Sensors and Technologies Center (EEC-1160483). JJA and IDJ acknowledge support from the Army Research Office (W911NF-17-1-0216). This work, specifically SEM and TOF-SIMS, was performed in part

at the Analytical Instrumentation Facility (AIF) at North Carolina State University, which is supported by the State of North Carolina and the National Science Foundation (ECCS-1542015). The AIF is a member of the North Carolina Research Triangle Nanotechnology Network (RTNN), a site in the National Nanotechnology Coordinated Infrastructure (NNCI). XPS was performed at the Shared Materials Instrumentation Facility (SMiF) in Duke University.

## References

- (1) Lipomi, D. J. Stretchable Figures of Merit in Deformable Electronics. *Adv. Mater.* **2016**, 28 (22), 4180–4183.
- (2) Joshipura, I. D.; Ayers, H. R.; Majidi, C.; Dickey, M. D. Methods to Pattern Liquid Metals. *J. Mater. Chem. C* **2015**, 3, 3834–3841.
- (3) Khondoker, M. A. H.; Sameoto, D. Fabrication Methods and Applications of Microstructured Gallium Based Liquid Metal Alloys. *Smart Mater. Struct.* **2016**, 25 (9), 93001.
- (4) Dickey, M. D. Emerging Applications of Liquid Metals Featuring Surface Oxides. *ACS Appl. Mater. Interfaces* **2014**, 6 (21), 18369–18379.
- (5) Kazem, N.; Hellebrekers, T.; Majidi, C. Soft Multifunctional Composites and Emulsions with Liquid Metals. *Adv. Mater.* **2017**, 29 (27).
- (6) Dickey, M. D. Stretchable and Soft Electronics Using Liquid Metals. *Adv. Mater.* **2017**, 1606425.
- (7) Khan, M. R.; Eaker, C. B.; Bowden, E. F.; Dickey, M. D. Giant and Switchable Surface Activity of Liquid Metal via Surface Oxidation. *Proc. Natl. Acad. Sci.* **2014**, 111 (39), 14047–14051.
- (8) Wu, P. C.; Zhu, W.; Shen, Z. X.; Chong, P. H. J.; Ser, W.; Tsai, D. P.; Liu, A.-Q. Broadband Wide-Angle Multifunctional Polarization Converter via Liquid-Metal-Based Metasurface. *Adv. Opt. Mater.* **2017**.
- (9) Wang, J.; Liu, S.; Nahata, A. Reconfigurable Plasmonic Devices Using Liquid Metals. *Opt. Express* **2012**, 20 (11), 12119–12126.
- (10) Wilkinson, W. D. *Properties of Gallium. Summary of Published Data on Alloys, Physical Properties and Chemistry*; ANL-4109; Argonne National Lab., Lemont, Ill., 1948.
- (11) Zakharov, D. Eutectic Point of Gallium-Indium System. *Zhurnal Fiz. Khimii* **1975**, 49 (9), 2208–2210.
- (12) Liu, T.; Sen, P.; Kim, C. J. Characterization of Nontoxic Liquid-Metal Alloy Galinstan for Applications in Microdevices. *J. Microelectromechanical Syst.* **2012**, 21 (2), 443–450.
- (13) Park, J.; You, I.; Shin, S.; Jeong, U. Material Approaches to Stretchable Strain Sensors. *ChemPhysChem* **2015**, 16 (6), 1155–1163.
- (14) Li, G.; Wu, X.; Lee, D.-W. Selectively Plated Stretchable Liquid Metal Wires for Transparent Electronics. *Sens. Actuators B Chem.* **2015**, 221, 1114–1119.
- (15) Zhu, S.; So, J.-H.; Mays, R.; Desai, S.; Barnes, W. R.; Pourdeyhimi, B.; Dickey, M. D. Ultrastretchable Fibers with Metallic Conductivity Using a Liquid Metal Alloy Core. *Adv. Funct. Mater.* **2013**, 23 (18), 2308–2314.
- (16) Pourghorban Saghati, A.; Singh Batra, J.; Kameoka, J.; Entesari, K. A Microfluidically-Reconfigurable Dual-Band Slot Antenna With a Frequency Coverage Ratio of 3:1. *IEEE Antennas Wirel. Propag. Lett.* **2015**, PP (99), 1–1.
- (17) Jeong, S. H.; Hjort, K.; Wu, Z. Tape Transfer Atomization Patterning of Liquid Alloys for Microfluidic Stretchable Wireless Power Transfer. *Sci. Rep.* **2015**, 5, 8419.
- (18) Kubo, M.; Li, X.; Kim, C.; Hashimoto, M.; Wiley, B. J.; Ham, D.; Whitesides, G. M. Stretchable Microfluidic Radiofrequency Antennas. *Adv. Mater.* **2010**, 22 (25), 2749–2752.

- (19) So, J.-H.; Thelen, J.; Qusba, A.; Hayes, G. J.; Lazzi, G.; Dickey, M. D. Reversibly Deformable and Mechanically Tunable Fluidic Antennas. *Adv. Funct. Mater.* **2009**, *19* (22), 3632–3637.
- (20) Yoon, S. G.; Koo, H.-J.; Chang, S. T. Highly Stretchable and Transparent Microfluidic Strain Sensors for Monitoring Human Body Motions. *ACS Appl. Mater. Interfaces* **2015**, *7* (49), 27562–27570.
- (21) Kong, T. F.; Nguyen, N.-T. Liquid Metal Microcoils for Sensing and Actuation in Lab-on-a-Chip Applications. *Microsyst Technol* **2015**, *21* (3), 519–526.
- (22) Kim, S.; Lee, J.; Choi, B. Stretching and Twisting Sensing with Liquid-Metal Strain Gauges Printed on Silicone Elastomers. *IEEE Sens. J.* **2015**, *PP* (99), 1–1.
- (23) Lu, T.; Finkenauer, L.; Wissman, J.; Majidi, C. Rapid Prototyping for Soft-Matter Electronics. *Adv. Funct. Mater.* **2014**, *24* (22), 3351–3356.
- (24) Menguc, Y.; Park, Y.-L.; Pei, H.; Vogt, D.; Aubin, P. M.; Winchell, E.; Fluke, L.; Stirling, L.; Wood, R. J.; Walsh, C. J. Wearable Soft Sensing Suit for Human Gait Measurement. *Int. J. Robot. Res.* **2014**, *33* (14), 1748–1764.
- (25) Chiechi, R. C.; Weiss, E. A.; Dickey, M. D.; Whitesides, G. M. Eutectic Gallium–Indium (EGaIn): A Moldable Liquid Metal for Electrical Characterization of Self-Assembled Monolayers. *Angew. Chem. Int. Ed.* **2008**, *47* (1), 142–144.
- (26) Dickey, M. D.; Chiechi, R. C.; Larsen, R. J.; Weiss, E. A.; Weitz, D. A.; Whitesides, G. M. Eutectic Gallium-Indium (EGaIn): A Liquid Metal Alloy for the Formation of Stable Structures in Microchannels at Room Temperature. *Adv. Funct. Mater.* **2008**, *18* (7), 1097–1104.
- (27) Gao, Y. H.; Bando, Y. Carbon Nanothermometer Containing Gallium - Gallium's Macroscopic Properties Are Retained on a Miniature Scale in This Nanodevice. *Nature* **2002**, *415* (6872), 599–599.
- (28) Gao, Y.; Bando, Y.; Liu, Z.; Golberg, D.; Nakanishi, H. Temperature Measurement Using a Gallium-Filled Carbon Nanotube Nanothermometer. *Appl. Phys. Lett.* **2003**, *83* (14), 2913–2915.
- (29) Carey, B. J.; Ou, J. Z.; Clark, R. M.; Berean, K. J.; Zavabeti, A.; Chesman, A. S. R.; Russo, S. P.; Lau, D. W. M.; Xu, Z.-Q.; Bao, Q.; et al. Wafer-Scale Two-Dimensional Semiconductors from Printed Oxide Skin of Liquid Metals. *Nat. Commun.* **2017**, *8*, 14482.
- (30) Ilyas, N.; Butcher, D. P.; Durstock, M. F.; Tabor, C. E. Ion Exchange Membranes as an Interfacial Medium to Facilitate Gallium Liquid Metal Alloy Mobility. *Adv. Mater. Interfaces* **2016**, *3* (9).
- (31) Kim, D.; Lee, Y.; Lee, D.-W.; Choi, W.; Yoo, K.; Lee, J.-B. (JB). Hydrochloric Acid-Impregnated Paper for Gallium-Based Liquid Metal Microfluidics. *Sens. Actuators B Chem.* **2015**, *207*, Part A, 199–205.
- (32) Kim, D.; Thissen, P.; Viner, G.; Lee, D.-W.; Choi, W.; Chabal, Y. J.; Lee, J.-B. (J. B. . Recovery of Nonwetting Characteristics by Surface Modification of Gallium-Based Liquid Metal Droplets Using Hydrochloric Acid Vapor. *ACS Appl. Mater. Interfaces* **2013**, *5* (1), 179–185.
- (33) Fogg, H. C. A Review of the Electrochemistry of Gallium. *Trans. Electrochem. Soc.* **1934**, *66* (1), 107–115.
- (34) Wang, J.; Liu, S.; Guruswamy, S.; Nahata, A. Reconfigurable Liquid Metal Based Terahertz Metamaterials via Selective Erasure and Refilling to the Unit Cell Level. *Appl. Phys. Lett.* **2013**, *103* (22), 221116.

- (35) Kim, D.; Pierce, R. G.; Henderson, R.; Doo, S. J.; Yoo, K.; Lee, J.-B. Liquid Metal Actuation-Based Reversible Frequency Tunable Monopole Antenna. *Appl. Phys. Lett.* **2014**, *105* (23), 234104.
- (36) Cumby, B. L.; Hayes, G. J.; Dickey, M. D.; Justice, R. S.; Tabor, C. E.; Heikenfeld, J. C. Reconfigurable Liquid Metal Circuits by Laplace Pressure Shaping. *Appl. Phys. Lett.* **2012**, *101* (17), 174102.
- (37) Li, G.; Parmar, M.; Kim, D.; Lee, J.-B. (JB); Lee, D.-W. PDMS Based Coplanar Microfluidic Channels for the Surface Reduction of Oxidized Galinstan. *Lab. Chip* **2014**, *14* (1), 200.
- (38) Holcomb, S.; Brothers, M.; Diebold, A.; Thatcher, W.; Mast, D.; Tabor, C.; Heikenfeld, Jason. Oxide-Free Actuation of Gallium Liquid Metal Alloys Enabled by Novel Acidified Siloxane Oils. *Langmuir* **2016**.
- (39) Khan, M. R.; Trlica, C.; So, J.-H.; Valeri, M.; Dickey, M. D. Influence of Water on the Interfacial Behavior of Gallium Liquid Metal Alloys. *ACS Appl. Mater. Interfaces* **2014**, *6* (24), 22467–22473.
- (40) Koo, C.; LeBlanc, B. E.; Kelley, M.; Fitzgerald, H. E.; Huff, G. H.; Han, A. Manipulating Liquid Metal Droplets in Microfluidic Channels With Minimized Skin Residues Toward Tunable RF Applications. *J. Microelectromechanical Syst.* **2015**, *24* (4), 1069–1076.
- (41) Kim, M.; Alrowais, H.; Pavlidis, S.; Brand, O. Size-Scalable and High-Density Liquid-Metal-Based Soft Electronic Passive Components and Circuits Using Soft Lithography. *Adv. Funct. Mater.* **2017**, *27* (3).
- (42) Ilyas, N.; Cook, A.; Tabor, C. E. Designing Liquid Metal Interfaces to Enable Next Generation Flexible and Reconfigurable Electronics. *Adv. Mater. Interfaces* n/a-n/a.
- (43) Kim, D.; Jung, D.; Yoo, J. H.; Lee, Y.; Choi, W.; Lee, G. S.; Yoo, K.; Lee, J.-B. Stretchable and Bendable Carbon Nanotube on PDMS Super-Lyophobic Sheet for Liquid Metal Manipulation. *J. Micromechanics Microengineering* **2014**, *24* (5), 55018.
- (44) Kadlaskar, S. S.; Yoo, J. H.; Abhijeet; Lee, J. B.; Choi, W. Cost-Effective Surface Modification for Galinstan® Lyophobicity. *J. Colloid Interface Sci.* **2017**, *492*, 33–40.
- (45) Jiang, Y.; Su, S.; Peng, H.; Kwok, H. S.; Zhou, X.; Chen, S. Selective Wetting/Dewetting for Controllable Patterning of Liquid Metal Electrodes for All-Printed Device Application. *J. Mater. Chem. C* **2017**.
- (46) Kim, D.; Lee, D.-W.; Choi, W.; Lee, J.-B. A Super-Lyophobic 3-D PDMS Channel as a Novel Microfluidic Platform to Manipulate Oxidized Galinstan. *J. Microelectromechanical Syst.* **2013**, *22* (6), 1267–1275.
- (47) Kramer, R. K.; Boley, J. W.; Stone, H. A.; Weaver, J. C.; Wood, R. J. Effect of Microtextured Surface Topography on the Wetting Behavior of Eutectic Gallium–Indium Alloys. *Langmuir* **2014**, *30* (2), 533–539.
- (48) Kramer, R. K.; Majidi, C.; Wood, R. J. Masked Deposition of Gallium-Indium Alloys for Liquid-Embedded Elastomer Conductors. *Adv. Funct. Mater.* **2013**, *23* (42), 5292–5296.
- (49) Law, K.-Y.; Zhao, H. *Surface Wetting - Characterization, Contact Angle, and Fundamentals*; Springer, 2016.
- (50) Gao, L.; McCarthy, T. J. Wetting 101°. *Langmuir* **2009**, *25* (24), 14105–14115.
- (51) Doudrick, K.; Liu, S.; Mutunga, E. M.; Klein, K. L.; Damle, V.; Varanasi, K. K.; Rykaczewski, K. Different Shades of Oxide: From Nanoscale Wetting Mechanisms to Contact Printing of Gallium-Based Liquid Metals. *Langmuir* **2014**, *30* (23), 6867–6877.

- (52) Ye, Z.; Lum, G. Z.; Song, S.; Rich, S.; Sitti, M. Phase Change of Gallium Enables Highly Reversible and Switchable Adhesion. *Adv. Mater.* **2016**, *28* (25), 5088–5092.
- (53) Yunusa, M.; Amador, G. J.; Drotlef, D.-M.; Sitti, M. Wrinkling Instability and Adhesion of a Highly Bendable Gallium Oxide Nanofilm Encapsulating a Liquid-Gallium Droplet. *Nano Lett.* **2018**.
- (54) Li, G.; Parmar, M.; Lee, D.-W. Oxidized Liquid Metal Based Microfluidic Platform for Tunable Electronic Devices Applications. *Lab. Chip* **2014**, 766–775.
- (55) Bico, J.; Thiele, U.; Quéré, D. Wetting of Textured Surfaces. *Colloids Surf. Physicochem. Eng. Asp.* **2002**, *206* (1–3), 41–46.
- (56) Quéré, D. Rough Ideas on Wetting. *Phys. Stat. Mech. Its Appl.* **2002**, *313* (1–2), 32–46.
- (57) Tian, X.; Shaw, S.; Lind, K. R.; Cademartiri, L. Thermal Processing of Silicones for Green, Scalable, and Healable Superhydrophobic Coatings. *Adv. Mater.* **2016**, *28* (19), 3677–3682.
- (58) Lafuma, A.; Quéré, D. Superhydrophobic States. *Nat. Mater.* **2003**, *2* (7), 457–460.
- (59) Gao, L.; McCarthy, T. J. The “Lotus Effect” Explained: Two Reasons Why Two Length Scales of Topography Are Important. *Langmuir* **2006**, *22* (7), 2966–2967.
- (60) Weisensee, P. B.; Tian, J.; Miljkovic, N.; King, W. P. Water Droplet Impact on Elastic Superhydrophobic Surfaces. *Sci. Rep.* **2016**, *6*, 30328.
- (61) Sharma, V.; Dhayal, M.; Govind; Shivaprasad, S. M.; Jain, S. C. Surface Characterization of Plasma-Treated and PEG-Grafted PDMS for Micro Fluidic Applications. *Vacuum* **2007**, *81* (9), 1094–1100.
- (62) Schnyder, B.; Lippert, T.; Kötz, R.; Wokaun, A.; Graubner, V.-M.; Nuyken, O. UV-Irradiation Induced Modification of PDMS Films Investigated by XPS and Spectroscopic Ellipsometry. *Surf. Sci.* **2003**, 532–535, 1067–1071.
- (63) Sikka, V. K.; Hurley, M.; Lim, Z. W. United States Patent: 9139744 - Composition and Coating for Hydrophobic Performance. 9139744, September 22, 2015.
- (64) Jiang, L.; Park-Lee, K. J.; Clinton, R. M.; Tang, Z.; Breedveld, V.; Hess, D. W. Mechanical Durability of Liquid Repellent Coatings. *Surf. Coat. Technol.* **2017**, *328*, 182–191.
- (65) Efimenko, K.; Wallace, W. E.; Genzer, J. Surface Modification of Sylgard-184 Poly(dimethyl Siloxane) Networks by Ultraviolet and Ultraviolet/Ozone Treatment. *J. Colloid Interface Sci.* **2002**, *254* (2), 306–315.
- (66) Lazarus, N.; Meyer, C. D.; Turner, W. J. A Microfluidic Wireless Power System. *RSC Adv.* **2015**, *5* (96), 78695–78700.
- (67) Gozen, B. A.; Tabatabai, A.; Ozdoganlar, O. B.; Majidi, C. High-Density Soft-Matter Electronics with Micron-Scale Line Width. *Adv. Mater.* **2014**, *26* (30), 5211–5216.
- (68) Lin, Y.; Gordon, O.; Khan, M. R.; Vasquez, N.; Genzer, J.; Dickey, M. D. Vacuum Filling of Complex Microchannels with Liquid Metal. *Lab. Chip* **2017**.

## **CHAPTER 4**

# **ARE CONTACT ANGLE MEASUREMENTS USEFUL FOR OXIDE-COATED LIQUID METALS?**

## **Abstract**

This work investigates the validity of conventional wetting measurements for oxide-coated liquid metals. Liquid metals are useful soft and fluidic conductors for electronics, composites, and microfluidics. These metals bear a thin ( $\sim 3$  nm) surface oxide that acts as an elastic, solid shell and adheres to many surfaces. Using conventional tools for measuring contact angles, this work compares the wetting behavior of liquid metals with water. Regardless of the substrate hydrophilicity, advancing angles for the metal are always high ( $>140^\circ$ ) due to the high surface tension of the metal and the need to rupture the oxide in tension to advance the droplet. During the receding measurements, the contact angle never achieves an equilibrium value because the oxide pins at the perimeter of the drop; it is only on rough surfaces that the oxide does not pin. For sliding angle measurements, the results depend on whether the oxide ruptures when placing the drop on the substrate. This work suggests that conventional wetting measurements (contact angles, tilt or sliding angle) for oxide-coated liquid metals are subject to different interpretations than water. Moreover, the results provide fundamental insights on the adhesion of the oxide to substrates, which is important for patterning metals and reconfigurable electronics.

## **Introduction**

This work studies the wetting and adhesion behavior of liquid metals that possess a surface oxide ‘skin’. The goal of this work is to show that conventional measurements for studying wetting behavior (dynamic contact angles and tilt angles) are difficult to interpret and even misleading if evaluated in the same way as fluids such as water. In addition, this study explores the feasibility of alternative methods to measure the adhesion of oxide-coated liquid metals. Although this work utilizes liquid metals, which have melting points near room temperature, insights from this work may be applied to all molten metals with surface oxides.

Liquid metals offer high electrical and thermal conductivity of metals, and low viscosity of liquids. As a result, these materials are promising for use in flexible, stretchable, and reconfigurable electronics.<sup>[1-3]</sup> In addition, the high thermal conductivity of the metal offers opportunities for thermal or heat transfer management at the micro-scale.<sup>[4,5]</sup> The wetting and adhesion of these liquid metals play an important role in enabling such applications. Patterning the metal for interconnects and conductive pathways in electronics relies on the wetting of the metal to the underlying substrate; this wetting is particularly important for additive manufacturing techniques, such as 3-D printing and ink-jet printing.<sup>[6-11]</sup> Meanwhile, reconfiguring and flowing the liquid metal, in a reversible manner, requires surfaces to either minimize or entirely prevent adhesion.<sup>[12-15]</sup> In addition, the wetting of liquid metal onto other metals can lead to embrittlement, which can cause structural failure of metal parts and components.<sup>[16,17]</sup> Preventing the adhesion of these metals to surfaces may be useful for enabling reconfigurable electronics as well to improve handling and contamination of liquid metals. Ultimately, understanding the adhesion of oxide is important for both promoting it (for patterning) as well as preventing it (reconfigurability and material safety).

Specifically, this work utilizes a eutectic alloy of gallium and indium ('EGaIn', 75% Ga, 25% In, by weight), which exhibits a melting point of 15.5 °C. Due to this low melting point, the metal remains a liquid at or near room temperature.<sup>[18]</sup> Unlike other liquid metals such as toxic mercury (Hg), Ga and their alloys have relatively low toxicities.<sup>[19-22]</sup>

### *Oxide 'Skin' of Liquid Metals*

Alloys of Ga forms a surface oxide in the presence of oxygen, which plays an important role in its use. The oxide 'skin' is thin (~3-5 nm), passivating at ambient conditions, and primarily composed of Ga.<sup>[23-26]</sup> Accordingly, the surface oxide acts as solid-like shell or membrane

encompassing the liquid. This oxide ‘skin’ also exhibits a yield stress, which allows liquid drops to form into non-spherical shapes. For example, **Figure 4–1** shows two droplets of liquid metal stacked atop each other; the drops remain stable despite not being symmetric to one another and do not coalesce unless perturbed mechanically. Importantly, the oxide is known to adhere to a variety of surfaces, which is the primary focus of this work.

Although this oxide ‘skin’ is often considered to be a nuisance, it can be utilized for a variety of applications. For example, the oxide allows for the metal to distort into shapes such as wires or cones that would not be possible with water.<sup>[26–28]</sup> In addition, the metal may be injected into microfluidic networks and remain stable (despite high Laplace pressure) due to the adhesion of the oxide onto the walls of the microchannels.<sup>[25]</sup> Thus, the metal may integrate with soft materials (such as elastomers and gels) to realize soft and deformable electronics as well as electrodes in microfluidic applications.<sup>[2,3,29–31]</sup> The oxide-enabled stability in microchannels allows the liquid to be ‘self-healing’; formation of the oxide preventing the metal from ‘oozing’ out when the microchannel is broken (or cut).<sup>[38–40]</sup> Because the oxide prevents liquid drops from coalescing, it is possible to utilize sonication or flow-focusing to form liquid droplets that are stable in shape.<sup>[32–35]</sup> The oxide can also serve as a template for other materials. For example, the oxide skin may be functionalized with chemical moieties<sup>[12,26,36]</sup> (i.e., silanes, thiols, and other polymers) as well as biomolecules (i.e., drug delivery agents).<sup>[21]</sup> In addition, the metal oxide can be transformed into semiconductor, chalcogenides, and 2D materials<sup>[37]</sup> or serve as a useful surface for growing other materials, such as graphene.



**Figure 4-1:** Two drops of eutectic gallium indium (‘EGaIn’) sitting atop each other in an asymmetric orientation. The bottom drop exhibits an asymmetric apparent contact angle ( $119^\circ$  on left and  $115^\circ$  on right). Scale bar is 1.0 mm.

In principle, metal droplets (without a surface oxide) should be non-wetting to most substrates due to their enormous surface tension — an exception to this behavior would be for metallic substrates, where ‘reactive wetting’ may occur across the interface. However, the presence of the surface oxide complicates the interfacial behavior of these liquid droplets. Firstly, the yield stress of the oxide complicates its hydrodynamic behavior (i.e., flow and expansion of droplets). To expand a drop or cause the liquid to flow, the oxide must rupture. As the oxide ruptures, new oxide will form as oxygen contacts the freshly exposed metal. Studies show that rupturing and forming new oxide promotes adhesion.<sup>[41,42]</sup> The formation of a new oxide may be occurring on

the order of microseconds.<sup>[43,44]</sup> In addition, the tension of the oxide is not necessarily isotropic, particularly when droplets are deflated.

### *Conventional Contact Angle Measurements*

Contact angle measurements typically quantify the wetting behavior of liquids on surfaces. Despite their simplicity, there remains ongoing discussion in the literature about how to interpret contact angle measurements.<sup>[45,46]</sup> The contact angle results from a force balance at the three-phase line (i.e. the point where a liquid and vapor meet a solid substrate). Equation 1 is the Young's equation, which defines the contact angle ( $\theta$ ) as a balance of three interfacial forces ( $\gamma_i$ ) at a solid(s)-liquid(l)-gas(g) interface. This equation is valid if the interactions between the three interfaces are at physical and chemical equilibrium. Accordingly, these interfaces must be homogenous and non-reactive, clean, macroscopically flat, and chemical homogenous (relative to the size of the drop). Likewise, the probe fluid must be pure and free of surface active species (i.e., contaminants, surfactants, and colloids).

$$\gamma_{sg} = \gamma_{sl} + \gamma_{lg} * \cos(\theta) \quad \text{(Equation 1)}$$

By itself, the contact angle of a static drop ( $\theta_s$ ) provides limited information because of the tendency of liquids to get trapped in energy minima.<sup>[45,46]</sup> Surfaces will display a range of angles, two of which are at equilibrium; these two angles are referred to as advancing and receding contact angle ( $\theta_A$  and  $\theta_R$ , respectively). The  $\theta_A$  relates to the wetting force at the contact line (i.e., ability of the drop to spread). Meanwhile, the  $\theta_R$  relates to the adhesion forces at the interface between the drop and substrate. Moreover, the  $\theta_R$  measures the ability of a drop to de-pin at the contact line. Therefore, low values of  $\theta_R$  indicate that the interactions between the liquid and solid (i.e., adhesion) are more favorable than liquid-liquid (i.e, cohesion). As a result, dynamic contact angle

measurements are often performed to obtain  $\theta_A$  and  $\theta_R$  to provide more information on the wettability and adhesion for a given surface.

Dynamic contact angle measurements involve placing a drop on a given surface and measuring the contact angle while increasing the drop volume at a steady rate. After reaching an equilibrium angle ( $\theta_A$ ), the liquid volume is reduced until the second equilibrium angle is obtained ( $\theta_R$ ). Larger  $\theta_A$  are associated with surfaces that exhibit less wetting. Meanwhile, the  $\theta_R$  relates to the work of adhesion between the liquid and substrate; thus, lower receding angles (i.e., less than  $90^\circ$ ) relate to higher adhesion.<sup>[45,47]</sup> The difference between the two angles (e.g., contact angle hysteresis) is often reported to characterize the wetting properties of a surface. However, this metric does not necessarily measure directly the wettability or adhesion of a liquid onto a surface.<sup>[46]</sup> Many parameters, including but not limited to chemical composition, chemical homogeneity, surface roughness, contribute to contact angle hysteresis.<sup>[46–49]</sup>

Interpreting advancing and receding contact angles is already complex with simple fluids, such as water.<sup>[45,46]</sup> In the case of Ga alloys, the surface oxide is a solid ‘skin’ that envelops the drop and has mechanical properties that impede the liquid from assuming shapes that minimize interfacial energy of the liquid. The surface oxide also dominates and complicates the interfacial behavior of liquid metal drops against surfaces; for example, the oxide-coated metal pins to most surfaces it contacts, which leads to irreversible adhesion in such cases.

However, in absence of the oxide, the metal drop readily beads up on most surfaces; the contact angle likely approaches  $180^\circ$  but such a large angle is difficult to measure. Metal substrates are an exception since either Ga or In can either form metallic bonds with the substrate or diffuse within grain boundaries (i.e., ‘reactive wetting’). Consequently, the interface between the metal drop and metal substrate changes in time (with respect to morphology and chemical composition).

In addition, the oxide makes it possible to physically manipulate the apparent contact angle (i.e., deforming, squishing, dragging, etc.)<sup>[50]</sup> and are therefore subject to hysteresis effects. Although sessile and pendant drops of these liquid metals are almost entirely liquid, the mechanics of the oxide ‘skin’ complicates the use of conventional models that are useful for assessing the wetting and interfacial of liquids. This work shows that the pinning of the oxide to solid surfaces leads to misleading interpretations of contact angle measurements.

### *Sliding angle measurements*

Sliding angle measurements are helpful in determining the mobility of a drop across a given surface. This measurement involves placing a drop of the probe liquid on a horizontal surface. Thereafter, the surface is slowly tilted until the drop begins to translate across the surface; the angle between the substrate and horizontal surface underneath is the sliding angle ( $\alpha$ ). At  $\alpha$ , the drop may exhibit two different contact angles (at the front and back of the drop). Contrary to popular belief, these angles do not provide the same values for  $\theta_A$  and  $\theta_R$  from dynamic contact angle measurements of sessile drops.<sup>[47,51]</sup>  $\theta_A$  and  $\theta_R$  principally represent equilibrium energy states for a given surface, whereas the angles observed on the liquid drop from sliding angle measurements are not equilibrium values (i.e., the drop is moving and thus not at equilibrium). In addition, there is also no correlation between the contact angle hysteresis (the difference between  $\theta_A$  and  $\theta_R$ ) and  $\alpha$ .<sup>[47]</sup>

Despite these complications with interpreting sliding angle experiments, this measurement serve as useful and complimentary experiments to traditional contact angle experiments. In particular, tilt angle experiments are useful in identifying Cassie-Baxter wetting states — surfaces in Cassie-Baxter states exhibit low  $\alpha$  ( $1^\circ$  to  $6^\circ$ , for water), along with high  $\theta_A$  from contact angle measurements.<sup>[45]</sup> In addition, sliding angle measurements are useful for applications that involve

the mobility or sliding of droplets across a surface (i.e., self-cleaning surfaces, anti-icing coatings, and applications involving thermal management). In this work, we utilize sliding angle experiments to provide further clarity and consideration on the behavior of oxide-coated liquid metals in a ‘flowing’ condition.

## **Results**

### *Dynamic contact angle measurements*

We apply these techniques on drops of EGaIn and DI water on surfaces of varying hydrophobicity. To simplify an already complex system, we initially focus on only flat and smooth surfaces. To provide context and additional surface characterization, we report advancing ( $\theta_A$ ) and receding angles ( $\theta_R$ ) for water. In the case of surface-oxidized liquid metals, the reported angle should not be considered as a classical “contact angle”; instead, they are an apparent angle at the interface of the oxide-substrate-air interface.

We questioned whether experimental conditions for the dynamic contact angles played a role in the apparent  $\theta_A$  and  $\theta_R$  for EGaIn. Firstly, we considered whether the volumetric flow rate of the drop affected the measurement. We reasoned that the rate or magnitude of rupturing the oxide may affect the observed contact angle. **Figure C–1 in Appendix C** shows that  $\theta_A$  for both EGaIn and water is essentially invariant versus flow rates spanning an order of magnitude, although the standard deviation increases slightly. The results from these experiments are also enumerated in **Table C–1** (for water) and **Table C–2** (for EGaIn) in Appendix C. In addition, we found the needle height (distance between the nozzle of needle and substrate) effect the receding measurements. **Fig. C–2** in Appendix C shows that needle heights greater than 1 mm cause the drop to prematurely break from the needle and remain on the substrate. As a result, the

measurement is aborted prior to removing all the volume from the substrate. Unless otherwise noted, the remaining experiments were performed with a needle height of  $\sim 0.6$  mm.

*Dynamic contact angle measurements: Advancing measurements*

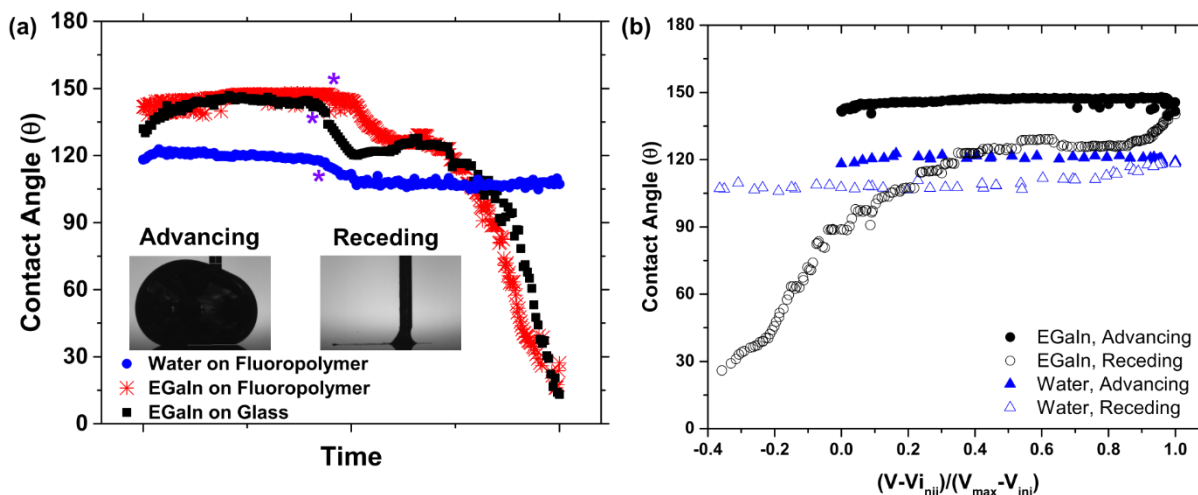


**Figure 4-2:** Advancing and receding contact angle measurements of EGaIn and water on hydrophobic (fluoropolymer) and hydrophilic substrates (glass). (a) Apparent contact angle versus time for EGaIn on a hydrophobic substrate (fluoropolymer, red star) and on hydrophilic substrate (glass, black squares), and water on fluoropolymer (blue, circle, control experiment). A purple star denotes the time at which volume recedes from the drop. Images of EGaIn on hydrophobic substrate are shown as insets for advancing portion (left) and receding portion (right) for the measurement. (b) Advancing and receding contact angle on the hydrophobic substrate as a function of the volume of the drop. The abscissa on this group is a scaled function of the volume to show the evolution and hysteresis curve of the contact angle.

We find that regardless of the substrate, the advancing angle is always high ( $\sim 140^\circ$  or greater), yet adhesion is observed upon receding the drop. **Figure 4-2a** shows a graph of the measured  $\theta$  during the dynamic contact angle measurements. It is plotted with respect to time to reflect the progression of the experiment: volume increases and then decreases (denoted by a purple star in the plot). As a control experiment, we use DI water on a flat and hydrophobic substrate (Si wafer with a spin-coated fluoropolymer coating, FluoroPel). For water, as the drop of the volume increases, the  $\theta$  increases to a stable value of  $120.0^\circ \pm 1.8$  ( $n=3$ ); we designate the average value in this region as the advancing angle ( $\theta_A$ ). Upon receding the volume, the  $\theta$  decreases

to a stable value of  $107^\circ \pm 0.9^\circ$  ( $n=3$ ), which we designate as the receding angle ( $\theta_R$ ). This experiment shows that for water, the angles reach equilibrium values, as expected.

In contrast, oxide-coated liquid metals behave differently. For the case of EGaIn on the hydrophobic surface, the metal drop reaches a high angle ( $158.1^\circ \pm 1.7$ ,  $n=4$ ) during the advancing measurement; an inset in Fig. 4–2a (bottom, left) shows an image of an EGaIn drop on a fluoropolymer during the advancing measurement. We note that although the drop does not always grow symmetric to the needle, the contact angles are often within a few degrees. Accordingly, the reported contact angles for EGaIn are averages of the left and right side of the drop. Upon receding the volume, the apparent  $\theta$  for EGaIn decrease but never stabilizes at an equilibrium value. In fact, the contact angle of EGaIn initially decreases sharply then increases again. Thereafter, the contact angle drops sharply again but does not reach an equilibrium. An inset in Fig. 4–2a (bottom, right) shows the liquid metal at the end of measurement. We observe the same behavior for EGaIn on glass, which is hydrophilic. That is, EGaIn exhibits a high contact angle on glass ( $139.6^\circ \pm 0.77^\circ$ ,  $n=4$ ) during the advancing measurement, yet never achieves a steady angle during the receding measurement.

We plot the  $\theta$  versus volume of the drop in Fig. 4–2b to better visualize the advancing (closed symbols) and receding (open symbols) measurements. Controlling the volume of the drop across all experiments is difficult due to the difference in densities between water and EGaIn, as well as the yield stress of the oxide. Therefore, we normalize the volume based on the initial volume ( $V_{ini}$ ) and the maximum volume of the drop ( $V_{max}$ , which is always at the transition between the advancing and receding measurements). After the scaling, the advancing measurement of the experiment always begins at zero (where  $V=V_{ini}$ ) and proceeds to one (where  $V=V_{max}$ ). In general, this graph shows that the  $\theta$  for EGaIn continues to decrease as liquid is removed from the

drop. Meanwhile,  $\theta$  for water remains stable as the volume decreases. This scaling analysis is applied for other experiments presented later in this work.

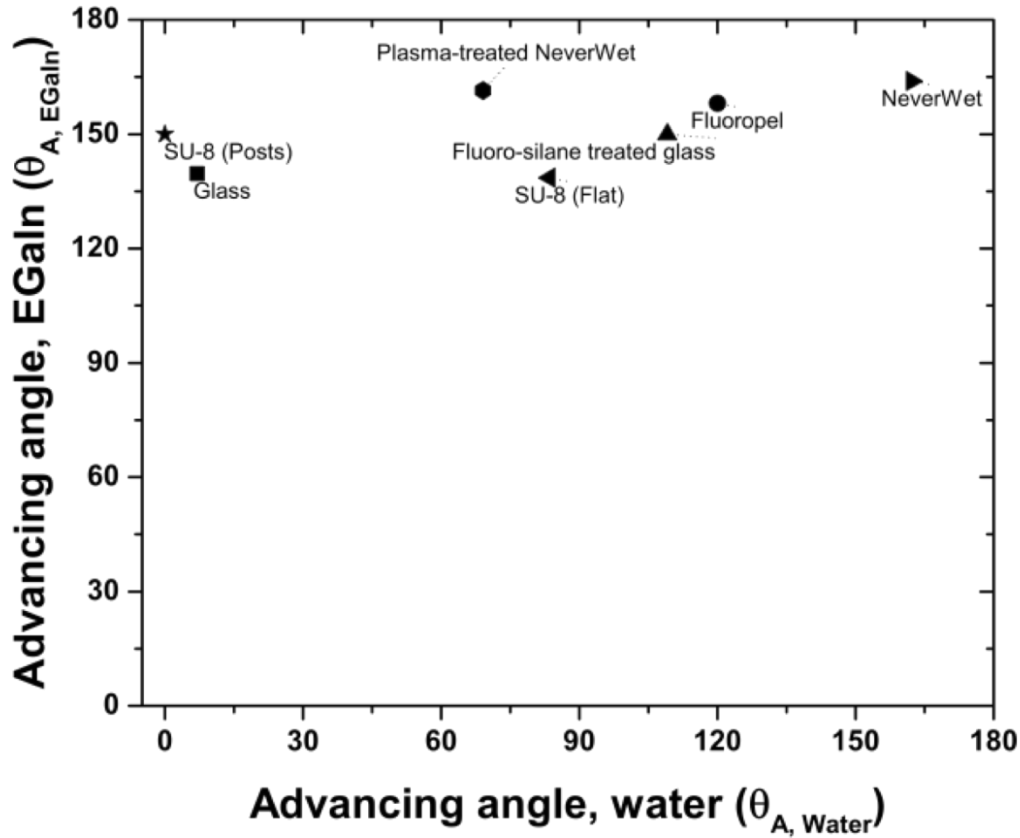


**Figure 4-3:** A plot of advancing angle of EGaIn vs. advancing angle of water for various substrates.  $\theta_{A, \text{water}}$  for glass<sup>[52]</sup> and SU-8 (flat)<sup>[53]</sup> are from literature. Water wets into the SU-8 posts (hence  $\theta_{A, \text{water}}$  of  $0^\circ$ ), which are  $200 \mu\text{m}$  squares with  $200 \mu\text{m}$  spacing.

We observe this same wetting behavior for EGaIn on flat surfaces regardless of the surface energy. **Figure 4-3** compares the apparent  $\theta_A$  of EGaIn vs. the  $\theta_A$  for water for various substrates. Although there is a slight positive trend between the two values, the main takeaway from this plot is the advancing angle of EGaIn is always large regardless ( $\sim 140^\circ$  or greater) of the hydrophobicity or hydrophilicity of the substrate. We reason that the advancing angle always must be greater than  $90^\circ$  to ensure the oxide experiences the tensile stresses necessary to yield the oxide. Upon receding the drop volume, the oxide pins to flat substrates regardless of  $\theta_A$  for EGaIn and DI

water. These results may appear to be trivial because it has been documented that the advancing angle is not related to adhesion.<sup>[54]</sup> However, the reader should take away that either  $\theta_s$  or  $\theta_A$  of water on a substrate provides either no empirical evidence or physical insight on how a drop of oxide-coated liquid metal would behave on flat substrates.

*Dynamic contact angle measurements: Receding measurements*

Another key difference between water and EGaIn in dynamic contact angles appears in the receding measurements. For water, in general, the contact angle initially lowers from the value of  $\theta_A$  then reaches another plateau for the  $\theta_R$ . Fig. 4–2b shows the evolution of the contact angle for water on a fluoropolymer substrate. As the volume retreats towards its original value, the  $\theta_R$  reaches an equilibrium value at  $107^\circ \pm 0.9^\circ$  (n=3). We observe similar behavior for water on fluorosilane-treated glass ( $\theta_A$  of  $109^\circ \pm 0.69^\circ$  (n=9),  $\theta_R$  of  $86.6^\circ \pm 0.55^\circ$  (n=9)), which is shown in Fig. 4–2a and tabulated in Table C–1 and C–2 in Appendix C. These results illustrate typical behavior of dynamic contact angles for water and other simple fluids. In contrast to the water results, the measured  $\theta_R$  never reaches an equilibrium value for EGaIn, on both hydrophobic and hydrophilic substrates. Fig. 4–2b shows the evolution of the contact angle for EGaIn on glass and hydrophobic substrates; the lower portion of the curves for EGaIn represent the receding measurement.

To distinguish data between advancing and receding measurements in Fig. 4–2, **Figure 4–4** shows an exploded view of only the receding measurement for EGaIn on a hydrophobic. For further clarity on the behavior of EGaIn in the receding measurement, we divide this data into distinct regimes (A, B, and C), as denoted in Fig. 4–4. Regime A refers to the beginning of the receding measurements, where volume is initially removed from the drop. During Regime A, the contact angle sharply decreases. Concurrently, the base of the drop expands outwards despite the

volume decreasing. Notably, the drop appears to sag as it loses tension, which leads to the expansion of the base of the drop; we refer to this behavior as baseline expansion and describe it in more detail further below. Thereafter, in Regime B, the contact angle remains steady as volume is removed. However, perimeter of the drop does not retract inward as the oxide pins to the substrate. Upon continuing to remove volume, the contact angle begins to sharply decrease again; the sharp decline marks the beginning of Regime C. As majority of the volume is removed, the apparent contact angle does not reach a stable value.

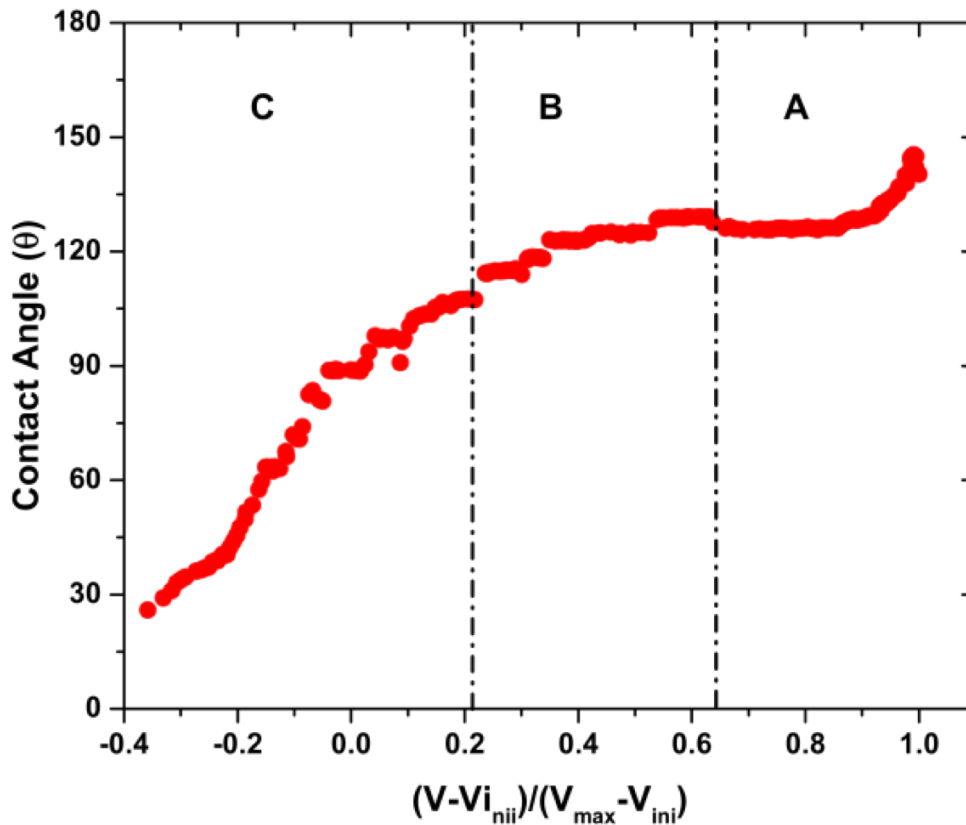


**Figure 4-4:** Receding measurement divided into three regimes (A, B, and C) for EGaIn on a hydrophobic substrate.

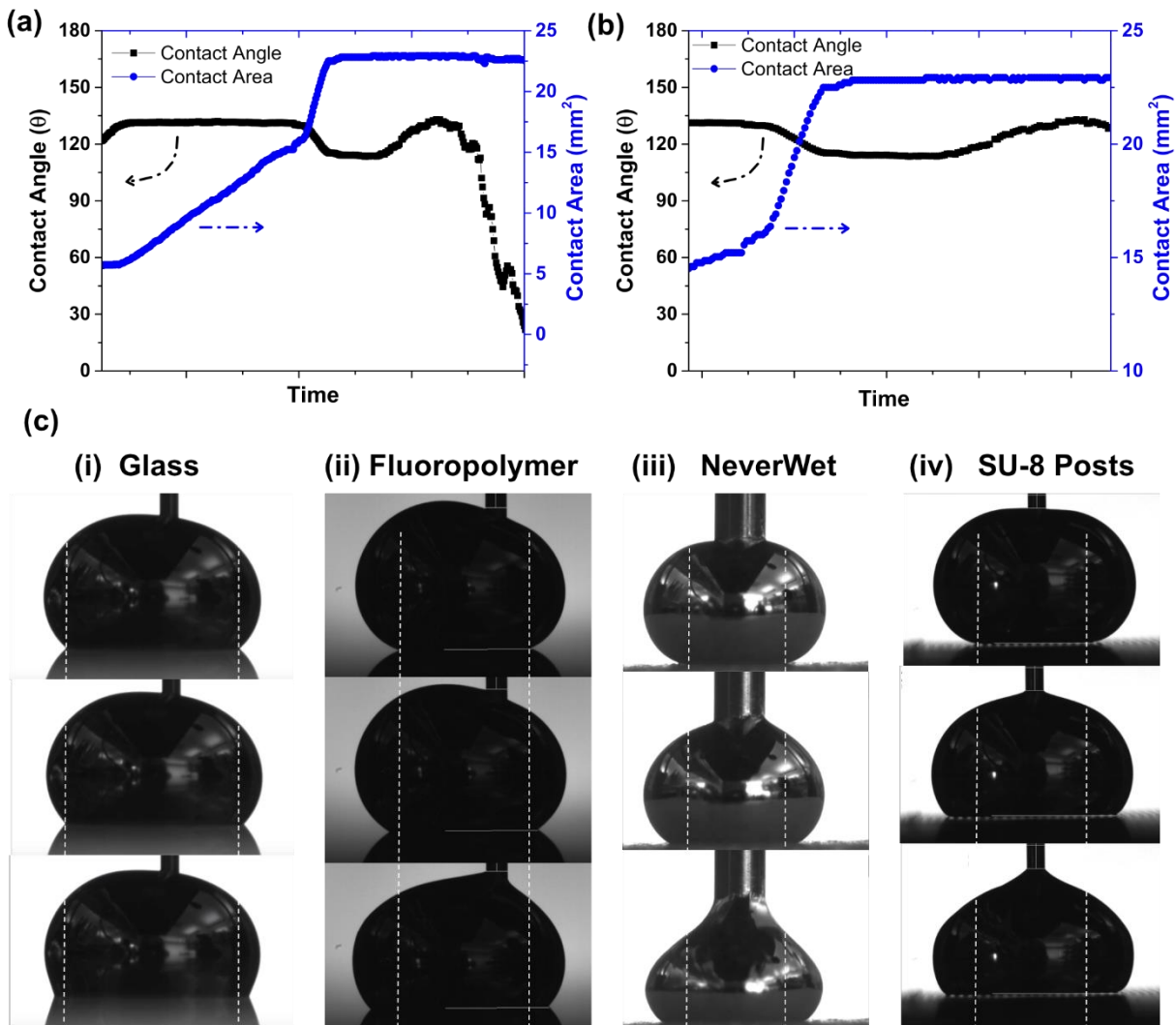


**Figure 4-5:** a) Advancing and receding contact angle measurement of EGaIn on a plasma-treated silicon wafer. (b) An exploded view of the (a) during Regime A (beginning of receding angle). (c) Side-view micrographs of EGaIn drops undergoing baseline expansion on various substrates (i: Silicon wafer, ii: Fluoropolymer, iii: NeverWet, iv: SU-8 posts). The top images for all columns show the drop prior to baseline expansion. White dotted vertical lines extend from contact line of the top images to the final row of images; these lines serve as guides to show the expansion of the baseline on each substrate.

We observe the baseline expansion behavior during Regime A irrespective of the underlying solid surfaces. **Figure 4-5c** shows the expansion of the baseline of EGaIn on various flat substrates. The expansion occurs on both hydrophilic (Fig. 4-5c, i) and hydrophobic (Fig. 4-5c, ii). In addition, we observe baseline expansion occurring even on rough or textured surfaces. Fig. 4-5c, iii shows baseline expansion on a surface where adhesion does not occur (NeverWet), preventing adhesion on surfaces was studied more extensively in Chapter 3. (Fig. 4-5c, iv) shows

EGaIn resting over square posts made from a photocurable polymer (SU-8 photoresist). Upon decreasing the volume, the drop expands over and encounters adjacent posts. Based on these results, baseline expansion occurs even on surfaces where pinning does not occur. We hypothesize the drop sagging that leads to baseline expansion is driven by gravity. To test this hypothesis, we perform experiments with pendant drops (hanging from needle in air) that are expanded and reduced in volume (i.e., advancing and receding the drop without a substrate). **Figure C-3a** in Appendix C shows that upon reducing the drop volume, the drop elongates (i.e. sags) and the oxide skin buckles due to compression. The formation of buckles suggest that surface tension of the oxide-coated drop is not isotropic. Similar buckling and non-isotropic surface tension behavior has been observed on pendant drops of bacteria films aging<sup>[55]</sup> (Fig. C-3b) as well as a free-standing polymeric shell (Fig. C-3c).<sup>[56]</sup>

After the baseline expansion,  $\theta$  gradually increases and reaches what appears to be a stable value. We refer to this portion of the receding measurement as Regime B. Interestingly,  $\theta$  is often near  $\sim 120^\circ$  in Regime B regardless of the chemical composition of the substrate. Upon removing further volume from the drop,  $\theta$  begins to sharply decrease again; we designate this portion of the receding measurement (at the onset of the second decrease in  $\theta$ ) as Regime C. In Regime C,  $\theta$  continues to decrease until either much of the volume of drop is removed or the needle detaches from the drop. It should be noted that not all the liquid from the drop can be removed during Regime C, even if the needle is within 100 microns of the surface, which was the resolution of actuator in our experimental setup. As a result, there is always metal residue on the surface for any substrates in which the oxide pins.

Perhaps more importantly, drops of the metal never truly recede from the contact line due to the pinning of the oxide. That is, after the baseline expansion in Regime B, the baseline of drop

remains pinned to the outer perimeter. **Figure 4–5a** shows that the interfacial contact area of the drop (i.e., area of sessile drop in contact with substrate) remains constant through the end of the experiment. Fig. 4–5b shows an exploded view of Fig. 4–5a during Regime B. The increase in contact area in Fig. 4–5b highlights the expansion of the baseline (as the contact angle decreases). Subsequently, the contact area remains constant due to pinned oxide. Thus, the residue of liquid metal observed at end of the experiment is due to pinning of oxide to the substrate.

In addition to interactions with the substrate, the oxide also modifies the interfacial tension of the metal; this change in interfacial tension makes contact angles measurements difficult to interpret because the contact angle represents a balance of interfacial forces at the perimeter of the drop.<sup>[50]</sup> To further complicate the interface, it's likely that the surface tension of the oxide-skin is not isotropic (unlike conventional liquids). Consequently, the interpretation of contact angles for liquid metals is significantly more complex than water and perhaps misleading if interpreted in the same way as fluids such as water.

## Oxide spider-web patterns

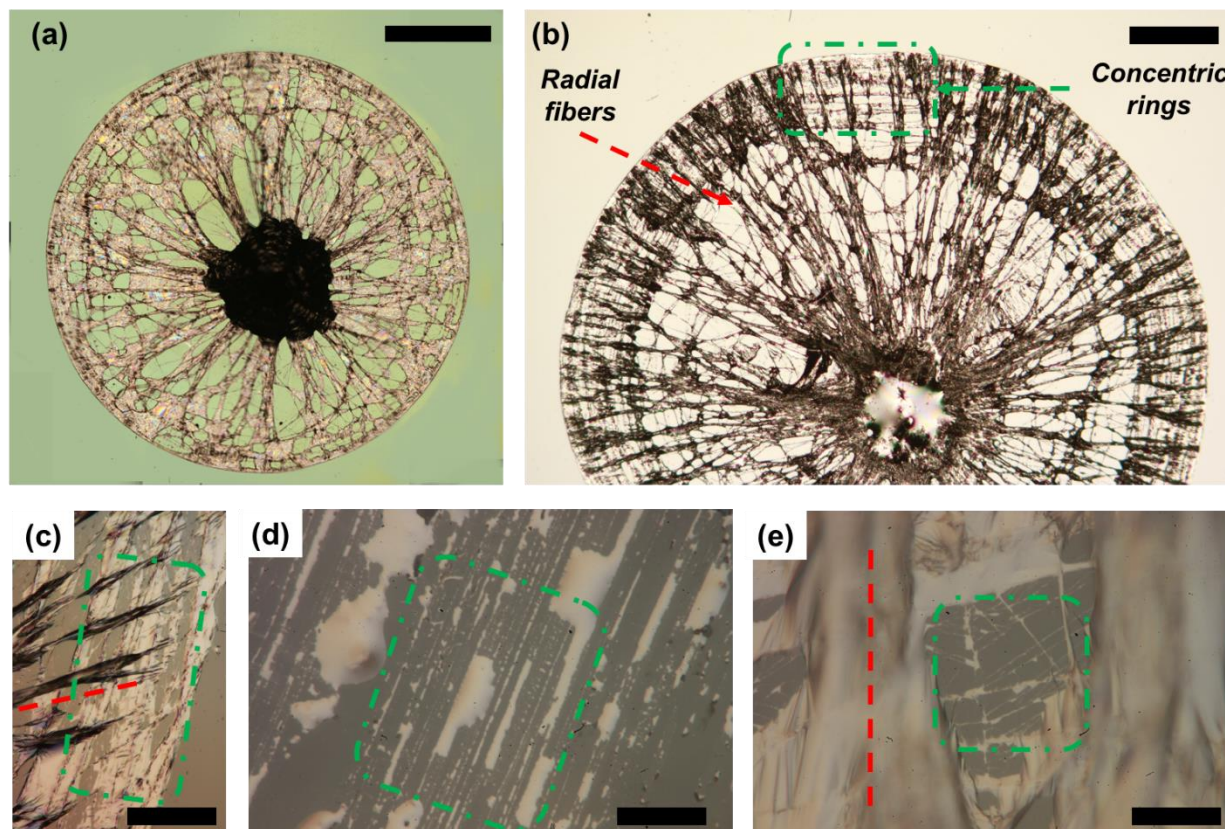


**Figure 4-6:** Oxide ‘spider-web’ residue. (a) Optical micrograph of EGaIn residue on flat SU-8 (hydrophilic) after dynamic contact angle measurement. Green background is due to polarization of light. Scale bar is 1.0 mm, (b) Optical micrograph of EGaIn residue on hydrophobic substrate (fluoropolymer). Red and green dotted lines indicate radial fibers and concentric rings, respectively for (b-e). Scale bar is 1.0 mm for (b), (c) Optical micrograph at 50 $\times$  magnification at the edge of the drop from image in (b). Scale bar is 100  $\mu\text{m}$ , (d) Optical micrograph at 100 $\times$  magnification within the drop. Diagonal lines show pinning of the drop during advancing measurement. Scale bar is 50  $\mu\text{m}$ . (e) Optical micrograph at 100 $\times$  magnification of (b) between two radial fibers. Scale bar is 50  $\mu\text{m}$ .

We utilized optical and electron microscopy to verify the pinning of the oxide to the outer perimeter of the drop. **Figure 4-6** shows optical micrographs of EGaIn drops on SU-8 (hydrophilic, Fig. 4-6a) and FluoroPel (hydrophobic, Fig. 4-6b); the drops are imaged (top-down) upon completion of the dynamic contact angle measurements. For both substrates, concentric rings span the drop from the center to the outer perimeter, which are marked by green dotted lines in Fig. 4-6. In addition, there are radial residues of metal that extend from the center of the drop to the outer perimeter, which are marked by red dotted lines in Fig. 4-6. Together, the features from the drop residues resemble the pattern of a spider web; henceforth, we refer to these patterns as

“oxide spider-webs.” Fig. 4–6c shows a zoomed view of the outer edge of the oxide spider-web. This image reveals the several concentric rings at the edges of the oxide spider-web; these outer rings are closely spaced relative to the rings within the drop, which are shown in Fig. 4–6d. The rings at the outer edge may be indicators for the baseline expansion effect. Meanwhile, Fig. 4–6d shows the rings on the interior of the drop may be from pinning during the advancing measurement of the drop (i.e., pinning as the drop is expanding or spreading over the substrate). Figures 4–6 a, b, and c also shows that the radial fibers extend from edge of the drop to its center, where there is a conical shaped residue of the liquid from the needle. Fig. 4–6c also shows that radial fibers are not attached to the substrate but instead pinned to the concentric rings (based slight difference in the focal planes that allow us to sharply image either the rings or fibers). This observation suggests that the radial fibers are from the exterior of the hemispherical drop that collapse onto the substrate during the receding measurement. These fibers form due to buckling of the oxide during the receding measurements, which are also visible from side-view cameras during dynamic contact angle experiments. During Regimes B and C, the oxide layer presumably maintains constant surface area on the exterior of the droplet. Consequently, the oxide forms buckles and wrinkles to accommodate the shrinking volume.<sup>[27,41]</sup> This buckling likely stiffens the surface and affects the ability of the drop to flow freely and minimize energy; accordingly, these radial fibers visible on the micrographs are ‘artifacts’ of the buckling of the hemispherical drop. Interestingly, at higher magnifications, we also observe thin fibers ( $\sim 1 \mu\text{m}$ , in diameter) of liquid metal in regions between the radial fibers and concentric rings, which are shown within green dotted lines in Fig. 4–6e.

Overall, the oxide spider-web pattern appears for all cases when pinning to a substrate occurs. The complex feature of these patterns reflects the unusual wetting and adhesion behavior

exhibited by oxide-coated liquid metals. Moreover, they provide further evidence that the liquid metal never truly recedes from the substrate because the oxide pins to the perimeter of the drop.

We reasoned that the formation of these spider-web patterns may be useful for patterning the metal either to form thin fibers or thin films of the liquid metal. To demonstrate the formation of these membranes, we perform dynamic contact angle measurements over patterned post structures. To form these structures, we pattern SU-8 using direct-write photolithography (Heidelberg  $\mu$ PG-101) into square posts with a width of  $100\ \mu\text{m}$  with a spacing of  $100\ \mu\text{m}$  between the posts in each direction. To promote pinning to the posts, we treat the posts with an perfluoro-alkyltrichlorosilane; the chlorine groups on the silane may be reacting with SU-8, which comprises of epoxy groups and thereby promotes adhesion.

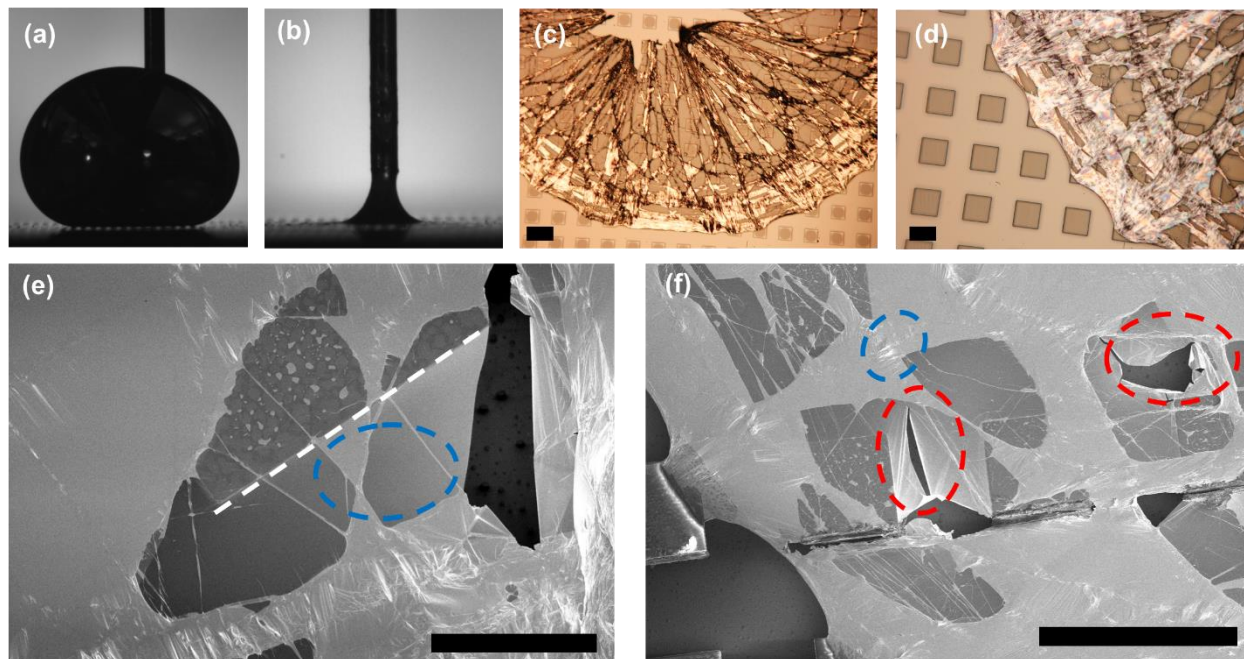


**Figure 4-7:** EGaln dynamic contact angle experiment on square posts made from SU-8 ( $100\ \mu\text{m}$  squares, with  $100\ \mu\text{m}$  spacing). (a) EGaln advancing. (b) EGaln residue at end of receding measurement (Regime C). For (a) and (b), needle diameter of  $0.39\ \text{mm}$  serves as a scale bar. (c and d) Optical micrographs of oxide residue on square posts. The radial fibers suggest a thin film or membrane of oxide suspended between posts. Scale bar is  $100\ \mu\text{m}$  (e) SEM image of oxide membrane (blue circle) between posts (white dotted line marks the edge of a post). Scale bar is  $50\ \mu\text{m}$ . (f) SEM image of oxide membrane (blue circle) that is ruptured in certain locations (red circles). Scale bar is  $200\ \mu\text{m}$ . SEM Operating Conditions (e-g): FEI Verios 460L,  $2.00\ \text{kV}$ ,  $13\ \text{pA}$ ,  $6.1\ \text{mm}$  WD with TLD detector in secondary electron mode.

**Figure 4–7a** shows side-view images from contact angle experiments of the liquid metal drop resting on the posts. The liquid does not penetrate the void space between the posts due to a combination of Laplace pressure and oxide adhesion to the edges of the posts. After receding the metal, a spider-web formation remains atop the square posts, as shown in Fig. 4–7b. At the outer edge of the drop, the oxide appears to pin above the posts (as shown in Fig. 4–7b); as a result, the drop exhibits periodic concave pattern for the outer edge of the drop (instead of a smooth curved pattern on a flat substrate). Interestingly, a thin film or membrane of a liquid forms appears between the posts. These membranes are apparent when comparing the contrast in the areas between square posts within the drop, relative to the area between square posts on the outside of the drop. Scanning electron microscopy of the samples (Fig. 4–7e and 4–7f) confirms the formation of these membranes (blue circle in Fig. 4–7e) between the posts (marked by white dotted line in Fig. 4–7e). In some areas, the membrane appears ruptured (marked by red circles in Fig. 4–7f), yet still overhanging areas between the posts. These images suggest that pinning of the liquid metal may be useful in forming thin membranes or films of metal oxides.

#### *Sliding angle measurements*

To further examine oxide adhesion to surfaces, we measure the tilt angle at which the droplet rolls. Tilt angle experiments in this work involve placing a drop of liquid metal against a test surface that rests horizontally. Next, the surface is inclined slowly and the angle at which the drop rolls is reported. As the droplet subsequently propagates across the surface, the metal will leave residue if it pins to the surface and will not in the case of ‘non-wetting’ surfaces.

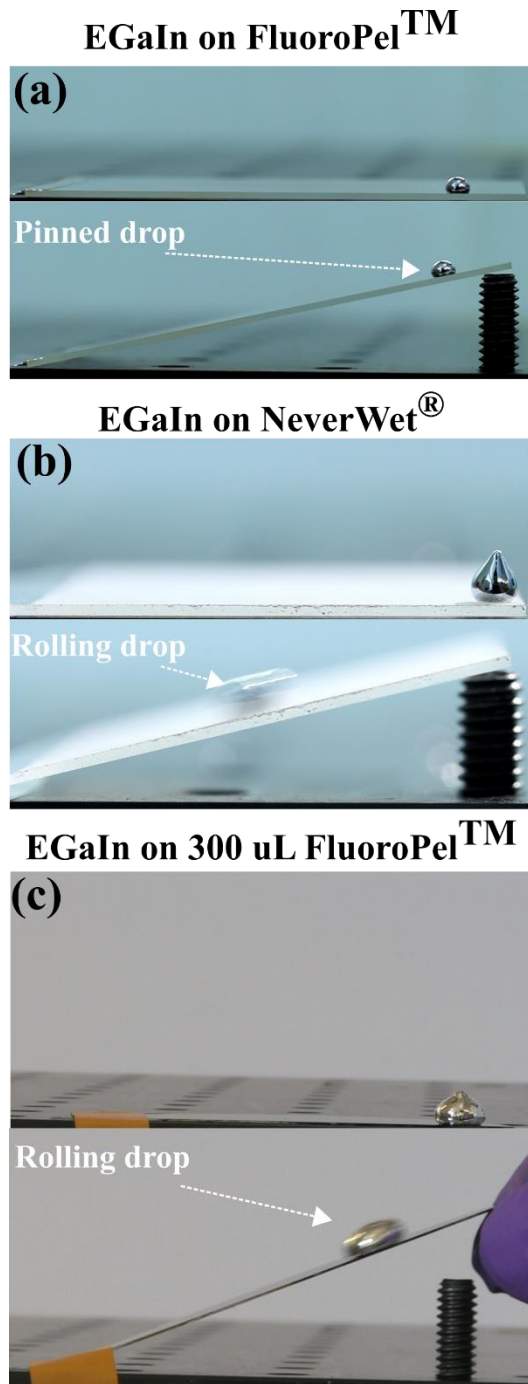


**Figure 4-8:** For sliding angle experiments (a-c), a drop of liquid metal is placed atop a surface of interest, which is oriented horizontally and subsequently tilted (via a screw under the substrate). d) (a) On FluoroPel, the drop of liquid metal remains affixed to its original placement due to pinning of the oxide (a, bottom) when tilted to  $30^\circ$ . (b) On NeverWet, the drop of liquid metal readily slides upon reaching a tilt angle of  $14.6^\circ$ . (c) Sliding angle experiment on larger droplet. (top) Large drop of EGaIn ( $\sim 300 \mu\text{L}$ ) resting on a flat and horizontal substrate (Si wafer, coated with FluoroPel™). (bottom) Drop slides down substrate when tilted to  $20^\circ$ .

**Figure 4–8** show the results of tilt angle experiments for EGaIn on (i) Fluoropel-treated glass and (ii) NeverWet coated glass. We choose these two surfaces because they both exhibit high apparent  $\theta_A$  for EGaIn ( $>140^\circ$ ) yet differ in surface roughness. As shown in Fig. 4–8a a drop of EGaIn ( $\sim 10 \mu\text{L}$ ) rests on Fluoropel-treated glass that is initially horizontal (tilt angle of zero degrees). Upon increasing the tilt angle to  $30^\circ$ , EGaIn remains pinned to its initial spot of placement (Fig. 4–8a). The metal drop remains pinned at its spot of contact all the way to complete inversion (i.e.,  $180^\circ$ ). In contrast, a drop of EGaIn on NeverWet rolls readily upon tilting to  $14.6^\circ \pm 2.3^\circ$  (Fig. 4–8b). More importantly, the metal drop does not leave behind a trail of oxide residue on the NeverWet substrate as it rolls down the incline. For the case of EGaIn on FluoroPel, the adhesion is likely due to the pinning of the oxide and yield stress of the native oxide.<sup>[25]</sup> The force of gravity cannot overcome the yield stress of the oxide, which prevents the liquid from flowing.

We hypothesize that drops of larger volume flow or roll due to the force of gravity overcoming the yield stress of the oxide. To do so, we repeat the experiments with larger volumes (100 to 300  $\mu\text{L}$ ) of EGaIn (Fig. 4–8c). Indeed, large drops of EGaIn slide along the surface of FluoroPel at high tilt angles ( $>45^\circ$ ). However, a ‘trail’ of oxide does not always form as the drop slides along the surface of FluoroPel. If a drop is placed gently onto the surface, there is no pinning and the drop will roll along the stage once tilted. Meanwhile, dispensing the drop against the surface (i.e., smearing drop) results in a trail or ‘river’ of the metal film that follows the drop as it slides down the tilted surface. In contrast to EGaIn on FluoroPel, EGaIn on NeverWet does not leave residue after rolling across the tilted sample; this result occurs irrespective of whether the drop is placed gently on the surface or smeared. These results are consistent with other work from literature that report the dependency of force of contact with the substrate with irreversible

adhesion. [41,42,57,58] In fact, recent work suggests that the oxide may rupture beyond a threshold normal force of  $\sim 4$  mN.<sup>[58]</sup>

In addition to the drop placement, several other factors may complicate the sliding angle experiments for liquid metals. The oxide exhibits a yield stress, which presumably suppresses or delays the movement or flow of the metal. Such is the case even when oxide adhesion does not occur. For example, on NeverWet, liquid metal droplets slide at  $14.6^\circ \pm 2.3^\circ$ . In comparison, water slides readily close to  $2$  to  $3^\circ$ . If gravity is the driving force for this movement, then shouldn't EGaIn, which is six times denser than water, slide at lower angles? Instead, the oxide mechanically stabilizes the metal drop and prevents the drop from moving until the force of gravity overcomes the yield stress and force at the contact line due to the balance of surface tensions. In addition, the size of the drop is an important factor for these measurements. Ideally, drops should be at or below the capillary length of the liquid ( $\lambda_c \sim 3.3$  mm for EGaIn (18  $\mu\text{L}$ ) and 2.7 mm for DI water (10  $\mu\text{L}$ )) so that gravity and surface tension are adequately balanced. Because the oxide envelopes and mechanically stabilizes the drop, it is difficult to form drops that uniformly sized. Due to the formation of oxide 'tips', the center of gravity can be manipulated in any direction. Consequently, these mechanical considerations complicate the results and subsequent interpretations of the sliding angle experiments. Similar observations regarding the geometry of the drop have been reported for water.<sup>[51]</sup> Overall, these sliding angle experiments cannot reliably predict whether the liquid metal will adhere to a given substrate.

## **Discussion**

The results presented here, along with other work in literature, suggest that traditional wetting tools (contact angle and sliding angle) are complicated for oxide-coated liquid metals. Notably, it is not meaningful to use contact angle of water or other probe fluids as a determinant

for whether oxide adhesion occurs on a surface. Likewise, a contact angle for the liquid metal can be measured because an angle can be drawn at the contact line. However, this angle is not the “contact angle” from the Young’s equation, which is a balance of forces at the contact line (not necessarily only surface tension). In the case of advancing liquid metal, the contact angle appears due to the surface tension of the metal and the mechanical force required to yield the oxide and is therefore always large. During the receding measurement, the pinning of the oxide and sagging of drop causes the drop to change from a convex (i.e., spherical or hemispherical drop) to a concave curvature. During this process, the oxide on the exterior of the drop collapses onto the substrate as further liquid within the drop is removed. Accordingly, the measured angle during receding measurement is not reflective of the local variation in the surface energy of a substrate, but instead altered by pinning of the oxide and sagging of the drop.

The purpose of this work is not to discourage the use of these tools; they do indeed provide route to arrive at a binary conclusion: either adhesion occurs on a substrate or not. This determination is important from a practical standpoint. Instead, we caution researchers to not utilize these measurements as a quantitative tool.

Moreover, this work encourages new methods to quantitatively and more accurately assess the wetting and adhesion of oxide-coated liquid metals. One promising tool is to utilize either a tensiometer <sup>[47,58]</sup> or surface force apparatus <sup>[59,60]</sup> to measure pull-off forces. These tools are available commercially and can also be custom-built with the careful choice of load cells and stage actuators. Concurrently, utilizing optical microscopy from side-view as well as bottom-view (inverted) are necessary for observing the interface during the measurement; in particular, the imaging is necessary for determining whether the oxide is ruptured upon contact. Moreover, the simultaneous use of microscopy (to measure the change in contact area) with pull-off forces would

be necessary to utilize JKR theory or other theories for quantifying adhesion.<sup>[58]</sup> Similarly, capillary meniscus dynamometry (CMD) may also provide similar forces.<sup>[61]</sup>

One important consideration for pull-off forces, which has been reported in literature, is whether the oxide ruptures during the experiment.<sup>[58]</sup> If the oxide is not ruptured, then the pull-force will indicate the adhesion between the native oxide-skin and the substrate. However, in most cases, the oxide ruptures and a new oxide presumably forms. For practical considerations, it may be important to rupture the oxide during the measurement (i.e., pre-load the drop). In addition, rheology and tribology measurements may be useful for examining the metal under conditions of shear (i.e., microfluidics, direct-write printing).<sup>[62]</sup> The friction of a substrate may play an important role in whether an oxide ruptures under the shear and thus these tools may be useful for assessing this scenario.

*Because the adhesion of the metal can be either useful or problematic, depending on the application or end-use, it is critical to understand how to control its adhesion. Therefore, what drives adhesion and unusual wetting behavior of these liquid metal to other surfaces?*

In addition, the adhesion may be driven by intermolecular forces between the substrate and liquid metal. The presence of an oxide and an underlying metal that can oxidize upon exposure further complicate the potential interactions. In addition, the surface of the liquid metal may be charged. Thus, electrostatic attraction (if the surface is positively charged) may be possible route to adhesion or patterning of the metal.<sup>[14,63–65]</sup> A substrate does not need to hold charge across its entire surface to promote or cause adhesion. The micrographs presented in Fig. 4–6 and 4–7 suggest that pinning occurs in certain locations. Therefore, localized charges may be sufficient to induce pinning and subsequently leave behind residues of the drop. Another possibility that leads to adhesion is the presence of van der Waals (vdW) forces; the presence of oxygen from the oxide

or hydroxyl groups in some cases may allow for vdW forces between the liquid drop and substrate. From a practical consideration, non-uniformity in the chemical composition or morphology of a given surface or coating may be sufficient to either cause pinning or expose an underlying ‘adhesive’ surfaces (i.e., Si wafer or glass slide).

Another possibility for the adhesion may be the formation of chemical bonds between the metal drop and the substrate. For the case of glass, silicones, and silicates, the oxygen from the metal oxide may react with the surface hydroxyl group. For metal substrates, alloying and interatomic diffusion are the likely driving force for the ‘reactive’ wetting process.

## **Conclusions**

This work cautions the use of conventional contact angle experiments for liquid metals that possess surface oxides. From dynamic contact angle measurements, advancing angle is high due to its larger surface tension and the need to rupture the oxide during expansion; however, adhesion still occurs to flat substrates. During the receding measurements, the droplet pins to the substrate and never truly recedes from the substrate (hence, does not reach an equilibrium contact angle). Moreover, the oxide ‘skin’ maintains a constant surface area and loses tension as the volume decreases. During this process, the contact line of the drop expands outward due to sagging of the drop. Thereafter, a residue of the collapsed oxide remains on the substrate. The formation of buckles and wrinkles, in addition to the baseline expansion, suggests that the surface tension of these drops is not isotropic, which further complicates the interfacial behavior of these liquids. Similarly, sliding angle experiments are not useful either due to adhesion of the drop as well as the yield stress of the oxide. The results from these experiments differ based on how a drop is placed onto a surface.

Ultimately, because of the presence of an oxide ‘skin’, these angles are not in fact “contact angles” based on Young’s angle. Overall, these results suggest that the numerical values of conventional tools used to assess wetting should not be taken at face value. Instead, these measurements provide only a binary response: either oxide adhesion occurs or not when the native oxide is ruptured. Alternatively, pull-off force measurements may serve as more reliable tools for quantifying adhesion; however, challenges remain due to the properties of the oxide skin.

### **Acknowledgements**

I would like to thank Chujun Ni, K. Alexander Persson, Mohanad Alsafatwi for help with collecting contact angle measurements of liquid metals. Thanks for your hard work and attention to detail with these measurements. I also would like to thank Mr. Dishit Parekh, Prof. Jan Genzer, Prof. Jason Patrick, and Prof. Hong Zhao for helpful discussions and guidance on wetting and contact angle measurements. Finally, thanks to Mr. Greg Allion of NNF for help using the Heidelberg direct-write lithograph tool.

## References

- (1) Daeneke, T.; Khoshmanesh, K.; Mahmood, N.; Castro, I. A. de; Esrafilzadeh, D.; Barrow, S. J.; Dickey, M. D.; Kalantar-zadeh, K. Liquid Metals: Fundamentals and Applications in Chemistry. *Chem. Soc. Rev.* **2018**.
- (2) Dickey, M. D. Stretchable and Soft Electronics Using Liquid Metals. *Adv. Mater.* **2017**, 1606425.
- (3) Minev, I. R.; Musienko, P.; Hirsch, A.; Barraud, Q.; Wenger, N.; Moraud, E. M.; Gandar, J.; Capogrosso, M.; Milekovic, T.; Asboth, L.; et al. Electronic Dura Mater for Long-Term Multimodal Neural Interfaces. *Science* **2015**, 347 (6218), 159–163.
- (4) Yang, T.; Kwon, B.; Weisensee, P. B.; Kang, J. G.; Li, X.; Braun, P.; Miljkovic, N.; King, W. P. Millimeter-Scale Liquid Metal Droplet Thermal Switch. *Appl. Phys. Lett.* **2018**, 112 (6), 63505.
- (5) Zhu, J. Y.; Tang, S.-Y.; Khoshmanesh, K.; Ghorbani, K. An Integrated Liquid Cooling System Based on Galinstan Liquid Metal Droplets. *ACS Appl. Mater. Interfaces* **2016**, 8 (3), 2173–2180.
- (6) Joshipura, I. D.; Ayers, H. R.; Majidi, C.; Dickey, M. D. Methods to Pattern Liquid Metals. *J. Mater. Chem. C* **2015**, 3, 3834–3841.
- (7) Khondoker, M. A. H.; Sameoto, D. Fabrication Methods and Applications of Microstructured Gallium Based Liquid Metal Alloys. *Smart Mater. Struct.* **2016**, 25 (9), 93001.
- (8) Trlica, C.; Parekh, D. P.; Panich, L.; Ladd, C.; Dickey, M. D. 3-D Printing of Liquid Metals for Stretchable and Flexible Conductors. In *Proceedings of SPIE*; 2014; Vol. 9083, p 90831D–90831D–10.
- (9) Parekh, D. P.; Ladd, C.; Panich, L.; Moussa, K.; Dickey, M. D. 3D Printing of Liquid Metals as Fugitive Inks for Fabrication of 3D Microfluidic Channels. *Lab. Chip* **2016**, 16 (10), 1812–1820.
- (10) Boley, J. W.; White, E. L.; Chiu, G. T.-C.; Kramer, R. K. Direct Writing of Gallium-Indium Alloy for Stretchable Electronics. *Adv. Funct. Mater.* **2014**, 24 (23), 3501–3507.
- (11) Mohammed, M. G.; Kramer, R. All-Printed Flexible and Stretchable Electronics. *Adv. Mater.* **2017**, 29 (19).
- (12) Ilyas, N.; Cook, A.; Tabor, C. E. Designing Liquid Metal Interfaces to Enable Next Generation Flexible and Reconfigurable Electronics. *Adv. Mater. Interfaces* n/a-n/a.
- (13) Eaker, C. B.; Dickey, M. D. Liquid Metal Actuation by Electrical Control of Interfacial Tension. *Appl. Phys. Rev.* **2016**, 3 (3), 31103.
- (14) Holcomb, S.; Brothers, M.; Diebold, A.; Thatcher, W.; Mast, D.; Tabor, C.; Heikenfeld, Jason. Oxide-Free Actuation of Gallium Liquid Metal Alloys Enabled by Novel Acidified Siloxane Oils. *Langmuir* **2016**.
- (15) Gough, R. C.; Morishita, A. M.; Dang, J. H.; Hu, W.; Shiroma, W. A.; Ohta, A. T. Continuous Electrowetting of Non-Toxic Liquid Metal for RF Applications. *IEEE Access* **2014**, 2, 874–882.
- (16) Nicholas, M. G.; Old, C. F. Liquid Metal Embrittlement. *J. Mater. Sci.* **1979**, 14 (1), 1–18.
- (17) Pereiro-Lopez, E.; Ludwig, W.; Bellet, D. Discontinuous Penetration of Liquid Ga into Grain Boundaries of Al Polycrystals. *Acta Mater* **2004**, 52 (2), 321–332.
- (18) Svirbely, W. J.; Selis, S. M. The Gallium-Indium System. *J. Phys. Chem.* **1954**, 58 (1), 33–35.

- (19) Kim, J.-H.; Kim, S.; So, J.-H.; Kim, K.; Koo, H.-J. Cytotoxicity of Gallium–Indium Liquid Metal in Aqueous Environment. *ACS Appl. Mater. Interfaces* **2018**.
- (20) Filon, F. L. Penetration of Metals Through the Skin Barrier. In *Metal Allergy*; Springer, Cham, 2018; pp 67–74.
- (21) Lu, Y.; Hu, Q.; Lin, Y.; Pacardo, D. B.; Wang, C.; Sun, W.; Ligler, F. S.; Dickey, M. D.; Gu, Z. Transformable Liquid-Metal Nanomedicine. *Nat. Commun.* **2015**, *6*, 10066.
- (22) Yan, J.; Lu, Y.; Chen, G.; Yang, M.; Gu, Z. Advances in Liquid Metals for Biomedical Applications. *Chem. Soc. Rev.* **2018**.
- (23) Carli, R.; Bianchi, C. L. XPS Analysis of Gallium Oxides. *Appl. Surf. Sci.* **1994**, *74* (1), 99–102.
- (24) Shallenberger, J. R.; Cole, D. A.; Novak, S. W.; Moore, R. L.; Edgell, M. J.; Smith, S. P.; Hitzman, C. J.; Kirchhoff, J. F.; Principe, E.; Biswas, S.; et al. Oxide Thickness Determination by XPS, AES, SIMS, RBS and TEM. In *1998 International Conference on Ion Implantation Technology Proceedings*; 1999; Vol. 1, pp 79–82 vol.1.
- (25) Dickey, M. D.; Chiechi, R. C.; Larsen, R. J.; Weiss, E. A.; Weitz, D. A.; Whitesides, G. M. Eutectic Gallium-Indium (EGaIn): A Liquid Metal Alloy for the Formation of Stable Structures in Microchannels at Room Temperature. *Adv. Funct. Mater.* **2008**, *18* (7), 1097–1104.
- (26) Chiechi, R. C.; Weiss, E. A.; Dickey, M. D.; Whitesides, G. M. Eutectic Gallium–Indium (EGaIn): A Moldable Liquid Metal for Electrical Characterization of Self-Assembled Monolayers. *Angew. Chem. Int. Ed.* **2008**, *47* (1), 142–144.
- (27) Ladd, C.; So, J.-H.; Muth, J.; Dickey, M. D. 3D Printing of Free Standing Liquid Metal Microstructures. *Adv. Mater.* **2013**, *25* (36), 5081–5085.
- (28) Lin, Y.; Ladd, C.; Wang, S.; Martin, A.; Genzer, J.; Khan, S. A.; Dickey, M. D. Drawing Liquid Metal Wires at Room Temperature. *Extreme Mech. Lett.* **2016**, *7*, 55–63.
- (29) Shay, T.; Velev, O.; Dickey, M. D. Soft Electrodes Combining Hydrogel and Liquid Metal. *Soft Matter* **2018**.
- (30) So, J.; Koo, H.; Dickey, M. D.; Velev, O. D. Ionic Current Rectification in Soft-Matter Diodes with Liquid-Metal Electrodes. *Adv. Funct. Mater.* **2012**, *22* (3), 625–631.
- (31) Koo, H.; So, J.; Dickey, M. D.; Velev, O. D. Towards All-Soft Matter Circuits: Prototypes of Quasi-Liquid Devices with Memristor Characteristics. *Adv. Mater.* **2011**, *23* (31), 3559–3564.
- (32) Yamaguchi, A.; Mashima, Y.; Iyoda, T. Reversible Size Control of Liquid-Metal Nanoparticles under Ultrasonication. *Angew. Chem.* **2015**, n/a-n/a.
- (33) Lin, Y.; Cooper, C.; Wang, M.; Adams, J. J.; Genzer, J.; Dickey, M. D. Handwritten, Soft Circuit Boards and Antennas Using Liquid Metal Nanoparticles. *Small* **2015**, *11* (48), 6397–6403.
- (34) Thelen, J.; Dickey, M. D.; Ward, T. A Study of the Production and Reversible Stability of EGaIn Liquid Metal Microspheres Using Flow Focusing. *Lab. Chip* **2012**, *12* (20), 3961–3967.
- (35) Tang, S.-Y.; Joshipura, I. D.; Lin, Y.; Kalantar-Zadeh, K.; Mitchell, A.; Khoshmanesh, K.; Dickey, M. D. Liquid-Metal Microdroplets Formed Dynamically with Electrical Control of Size and Rate. *Adv. Mater.* **2016**, *28* (4), 604–609.
- (36) Cademartiri, L.; Thuo, M. M.; Nijhuis, C. A.; Reus, W. F.; Tricard, S.; Barber, J. R.; Sodhi, R. N. S.; Brodersen, P.; Kim, C.; Chiechi, R. C.; et al. Electrical Resistance of Ag-

- TS-S(CH<sub>2</sub>)(n-1)CH<sub>3</sub>//Ga<sub>2</sub>O<sub>3</sub>/EGaIn Tunneling Junctions. *J. Phys. Chem. C* **2012**, *116* (20), 10848–10860.
- (37) Carey, B. J.; Ou, J. Z.; Clark, R. M.; Berean, K. J.; Zavabeti, A.; Chesman, A. S. R.; Russo, S. P.; Lau, D. W. M.; Xu, Z.-Q.; Bao, Q.; et al. Wafer-Scale Two-Dimensional Semiconductors from Printed Oxide Skin of Liquid Metals. *Nat. Commun.* **2017**, *8*, 14482.
- (38) Palleau, E.; Reece, S.; Desai, S. C.; Smith, M. E.; Dickey, M. D. Self-Healing Stretchable Wires for Reconfigurable Circuit Wiring and 3D Microfluidics. *Adv. Mater.* **2013**, *25* (11), 1589–1592.
- (39) Chu, K.; Song, B. G.; Yang, H.-I.; Kim, D.-M.; Lee, C. S.; Park, M.; Chung, C.-M. Smart Passivation Materials with a Liquid Metal Microcapsule as Self-Healing Conductors for Sustainable and Flexible Perovskite Solar Cells. *Adv. Funct. Mater.* **2016**, *28* (22), 1800110.
- (40) Blaiszik, B. J.; Jones, A. R.; Sottos, N. R.; White, S. R. Microencapsulation of Gallium–indium (Ga–In) Liquid Metal for Self-Healing Applications. *J. Microencapsul.* **2014**, *31* (4), 350–354.
- (41) Doudrick, K.; Liu, S.; Mutunga, E. M.; Klein, K. L.; Damle, V.; Varanasi, K. K.; Rykaczewski, K. Different Shades of Oxide: From Nanoscale Wetting Mechanisms to Contact Printing of Gallium-Based Liquid Metals. *Langmuir* **2014**, *30* (23), 6867–6877.
- (42) Ye, Z.; Lum, G. Z.; Song, S.; Rich, S.; Sitti, M. Phase Change of Gallium Enables Highly Reversible and Switchable Adhesion. *Adv. Mater.* **2016**, *28* (25), 5088–5092.
- (43) Regan, M. J.; Tostmann, H.; Pershan, P. S.; Magnussen, O. M.; DiMasi, E.; Ocko, B. M.; Deutsch, M. X-Ray Study of the Oxidation of Liquid-Gallium Surfaces. *Phys. Rev. B Condens. Matter* **1997**, *55* (16), 10786–10790.
- (44) Regan, M. J.; Pershan, P. S.; Magnussen, O. M.; Ocko, B. M.; Deutsch, M.; Berman, L. E. X-Ray Reflectivity Studies of Liquid Metal and Alloy Surfaces. *Phys. Rev. B* **1997**, *55* (23), 15874–15884.
- (45) Law, K.-Y.; Zhao, H. *Surface Wetting - Characterization, Contact Angle, and Fundamentals*; Springer, 2016.
- (46) Gao, L.; McCarthy, T. J. Wetting 101°. *Langmuir* **2009**, *25* (24), 14105–14115.
- (47) Samuel, B.; Zhao, H.; Law, K.-Y. Study of Wetting and Adhesion Interactions between Water and Various Polymer and Superhydrophobic Surfaces. *J. Phys. Chem. C* **2011**, *115* (30), 14852–14861.
- (48) Extrand, C. W.; Kumagai, Y. An Experimental Study of Contact Angle Hysteresis. *J. Colloid Interface Sci.* **1997**, *191* (2), 378–383.
- (49) Gao, L.; McCarthy, T. J. Contact Angle Hysteresis Explained. *Langmuir* **2006**, *22* (14), 6234–6237.
- (50) Khan, M. R.; Eaker, C. B.; Bowden, E. F.; Dickey, M. D. Giant and Switchable Surface Activity of Liquid Metal via Surface Oxidation. *Proc. Natl. Acad. Sci.* **2014**, *111* (39), 14047–14051.
- (51) Krasovitski, B.; Marmur, A. Drops Down the Hill: Theoretical Study of Limiting Contact Angles and the Hysteresis Range on a Tilted Plate. *Langmuir* **2005**, *21* (9), 3881–3885.
- (52) Extrand, C. W. Origins of Wetting. *Langmuir* **2016**, *32* (31), 7697–7706.
- (53) Delplanque, A.; Henry, E.; Lautru, J.; Leh, H.; Buckle, M.; Nogues, C. UV/Ozone Surface Treatment Increases Hydrophilicity and Enhances Functionality of SU-8 Photoresist Polymer. *Appl. Surf. Sci.* **2014**, *314*, 280–285.
- (54) Law, K.-Y. Definitions for Hydrophilicity, Hydrophobicity, and Superhydrophobicity: Getting the Basics Right. *J. Phys. Chem. Lett.* **2014**, *5* (4), 686–688.

- (55) Vaccari, L.; B. Allan, D.; Sharifi-Mood, N.; R. Singh, A.; L. Leheny, R.; J. Stebe, K. Films of Bacteria at Interfaces: Three Stages of Behaviour. *Soft Matter* **2015**, *11* (30), 6062–6074.
- (56) D. Cramer, A.; Gambinossi, F.; Wischerhoff, E.; Laschewsky, A.; Miller, R.; K. Ferri, J. Flexible Thermo-responsive Nanomembranes at the Aqueous–air Interface. *Chem. Commun.* **2015**, *51* (5), 877–880.
- (57) Kramer, R. K.; Boley, J. W.; Stone, H. A.; Weaver, J. C.; Wood, R. J. Effect of Microtextured Surface Topography on the Wetting Behavior of Eutectic Gallium–Indium Alloys. *Langmuir* **2014**, *30* (2), 533–539.
- (58) Yunusa, M.; Amador, G. J.; Drotlef, D.-M.; Sitti, M. Wrinkling Instability and Adhesion of a Highly Bendable Gallium Oxide Nanofilm Encapsulating a Liquid-Gallium Droplet. *Nano Lett.* **2018**.
- (59) Roberts, P.; Pilkington, G. A.; Wang, Y.; Frechette, J. A Multifunctional Force Microscope for Soft Matter with in Situ Imaging. *Rev. Sci. Instrum.* **2018**, *89* (4), 43902.
- (60) Israelachvili, J. N. Thin Film Studies Using Multiple-Beam Interferometry. *J. Colloid Interface Sci.* **1973**, *44* (2), 259–272.
- (61) Danov, K. D.; Stanimirova, R. D.; Kralchevsky, P. A.; Marinova, K. G.; Alexandrov, N. A.; Stoyanov, S. D.; Blijdenstein, T. B. J.; Pelan, E. G. Capillary Meniscus Dynamometry – Method for Determining the Surface Tension of Drops and Bubbles with Isotropic and Anisotropic Surface Stress Distributions. *J. Colloid Interface Sci.* **2015**, *440*, 168–178.
- (62) Scherge, M.; Gorb, S. *Biological Micro- and Nanotribology: Nature's Solutions*; NanoScience and Technology; Springer-Verlag: Berlin Heidelberg, 2001.
- (63) Diebold, A. V.; Watson, A. M.; Holcomb, S.; Tabor, C.; Mast, D.; Dickey, M. D.; Heikenfeld, J. Electrowetting-Actuated Liquid Metal for RF Applications. *J. Micromechanics Microengineering* **2017**, *27* (2), 25010.
- (64) Wan, Z.; Zeng, H.; Feinerman, A. Reversible Electrowetting of Liquid-Metal Droplet. *J. Fluids Eng.* **2007**, *129* (4), 388–394.
- (65) Liu, T.; Sen, P.; Kim, C. J. Characterization of Nontoxic Liquid-Metal Alloy Galinstan for Applications in Microdevices. *J. Microelectromechanical Syst.* **2012**, *21* (2), 443–450.

**CHAPTER 5**  
**STRETCHABLE BIOELECTRONICS—**  
**CURRENT AND FUTURE<sup>2</sup>**

---

<sup>2</sup> This work is published in *MRS Bulletin* in 2017 with Mickey Finn III, Siew Ting Melissa Tan, Michael D. Dickey, and Darren J. Lipomi as co-contributors. Full citation below:  
Joshipura, I. D., Finn, M., Tan, S. T. M., Dickey, M. D. & Lipomi, D. J. Stretchable bioelectronics—Current and future. *MRS Bulletin* **42**, 960–967 (2017).

## **Abstract**

Materials used in wearable and implantable electronic devices should match the mechanical properties of biological tissues, which are inherently soft and deformable. In comparison to conventional rigid electronics, soft bioelectronics can provide accurate and real-time monitoring of physiological signals, improve comfort, and enable altogether new modalities for sensing. This article highlights recent progress, identifies technical challenges, and offers possible solutions for the emerging field of stretchable bioelectronics. We organize the content into three topical categories: (1) biological integration of soft electronic materials, (2) materials and mechanics, and (3) soft robotics. Finally, we conclude this article with a discussion on the outlook of the field and future challenges.

## **Introduction**

Materials used in wearable and implantable bioelectronic devices need to be soft and deformable to form intimate mechanical interfaces with biological tissue to enable effective biochemical and physical sensing, delivery of localized therapeutics, and restoration of damaged tissues.<sup>1-3</sup> These types of deformable sensors and power sources, combined with soft actuators, permit soft robotic devices that can both “feel” and move, and could lead to integrated wearable devices that can provide tactile or kinesthetic cues to the user.

The content of this article is based on scientific progress presented and discussed at the MRS/Kavli Future of Materials Workshop on “Flexible and Stretchable Bioelectronics,” which was held after the 2017 MRS Spring Meeting. This article covers biological integration of soft electronic materials, materials and mechanics, and soft robotics, and concludes with a discussion on the outlook and future challenges associated with the field. Bioelectronics is admittedly a large

field with a long history. We restrict our attention, in the interest of space, to bioelectronic devices whose key characteristic is mechanical deformability, which were the subject of this workshop.

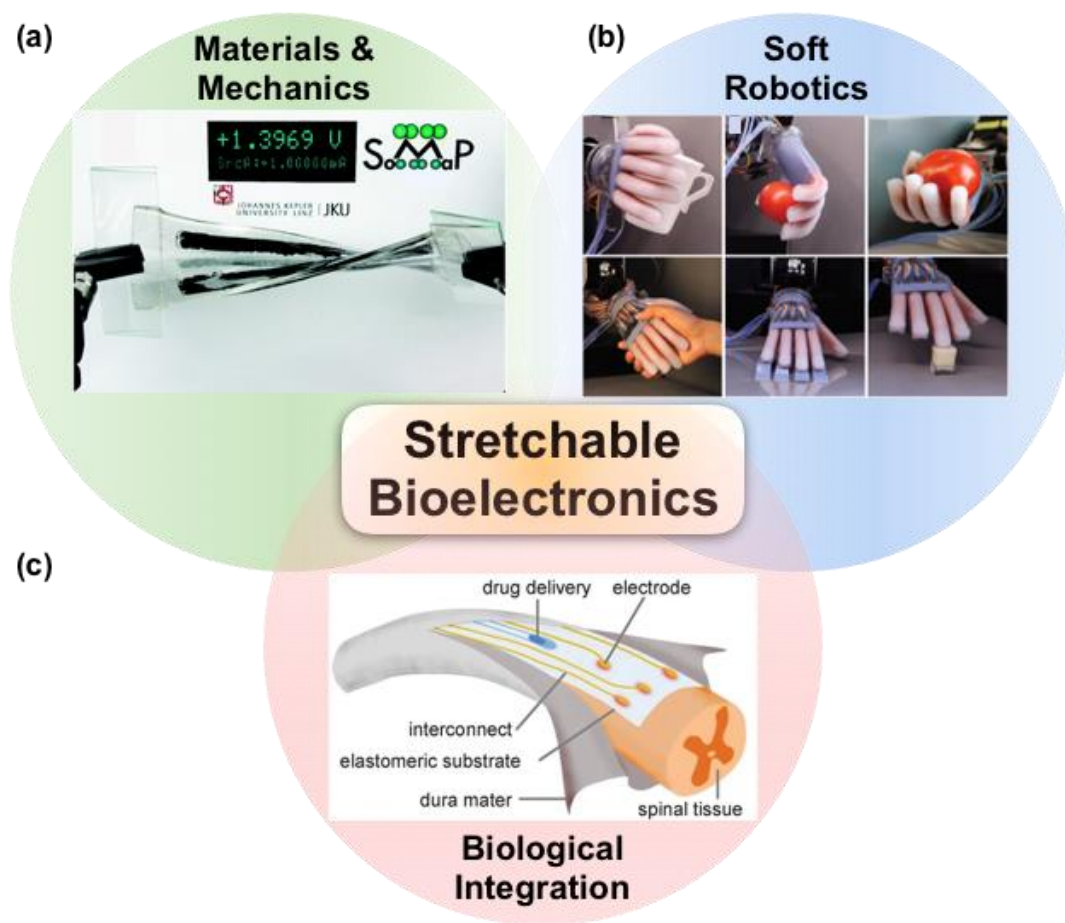


**Figure 5-1:** A Venn diagram shows the organization of stretchable bioelectronics into three categories: (a) materials and mechanics, (b) soft robotics, and (c) biological integration. (a) Illustration of stretchable rechargeable battery using hydrogel and conductive paste. Reproduced with permission from Reference 13. © 2013 Royal Society of Chemistry. (b) Soft robotic gripper that uses an optical signal feedback to sense and handle soft and fragile objects. Reprinted with permission from Reference 69. © 2016 AAAS. (c) Soft device, called “e-dura,” which is implanted into damaged spinal tissue to restore its function. The device consists of a patterned microfluidic device that enables drug delivery and soft and flexible electrodes to transmit an electrical signal and excite surrounding nervous tissue. Reprinted with permission from Reference 15. © 2015 AAAS. Rigid to Stretchable: Challenges.

There are several challenges associated with creating stretchable bioelectronics, such as unwanted changes in the electrical properties resulting from deformation, mechanical mismatches between materials, integrating sources of power, and environmental stability. To elaborate on the first of these challenges, most materials exhibit an incidental change in electrical conductivity in response to strain and change in temperature—stretching an isotropic conductor produces an

increase in resistance. Likewise, most materials have a nonzero temperature coefficient of resistance. Therefore, a challenge in stretchable electronics is to produce stretchable wiring whose resistance is invariant with strain and temperature.<sup>4,5</sup> Materials intended to have a strain response can measure voluntary motions, including facial expressions and involuntary motions, such as pulse and respiration.<sup>6-9</sup> Other mechanisms of detecting motion and pressure include capacitive sensing and resonant frequencies of patterned metals. Wearable devices may also measure other physical signals such as forms of electromagnetic radiation (i.e., visible light and UV radiation).<sup>10-12</sup> Finally, these materials may be utilized as wearable or implantable energy harvesting devices, such as a stretchable battery (as shown in **Figure 1a**).<sup>13</sup>

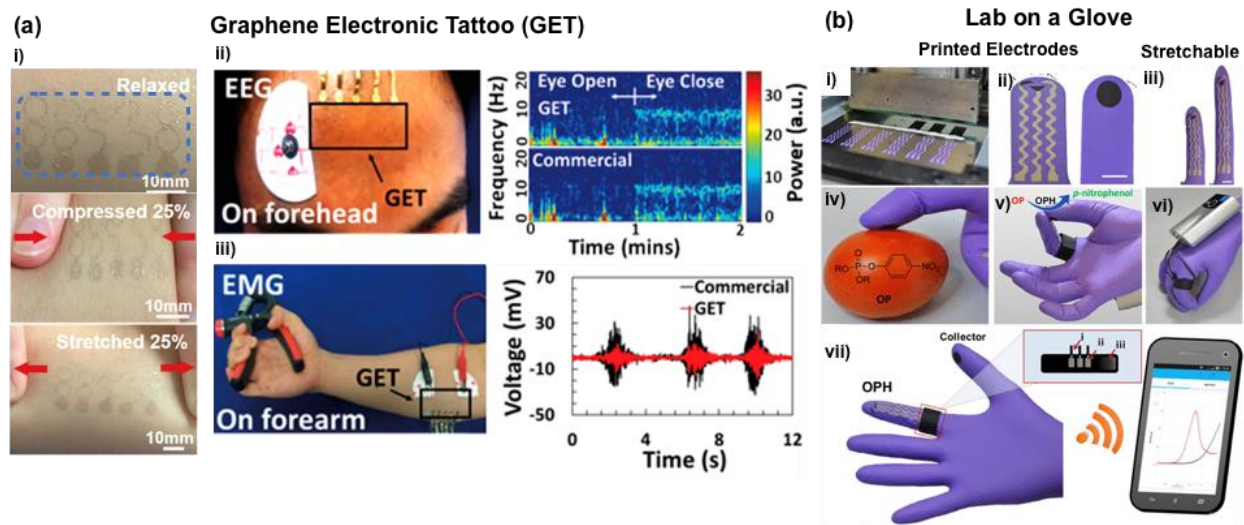


**Figure 5-2:** (a) Graphene is printed onto a thin, flexible polymer to form (i) a transparent electronic tattoo. The serpentine pattern of the graphene traces allows it to function while undergoing deformations. The top image shows the tattoo in its relaxed state. Due to the elasticity of the tattoo and skin, the tattoo can function while being compressed (middle) or stretched (bottom). The tattoo sensor can monitor physiological activities, (ii) electroencephalogram (EEG), (iii) electromyogram (EMG). The EEG sensor is placed on the forehead (ii, left) to measure neurophysiological activities such as (right) blinking of eyelids. (iii, left) The EMG sensor is placed on the forearm to show sensing of muscle movements, such as hand clenching. A common commercial sensor is placed nearby the tattoo sensor to benchmark the performance. (Right) The accuracy of the tattoo sensors and commercial sensors are similar. Adapted with permission from Reference 23. © 2017 American Chemical Society. (b[i]) Three individual electrodes are screen printed onto a nitrile glove to (ii) serve as a traditional three-electrode electrochemical cell (ii). Scale bar = 10 mm. (Left, ii) The three electrodes are printed onto the index finger. (Right, ii) The thumb contains a collector pad that accumulates or gathers the chemical or biomarker of interest. The collector pad contains immobilized enzyme (OPH) that reacts with the biomarkers. (iii) The electrodes are printed on a glove, and the sensors are flexible and stretchable up to 50% of its original length. Scale bar = 10 mm. The electrodes sense electrochemical reactions with (iv) biomarkers and (v) chemicals based on a change in current. (vi) A portable potentiostat is placed onto the back of the hand and wirelessly transmits a voltamogram to (vii) a mobile device. The inset of (vii) shows (I and II) the three electrode pins that are placed on (III) an adjustable Velcro ring. Adapted with permission from Reference 34. © 2017 American Chemical Society. Note: OP, organophosphate; OPH, organophosphate hydrolyase; R, any chemical group containing a hydrocarbon that is attached to the chemical functional group.

Biological integration refers to wearable and implantable devices that monitor physiological activities,<sup>14–16</sup> either sense or regulate biochemical and metabolic processes,<sup>17</sup> or deliver drugs.<sup>18–21</sup> Biological systems also provide inspiration for new sensing and actuating mechanisms. For example, mechanoreceptors in the skin convert pressure into an AC signal that is registered in the brain as touch. Similarly, this concept has been demonstrated using printed organic pressure sensors and other circuit elements on thin plastic foils. Using techniques of optogenetics, it was possible to transmit this signal to simulate neurons *in vitro*. Sensors from this

work and others show promise for integrating touch sensation and feedback to damaged limbs or prosthetics.<sup>15,22</sup> An example of a flexible device implanted into spinal tissue is shown in Figure 1c.

Devices worn directly on the body need to be thin (or inherently soft) to conform to the topography of the skin. Devices meeting this criterion have been called epidermal electronics.<sup>14</sup> Such conformal devices can measure a range of physical and chemical signals. Epidermal electronic devices also contain antennas that transmit data to mobile phones and computers to provide instantaneous and real-time monitoring.<sup>2</sup> Thin and transparent devices worn directly atop the skin are also called electronic tattoos. **Figure 2a** shows electronic tattoos made from graphene that monitor heart and brain activity, the results of which were on par with commercial sensors.<sup>23</sup> MC-10, Inc., which commercializes epidermal electronics, recently announced a disposable patch that uses UV-sensitive dyes to monitor sun exposure; this patch is made in partnership with L’Oreal.<sup>12</sup> The patch wirelessly transmits data to the wearer’s mobile phone. Closely related to epidermal electronics is imperceptible electronics.<sup>24,25</sup> While the difference between these terms is not distinct, the latter emphasizes the mechanical invisibility of devices when worn on the skin. Recently, the development of “imperceptible electronics,” which compose organic circuitry on ultrathin plastic foils (~2  $\mu\text{m}$ ), allows such devices to function even under bending radii of <50  $\mu\text{m}$ .<sup>24,25</sup>

While sensors of physical stimuli have a ubiquitous presence in the wearable electronics community, a new vein of research is emerging that focuses on sensing chemical signals, including biochemical markers. For example, collecting and sensing analytes in sweat<sup>26–28</sup> or blood,<sup>29</sup> in a minimally invasive or noninvasive manner, are growing in popularity. Similarly, sensing volatile organic compounds and toxic gases is important for monitoring environmental health.<sup>30,31</sup> Some

recent encouraging results include organic thin films containing catalytic particles that are capable of detecting disease markers in the breath.<sup>32</sup>

Alternatively, electrochemical reactions can be useful for monitoring levels of glucose, alcohol, and electrolytes.<sup>33</sup> One approach involves screen printing conductive inks and pastes onto textiles or thin polymers to form electronic tattoos.<sup>23</sup> Devices that are integrated with textiles can withstand numerous laundry cycles of washing and drying. The printed material consists of carbon or silver electrodes with immobilized enzymes to sense compounds of interest. Similarly, Figure 2b demonstrates a “lab-on-glove” system—a glove with printed sensors to detect harmful chemical agents or allergens, or identify different objects.<sup>34</sup> There is hope that such soft and stretchable electrochemical sensors may eventually interface directly with the nervous system.<sup>13,15,35</sup>

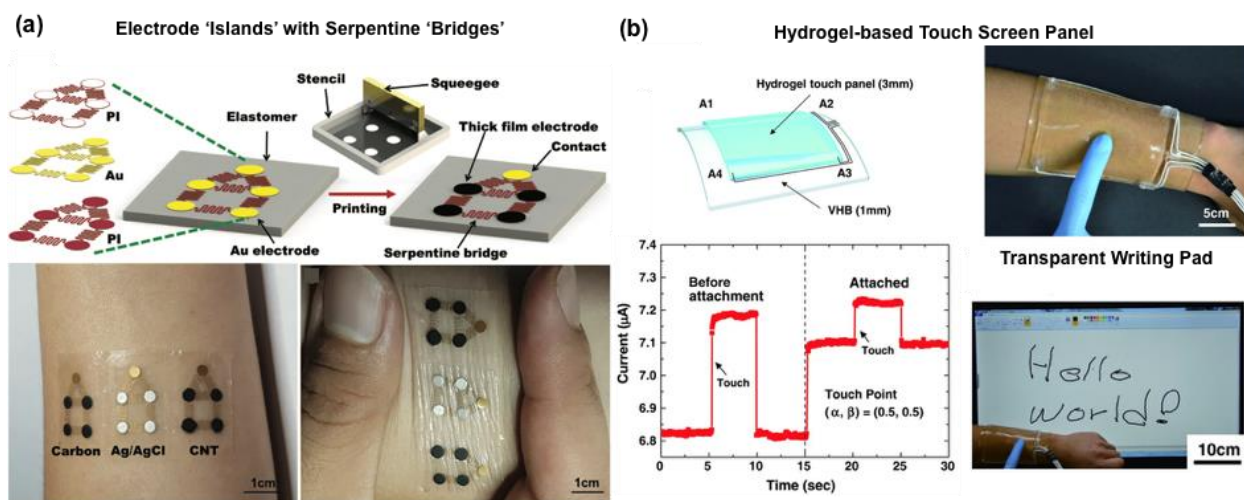


**Figure 5-3:** Materials and mechanics. (a) (Top) A wearable tattoo sensor is composed of screen-printed metal contacts (islands) with serpentine-shaped bridges. (Bottom, left) Several types of conductor materials (carbon, Ag/AgCl, and CNT) can be screen printed. (Bottom, right) The serpentine bridges serve as stretchable interconnects. Adapted with permission from Reference 39. © 2017 Wiley. (b) A hydrogel piece mounted on (top, left) of 3M very high bond (VHB) film is utilized as a (top, right) wearable transparent, conductive touch screen. The touch sensing mechanism works based on change in (bottom, left) current. The authors demonstrate a (bottom, right) touch-screen for writing, playing music (not shown), or games (not shown). Reprinted with permission from Reference 50. © 2016 AAAS. Note: CNT, carbon nanotube; A1–A4, separate current collectors that provide the location and sensitivity of the touch point;  $\alpha$ ,  $\beta$ , normalized Cartesian coordinates on the hydrogel touch panel.

## Materials and mechanics

The development of materials that combine state-of-the-art electronic properties with mechanical softness, along with bio- compatibility, is central to stretchable bioelectronics. Elastomers (e.g., silicone rubber, thermoplastic polyurethane, and natural silk fibroin) and hydrogels (e.g., polyacrylamide) often comprise the bulk of stretchable bioelectronics devices because they are soft (Young's modulus <10 MPa) and easy to process. There have been considerable efforts to develop soft conductive materials that are also highly stretchable, including a conductor with up to 1000% stretchability.<sup>36</sup> For most biological applications, however, stretchability commensurate with that of human skin (strain  $\leq 50\%$ ) is probably sufficient. Thus, the remarkable progress made in achieving high stretchability in conductive composites suggests that other goals may take priority. These goals include, but are not limited to, improving electrical conductivity, developing intrinsically stretchable semiconductors, improving adhesion and strain relief at dis-similar interfaces, and achieving energy-harvesting capabilities.

There are several strategies to achieve stretchable conductors. A common strategy is to create composite materials of elastomers and conductive fillers, such as carbon nanomaterials or silver nanowires. However, there are several disadvantages to using composites, including lower conductivity than metals and hysteresis from stretching.<sup>37</sup> Another approach is to pattern conductive traces into serpentine shapes around rigid electronic components (i.e., capacitors or transistors).<sup>38</sup> Upon stretching, the serpentine patterns straighten out to maintain electrical conductivity. **Figure 3a** shows an example of serpentine electrodes.<sup>39</sup> Both composite materials and those with serpentine traces have finite limits of extensibility (i.e., maximum strain before loss of conductivity). Alternatively, one may use intrinsically stretchable conductors, such as organic conductors (e.g., conjugated polymers).<sup>3,40-43</sup>

Similarly, room-temperature liquid metals, especially eutectic alloys of gallium, are also promising soft conductors.<sup>44,45</sup> These classes of metals possess low toxicity, display higher electrical conductivities than composites, and are softer than biological tissues. Due to their fluidic nature, they retain conductivity while undergoing large deformations and are self-healing. However, gallium diffuses into many metals, which poses a materials challenge for long-term use.<sup>44–48</sup>

A new form of stretchable conductor has recently emerged based on ionic hydrogels.<sup>49</sup> Hydrogel materials are well-suited for implantable devices because they are soft and biocompatible. Like biological systems, hydrogels transduce signals over long distances using ions. While optical transparency is difficult to achieve in conventional electronic conductors, ionically conductive hydrogels are inherently transparent because they comprise mostly water.<sup>49</sup> Figure 3b demonstrates transparent touch-screen panels that register pressure through changes in capacitance.<sup>50</sup> Recent studies have attempted to increase the stretchability and toughness of ionic hydrogels and also to render them self-healing.<sup>36,51–57</sup>

A major challenge with ionically conductive devices is that they are limited to a narrow operating voltage due to electrochemical reactions that can take place within the material. Moreover, ionic systems also suffer from large impedances at interfaces with metals; likewise, corrosion is also a risk at this interface. Fortunately, there has been progress on overcoming issues with electrochemical reactions at the hydrogel–electrode interface. This involves placing a dielectric capacitor in series with the hydrogel to lower the voltage across the hydrogel–electrode interface.<sup>49</sup> This approach has enabled transparent ionic actuators, which can also be useful for soft robotics.

Mismatch of mechanical properties at the interface of soft and rigid components is an ongoing challenge. Various approaches have been developed to reduce the strain at interfaces. Notably, serpentine patterns minimize strain on “islands” of rigid components. When patterned onto pre-strained elastomers, the two-dimensional serpentine structures transform into three-dimensional (3D) buckled structures to improve stretchability.<sup>58,59</sup> Another approach to reduce strains at soft–rigid interfaces is to use modulus gradients that dissipate the buildup of stress; that is, to place several materials of varying elastic moduli at the interface.<sup>60,61</sup> However, this approach may add unwanted thickness to a device or complicate processing steps. Adhesion of soft components to a variety of surfaces can also be accomplished using the “super glue” method, which makes it possible to bond hydrogels with elastomers by creating a dispersion of cyanoacrylates with organic solvents.<sup>62</sup> In addition, bioinspired “adhesives” are gaining popularity, such as the suction cups of cephalopods,<sup>63</sup> van der Waals forces inspired by geckos,<sup>64</sup> and catechol chemistry, which are a class of organic functional groups found in many living systems, most notably by mussels.<sup>65,66</sup>

## Soft Robotics

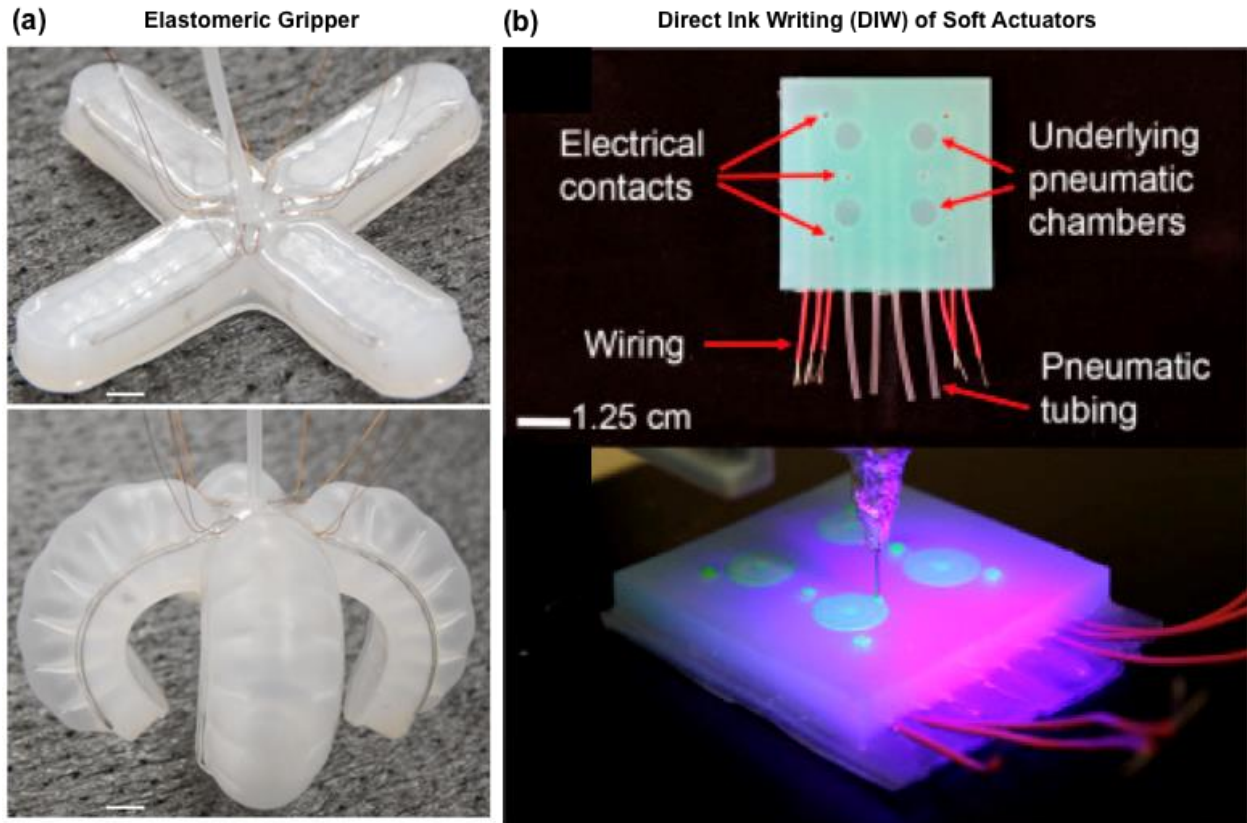


**Figure 5-4:** Soft robotics. (a) Elastomeric grippers are produced by molding an uncured elastomer. (Top) A gallium alloy liquid metal is injected into hollow cavities of the elastomer to form a monolithic conductive element. (Bottom) A pneumatic feed inflates cavities with air to actuate the gripper. Scale bar = 1.0 cm for both top and bottom images. Reprinted with permission from Reference 47. © 2015 IEEE. (b) Soft pneumatic actuators are fabricated with direct ink writing of two different inks. (Top) A side view image shows the architecture of the soft actuator, which consists of embedded pneumatic chambers with adjacent electrical conductors. Metallic wiring and pneumatic tubing (shown at bottom of image) are embedded within the composite. (Bottom) The two inks (one of conductive hydrogel and the other of an insulating elastomer) are printed in an alternating fashion and cured under UV light. Electrical contacts from metallic wires and tubing for pneumatic control are embedded within the hydrogel material. Reprinted with permission from Reference 75. © 2015 Elsevier.

Soft robots are networks of sensors, actuators, and controllers that perform specific tasks.

Similar to flexible and stretchable bioelectronic devices, these robots are made of soft materials.

This field draws significant inspiration from nature, especially from cephalopods (e.g., octopi and squid). These living organisms are inspirational because they are composed almost entirely of soft materials, can perform tasks (including problem solving), and are autonomously powered. In particular, octopi are interesting because they can alter their skin color and texture on demand to

camouflage with their surrounding environment.<sup>67,68</sup> Figure 1b<sup>69</sup> shows an example of a soft robot that manipulates or interacts with fragile objects without sophisticated control mechanisms. The force an elastomeric actuator can exert is self-limited by the material itself. Soft robots must be robust to be useful; they should be capable of exerting or receiving large forces without failure. Like octopi, soft robots could also be made to have displays or color outputs that are either static or dynamic, based on the environment, with capabilities of high ON-OFF switching and a range of color.<sup>70-72</sup> Soft robots can also change size and shape to either access “denied spaces” or limit human presence in hazardous environments (such as in search and rescue operations). Finally, it seems likely that devices designed for human–machine interfaces (e.g., androids) will have soft components.

Soft robotics has stimulated the development of several manufacturing technologies. Conventional forms of soft lithography use planar masters with a single level of relief, which are features that appear as protrusions from a background plane (i.e., elastomer with arbitrary heights of protrusions based on a mold). However, a single level of relief may be insufficient to generate complex curvilinear structures. Therefore, recent focus has been on direct-writing and 3D printing of elastomers and hydrogels.<sup>56,69,73,74</sup> For example, **Figure 4a** shows a recent approach that involves direct ink writing of two different UV-curable inks—one composed of hydrogel and the other silicone-based.<sup>75</sup> In general, sensors, actuators, and other components of current soft robots are all made of different materials. Fabricating these structures separately and then combining them may be difficult. Recent progress has yielded a two-step method for creating a “monolithic” soft robot. As shown in Figure 4b, such a robot consists of a molded elastomer that is pneumatically actuated. Liquid metal, injected into hollow cavities of the elastomer, serves as a sensor element.<sup>47</sup>

There are many opportunities for improving integration of different components of soft robots. For example, a soft robot may comprise many sensors; handling and synchronizing their outputs with better signal processing would improve control systems and automation, and integrating sensing and actuation at the molecular and microstructural level. Actuators and controllers must also enable higher degrees of freedom for motion to endow soft robots with complex movements. Likewise, many soft actuators lack either speed or force of actuation to be useful, especially when compared to soft species in nature (e.g., octopus).<sup>67</sup> Ideally, robots should function autonomously. However, pneumatic pressure lines tether most soft robots for actuation. Therefore, “untethering” robots, perhaps by using miniaturized hydraulics, may improve autonomous function and range of motion. A key challenge to doing so would be to integrate these pumps without compromising the soft structure of the robot.

### **Outlook and future challenges**

There are several important challenges that can be identified with respect to biological integration, materials and mechanics, power sources, and the pathway toward devices that operate in the real world.

#### *Biological integration*

Environmental stability of biomaterials is important for long-term use. For example, biological fluids may accelerate degradation, biofouling, or corrosion (e.g., Si leaching) of implantable devices. Likewise, creating a water (either liquid or vapor) barrier around electronics is also vital, but such barriers often change the mechanics of the devices due to their thickness. Within the biosensing research community, monitoring interstitial fluids in a noninvasive manner remains a challenge and an active field of study. Such fluids surround tissues and can provide real-time information on the state of the body, such as stress, or the function of an organ. However,

accurate sensing by wearable, noninvasive devices is not easy because of the complexities of biochemistry and variations across individuals, as well as temporal fluctuations of biomarkers in the body.<sup>29</sup>

Integrating soft devices with organs and tissues is also a challenge due to issues with adhesion, especially for “wet” conditions as well as with hydrogels.<sup>76</sup> Likewise, reducing artifacts of motion and electromagnetic interference remain challenges for wearable sensors. An emerging area that combines sensing and actuation is haptics—wearable devices that interact with the tactile and kinesthetic senses to provide a more lifelike experience for virtual and augmented reality.

### *Materials and mechanics*

The interfaces of materials are of great significance and there remain many challenges related to interfacial phenomena. A major hurdle within soft and stretchable electronics—not just bioelectronics—is the mechanical mismatch at the interface of soft and hard substrates. For example, the point of failure for most soft devices occurs at the interface of an elastomer and traditional rigid electronics (i.e., printed circuit boards) needed to interface devices with laboratory equipment. Improving the toughness of stretchable materials is one route to increase the durability of materials. Alternatively, the ability of a material to self-heal is also an attractive property.<sup>73,77,78</sup> Although many systems exhibit self-healing behavior, future work should focus on improving self-healing such that it is rapid and repeatable even when ruptured multiple times.

### *Power*

Performing functions such as sensing, actuating, haptic feedback (i.e., vibrations or other kinesthetic motions), and transmitting data all require power. Energy sources, whether harvesters or batteries, should be stretchable, durable, and self-healing, and serve continuously for long lifespans, where appropriate. In particular, implantable systems require power sources that are safe

and have longevity on the order of tens of years. For example, patients with modern pacemakers often undergo follow-up surgical procedures approximately five to 15 years only to replace the battery.<sup>79</sup> Devices for energy storage include flexible and stretchable batteries,<sup>13,80–85</sup> and those for energy harvesting include piezoelectric devices,<sup>86–90</sup> wearable solar “stickers,”<sup>91</sup> and wearable biofuel cells that extract energy from sweat.<sup>92,93</sup> Despite recent work on stretchable batteries (as shown in Figure 1a), these batteries are not yet mature for stretchable bioelectronics. Meanwhile, organic solar cells are promising for wearable devices, but not practical for implanted systems.<sup>91,94–96</sup> Finally, the small form factors and the relatively small amount of power available from energy harvesters require transmitters and receivers to operate either with low power<sup>97</sup> or in passive manners.<sup>98</sup>

### *Creating real-world solution*

There is an inherent motivation in the field of stretchable bioelectronics to create devices that function in the real world. Because this field is relatively new, the onus lies on academic labs to make strides toward transitioning discoveries into real-world solutions. Thus, moving devices from bench spaces to working prototypes should be encouraged by academic and research enterprises. Electronics with a focus on healthcare is of major interest. It was suggested that researchers should engage in more collaborations with the medical community (i.e., physicians, healthcare providers). Researchers should be interested in working with health specialists and take a needs-based approach to the development of technology, as opposed to creating solutions in search of problems.

### **Conclusions**

Conventional electronic devices are made from rigid materials and cannot be easily integrated or implanted with the biological milieu. Because biological tissues are inherently soft

and deformable, bioelectronic devices made of soft and stretch- able materials are desirable. Beyond comfort, the use of soft electronic materials has the potential to provide more accurate monitoring of physiological activities, such as EEGs and ECGs, by making conformal contact with the skin. Skin itself provides a biological inspiration for soft electronics because skin is stretchable, self-healing, and capable of multimodal sensing; researchers are currently seeking material strategies to mimic these functions. In the case of implanted systems, soft or stretchable bioelectronics offer the ability to monitor the function of organs in real time, regulate metabolic activities, and in some cases, restore function to damaged tissues (i.e., paralyzed limbs or nerves). Likewise, these systems can be integrated with textiles and clothing to enable new wear- able platforms. Opportunities remain to improve wearables, thus allowing users to be more proactive with managing their health. For example, future work could focus on sensors that provide more medically relevant information for health monitoring, environmental sensing, and medication compliance. Finally, soft and stretchable materials are important for soft robotic systems that provide greater degrees of freedom of movement relative to conventional robots while using materials and modes of movement that are safe for interfacing with humans. Soft and stretchable electronics, sensors, and actuators are critical to the operation and function of these soft robots. This field is still in its infancy, and current systems are far from mimicking the elegance of biological systems, such as an octopus. In conclusion, we hope this article provides guidance and inspiration for those outside and within the com- munity and serves as a springboard for new ideas, challenges, and opportunities.

### **Acknowledgements**

This report summarizes scientific progress presented and discussed at the MRS/Kavli Future of Materials Workshop on “Flexible and Stretchable Bioelectronics.” This workshop,

sponsored by *MRS Bulletin* and the Kavli Foundation, was held after the 2017 MRS Spring Meeting in Phoenix, Ariz. The purpose of the meeting was to identify trends, challenges, and blind spots in the basic materials science, biological integration, and commercialization for this interdisciplinary field. The authors thank the speakers and panelists at the workshop for their inspirational talks and the attendees for their participation in discussions. D.J.L. acknowledges support from the National Institutes of Health Director's New Innovator Award 1DP2EB022358-01.

## References

- (1) T. Someya, Z. Bao, G.G. Malliaras, *Nature* **540**, 379 (2016).
- (2) J.A. Rogers, R. Ghaffari, D.-H. Kim, Eds., *Stretchable Bioelectronics for Medical Devices and Systems, Microsystems and Nanosystems Series* (Springer International Publishing, Cham, 2016, <http://link.springer.com/10.1007/978-3-319-28694-5>).
- (3) D.J. Lipomi, Z. Bao, *MRS Bull.* **42** (2), 93 (2017).
- (4) B.C. Marin, S.E. Root, A.D. Urbina, E. Aklile, R. Miller, A.V. Zaretski, D.J. Lipomi, *ACS Omega* **2**, 626 (2017).
- (5) Y.-Y. Lee, H.-Y. Kang, S.H. Gwon, G.M. Choi, S.-M. Lim, J.-Y. Sun, Y.-C. Joo, *Adv. Mater.* **28**, 1636 (2016).
- (6) S. Kano, K. Kim, M. Fujii, *ACS Sens.* **2**, 828 (2017).
- (7) E. Koch, A. Dietzel, *Sens. Actuators Phys.* **250**, 138 (2016).
- (8) F. Güder, A. Ainla, J. Redston, B. Mosadegh, A. Glavan, T.J. Martin, G.M. Whitesides, *Angew. Chem. Int. Ed. Engl.* **128**, 5821 (2016).
- (9) D. Chen, Q. Pei, *Chem. Rev.* (2017), doi:10.1021/acs.chemrev.7b00019.
- (10) P.S. Khiabani, A.H. Soeriyadi, P.J. Reece, J.J. Gooding, *ACS Sens.* **1**, 775 (2016).
- (11) M.E. Lee, A.M. Armani, *ACS Sens.* **1**, 1251 (2016).
- (12) V. Gomelsky, “L’Oréal’s Technology Incubator: Creating the Future of Beauty,” *New York Times* (2017), <https://www.nytimes.com/2017/03/30/fashion/craftsmanship-loreal-beauty-technology.html>.
- (13) G. Kettlgruber, M. Kaltenbrunner, C.M. Siket, R. Moser, I.M. Graz, R. Schwödiauer, S. Bauer, *J. Mater. Chem. A* **1**, 5505 (2013).
- (14) D.-H. Kim, N. Lu, R. Ma, Y.-S. Kim, R.-H. Kim, S. Wang, J. Wu, S.M. Won, H. Tao, A. Islam, K.J. Yu, T. Kim, R. Chowdhury, M. Ying, L. Xu, M. Li, H.-J. Chung, H. Keum, M. McCormick, P. Liu, Y.-W. Zhang, F.G. Omenetto, Y. Huang, T. Coleman, J.A. Rogers, *Science* **333**, 838 (2011).
- (15) I.R. Mineev, P. Musienko, A. Hirsch, Q. Barraud, N. Wenger, E.M. Moraud, J. Gandar, M. Capogrosso, T. Milekovic, L. Asboth, R.F. Torres, N. Vachicouras, Q. Liu, N. Pavlova, S. Duis, A. Larmagnac, J. Vörös, S. Micera, Z. Suo, G. Courtine, S.P. Lacour, *Science* **347**, 159 (2015).
- (16) S.J. Kim, H.R. Cho, K.W. Cho, S. Qiao, J.S. Rhim, M. Soh, T. Kim, M.K. Choi, C. Choi, I. Park, N.S. Hwang, T. Hyeon, S.H. Choi, N. Lu, D.-H. Kim, *ACS Nano* **9**, 2677 (2015).
- (17) K. Kalantar-zadeh, N. Ha, J.Z. Ou, K.J. Berean, *ACS Sens.* **2**, 468 (2017).
- (18) D. Son, J. Lee, S. Qiao, R. Ghaffari, J. Kim, J.E. Lee, C. Song, S.J. Kim, D.J. Lee, S.W. Jun, S. Yang, M. Park, J. Shin, K. Do, M. Lee, K. Kang, C.S. Hwang, N. Lu, T. Hyeon, D.-H. Kim, *Nat. Nanotechnol.* **9**, 397 (2014).
- (19) J. Di, S. Yao, Y. Ye, Z. Cui, J. Yu, T.K. Ghosh, Y. Zhu, Z. Gu, *ACS Nano* **9**, 9407 (2015).
- (20) S.Y. Chin, Y.C. Poh, A.-C. Kohler, J.T. Compton, L.L. Hsu, K.M. Lau, S. Kim, B.W. Lee, F.Y. Lee, S.K. Sia, *Sci. Robot.* **2** (2017), doi:10.1126/scirobotics.aah6451.
- (21) T.M. Reineke, *ACS Macro Lett.* **5**, 14 (2016).
- (22) B.C.-K. Tee, A. Chortos, A. Berndt, A.K. Nguyen, A. Tom, A. McGuire, Z.C. Lin, K. Tien, W.-G. Bae, H. Wang, P. Mei, H.-H. Chou, B. Cui, K. Deisseroth, T.N. Ng, Z. Bao, *Science* **350**, 313 (2015).

- (23) S. Kabiri Ameri, R. Ho, H. Jang, L. Tao, Y. Wang, L. Wang, D.M. Schnyer, D. Akinwande, N. Lu, *ACS Nano* 11, 7634 (2017).
- (24) M. Kaltenbrunner, T. Sekitani, J. Reeder, T. Yokota, K. Kuribara, T. Tokuhara, M. Drack, R. Schwödianer, I. Graz, S. Bauer-Gogonea, S. Bauer, T. Someya, *Nature* 499, 458 (2013).
- (25) M. Drack, I. Graz, T. Sekitani, T. Someya, M. Kaltenbrunner, S. Bauer, *Adv. Mater.* 27, 34 (2014).
- (26) Z. Sonner, E. Wilder, T. Gaillard, G. Kasting, J. Heikenfeld, *Lab Chip* 17, 2550 (2017).
- (27) A.J. Bandodkar, I. Jeerapan, J. Wang, *ACS Sens.* 1, 464 (2016).
- (28) J. Heikenfeld, *Nature* 529, 475 (2016).
- (29) Z. Sonner, E. Wilder, J. Heikenfeld, G. Kasting, F. Beyette, D. Swaile, F. Sherman, J. Joyce, J. Hagen, N. Kelley-Loughnane, R. Naik, *Biomicrofluidics* 9, 31301 (2015).
- (30) Y.H. Kim, S.J. Kim, Y.-J. Kim, Y.-S. Shim, S.Y. Kim, B.H. Hong, H.W. Jang, *ACS Nano* 9, 10453 (2015).
- (31) M. Kim, H. Alrowais, C. Kim, P. Yeon, M. Ghovanloo, O. Brand, *Lab Chip* 17, 2323 (2017).
- (32) F. Zhang, G. Qu, E. Mohammadi, J. Mei, Y. Diao, *Adv. Funct. Mater.* 27 (2017), doi:10.1002/adfm.201701117.
- (33) W. Gao, S. Emaminejad, H.Y.Y. Nyein, S. Challa, K. Chen, A. Peck, H.M. Fahad, H. Ota, H. Shiraki, D. Kiriya, D.-H. Lien, G.A. Brooks, R.W. Davis, A. Javey, *Nature* 529, 509 (2016).
- (34) R.K. Mishra, L.J. Hubble, A. Martín, R. Kumar, A. Barfidokht, J. Kim, M.M. Musameh, I.L. Kyratzis, J. Wang, *ACS Sens.* 2, 553 (2017).
- (35) S.P. Lacour, G. Courtine, J. Guck, *Nat. Rev. Mater.* 1 (2016), doi:10.1038/natrevmats.2016.63.
- (36) G. Cai, J. Wang, K. Qian, J. Chen, S. Li, P.S. Lee, *Adv. Sci. U.S.A.* 4 (2017), doi:10.1002/advs.201600190.
- (37) D.J. Lipomi, *Adv. Mater.* 28, 4180 (2016).
- (38) D.-H. Kim, J. Song, W.M. Choi, H.-S. Kim, R.-H. Kim, Z. Liu, Y.Y. Huang, K.-C. Hwang, Y. Zhang, J.A. Rogers, *Proc. Natl. Acad. Sci.* 105, 18675 (2008).
- (39) A.M.V. Mohan, N. Kim, Y. Gu, A.J. Bandodkar, J.-M. You, R. Kumar, J.F. Kurniawan, S. Xu, J. Wang, *Adv. Mater. Technol.* 2 (2017), doi:10.1002/admt.201600284.
- (40) S.E. Root, S. Savagatrup, A.D. Printz, D. Rodriguez, D.J. Lipomi, *Chem. Rev.* 117, 6467 (2017).
- (41) S. Savagatrup, A.D. Printz, T.F. O'Connor, A.V. Zaretski, D.J. Lipomi, *Chem. Mater.* 26, 3028 (2014).
- (42) G. Qu, J.J. Kwok, Y. Diao, *Acc. Chem. Res.* 49, 2756 (2016).
- (43) H. Chung, Y. Diao, *J. Mater. Chem. C* 4, 3915 (2016).
- (44) M.D. Dickey, *Adv. Mater.* (2017), doi:10.1002/adma.201606425.
- (45) N. Kazem, T. Hellebrekers, C. Majidi, *Adv. Mater.* 29 (2017), doi:10.1002/adma.201605985.
- (46) M.G. Mohammed, R. Kramer, *Adv. Mater.* 29 (2017), doi:10.1002/adma.201604965.
- (47) R.A. Bilodeau, E.L. White, R.K. Kramer, *Proc. IEEE/RSJ Inter. Conf. Intell. Robots Syst. (IROS)* (2015), pp. 2324–2329.
- (48) R.K. Kramer, (2015), <http://dx.doi.org/10.1117/12.2176581>.
- (49) C. Keplinger, J.-Y. Sun, C.C. Foo, P. Rothmund, G.M. Whitesides, Z. Suo, *Science* 341,

- 984 (2013).
- (50) C.-C. Kim, H.-H. Lee, K.H. Oh, J.-Y. Sun, *Science* 353, 682 (2016).
- (51) J. Ma, J. Lee, S.S. Han, K.H. Oh, K.T. Nam, J.-Y. Sun, *ACS Appl. Mater. Interfaces* 8, 29220 (2016).
- (52) F. Zhu, L. Cheng, Z.J. Wang, W. Hong, Z.L. Wu, J. Yin, J. Qian, Q. Zheng, *ACS Appl. Mater. Interfaces* 9, 11363 (2017).
- (53) J.P. Gong, *Soft Matter* 6, 2583 (2010).
- (54) J.-Y. Sun, X. Zhao, W.R.K. Illeperuma, O. Chaudhuri, K.H. Oh, D.J. Mooney, J.J. Vlassak, Z. Suo, *Nature* 489, 133 (2012).
- (55) T.L. Sun, T. Kurokawa, S. Kuroda, A.B. Ihsan, T. Akasaki, K. Sato, M.A. Haque, T. Nakajima, J.P. Gong, *Nat. Mater.* 12, 932 (2013).
- (56) M.C. Darnell, J.-Y. Sun, M. Mehta, C. Johnson, P.R. Arany, Z. Suo, D.J. Mooney, *Biomaterials* 34, 8042 (2013).
- (57) J. Odent, T.J. Wallin, W. Pan, K. Kruemplestaedter, R.F. Shepherd, E.P. Giannelis, *Adv. Funct. Mater.*, doi:10.1002/adfm.201701807.
- (58) Y. Su, X. Ping, K.J. Yu, J.W. Lee, J.A. Fan, B. Wang, M. Li, R. Li, D.V. Harburg, Y. Huang, C. Yu, S. Mao, J. Shim, Q. Yang, P.-Y. Lee, A. Armonas, K.-J. Choi, Y. Yang, U. Paik, T. Chang, T.J. Dawidczyk, Y. Huang, S. Wang, J.A. Rogers, *Adv. Mater.* 29 (2017), doi:10.1002/adma.201604989.
- (59) Y. Zhang, S. Wang, X. Li, J.A. Fan, S. Xu, Y.M. Song, K.-J. Choi, W.-H. Yeo, W. Lee, S.N. Nazaar, B. Lu, L. Yin, K.-C. Hwang, J.A. Rogers, Y. Huang, *Adv. Funct. Mater.* 24, 2028 (2014).
- (60) N. Naserifar, P.R. LeDuc, G.K. Fedder, *Adv. Mater.* 28, 3584 (2016).
- (61) R. Libanori, R.M. Erb, A. Reiser, H. Le Ferrand, M.J. Süess, R. Spolenak, A.R. Studart, *Nat. Commun.* 3, 1265 (2012).
- (62) D. Wirthl, R. Pichler, M. Drack, G. Kettlguber, R. Moser, R. Gerstmayr, F. Hartmann, E. Bradt, R. Kaltseis, C.M. Siket, S.E. Schausberger, S. Hild, S. Bauer, M. Kaltenbrunner, *Sci. Adv.* 3, e1700053 (2017).
- (63) M.K. Choi, O.K. Park, C. Choi, S. Qiao, R. Ghaffari, J. Kim, D.J. Lee, M. Kim, W. Hyun, S.J. Kim, H.J. Hwang, S.-H. Kwon, T. Hyeon, N. Lu, D.-H. Kim, *Adv. Healthc. Mater.* 5, 80 (2016).
- (64) M. Sitti, R.S. Fearing, *J. Adhes. Sci. Technol.* 17, 1055 (2003).
- (65) J.H. Waite, *J. Exp. Biol.* 220, 517 (2017).
- (66) B.P. Lee, S. Konst, *Adv. Mater.* 26, 3415 (2014).
- (67) C. Laschi, M. Cianchetti, B. Mazzolai, L. Margheri, M. Follador, P. Dario, *Adv. Robot.* 26, 709 (2012).
- (68) I.A. Anderson, T.A. Gisby, T.G. McKay, B.M. O'Brien, E.P. Calius, *J. Appl. Phys.* 112, 41101 (2012).
- (69) H. Zhao, K. O'Brien, S. Li, R.F. Shepherd, *Sci. Robot.* 1 (2016), doi:10.1126/scirobotics.aai7529.
- (70) G. Cai, J. Wang, P.S. Lee, *Acc. Chem. Res.* 49, 1469 (2016).
- (71) C. Yan, W. Kang, J. Wang, M. Cui, X. Wang, C.Y. Foo, K.J. Chee, P.S. Lee, *ACS Nano* 8, 316 (2014).
- (72) S.A. Morin, R.F. Shepherd, S.W. Kwok, A.A. Stokes, A. Nemiroski, G.M. Whitesides, *Science* 337, 828 (2012).
- (73) T.J. Wallin, J.H. Pikul, S. Bodkhe, B.N. Peele, B.C.M. Murray, D. Therriault, B.W.

- McEnerney, R.P. Dillon, E.P. Giannelis, R.F. Shepherd, J. Mater. Chem. B 5, 6249 (2017).
- (74) S.A. Morin, Y. Shevchenko, J. Lessing, S.W. Kwok, R.F. Shepherd, A.A. Stokes, G.M. Whitesides, *Adv. Mater.* 26, 5991 (2014).
- (75) S.S. Robinson, K.W. O'Brien, H. Zhao, B.N. Peele, C.M. Larson, B.C. Mac Murray, I.M. Van Meerbeek, S.N. Dunham, R.F. Shepherd, *Extreme Mech. Lett.* 5, 47 (2015).
- (76) J. Li, A.D. Celiz, J. Yang, Q. Yang, I. Wamala, W. Whyte, B.R. Seo, N.V. Vasilyev, J.J. Vlassak, Z. Suo, D.J. Mooney, *Science* 357, 378 (2017).
- (77) F. Herbst, D. Döhler, P. Michael, W.H. Binder, *Macromol. Rapid Commun.* 34, 203 (2013).
- (78) W.H. Binder, *Self-Healing Polymers: From Principles to Applications* (Wiley, Weinheim, Germany, 2013).
- (79) Pacemaker-Results. Mayo Clinic, <http://www.mayoclinic.org/tests-procedures/pacemaker/details/results/rsc-20198673>.
- (80) M. Kaltenbrunner, G. Kettlgruber, C. Siket, R. Schwödiauer, S. Bauer, *Adv. Mater.* 22, 2065 (2010).
- (81) A.M. Gaikwad, A.M. Zamarayeva, J. Rousseau, H. Chu, I. Derin, D.A. Steingart, *Adv. Mater.* 24, 5071 (2012).
- (82) C. Wang, W. Zheng, Z. Yue, C.O. Too, G.G. Wallace, *Adv. Mater.* 23, 3580 (2011).
- (83) J. Ren, Y. Zhang, W. Bai, X. Chen, Z. Zhang, X. Fang, W. Weng, Y. Wang, H. Peng, *Angew. Chem. Int. Ed. Engl.* 126, 7998 (2014).
- (84) K. Xie, B. Wei, *Adv. Mater.* 26, 3592 (2014).
- (85) S. Xu, Y. Zhang, J. Cho, J. Lee, X. Huang, L. Jia, J.A. Fan, Y. Su, J. Su, H. Zhang, H. Cheng, B. Lu, C. Yu, C. Chuang, T. Kim, T. Song, K. Shigeta, S. Kang, C. Dagdeviren, I. Petrov, P.V. Braun, Y. Huang, U. Paik, J.A. Rogers, *Nat. Commun.* 4, 1543 (2013).
- (86) Y. Qi, N.T. Jafferis, K. Lyons, C.M. Lee, H. Ahmad, M.C. McAlpine, *Nano Lett.* 10, 524 (2010).
- (87) D. Maurya, Y. Zhou, Y. Wang, Y. Yan, J. Li, D. Viehland, S. Priya, *Sci. Rep.* 5 (2015), doi:10.1038/srep08595.
- (88) S. Priya, H.-C. Song, Y. Zhou, R. Varghese, A. Chopra, S.-G. Kim, I. Kanno, L. Wu, D.S. Ha, J. Ryu, R.G. Polcawich, *Energy Harvest. Syst.* 4, 3 (2017).
- (89) F. Invernizzi, S. Dulio, M. Patrini, G. Guizzetti, P. Mustarelli, *Chem. Soc. Rev.* (2016), doi:10.1039/C5CS00812C.
- (90) F. Suarez, D.P. Parekh, C. Ladd, D. Vashaee, M.D. Dickey, M.C. Öztürk, *Appl. Energy.* 202, 736 (2017).
- (91) T.F. O'Connor, A.V. Zaretski, S. Savagatrup, A.D. Printz, C.D. Wilkes, M.I. Diaz, E.J. Sawyer, D.J. Lipomi, *Sol. Energy Mater. Sol. Cells* 144, 438 (2016).
- (92) W. Jia, G. Valdés-Ramírez, A.J. Bandothkar, J.R. Windmiller, J. Wang, *Angew. Chem. Int. Ed. Engl.* 52, 7233 (2013).
- (93) W. Jia, X. Wang, S. Imani, A.J. Bandothkar, J. Ramírez, P.P. Mercier, J. Wang, *J. Mater. Chem. A* 2, 18184 (2014).
- (94) M. Kaltenbrunner, G. Adam, E.D. Głowacki, M. Drack, R. Schwödiauer, L. Leonat, D.H. Apaydin, H. Groiss, M.C. Scharber, M.S. White, N.S. Sariciftci, S. Bauer, *Nat. Mater.* 14, 1032 (2015).
- (95) T. Kim, J.-H. Kim, T.E. Kang, C. Lee, H. Kang, M. Shin, C. Wang, B. Ma, U. Jeong, T.-S. Kim, B.J. Kim, *Nat. Commun.* 6 (2015), doi:10.1038/ncomms9547.

- (96) D.J. Lipomi, B.C.-K. Tee, M. Vosgueritchian, Z. Bao, *Adv. Mater.* 23, 1771 (2011).
- (97) P.P. Mercier, A.C. Lysaght, S. Bandyopadhyay, A.P. Chandrakasan, K.M. Stankovic, *Nat. Biotechnol.* 30, 1240 (2012).
- (98) L.Y. Chen, B.C.-K. Tee, A.L. Chortos, G. Schwartz, V. Tse, D.J. Lipomi, H.-S.P. Wong, M.V. McConnell, Z. Bao, *Nat. Commun.* 5 (2014), doi:10.1038/ncomms6028.

## CHAPTER 6

### CONCLUSIONS AND FUTURE WORK

Although the presence of the oxide is considered a nuisance, it can be harnessed to pattern the liquid metal at room temperature and a useful electrochemical interface. In addition, there are rich opportunities to reconfigurable the shape of the liquid metal by preventing the adhesion of the oxide (without necessarily removing or modifying the oxide).

It is possible to electrically actuate the liquid metal via CEW; the displacement and velocities of the metal are comparable with and without the presence of the oxide. Although using NaOH to remove the oxide allows for larger displacements of the metal, the base dissolves Ga into the electrolyte solution that limits its life-span. In addition, EIS measurements show that the slip-layer enables CEW by exhibiting a large electrical resistance due to it being thin (~200 to 500 nm, in thickness). Moreover, aqueous electrolytes pose other challenges because water: (1) changes the morphology and mechanical properties of the oxide, (2) evaporates over time, and (3) absorbs RF radiations, which limits its use for reconfigurable electromagnetic (EM) components. This work shows it is possible to enable CEW in non-aqueous electrolytes. Therefore, future work should address other liquids or interfacial engineering approaches that can: (1) form stable slip-layers, (2) exhibit electrocapillarity, (3) do not absorb EM waves. Finally, the use of optical interferometry and non-linear EIS may provide useful insights on the electro-hydrodynamics of CEW.

Rough surfaces prevent the adhesion of the oxide by creating wetting states that are similar to Cassie-Baxter for conventional liquids. This work suggests that engineering the surface roughness rather than surface chemistry can provide a better route to preventing the adhesion of

the oxide. Commercially-available spray coatings are inexpensive and simple approaches to rendering surfaces “oxide-phobic”. These spray coatings can be applied to cavities and trenches to pattern the metal as well as to enable reconfigurability in closed systems. However, these coatings are limited to ~sub mm dimensions. Therefore, future work should focus on new approaches to forming rough surfaces within closed channels; silica filler-based systems may be one approach to render such channels “oxide-phobic”. Rough surfaces that are also electrically conductive may be useful for Ohmic contacts as well as for energy harvesting. Using structured surfaces that promote pinning of oxide could be useful for forming free-standing films or membranes of gallium oxide.

**Chapter 4:** Conventional tools for measuring contact angles are difficult to interpret for oxide-coated liquid metals (in comparison to simpler fluids such as water). During contact angle measurements, the oxide pins to the flat surfaces, which prevents the metal drops from fully receding. In addition, the oxide on the exterior of the drop collapses onto the substrate, which forms a residue at the end of the measurement. For sliding angle tests, the measurements depend on if the oxide is ruptured upon placing the drop on the substrate. Although the interpretation of the numerical values from these techniques are complicated, these tools can still assess the wettability of oxide-coated liquid metals to a surface (i.e., whether oxide adheres or not). Performing similar measurements for liquid metals without the presence of an oxide (i.e., in an inert, oxygen-free environment) would provide useful insights. Future work should explore other methods (i.e., pull-off forces, interfacial rheology, and tribology) that quantitatively assess the oxide-substrate interface. Finally, this work studied the effect of surface roughness and chemistry on the oxide adhesion. It would be interesting to assess whether surfaces with low coefficient of friction can prevent rupturing of the oxide. Thanks for reading. Please contact me at via electronic mail last name followed by first name (one word, no spaces) at gmail dot com for any discussions.

# APPENDICES

## APPENDIX A

### SUPPORTING INFORMATION FOR CHAPTER 2

*Materials:* Eutectic gallium-indium (Ga, 75%, wt., In, 25% wt.) is purchased at 99% purity from Indium Corporation. Sodium hydroxide and sodium fluoride are purchased from Sigma Aldrich and mixed with MilliQ-filter water to form electrolyte solutions. Pt wires (0.1 mm diameter) for the electrodes were purchased from Sigma Aldrich, stored in 0.1 M sulfuric acid, and rinsed with DI water before and after use. Glass capillaries (borosilicate, single circular without filaments, 7.5 cm in length, 1.0 mm in outer diameter, and 0.72 mm in inner diameter) were purchased from Hilgenberg GmbH. Glass capillaries were cleaned with oxygen plasma treatment prior to use.

*Minimizing Faradaic reactions at electrode-electrolyte interface*

This work utilizes Pt electrodes to minimize the electrochemical reactions at the metal-electrolyte interface. We chose this electrode by performing EIS on a capillary filled only with an electrolyte. We varied the electrode type between platinum (Pt), tungsten (W), and copper (Cu). Pt and W electrodes avoid Faradic reactions (as opposed to copper (Cu), which is susceptible to corrosion and electrochemical reactions). As summarized in Table 1, the studies found that the solution resistance was not affected by the electrode for 1 M NaOH solutions but varied for 1 M NaF. Overall, Pt electrodes consistently provided the lowest solution resistance (6-9 k $\Omega$ ). Based on these results, we chose to use Pt electrodes for the remaining EIS experiments because they provided the lowest solution resistance and avoided electrochemical reactions at the electrode-electrolyte interface.

**Table A-1:** Solution resistance values for Cu, W, and Pt electrodes. Solution resistance values for Cu, W, and Pt electrodes were measured using EIS of a glass capillary filled with an electrolyte (1 M NaOH and 1 M NaF). Tabulated values are impedance values at 100 kHz.

<b>Electrolyte  Electrode</b>	<b>Solution Resistance [k<math>\Omega</math>]</b>		
	Cu	W	Pt
<b>1 M NaOH</b>	6.0	6.0	6.0
<b>1 M NaF</b>	16	15	8.5

*Plug movement characterization*

CEW experiments were performed in a glass capillaries, which were first filled with the electrolyte solution using a disposable hypodermic needle inserted into the edge of the capillary. Thereafter, liquid metal was injected into the center of the glass capillary. When necessary, electrolyte was added again to the glass capillary to remove any air bubbles. Glass capillaries rested in a custom-built PTFE capillary holder. The capillary holder had rectangular wells on each end as a reservoir for the electrolyte. Pt wires rested inside the rectangular wells to apply voltage to the system. AC voltage was applied to end of the glass capillary using a Keithley 4490 Arbitrary Waveform Function Generator (in high-Z mode).

Movement characterization studies were performed with the aid of a camcorder attached to top-view optical microscope through an eye-piece adaptor. The position of the metal over time was determined by tracking the center of the metal plug; the measurement was done after 15-30 seconds after applying the voltage to allow the metal plug to reach uniform oscillations. Displacement was determined by calculating the difference in the position of the metal. Velocity was determined by calculating the quotient of the displacement over the time step.

**Table A-2:** Displacement and velocity comparison for 1 M NaOH for change in voltage (Voltage Ratio) at 0.5 Hz, 1.0 Hz, and 1 Hz.

Frequency [Hz]	Voltage Ratio	Displacement ( $\Delta x$ ) Ratio	Velocity ( $\Delta x/\Delta t$ ) Ratio
0.5	1 to 0.5	2.36	2.37
0.5	2 to 1	3.26	3.26
1	2 to 1	2.28	2.28
3	2 to 1	2.31	2.31
	<b>Average</b>	2.55	2.55
	<b>Std. Dev.</b>	0.47	0.47

**Table A-3:** Displacement and velocity ratios for 1 M NaF for changes in voltage (Voltage Ratio) at 0.5 Hz, 1.0 Hz, and 1 Hz.

Frequency [Hz]	Voltage Ratio	Displacement Ratio	Velocity Ratio
0.5	1 to 0.5	N/A	N/A
0.5	2 to 1	1.84	1.84
1	2 to 1	1.68	1.68
3	2 to 1	1.72	1.72
	<b>Average</b>	1.75	1.75
	<b>Std. Dev.</b>	0.08	0.08

**Table A-4:** Displacement and velocity ratios for changes in frequency (Frequency Ratio) for 1 M NaOH at 1.0 V and 2.0 V.

Frequency Ratio		1.0 V		2.0 V	
		Displacement Ratio	Velocity Ratio	Displacement Ratio	Velocity Ratio
1.0 to 0.5	0.500	1.41	0.70	2.02	1.01
3.0 to 1.0	0.333	1.50	0.50	1.49	0.49
3.0 to 0.5	0.167	2.12	0.35	3.00	0.49
	<b>Average</b>	1.68	0.52	2.17	0.66
	<b>Std. Dev.</b>	0.39	0.18	0.77	0.30

**Table A-5:** Displacement and velocity ratios for changes in frequency (Frequency Ratio) for 1 M NaF at 1.0 V and 2.0 V.

Frequency Ratio		1.0 V		2.0 V	
		Displacement Ratio	Velocity Ratio	Displacement Ratio	Velocity Ratio
1.0 to 0.5	0.500	1.19	0.59	1.30	0.65
3.0 to 1.0	0.333	1.38	0.46	1.35	0.45
3.0 to 0.5	0.167	1.64	0.27	1.76	0.29
<b>Average</b>		1.40	0.44	1.47	0.46
<b>Std. Dev.</b>		0.23	0.16	0.25	0.18

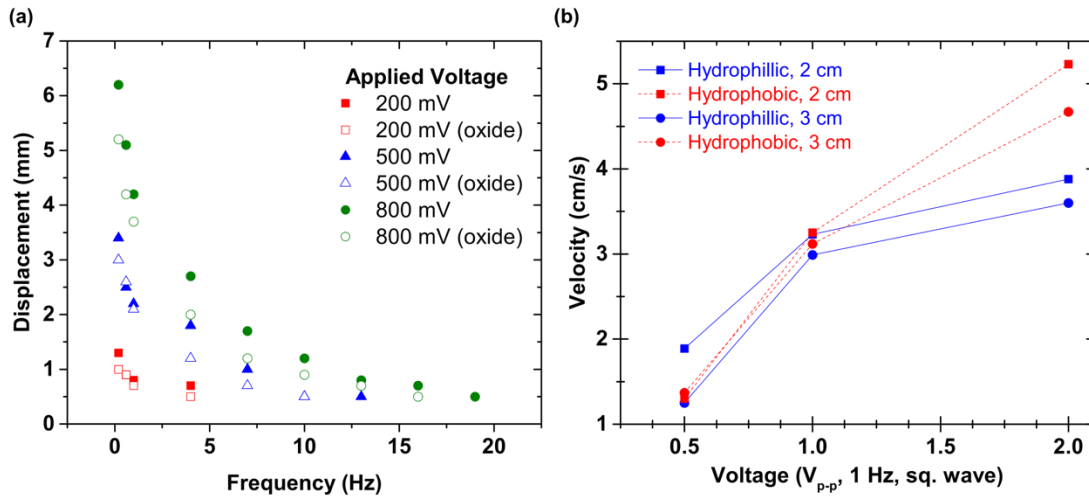


**Figure A-1:** a) Comparing the effect of a surface oxide on the movement of EGaIn plug (~1.0 cm, in length) using low AC voltages (200<sub>RMS</sub> to 800 mV<sub>RMS</sub>, sine wave). The closed data points are in 1 M NaOH, where there is no oxide present. The open data points are performed in 1 M NaF, where an oxide ‘skin’ is present. (b) Velocity measurements of EGaIn plug (2 and 3 cm, in length) in hydrophillic glass capillary (oxygen plasma cleaned, blue) and hydrophobic glass capillary (fluorosilane-treated, red).

### CEW in hydrophobic capillaries

We hypothesize that the slip-layer forms because the electrolyte wets the metal plug. That is, water forms a shell around the metal plug as it is injected into the capillary. This hypothesis can be confirmed by performing CEW in a hydrophobic glass capillary (treated with a hydrophobic silane group). A change in the meniscus of a water drop inside the glass capillary confirms the hydrophobicity. Thereafter, we compare the velocity of metal plugs in the hydrophobic capillaries

vs. hydrophilic capillaries, which is shown in **Figure A-1**. In comparison to the hydrophilic capillaries, we observed some different behaviors in the hydrophobic capillaries. At low voltages ( $\sim 1$  V), we measured the velocity of the plugs to be similar in both hydrophobic and hydrophilic capillaries. At higher voltage (2 V), we found that the plug moved faster in the hydrophobic capillary than the hydrophilic capillary. We attribute the higher velocity to either a thinner slip-layer or lower friction at walls of the capillary. In addition, when applying AC voltages to the hydrophobic setup, the plug would stop after moving before changing the direction of its movement (i.e., plug stops before moving again). In comparison, the metal plugs move in a seamless oscillatory fashion in the hydrophilic capillary. One possible reason for this behavior is the loss and reformation of a slip-layer in the hydrophobic capillary. Overall, these results suggest that CEW is possible in hydrophobic capillaries because water wets the liquid metal to form the slip-layer.

## Electrochemical Impedance Spectroscopy (EIS)

EIS measurements were performed using a Biologic SP-600 single-channel potentiostat. 10-15 mV sine wave (vs. open-circuit potential) was applied to the CEW system in a 2-electrode configuration using Pt electrodes. No DC bias was applied to the system. Model fits were done using E-Chem Analyst software by Gamry Instruments.

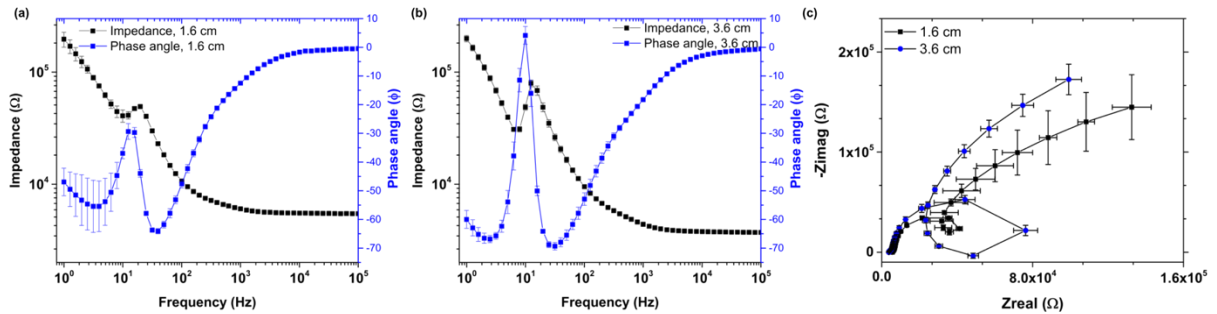


**Figure A-2:** EIS spectra of 10 consecutive measurements for 1.6 cm and 3.6 cm plugs in 1 M NaOH. (a and b) Bode diagrams for 1.6 cm (a) and 3.6 cm (b) showing impedance (left y-axis, black) and phase angle (right y-axis, blue). Error bars are standard deviations ( $n=10$ ) of impedance (black) and phase angle (blue) for a given frequency. (c) Nyquist diagram for both 1.6 cm (black) and 3.6 cm (blue). Each data point is for a specific frequency. X and y error bars are standard deviations ( $n=10$ ) for  $-Z_{\text{real}}$  and  $Z_{\text{imag}}$ .

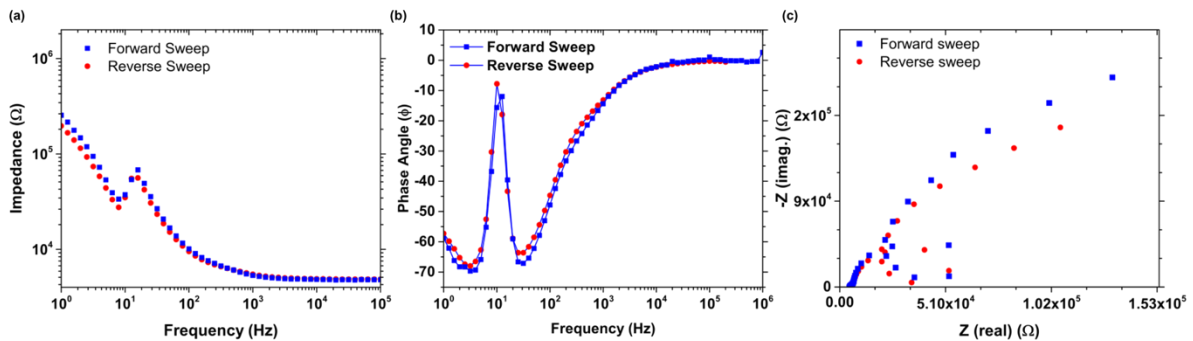


**Figure A-3:** EIS spectra of 2.6 cm EGaIn plug in 1 M NaOH comparing the direction of measured frequency. Forward sweep (blue, square) refers to measurements starting from 1 GHz to 1 Hz. Reverse sweep (red, circle) refers to EIS spectra measured starting from 1 Hz to 1 GHz.

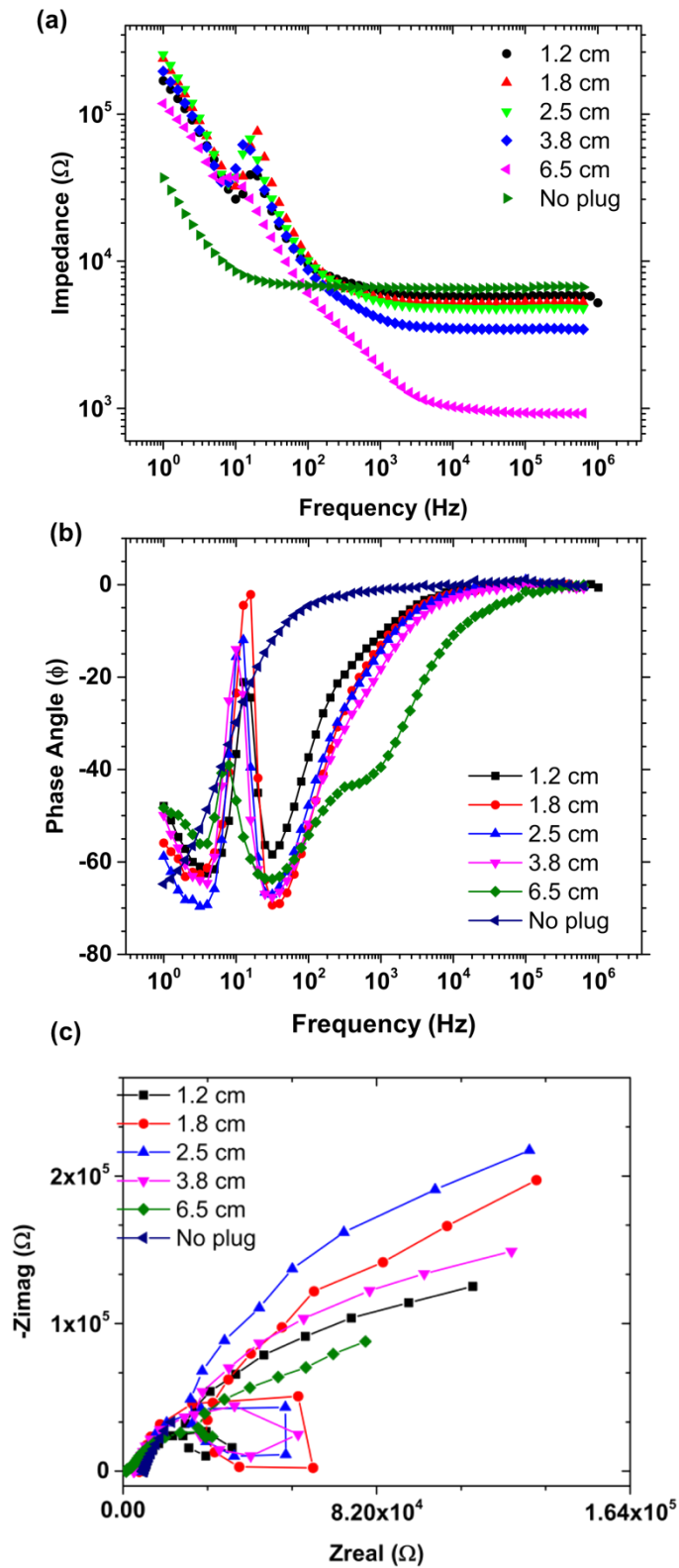


**Figure A-4:** Bode diagrams ((a) impedance and (b) phase angle) from EIS experiments of EGaIn in 1 M NaOH plugs of varying length from no plug (electrolyte only) to 6.5 cm.

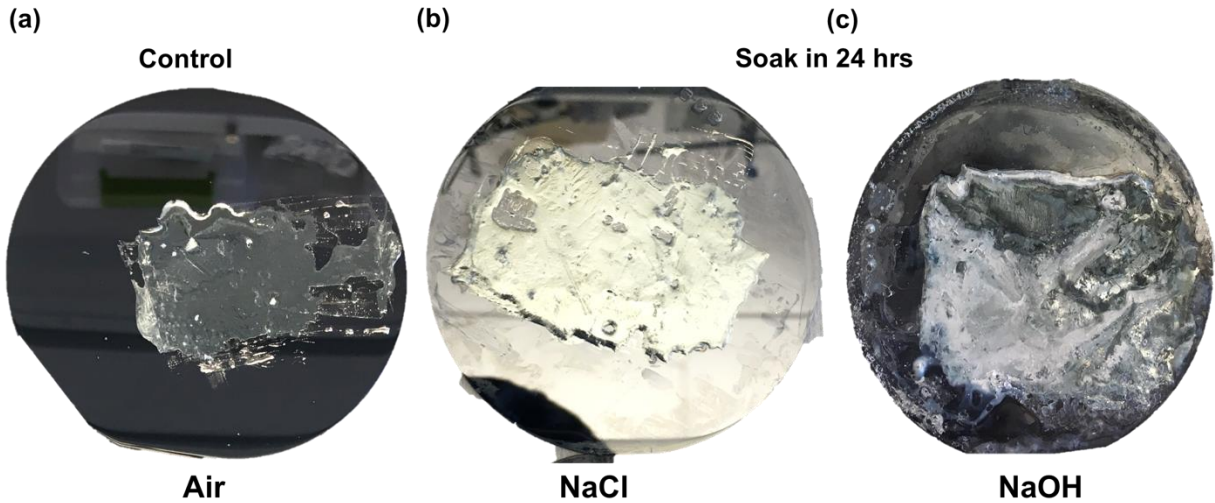


**Figure A-5:** Photographs of Ga film after 24 hour soak in air (a, left, control), 1 M NaCl (middle), 1 M NaOH (c, right). Prior to experiment Ga film is spread over a Si wafer (three inches, in diameter) and soaked into a petri dish containing the electrolyte. Scale bar is 1.5 inches or 3.8 cm.

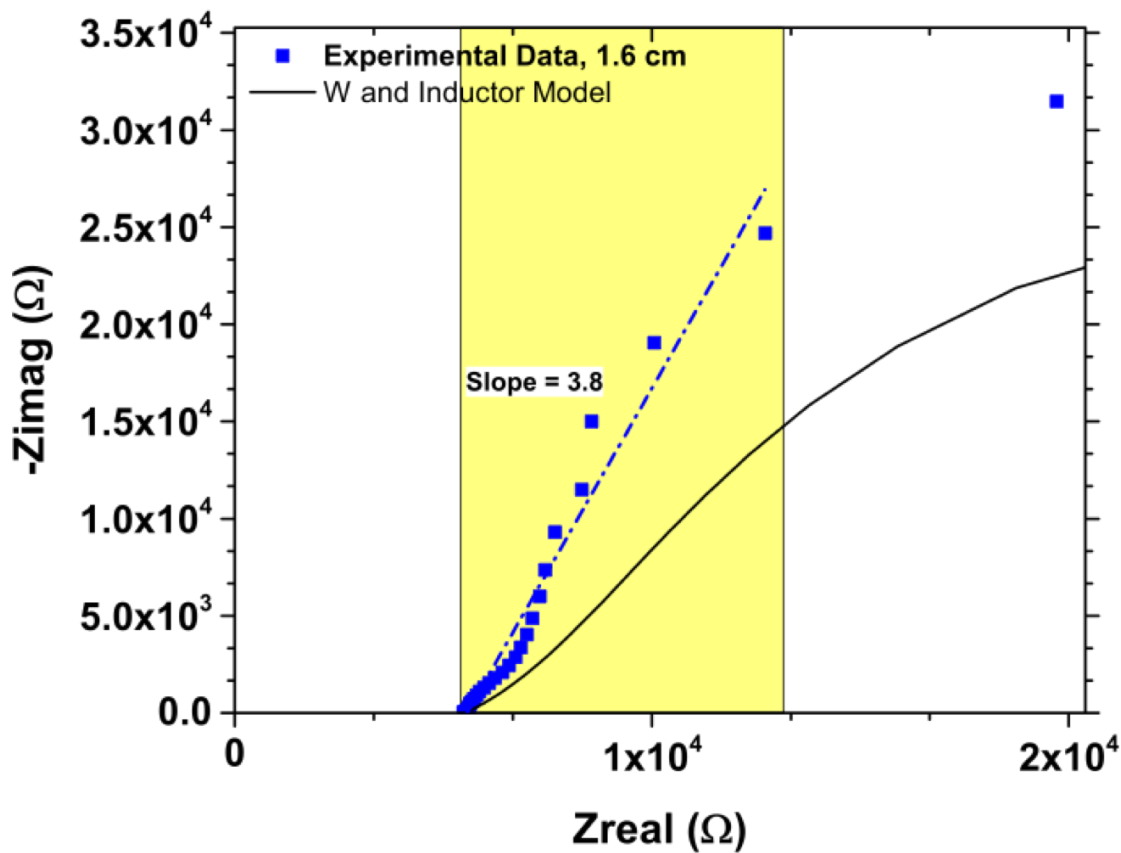


**Figure A-6:** Exploded view of Bode diagram of EGaIn (1.6 cm in length) from Fig. 2-9d at high frequency range. Blue square data points are of experimental data. Black line is the model fit of the Warburg model (with inductor element). Blue dotted line is a linear fit of experimental data in the region marked by yellow. Slope of fitted line is 3.8. Fitting is performed using Origin 2016 plotting software.

**Table A-6:** Model parameters for 1.6 cm EGaIn plug in 1 M NaOH. Standard deviations are from model fits of 100 iterations.

<b>Model   Component</b>	<b>Goodness of Fit</b>	<b>R<sub>elec</sub> (Ω)</b>	<b>Std. Dev.</b>	<b>R<sub>sol</sub> (Ω)</b>	<b>Std. Dev.</b>	<b>R<sub>slip</sub> (Ω)</b>	<b>Std. Dev.</b>
<b>Inductor</b>	1.53E-03	3.54E+05	1.13E+04	5.64E+03	0.00E+00	1.05E+04	6.96E+02
<b>Control (CPE, no Inductor)</b>	1.55E-02	3.79E+05	1.13E+04	5.64E+03	0.00E+00	1.05E+04	6.96E+02
<b>Inductor (W instead of CPE)</b>	2.26E-02	3.50E+05	0.00E+00	5.52E+03	0.00E+00	915.9	425.4

<b>Model Component</b>	<b>C<sub>elec</sub> [F]</b>	<b>Std. Dev.</b>	<b>Y<sub>o</sub> [S*s<sup>α</sup>]</b>	<b>Std. Dev.</b>	<b>α</b>	<b>Std. Dev.</b>	<b>Y<sub>o</sub> [S*s<sup>1/2</sup>]</b>	<b>Std. Dev.</b>	<b>L<sub>slip</sub> [H]</b>	<b>Std. Dev.</b>
<b>Inductor</b>	5.44E-07	8.08E-09	1.13E-06	6.84E-08	8.02E-01	9.77E-03	N/A	N/A	217.1	6.013
<b>Control (CPE, no Inductor)</b>	5.44E-07	8.08E-09	1.13E-06	6.84E-08	8.02E-01	9.77E-03	N/A	N/A	N/A	N/A
<b>Inductor (W instead of CPE)</b>	5.09E-07	0.00E+00	N/A	N/A	N/A	N/A	8.03E-06	1.40E-07	252.2	7.989

**Table A-7:** Model parameters for 3.6 cm EGaIn plug in 1 M NaOH. Standard deviations are from model fits of 100 iterations. Model parameters for 3.6 cm EGaIn plug in 1 M NaOH. Standard deviations are from model fits of 100 iterations.

Model Component	Goodness of Fit	R <sub>elec</sub> (Ω)	Std. Dev.	R <sub>sol</sub> (Ω)	Std. Dev.	R <sub>slip</sub> (Ω)	Std. Dev.
<b>Inductor</b>	4.07E-03	2.93E+05	1.04E+04	3.81E+03	2.85E+01	7.32E+03	5.10E+02
<b>Control (CPE, no Inductor)</b>	4.79E-02	3.83E+05	0.00E+00	3.91E+03	0.00E+00	2.69E+04	677.7
<b>Inductor (W instead of CPE)</b>	3.56E-02	2.51E+05	6.81E+03	3.16E+03	27.94	100.3	468.2

Model Component	C <sub>elec</sub> [F]	Std. Dev.	Y <sub>o</sub> [S*s <sup>α</sup> ]	Std. Dev.	α	Std. Dev.	Y <sub>o</sub> [S*s <sup>1/2</sup> ]	Std. Dev.	L <sub>slip</sub> [H]	Std. Dev.
<b>Inductor</b>	7.26E-07	1.05E-08	1.19E-06	5.06E-08	7.85E-01	7.06E-03	N/A	N/A	400.1	6.069
<b>Control (CPE, no Inductor)</b>	1.08E-06	1.90E-08	2.96E-07	1.83E-08	9.70E-01	9.69E-03	N/A	N/A	N/A	N/A
<b>Inductor (W instead of CPE)</b>	6.67E-07	9.65E-09	N/A	N/A	N/A	N/A	6.73E-06	9.75E-08	380.9	8.691

#### Capacitance estimation

Capacitance estimation for EIS spectra is done using a graphing analytical technique reported in literature for electrodes used for electrowetting systems.<sup>32</sup> The  $\alpha$  coefficient is determined based on the EIS model fit of the experimental data using Gamry E-Chem Analyst software. Thereafter, the effective capacitance ( $C_{eff}$ ) is calculated using Equation 1, where based  $f$  is for frequency and  $Z_j$  is the real component of impedance ( $Z_j$ ). An average of  $C_{eff}$  over all frequency determines the overall capacitance estimate

$$C_{eff} = \sin\left(\frac{\alpha\pi}{2}\right) \times \frac{-1}{Z_j(2\pi f)^\alpha} \quad (\text{Equation 1})$$

## APPENDIX B

### SUPPORTING INFORMATION FOR CHAPTER 3

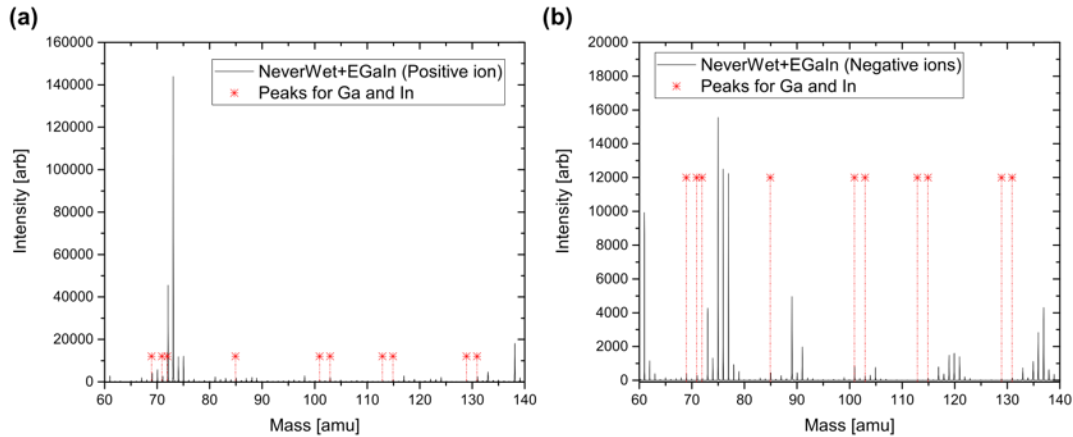


**Figure B-1:** TOF-SIMS spectra of NeverWet sample after being grazed with EGaIn; afterwards, the liquid metal or its oxide does not adhere to the surface or leave a microscopic residue. TOF-SIMS spectra shows that there is no nano-scale residue or imprint of Ga, In, and their oxides. Data shows spectra of positive ions (a) and negative ions (b) associated with NeverWet (black). Spectra associated with Ga, In, and their oxides are denoted by red star and dotted drop lines. The placement of the red stars, relative to the vertical axis, is arbitrary.

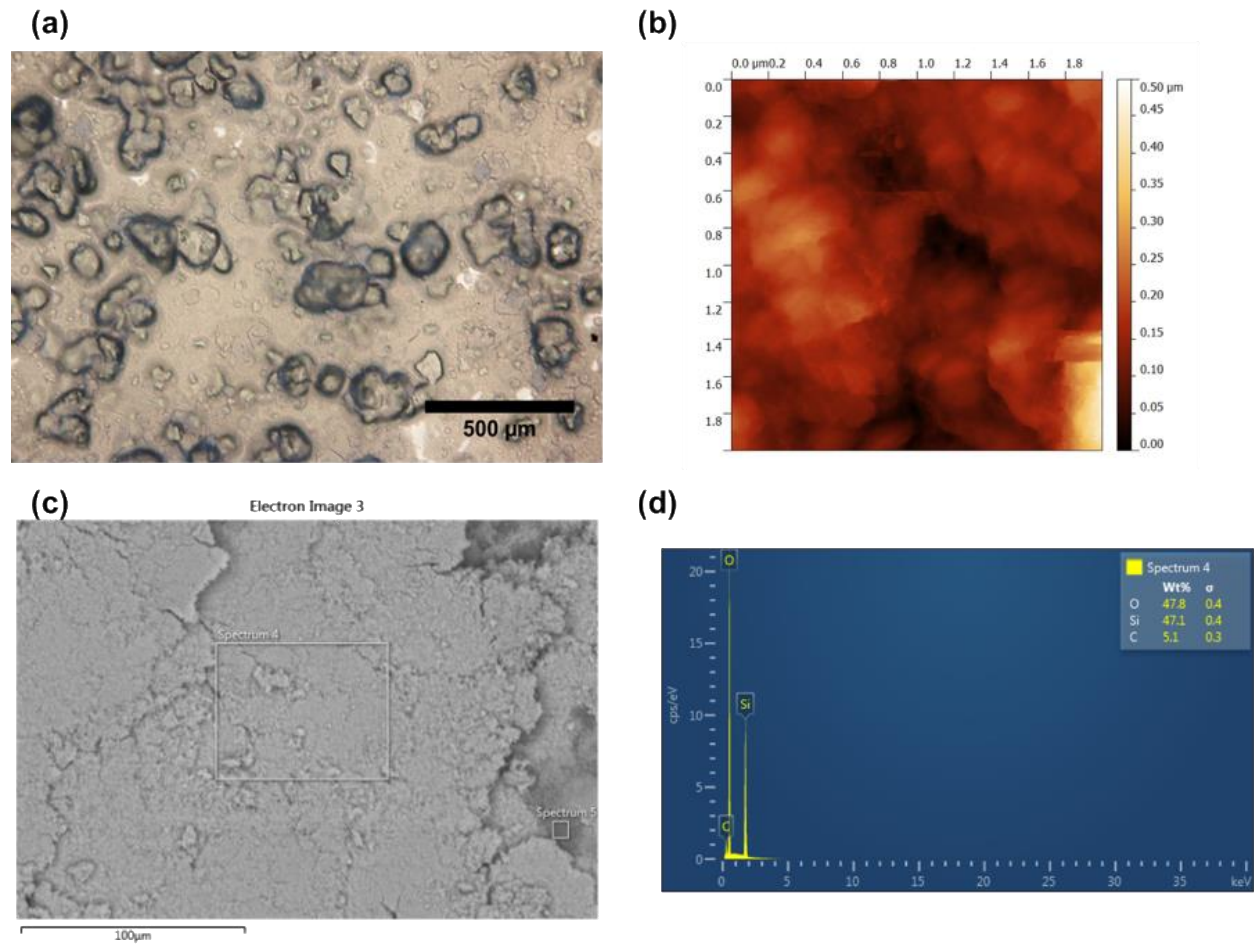


**Figure B-2:** Surface characterization of NeverWet. (a) Optical micrograph of NeverWet coating at 5x resolution. Large clusters of particles (~100 to 300 μm) are scattered across the surface, in a non-repetitive fashion. (b) AFM measurement of NeverWet coating shows spherical particles composing the NeverWet. (c) SEM micrograph of NeverWet at higher resolution shows clusters of nanoparticles that compose the surface of NeverWet. (d) EDS spectra of "Spectrum 4" (boxed area in (c)) shows that the surface comprises only of Si, C, and O.

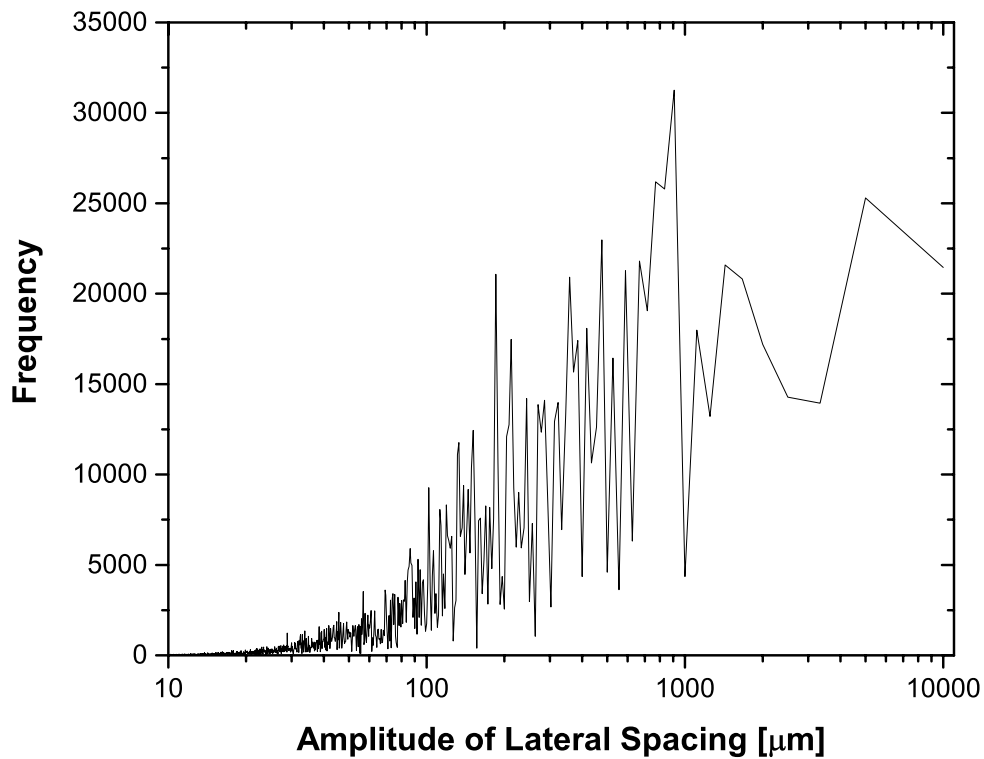


**Figure B-3:** Fast Fourier Transform (FFT) of profilometry scan (as shown in Fig. 2c). The graph depicts the frequency (y axis) of spacing between particle clusters that compose the surface (x axis, log-scale). Based on this analysis, the roughness of the surface varies from ~50s  $\mu\text{m}$  to ~1000  $\mu\text{m}$ . The roughness at larger length scales (~500  $\mu\text{m}$ s and greater) is likely due to variations in the thickness and uniformity of the surface coating (because it is spray coated by hand). Meanwhile, the roughness of lower length scales is due to the coating itself.

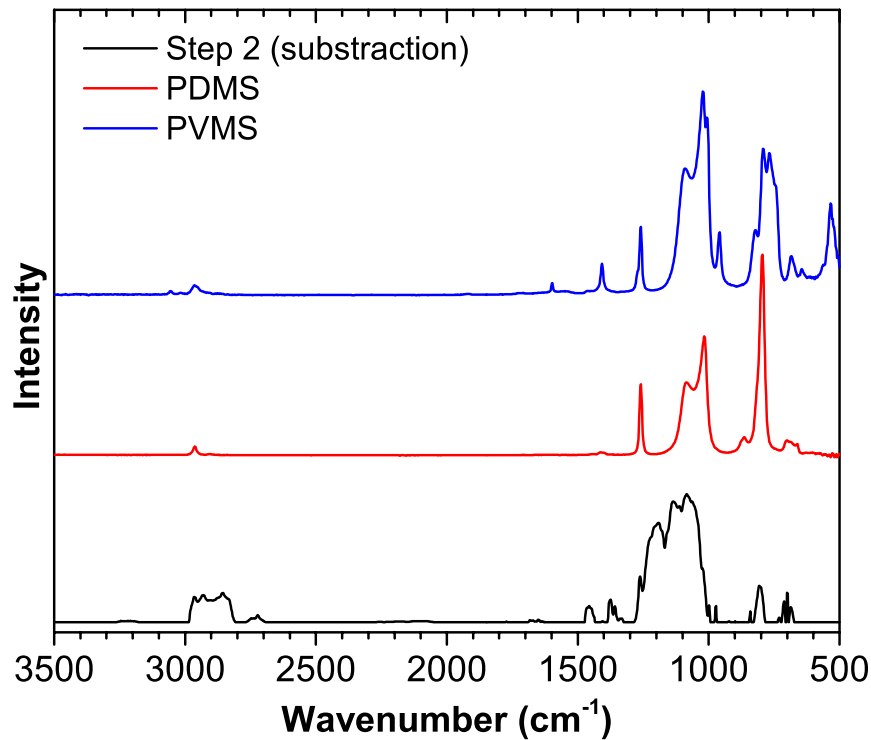


**Figure B-4:** FTIR spectra of Step 2 of NeverWet (subtraction, black bottom line) in comparison to PDMS (red line, middle) and PVMS (blue line, top).

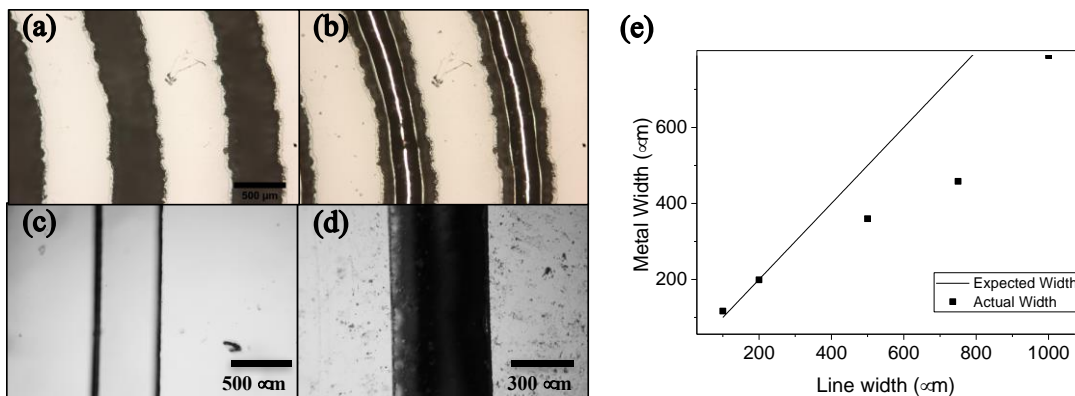


**Figure B-5:** Accuracy of patterning traces. (a) Laser cut channel before injection, (b) after injection, (c) PDMS microchannel (made using soft lithography) before injection (d) PDMS microchannel after injection, (e) Examining accuracy of laser cut channels as a function of line width. Y-axis shows the width of the metal within the channel. X-axis denotes the designed line-width (i.e., width of microchannel prior to injection). For larger widths ( $>500 \mu\text{m}$ ), the width of the metal in the microchannel does not follow a linear trend. This phenomenon occurs because the metal does not adhere to the side walls of the microchannel. Concurrently, the high surface tension of the metal causes the metal to minimize its surface area; thus, it retracts away from the side walls of the channel.

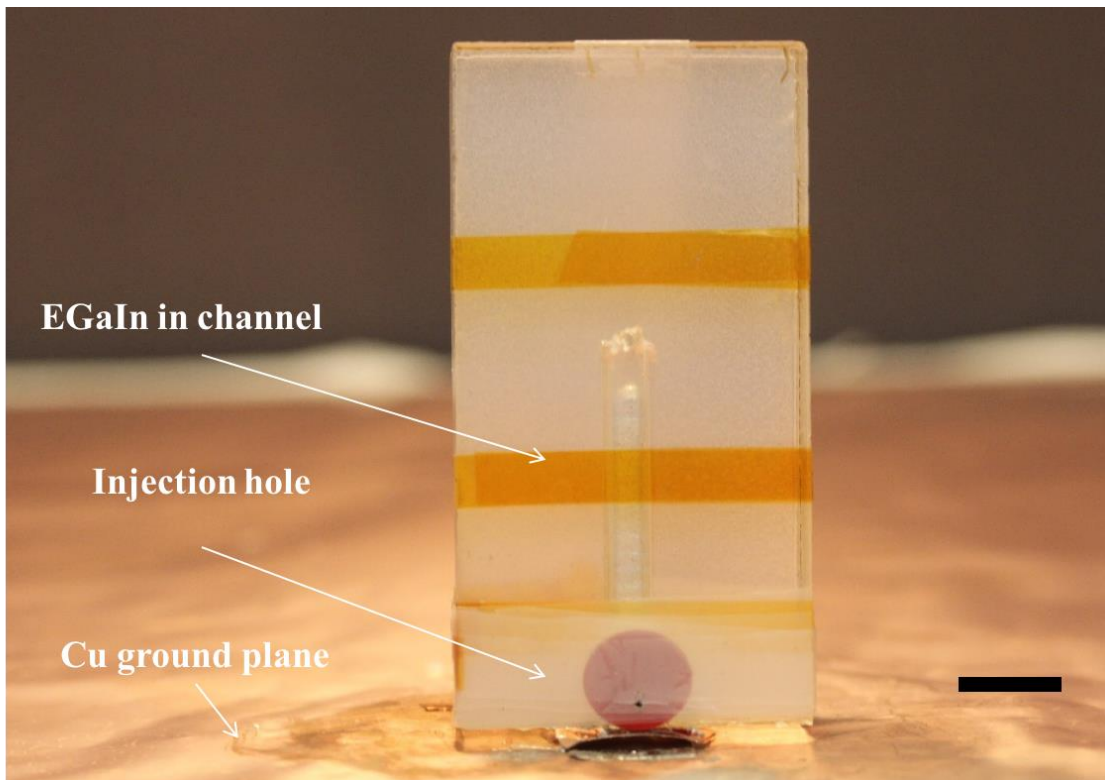


**Figure B-6:** Photograph of the prototype reconfigurable antenna shown in Figure 6. Scale bar is 1.0 cm.

#### *Coating procedure*

The durability of a NeverWet coating, as well as how much EGaIn might adhere to a given NeverWet coating, was highly dependent on the technique used to apply the NeverWet. The optimal coating were produced when only two light coats of base coat were used, followed by drying in a fume hood for 30 minutes. Thereafter, we applied four light coats of the top coat. Allowing the top coat dry overnight before use made the coats significantly less likely to begin to deteriorate with time; we note that only about 30 minutes was necessary for the surface to be effective. Here, we define a light coat as not spraying any part of the substrate for more than 2 seconds per coat. When too much base coat was used, we found that the resulting final coatings often tended to flake. When less top coat was used, we found that this often made the resulting surface less non-wetting. Furthermore, we found that when applying NeverWet to a soft surface such as PDMS, it was often better to use slightly less top coat in order to allow the NeverWet to

stretch and flex with the substrate without damaging the NeverWet coat. When applying NeverWet to the interior of microchannels, we found that it was very important to spray from all angles. Finally, for microchannels much smaller than 250  $\mu\text{m}$  in diameter we found that the NeverWet would tend to just coat over the channel instead of simply coating the walls.

#### *Procedure for patterning liquid metal traces*

For materials such as PDMS, which have a tendency to burn under the laser cutter, the process is more challenging. For these materials, it is necessary to make multiple low power passes with the laser cutter when patterning channels. This results in patterning materials such as PDMS, taking somewhat longer. Due to the flexibility of elastomer, it is difficult to inject liquid metal with even pressure when placed against a rigid NeverWet slide. Furthermore, PDMS channels often collapse when fabricated at very small scale patterns (i.e., less than 200  $\mu\text{m}$ ). To overcome these challenges, we ‘sandwich’ the patterned PDMS between two rigid sheets (i.e., PMMA). Syringe-sized holes are cut on one rigid sheet at the locations of the entry and exit holes for a given pattern. Meanwhile, the sheet in contact with the PDMS channel must be coated with NeverWet. This additional step allows for even pressure when injecting the liquid metal inside the PDMS microchannel.

This patterning method is limited by several factors. The total time for the process is limited to the speed of the ablation or cutting step; this time varies based on the desired depths of the microchannel and substrate. In addition, the feature size is also limited by the cutting or ablation process. For example, the resolution of a laser cutter is dependent on the wavelength ( $\lambda$ ) of laser source; this work uses a carbon dioxide laser ( $\lambda=10.6 \mu\text{m}$ ) with a resolution near 100  $\mu\text{m}$ . However, at this length scale, the presented patterning method is further complicated; applying even pressure to the substrate is difficult. As a result, liquid metal from spilling out of the channels

while injecting. First, the microchannels are not sealed permanently to the substrate. Thus, the metal can leak during injection if care is not taken to push the elastomer against the substrate. This challenge is likely due to the higher Laplace pressure required to inject metal into smaller microchannels.<sup>1</sup>

#### *Procedure of reversible actuation in closed channel*

To form this device, we apply NeverWet to both a flat substrate and another substrate with a molded channel. The two substrates are placed against each other to form the closed channel, whose walls are coated with NeverWet. In this work, polyamide tape secures both substrates; however, other methods of sealing the device are also possible. Placing a large puddle (~ 1 mL) of EGaIn at one end of the channel and encapsulating it with PDMS forms the reservoir.

Unfortunately, this method has certain number of limitations. First, this method is only effective for relatively large channels. As a result, we were able to simply etch the surface of a substrate using a laser writer creates the microchannels used for actuation rather than use photolithography. In addition, applying a uniform coating at the corners of the channels is a challenge. This issue is exasperated for smaller channel widths. For channels with a width or depth smaller than about 750  $\mu\text{m}$ , sticking of the metal to channel walls becomes significantly more likely. Furthermore, even for channels with mm-scale dimensions, sticking begins after 50 cycles of actuation if NeverWet is coated unevenly. Despite these limitations, this approach is a marked improvement for actuating liquid metal without any pre-treatment. Moreover, the coating is commercially available and the spray procedure is straightforward.

#### *Procedure for antenna device fabrication*

The PMMA block is secured atop a copper ground plane. We solder a panel SubMiniature A (SMA) connector such that the signal pin goes through the ground plane. The PMMA block and

ground plane are adhered using super glue to form a snug connection. An etched PMMA block and a planar glass slide form the antenna device, both of which are coated with NeverWet. A rectangular-shaped microchannel (4.75 cm, in length, and 5.0 mm, in width) is etched using a laser writer. Liquid metal injects through a small circular hole (one mm, in diameter) at the bottom of the channel. An elastic membrane covers this hole to form a septum for injecting liquid metal; this septum also prevents the metal from leaking out of the channel (due to gravity or external pressure). An additional hole ('signal pinhole', one mm, in diameter) is drilled into the bottom face of the PMMA. The signal pinhole extends from the bottom face of the PMMA to the injection hole. The purpose of the signal pinhole is to connect the PMMA block to the ground plane, which is made from a large copper sheet (64 cm, in both length and width). A glass substrate, coated with NeverWet, is placed over the PMMA block to close the microchannel. The glass substrate also contains a circular hole, slightly larger than one mm in diameter, that overlays over the injection hole. An elastic membrane is placed over the glass hole to form the septum. Finally, polyamide tape secures the PMMA block and glass slide together to form the device.

For antenna testing, antenna device connects to a network analyzer using a coaxial cable connected to the SMA connector. During antenna testing, the network analyzer feeds the antenna with signals at various frequencies. Thereafter, the instrument measures the amount of signal that returns; any energy that does not return is assumed to radiate.

#### *X-ray photoelectron spectroscopy (XPS)*

Surface chemical analysis was performed using a Kratos Analytical Axis Ultra spectrometer at a take-off angle of 90° (i.e., angle between the plane of the film and the entrance lens of the detector optics). The XPS used an aluminum monochromated x-ray source. The pass energies used were 160 and 20 eV for survey and high resolution respectively. The resolutions

used were 1 and 0.1 eV for survey and high resolution respectively. All spectra were calibrated to the carbon aliphatic peak (285 eV) and were analyzing using the CasaXPS software. All synthetic components were modeled using Gaussian-Lorentzian peaks.

#### *Fourier-transfer infrared spectroscopy (FT-IR)*

Infrared spectra were taken using a Nicolet 6700 infrared spectrometer in attenuated total reflection (ATR) mode scanning between 500 and 4000  $\text{cm}^{-1}$  with a resolution of 4  $\text{cm}^{-1}$  and 512 scans per sample.

#### *Roughness calculations*

The center line was determined by doing a linear regression on the raw data. For the arithmetic average roughness ( $R_a$ ) the following equation was used:

$$R_a = \frac{1}{n} \sum_{i=1}^n |y_i|$$

Where, n is the number of data points and  $y_i$  is the distance from the center line to the  $i^{\text{th}}$  data point

For the root mean squared roughness ( $R_{RMS}$ ) the following equation was used:

$$R_{RMS} = \sqrt{\frac{1}{n} \sum_{i=1}^n y_i^2}$$

#### **References**

- (1) Dickey, M. D.; Chiechi, R. C.; Larsen, R. J.; Weiss, E. A.; Weitz, D. A.; Whitesides, G. M. Eutectic Gallium-Indium (EGaIn): A Liquid Metal Alloy for the Formation of Stable Structures in Microchannels at Room Temperature. *Adv. Funct. Mater.* **2008**, 18 (7), 1097–1104.

## APPENDIX C

### SUPPORTING INFORMATION FOR CHAPTER 4

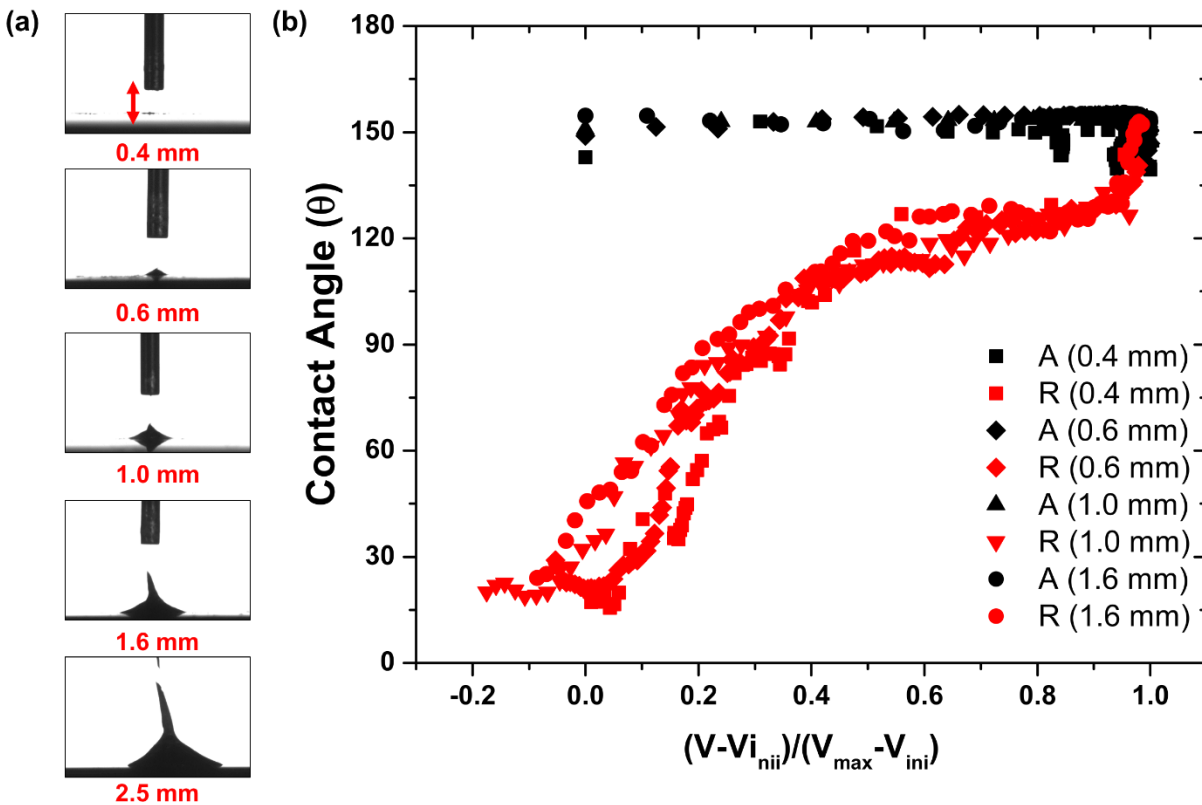


**Figure C-1:** (a) Side-view photographs of EGaIn residue on silane-treated glass after advancing and receding measurements varying in height between needle and substrate (red arrow on top photograph, height enumerated in red below each photograph). (b) Advancing (black) and receding (red) contact angle measurements as a function of scaled volume for varying needle heights.

Our initial experiments found that the position of the needle, relative to the drop and substrate, was an important parameter for the interpretation of the data from the receding phase of the experiment. For these experiments, we define ‘h’ as the distance between the end of the needle and substrate. First, we form a pendant drop of liquid metal and slowly make contact between the drop and the substrate. Thereafter, we adjust ‘h’ to the designated value for the experiment; in some cases, we lower the needle further into the drop to reach the desired ‘h’ value. **Figure C-1**

shows the contact evolution of the experiments, where  $h$  ranges from 0.4 mm to 2.5 mm. Fig. C-1a shows images, for several values of  $h$ , of the remaining residues of liquid metal drop.

In general, we find that  $h \geq 1$  mm is too far of a distance between the needle and substrate. In this regime, during the receding phase of the dynamic contact angle experiments, a liquid bridge forms between the end of the needle and majority of the liquid drop that rests on the surface. As more volume is withdrawn from the drop, the bridge becomes thinner and eventually breaks from the underlying drop. As a result, a substantial volume of the drop remains on the underlying substrate. This drop is shown in Fig. C-1a. Consequently, the value for  $\theta_R$  is too high of a value at the end of the experiment. Thus, having  $h \geq 1$  mm from the substrate can lead to misleading interpretation of  $\theta_R$ . Previous work from literature also cautions keeping the needle close to the substrate.<sup>[45]</sup>

Likewise, keeping the needle too close ( $h < 0.5$  mm) to the substrate is not ideal for both advancing and receding phases of the measurement. During the advancing phase, the drop does not grow in an axi-symmetric manner; that is, liquid expands preferentially to one side of drop when increasing the volume of the drop, as shown in Fig. C-1b. Consequently,  $\theta_A$  may vary between the left and right side of the drop. Although the necking instability that occurs in  $h \geq 1$  mm is avoided, having  $h < 0.4$  mm can also effect the receding phase of the measurements. Because the needle is not axisymmetric to the drop, the rate at which  $\theta_R$  decreases is not consistent around the perimeter of the drop (i.e., left and right side of the drop). Finally, we find that in the range of  $1 < h > 0.5$  mm, the drop is axisymmetric through the experiment. In addition, this needle height range avoids the necking instability and prevents the abrupt end to receding measurements. Accordingly, apparent receding angle reaches to lower values ( $< 90^\circ$ ) as the volume almost entirely recedes from the substrate.

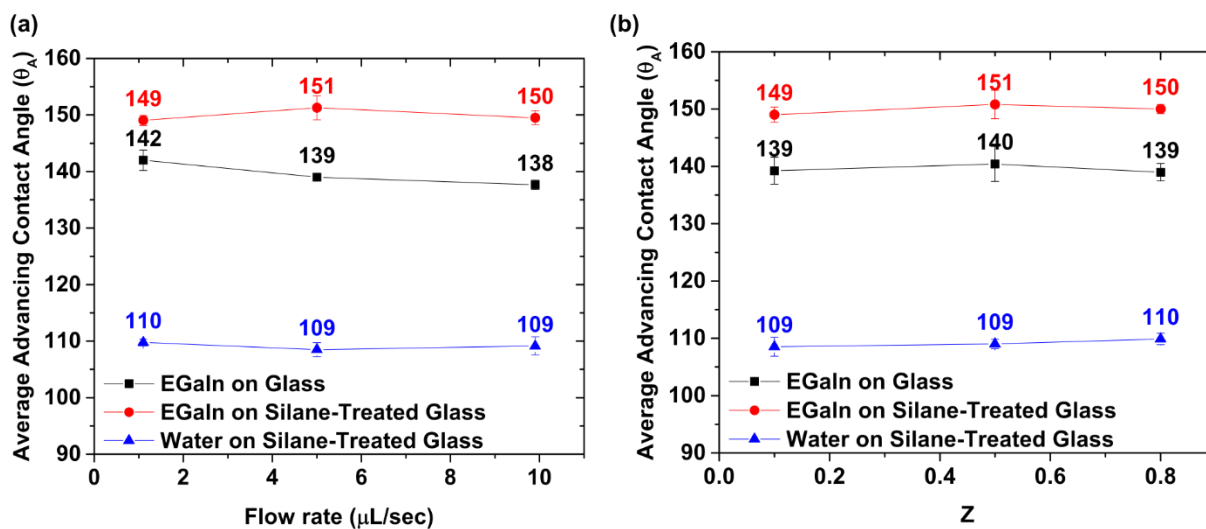


**Figure C-2:** (a) Average advancing angles of EGaIn on glass, EGaIn on fluoro-silane treated glass, and water on fluoro-silane treated glass as a function of the flow-rate. (b) Average advancing angles for the same surfaces as (a), as a function of Z, which is a ratio of the distance between the needle and substrate to axial length of the drop.

**Table C-1:** Effect of flow rate on advancing and receding contact angles for DI water on silane-treated glass. Average and standard deviation values are provided of three experimental trials. Total average and standard deviation values are of the average values for all flow rates.

Water on silane-treated glass				
Flow rate ( $\mu\text{L/sec}$ )	Average Advancing Angle	Std. Dev.	Average Receding Angle	Std. Dev.
1.1	109.8	0.6	86.9	0.2
5	108.5	1.2	86.4	2.4
9.9	109.1	1.6	86.4	1.17
<b>Total Average</b>	109.1		86.6	
<b>Std. Dev.</b>	0.64		0.25	

**Table C-2:** Effect of flow rate on advancing and receding contact angles for EGaIn on glass and silane-treated glass. Average and standard deviation values are provided of three experimental trials. Total average and standard deviation values are of the average values for all flow rates.

EGaIn on Glass			EGaIn on Silane-treated Glass	
Flow rate ( $\mu\text{L}/\text{sec}$ )	Average Advancing Angle	Std. Dev.	Average Advancing Angle	Std. Dev.
1.1	142.0	1.8	149.1	0.9
5	139.0	0.24	151.3	2.1
9.9	137.6	0.86	149.5	1.3
<b>Total Average</b>	139.6		150.0	
<b>Std. Dev.</b>	2.2		1.2	

*Further investigation on drop sagging: pendant drops in air*

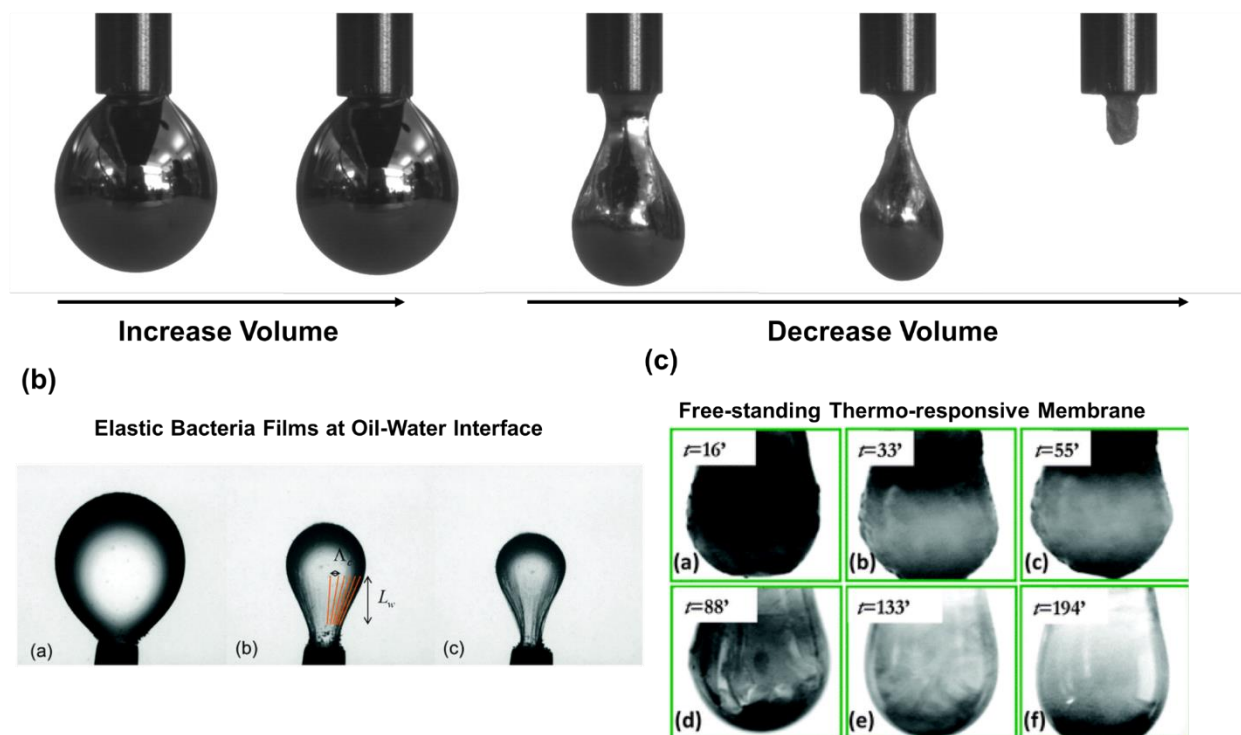


**Figure C-3** Pendant drop experiments. (a) Pendant drop of EGaIn increases in volume (first two images from left). As the volume is reduced from the drop (third and fourth image), the metal drop elongates due to gravity and forms wrinkles on its surface. At the end of the experiment, the remaining oxide skin hangs from the needle. (b) Buckling during compression of an elastic film of bacteria at the interface of oil and water. Reproduced from literature.<sup>[55]</sup> (c) Buckling of a thermo-responsive, free-standing membrane as the drop is compressed internally. Reproduced from literature.<sup>[56]</sup>

In addition, we perform experiments on pendant drops of the liquid metal (drops hanging in air from a needle and do not rest on any surfaces). **Figure C-3a** shows the time evolution of a pendant drop experiment. In these experiments, we first grow a drop of liquid metal to a given volume (to mimic or parallel the ‘advancing’ phase of dynamic contact angle measurement). Thereafter, we decrease the volume of the pendant drop. At the onset of the decreasing the volume, buckles appear at the top of the drop (where the oxide is in contact and pinned to the needle). Concurrently, the axial length of the drop (top to bottom of drop) elongates due to it losing tension. As more volume is removed (i.e., liquid enveloped by the oxide), the oxide ‘skin’ is compressed because it maintains roughly the same surface area. The compression causes further buckling of the skin, which now propagate through the exterior surface of the pendant drop. At the end of the experiment, the remaining oxide skin hangs from the needle, presumably with some nominal liquid on the interior; this structure is analogous to an empty pouch that does deform due to lack of an interior pressure. This sagging behavior is observed across a range of needle diameters (gauge 14 to 28) as well as for needle tips that are conical.